CLEAN METAL CASTING

FINAL REPORT

By

Makhlouf M. Makhlouf
Diran Apelian

February 5, 2002

Work Performed Under Contract No. DE-FC07-94ID13234

Prepared for
US Department of Energy
Office of Industrial Technologies

Prepared by
The Advanced Casting Research Center
Worcester Polytechnic Institute
Worcester, Massachusetts 01609

This report has been reproduced from the best available copy.

This report is available in paper copy and microfiche.

Number of pages in this report: 265

DOE and DOE contractors can obtain copies of this report from:
Office of Scientific and Technical Information
P.O. Box 62
Oak Ridge, TN 37831
(615) 576-8401

This report is publicly available from
Department of Commerce
National Technical Information Services
5285 Port Royal Road
Springfield, VA 22161
(703) 487-4650

REPORT DOCUMENTATION PAGE

1. AGENCY USE ONLY (LEAVE BLANK)

2. REPORT DATE

February 5, 2002

3. REPORT TYPE AND DATES COVERED

Final (project start – project end)

4. TITLE AND SUBTITLE

Clean Metal Casting

5. FUNDING NUMBERS

6. AUTHORS

Makhlouf M. Makhlouf and Diran Apelian

7. PERFORMING ORGANIZATION NAME(S) AND ADDRESSE(S)

Advanced Casting Research Center
Worcester Polytechnic Institute
Worcester, Massachusetts, 01609

8. PERFORMANCE ORGANIZATION REPORT NUMBER

9. SPONSORING MONITORING AGENCY NAME(S) AND ADDRESSE(S)

DOE Idaho Operations Office
850 Energy Drive, MS 1220
Idaho Falls, ID 83401-1563

10. SPONSORING MONITORING AGENCY REPORT NUMBER

11. SUUPLEMENTARY NOTES

Work performed under DOE contract number DE-FC07-94ID13234

12. a. DISTRIBUTION AVAILABILITY STATEMENT

Distribution of this document is unlimited.

12.b. DISTRIBUTION CODE

UC-108

13. ABSTRACT (*Maximum 200 words*)

The objective of this project is to develop a technology for clean metal processing that is capable of consistently providing a metal cleanliness level that is fit for a given application. The program has five tasks: Development of melt cleanliness assessment technology, development of melt contamination avoidance technology, development of high temperature phase separation technology, establishment of a correlation between the level of melt cleanliness and as cast mechanical properties, and transfer of technology to the industrial sector. Within the context of the first task, WPI has developed a standardized Reduced Pressure Test that has been endorsed by AFS as a recommended practice. In addition, within the context of task1, WPI has developed a melt cleanliness sensor based on the principles of electromagnetic separation. An industrial partner is commercializing the sensor. Within the context of the second task, WPI has developed environmentally friendly fluxes that do not contain fluorine. Within the context of the third task, WPI modeled the process of rotary degassing and verified the model predictions with experimental data. This model may be used to optimize the performance of industrial rotary degassers. Within the context of the fourth task, WPI has correlated the level of melt cleanliness at various foundries, including a sand casting foundry, a permanent mold casting foundry, and a die casting foundry, to the casting process and the resultant mechanical properties. This is useful in tailoring the melt cleansing operations at foundries to the particular casting process and the desired properties of cast components.

14. SUBJECT TERMS

Aluminum alloys, molten metal, casting.

15. NUMBER OF PAGES

265

16. PRICE CODE

17. SECURITY CLASSIFICATION OF REPORT

Unlimited

18. SECURITY CLASSIFICATION OF THIS PAGE

Unlimited

19. SECURITY CLASSIFICATION OF ABSTRACT

Unlimited

20. LIMITATION OF ABSTRACT

Unlimited

CONTENTS

EXECUTIVE SUMMARY

This program of research was initiated in June 1994 and was approved by DOE as a five-year program with milestones, and a go-no-go decision at the end of the second year. The second-year critical review took place on August 22, 1996. The recommendation of the review panel was that the program is valid and should be continued with some modifications of the tasks. A second critical review took place on September 1998. The recommendation of the review panel was that the program continues to be valid and should be continued with no modifications of the tasks.

The overall goal of the program is to secure for the US metal casting industry a preeminent position in the global market through technological competence and innovation, and through monitoring of international standards via benchmarking. The research focuses on developing a technology for clean metal processing that is capable of consistently providing a metal cleanliness level that is fit for a given application.

The program has five tasks: Development of melt cleanliness assessment technology, development of melt contamination avoidance technology, development of high temperature phase separation technology, establishment of a correlation between the level of melt cleanliness and as cast mechanical properties, and transfer of technology to the industrial sector. Within the context of the first task, WPI has developed a standardized Reduced Pressure Test that has been endorsed by AFS as a recommended practice. In addition, within the context of task1, WPI has developed a melt cleanliness sensor based on the principles of electromagnetic separation. An industrial partner is commercializing the sensor. Within the context of the second task, WPI has developed environmentally friendly fluxes that do not contain fluorine. Within the context of the third task, WPI modeled the process of rotary degassing and verified the model predictions with experimental data. This model may be used to optimize the performance of industrial rotary degassers. Within the context of the fourth task, WPI has correlated the level of melt cleanliness at various foundries, including a sand casting foundry, a permanent mold casting foundry, and a die casting foundry, to the casting process and the resultant mechanical properties. This is useful in tailoring the melt cleansing operations at foundries to the particular casting process and the desired properties of cast components.

Chapter 1

MELT CLEANLINESS ASSESSMENT

1. INTRODUCTION

Aluminum alloy cleanliness has been in the limelight during the last two decades and still remains one of the top concerns in the aluminum casting industry. In general, the cleanliness of an aluminum alloy is referred to as minimizing the following contaminants: 1) dissolved H, 2) alkaline elements, such as Na, Li and Ca, and 3) inclusions. Extensive research has made great progress in the fundamental understanding of the various aspects of these contaminants, and in many companies an inclusion removal practice has been established and routinely used, and the removal of H and alkaline elements has been an indispensable melt treatment procedure. However, with the ever-increasing demands for improved alloy properties, requirements for the alloy cleanliness become more and more stringent, and more and more foundries pay closer attention to their alloy cleanliness. This brings about a pressing need for more effort in this area. Accordingly, a major research project on aluminum alloy cleanliness has been funded by the U.S. Department of Energy and carried out at the Aluminum Casting Research Laboratory (ACRL) at Worcester Polytechnic Institute (WPI). As part of this project, a critical review of various aspects of aluminum alloy cleanliness has been conducted. The present contribution is a survey of the accomplishments in the research of H in aluminum alloys, its measurement and the development of H removal. In this survey, more attention is paid to the technical aspects, which are related to the production practice, than to the deep theoretical analysis and mathematical description of mechanisms involved. This technical information is presented in the following three sections. The first is a brief summary of the H initiation in aluminum alloys, the porosity formation, and its effects. The second is a comprehensive review of the H measurement, which is further divided into two portions: the H solubility measurement and the H content measurement. The last section concerns the H removal.

1.1 HYDROGEN IN ALUMINUM ALLOYS

Origins of Hydrogen and Its Content

Hydrogen is the only gas with significant solubility in molten aluminum. The principal source of H in aluminum alloys is the moisture in the air. Most of the commercial aluminum alloys are melted in the atmosphere which contains moisture, and the moisture reacts with the melt of aluminum in the oxide layer:

$$2Al + 3H_2O \Leftrightarrow 3H_2 + Al_2O_3 \qquad (1)$$

The H atoms then diffuse through the oxide and react with the melt:

$$H_2 \Leftrightarrow 2H \qquad (2)$$

The second the source of the H is alloy addition. Mg contains H of, typically, 0.5 to 8 ppm because of the high solubility of H in Mg. Other metals such as Ti, Mn and Fe also contain H and can be a major source. The third source is the secondary metal being remelted, which commonly has moisture on the surface. The fourth source is the fuel, oil or gas, used in the furnace, which produces water vapor during burning. Finally, the source can be the refractories and tools. Though there are so many sources for H, its initial concentration in the melt is chiefly determined by the humidity in the furnace atmosphere, and the melt temperature and the composition [1].

The moisture content in the atmosphere varies significantly in different weather conditions. For example, for a relative humidity of 50%, the partial pressure of water vapor in the atmosphere is 0.0443 lb/in^2 at 0°C and 0.535 lb/in^2 at 40°C. The difference is over 12 times. It implies that the alloys melted in hot, humid weather will contain high H content, while in the cold, dry season alloys with very low H content can be produced without degassing.

The H content and solubility in aluminum and its alloys are expressed in milliliters of hydrogen at standard temperature and pressure per 100 grams of metal (ml/100g, at 723 K (0 °C) and 1 atm) or part per million (ppm). Their relationship is: 1 ml/100g = 0.9 ppm = 0.00009%. As can be seen in the next section, Determination of Hydrogen Solubility and Content in Aluminum and Its Alloys, though several equations for calculating H solubility in liquid and solid aluminum and its alloys have been derived from experiments, none of them has been universally accepted. However, there is a consensus on several facts about H solubility among most researchers. The H solubility in both liquid and solid aluminum and its alloys is dependent on temperature, alloy composition, and H partial pressure over the metal. For pure aluminum, at the melting temperature, 660 °C, and 1 atm of H gas, its H solubilities are in the range of 0.67-0.77 ml/100g in liquid and about 0.035 ml/100g in solid. At 730 °C, it is between 1.07-1.25 ml/100g. In the temperature range between the melting point and about 300 °C above, the H solubility is doubling for each 100-120 °C increase in superheat. (The elements in the alloys, some increase and some decrease the H solubility.)

The H solubilities in foundry alloys range from about 0.6 to 1.5 ml/100g at their normal melting temperature range and 1 atm of hydrogen gas pressure. It is, however, very rare for normally produced melts to contain these levels of H [2]. This is because in production the H pressure above the melt is low and the oxide film readily formed on the alloy surface acts as a barrier isolating the melt from the atmosphere to impede excessive H dissolution. The metal from reduction cells contains commonly 0.3 to 0.6 ml/100g after it has been siphoned to the transfer crucible. The H content is further reduced when the metal is poured into the mixing furnace. Typical equilibrium H content in melts is 0.1-0.3 ml/100g alloy and the equilibrium is generally obtained after 2-4 hours of holding time [3]. Though the actual H content in the melt is much lower than its solubility, it is still too high in most cases. It may cause the formation of porosity and, therefore, degassing must be generally employed.

1.1.1 Formation of Porosity from Dissolved Hydrogen

Foundrymen have fought with the microporosity in aluminum alloy castings since the very beginning of the commercial use of aluminum alloys. However, fundamental mechanisms of microporosity formation are still not established very clearly. A generally accepted mechanism is as follows [4, 5]. Suppose that the solubility of H in liquid and solid alloy is in order of 0.65 and 0.035 ml/100, respectively, and the melt initial H content is about 0.2 ml/100g. During solidification, the interdendritic liquid is gradually enriched with H as the fraction solid increases, since most of the H is rejected at the solid-liquid interface. Figure 1 shows the variation of H concentration in the liquid. As solidification progresses, the H content in the liquid increases and eventually exceeds its solubility. Ideally, a gas pore should nucleate at this point. However, the creation of a new pore requires the establishment of a new surface. Because of this surface barrier, the H concentration in the liquid will continue to increase above the solubility until it reaches a value at which pores can form, stage I in Figure 1. At this point, pores begin to nucleate, stage II. This nucleation occurs predominantly at the root of dendrites or at other heterogeneous sites such as inclusions. Since the diameter of the pore is extremely small (<20μm) when the pore begins to grow, the pore grows at a slow rate. Thus, the H concentration in the liquid is not severely affected during this period. After the pore has grown to the full diameter, the bubble may detach itself from the dendrite arm and may be transported into the bulk liquid. During this stage (stage III), the bubble grows instantaneously and hence, the H content of the liquid drops rapidly. Subsequently, the rate of pore formation decreases slightly since the H concentration in the liquid is lowered because of the growth of pores (stage IV). Growth of pores continues until the casting is completely solid.

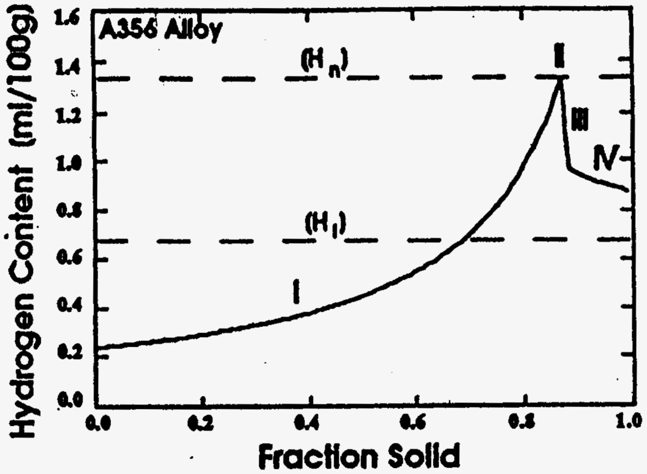

Figure 1. Hydrogen concentration in the dendritic liquid as a function of fraction solid [4].

The H concentration, at which pores begin to nucleate, is a critical value for the pore formation. It depends on the cooling rate rather than on the initial H content. The solid fraction at the beginning of pore nucleation is called threshold fraction of solid, which depends on factors such as alloy composition, initial H content and cooling rate. As the initial H content increases, the critical H concentration in the liquid is attained much faster. Hence, porosity begins to form at relatively small fractions of solid. For example, at a cooling rate of 0.1 °C/s, threshold fraction of solid at initial H contents of 0.1 and 0.5 ml/100g are typically of the order of 0.93 and 0.47, respectively. It is evident that higher initial H content gives pores a longer time to grow, resulting in a greater amount of total porosity and larger pore size. When the initial H content is below about 0.05 ml/100g, the threshold fraction of solid is 1.0, indicating that the porosity formation may be suppressed under these conditions. Because pores nucleate predominantly at the root of dendrites, the pore size will be determined by the dendrite arm spacing (DAS), which, in turn, is determined by the cooling rate. At a higher cooling rate, the size of nucleating pores decreases. Under these conditions the contribution of the surface term increases because of smaller pore size, and pore formation becomes difficult. Thus, greater amounts of H may be tolerated at a higher cooling rate. Shivkumar et al's [5] calculation suggests that at cooling rates of 0.1 and 20 °C/s, the H content that may be tolerated before the onset of porosity is of the order of 0.05 and 0.08 ml/100g. This critical value may be reduced significantly in the presence of large amounts of inclusions. For a given initial H content, an essentially constant value of porosity is observed beyond a cooling rate of about 5 °C/s. Though the pore size is affected by both the initial H content and cooling rate, it appears that the cooling rate has a greater influence. The density of pores is also a strong function of the cooling rate.

Thomas et al. conducted an experiment and analyzed the data obtained by the other researchers to define the H levels necessary to avoid porosity formation during the solidification of aluminum alloys [6]. In the investigation a series of six Al-8%Si alloys with H contents in the range of 0.10-0.82 ml/100g were cast in a water-cooled mold. The study showed that: (1) There was a linear relationship between the H content and level of porosity for the Al-8%Si alloys, which was similar to the results previously observed for other aluminum alloys. (2) A practical threshold H value of approximately 0.8 ml/100g could be defined below which porosity should not occur during solidification. The value was a relatively insensitive parameter and it should apply to most common casting conditions for probably all aluminum alloys. (3) The exact level of porosity is dependent on the local cooling conditions, the lowest porosity being found in the regions of the highest cooling rate.

The pores form mainly during the solidification. In addition, the supersaturated H in the solid may also diffuse, though at a much slower rate than in liquid, into the exiting pores causing porosity growth or even the formation of new pores during service and/or treatment of the casting, which are called the second porosity. This may be a problem in annealing ingots, especially when inclusions are present. However, generally the supersaturated H content is small, the total gas pressure within the pores is very low, and most of the H can escape from the product surface. The dissolved H should not add any significant amount of porosity. In the castings, which usually have a large surface area/volume ratio, the dissolved H is considered to have only a minor effect on the porosity formation.

1.1.2 Effects of Hydrogen on Product Properties

The effect of H on aluminum alloy performance takes place only when it forms pores. In aluminum alloy castings, pores can form because of H as well because of shrinkage. The latter is even more important in the porosity formation. It is very difficult to distinguish which pores form because of H and which because of shrinkage. Actually, most pores form because of both reasons. This renders it difficult to study the H effect, since H exercises the effect through forming pores. Thus, the study of the H effect is usually conducted on a comparative basis. It shows that, generally, H has a negative effect on tensile properties. Take the 356 alloy as an example; the tensile strength and the elongation both are significantly decreased with an increase of H concentration. The yield strength is only very slightly affected because this property is related more to the metallurgical state of the aluminum matrix than to the defects in the structure. The elongation is particularly affected in the castings solidified at high cooling rates, where all the benefits usually resulting from finer microstructures are lost due to porosity. Porosity can be the origin of fatigue cracks that act as sites for stress intensification, and therefore, porosity may reduce the fatigue resistance and impact the strength of the alloy. Porosity may also degrade the pressure tightness of the casting. In addition, porosity may cause a surface problem for the casting that needs to be machined, polished or anodized. In special applications, H may have a positive effect. For example, when the major concern for a casting is the integrity of its as-cast surface, adding H will be helpful, which can compensate the effect of shrinkage to prevent some surface defects. However, these applications are rare.

The tolerable H content in a casting depends on solidification condition, such as thickness of the casting and casting method, and properties required. A final H in the melt below 0.15 ml/100g is usually sufficient for extrusions. For beverage cans, foil, memory disk, and high integrity engineered and automotive aluminum castings a level of 0.10 ml/100g or lower may be required [7].

References

1 Guthrie, R.I.L. and Nilmani, M., "Impurity Sources and Control - - General Pranciples of Metal Treatment." Aluminum Metal Treatment & Casting, Edited by Nilmani, M., TMS, 1993, p85-104.
2 Grusleski, J. E., The Treatment of Liquid Aluminum-Silicon Alloys, AFS Inc. Des Plaines, Ill, 1990, p143-168.
3 Pendersen, T., "Refining Efficiency on Hydrogen, Alkaline Metals and Inclusions in the Hydro Metal Refining System," Light Metals 1991, TMS, Edited by Elwin L. Rooy, p1063-1067.
4 Zou, J., Tynelius, K., Shivkumar, S., and Apelian, D., "Microporosity Formation in A356.2 Castings," Proceedings of the International Symposium on Production, Refining, Fabrication and Recycling of Light Metals, Hamilton, Ontario, Canada, Aug. 26-29, published by the Canadian Institute of Metallurgists, 1990, p323-332.
5 Zou, J., Shivkumar, S., and Apelian, D., "Modeling of Porosity Formation in Grain Refined Aluminum Castings," Proceedings of the Symposium of Process Modeling, TMS-AIME Annual Meeting, Feb. 1991, published by TMS-AIME, Warrendale, PA.
6 Thomas, P. M., and Grusleski, J. E., "Threshold Hydrogen for Pore Formation During the Solidification of Aluminum Alloys -- Communications", Metall. Trans. B, March 1978, Vol. 9B, p139-141.
7 Neff, D. V., "Degassing and Cleaning of Molten Aluminum," Proceedings of 3rd International Conference on Aluminum Processing, Vol. I, May 26-29, 1994, Westin Regina Hotel-Cancun, Q. R., Mexico, p57-72.

1.2 DETERMINATION OF HYDROGEH SOLUBILITY IN ALUMINUM AND ITS ALLOYS

1.2.1 Measurement of H Solubility in Pure Liquid Aluminum

For aluminum and its alloys, information about hydrogen solubility is essential for understanding the hydrogen behavior in melting and casting of the alloys, the porosity formation and degassing. The values of H solubility are also the fundamental data for measuring H content using some H measurement equipment. Thus, the determination of H solubility started soon after aluminum alloys were in commercial use. It can be dated back to the early 1920's. Several methods were used for the measurement in the early study, including the sudden exhaustion of the atmosphere above the metal saturated with H, followed by degassing of the metal itself; quenching of the liquid metal after it has been saturated by contact with the desired atmosphere, followed by a determination of the gas retained in the solid solution; and the direct absorption method, the Sieverts' method. Among these methods only the direct absorption method was successful and it was used favorably by later researchers and considered to be the standard method. Because of the difficulty in the measurements the early data given by different researchers showed considerable divergence, especially at temperatures near the freezing point of the metal. By the late 1940's the H solubility in pure aluminum under 1 atm H_2 pressure and at about 700 °C varied in the range of 0.08 to 0.95 ml/100g reported by different research groups [1-4]. The generally accepted value at 700 °C was about 0.25 ml/100g and the interpolated value at 730 °C, the normal holding temperature for pure aluminum and its alloy during melting, was about 0.4 ml/100g. Feeling these values were too low, in 1948 Ransley et al. re-determined the values in the important temperature range of 660 - 850 °C using the direct absorption method [5]. The results indicated that in the temperature range 670 - 850 °C, the solubility *S* (ml/100g) was given by the equation:

$$\log\frac{S}{\sqrt{p}}=\frac{-2760}{T}+1.356 \qquad (3)$$

where *P* is the partial H_2 pressure in mm of mercury and *T* is the absolute temperature. At the standard hydrogen pressure P_o, 760 mm of mercury (1 atm), the solubility S_o would be:

$$\log S_o = \frac{-2760}{T} + 2.796 \qquad (4)$$

It has been recognized that Ransley's work offered the first reasonably accurate result and it has been frequently referred to. Since then many other researchers have made efforts to check and refine the results obtained previously. Among them the following work is representative.

In the 1950, Opie et al. [6] determined the solubility S_0 in pure aluminum and some of its binary alloys. For pure aluminum the S_0 at 700 °C to 1000 °C was given as:

$$\log S_0 = \frac{-2550}{T} + 2.62 \qquad (5)$$

In the middle 1980's, Talbot and Anyalebechi measured the H solubility of pure aluminum and some Al-Li binary alloys for temperatures of 943 to 1123 K (670 to 850 °C) and pressures of 67 to 113 Kpa (0.66 to 1.12 atm) [7]. Based on their results and combined with Ransley and Opie's results, they derived and recommended the following equation for the H solubility calculation in liquid pure aluminum:

$$\log\frac{S}{S^o} - \frac{1}{2}\log\frac{P}{P_o} = \frac{-2700}{T} + 2.72 \qquad (6)$$

where S^o is the standard value of solubility equal to 1 cm^3 of diatomic hydrogen gas, measured at standard conditions, 273 K (0 °C) and 101.325 Kpa (1 atm). This means:

$$\log S_0 = \frac{-2700}{T} + 2.72 \qquad (7)$$

Recently, Liu et al. [8, 9] determined the value again and gave the equation for the temperature range 700 - 850 °C as:

$$\log S_0 = \frac{-2980}{T} + 3.07 \qquad (8)$$

Measurement Principle and Procedures

These determinations all employed the direct absorption method. Though the apparatuses used by different groups were designed in slightly different ways, their principal components and operating procedures were basically the same. These can be illustrated using Liu's apparatus (Figure 2) as an example [8]. The apparatus can be divided into two sections: the absorption bulb, which contains the aluminum sample and is placed in a furnace, and the mercury barometer, which also works as the gas burette. The apparatus is connected to the vacuum system and gas (H_2 and reference gases) supply.

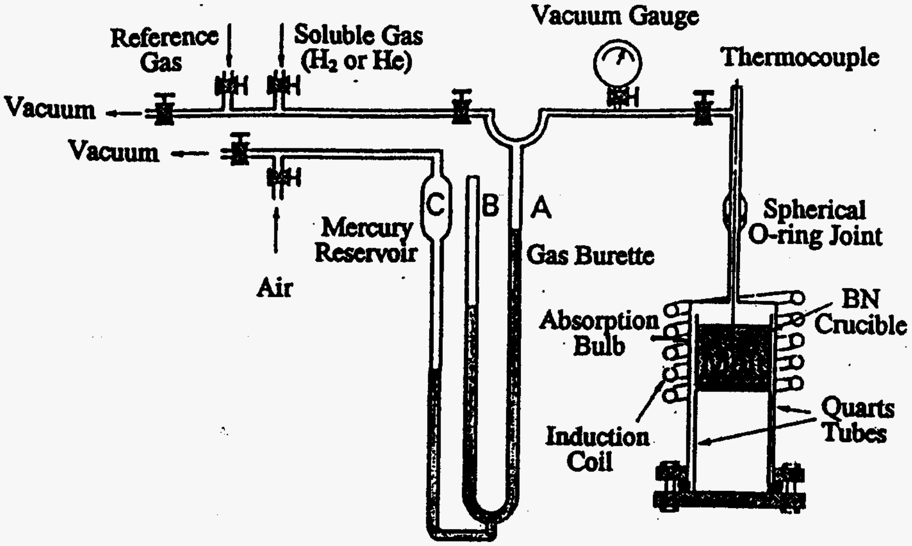

Figure 2. Schematic diagram of the apparatus for determining the solubility of hydrogen in liquid aluminum alloys in Liu et al's experiment [8].

The first step of the measurement is to determine the volume of the dead space (also referred to as free space or hot volume) in the absorption bulb. It starts with melting the sample to a predetermined temperature and degassing for about 30 min under at least 10^{-3} Pa. Evolution of the H initially present in the sample is monitored to ensure a thorough degassing. When it has ceased the melt temperature is adjusted to the testing value and maintained for about 5 min to stabilize. Insoluble reference gas is admitted into the gas burette and the manifold between the absorption bulb and mercury column A and adjusted to a preset pressure. Then the reference gas is introduced into the absorption bulb and later the pressure is readjusted to the original preset value by manipulating the gas burette. The volume of the dead space is thus calculated from the volume reduction of the reference gas in the burette. Because introducing the reference gas would decrease the melt temperature, before finally adjusting the gas pressure the melt temperature needs to be raised to the testing temperature and maintained at least 10 min, which is approximately equal to the maximum time for completing the H absorption in molten aluminum in the experiment. The second step, measuring the volume of absorbed H, follows the same procedure as described above, but using H_2 gas instead. The system is evacuated to the same level as that after degassing, the H_2

gas is first admitted into the space between the absorption bulb and mercury column and adjusted to the pressure earlier preset for the reference gas, and then introduced into the absorption bulb where the gas pressure is readjusted to maintain at the earlier preset value. Upon contacting the liquid aluminum, the H starts to be absorbed into the melt, which leads to volume reduction of the H_2 gas. When the absorption ceases, the quantity of H dissolved in the melt can be measured by the final volume reduction of the H_2 gas, which can be measured from the difference between the volumes of the reference gas and the H_2 gas left in the system under the same preset pressure. The H solubility can be calculated from the quantity of the absorbed H and the sample weight.

The major factors determining the accuracy in the measurement of the H solubility are considered to be: (1) the volume of the dead space of the absorption bulb, (2) the sample weight, (3) the property of the reference gas, and (4) the heating method. So far, the only suitable material for constructing the absorption bulb is fused silica. This material, when hot, is permeable to hydrogen. When the absorption bulb is hot, as when external heating is used, and the operation time is long, some amount of H may escape from the bulb and tube walls. This would cause experimental error and require a correction, which is uncertain and cumbersome to apply. Thus, an appropriate heating method, which can maintain the bulb and tube at lower temperature and reduce the process time, is preferred. A small amount of dead space is favorable to minimize the H loss and to achieve a precise measurement. A large sample weight can reduce the relative error. To ensure the measurement accuracy, the researchers in constructing their apparatus and selecting the reference gas applied different procedures. Consequently, several apparatuses and reference gases were used, which produced values somewhat different from each other, though the principle used was the same.

Reference Gases

To determine the system volume, the reference gas used should be inert to and insoluble in liquid aluminum and have the thermal characteristics similar to H_2. Neon (Ne), argon (Ar) and helium (He) have been used because these gases do not react with liquid aluminum. However, Liu et al. detected that He was soluble in liquid aluminum [8]. When He was used as the reference gas, the measured H solubility in liquid aluminum would be lower than its real value with a relative error of up to 20%. When Liu et al. used Ar as the reference gas, it was measured to have lower solubility in liquid aluminum. On the contrary, Opie et al. used He and thought that when Ar was used considerable error, due to the difference in heat conductivity of H_2 and Ar, would be introduced, resulting in lower solubility values [6]. Talbot and Anyalebechi also used Ne [7]. They considered that the insoluble gas, like Ar, which had high relative molar mass, may cause error in the measurement of the hot dead space volume of the absorption bulb through thermal mismatch. Ransley et al. used Ne in preference to Ar because of the following considerations: (1) Ne could be easily purified by passing through an activated charcoal tube cooled in liquid air, and (2) its thermal conductivity was higher than that of Ar and it was more nearly equivalent to H_2 in its behavior [5].

Apparatuses and Experimentation

The apparatus used by Ransley et al. is shown in Figure 3 [5]. The metal was in the form of a freshly turned cylinder weighing 30-40 g and was placed in an alumina crucible A. The crucible with the metal was introduced into the cylindrical bulb B and the umbrella-shaped base C was then inserted and sealed around the skirt with a small flame. The absorption vessel was supported by the central small-bore tube as shown. This tube passed out through the water-cooled metal head F, via an internal seal on a glassed copper thimble soldered into the bottom of F. The outer bulb D, which fitted over the internal assembly with a clearance of 1-2 mm, was sealed with an Apiezon wax into a groove in the top of the metal head.

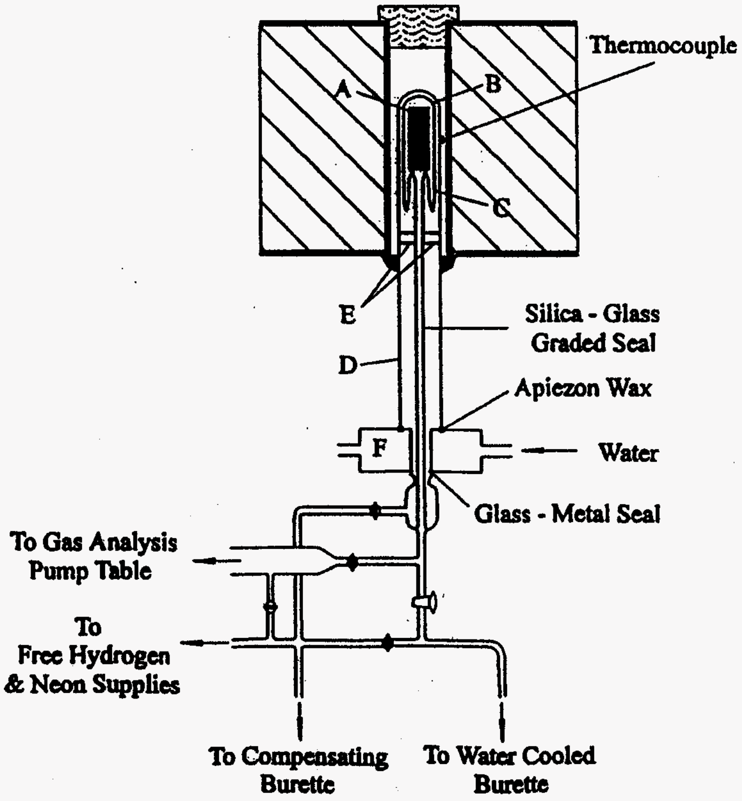

Figure 3. Schematic diagram of the apparatus for determining the solubility of hydrogen in liquid aluminum alloys in Ransley et al's experiment [5].

This bulb was heated by a silica-tube furnace. An insulating plug at the top of the furnace and two internal nickel discs E, serving as radiation screens at the bottom of the furnace, provided the furnace with a sufficiently uniform high-temperature zone. The temperature of the sample was measured by a Chromel-Alumel thermocouple placed on to the bulb D at the middle point of the crucible where the temperature was controlled to be constant to within ±5 °C.

The burette for admission of gas to the metal had the capacity of 25 cc, which could be read to ±0.01 cc, and was water-cooled to maintain it at a constant temperature. The volume of the connection from the burette to the absorption bulb was kept as small as possible, in the order of 10 cc in most experiments. The comparison burette was connected at the top to a large air reservoir and a mercury monometer, so that the pressure in the burette could be adjusted to any desired value. Actually, all their final measurements were carried out at a pressure of 760 mm of mercury. The outer jacket D was connected to a simple U-tube burette with an adjustable mercury reservoir so that the pressure in this bulb could be adjusted to be equal to that in the absorption vessel to compensate for any outward flow of hydrogen from the absorption vessel.

The whole apparatus was connected to a gas analysis pump table, which consisted of a two-stage diffusion pump discharging into a low-pressure analytical system backed by a three-stage diffusion pump. It can pump the apparatus to a pressure of 10^{-6} mm and can also collect and measure the gas evolved from either the sample or the outer jacket.

Their experiments indicated that the rate of solution of H in the metal was very slow and that the saturation value could be obtained only after exposure of several hours' duration. They considered this to be the reason for the lower values at lower temperatures reported by earlier researchers because in those earlier measurements, the time allowed for the H absorption might not have been sufficient for equilibrium to be obtained.

A sketch of Opie et al.'s system is shown in Figure 4 [6]. The following are salient features of this system: A gas purification system was associated for obtaining high purity H_2 and reference gas He. The specially prepared burette could be read to 0.01 cc. Large samples, weighing 105 to 158 g, were used. Its induction heating produced a stirring action, which expedited the degassing and the H absorption processes, comparing with resistant heating. Thus, the H absorption time was set for about 10 min.

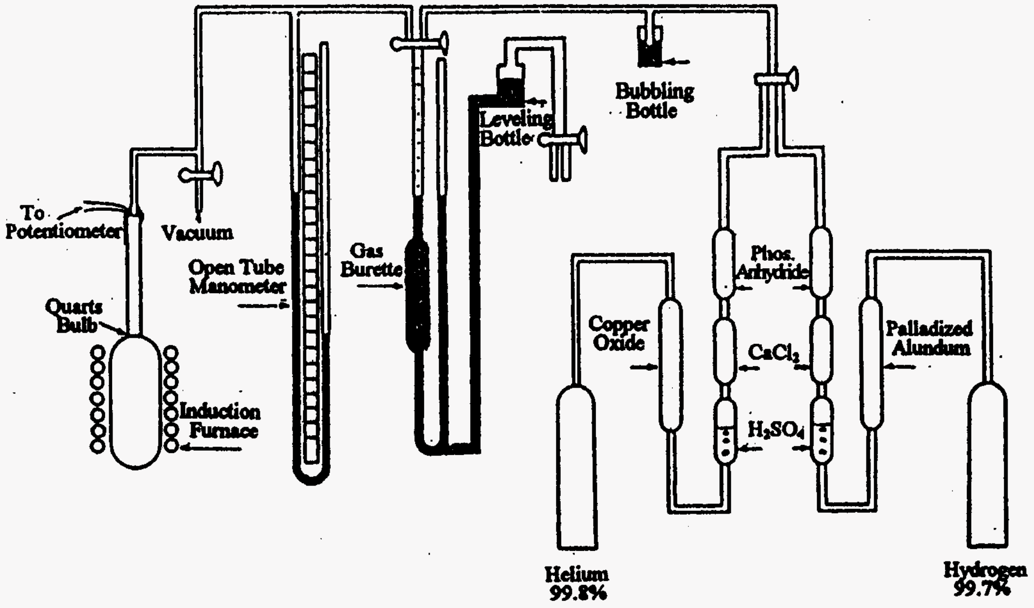

Figure 4. Schematic diagram of the apparatus for determining the solubility of hydrogen in liquid aluminum alloys in Opie et al's experiment [6].

Talbot and Anyalebechi's apparatus is shown in Figure 5 [7]. The crucible was made of recrystallised pure alumina with an internal dimension of 55 mm high and 38 mm diameter, which could contain the sample of about 100 g of aluminum. The absorption bulb was constructed around the crucible from two concentric hollow cylinders of fused silica with closed flat tops, sealed at the open ends remote from the sample. A short length of 6 mm bore silica tubing attached to the top of the bulb was connected to the system by a vacuum tight O-ring spherical joint, providing both a gas connection and an entry for a thermocouple inserted into the sample and protected by an alumina coating. This construction limited the dead space of the absorption system to ~15 cm^3. The H_2 and reference gas, He, had a purity of 99.999%. The gas burette had a range of 50 cm^3 and a sensitivity of 0.05 cm^3. The vacuum system had a capacity of an ultimate pressure of 1.3×10^{-4} Pa. The RF induction heating method was used, which could avoid directly heating the absorption bulb and also continuously disturb the oxide film by induction stirring, thereby eliminating the slow permeation of H through the thin oxide film inevitably present. Using RF induction heating, the equilibrium between gaseous H_2 and the metal was established within about 10 min at all the temperatures.

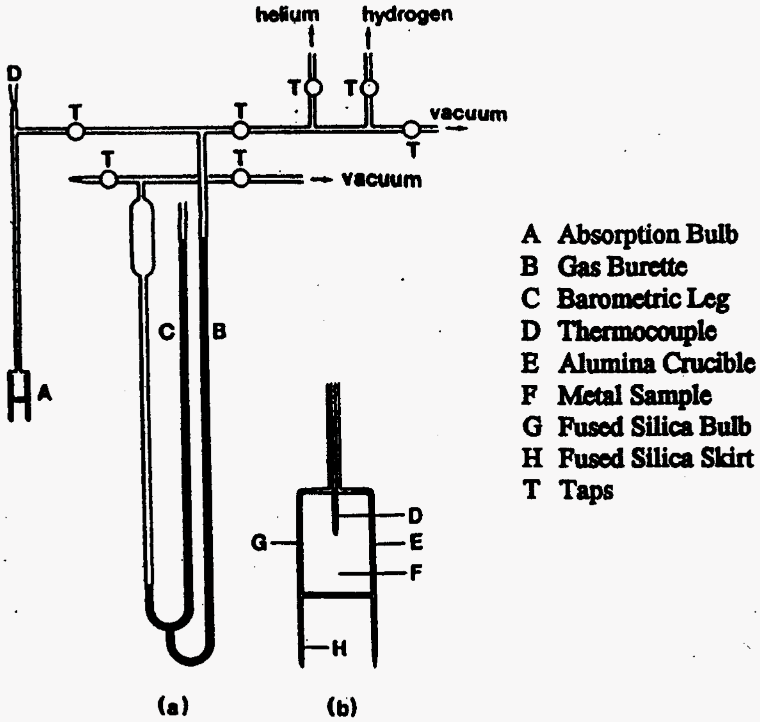

Figure 5. Schematic diagram of the apparatus for determining the solubility of hydrogen in liquid aluminum alloys in Talbot et al's experiment [7]. (a) General arrangement; (b) Detail of absorption bulb.

Liu's system (as shown in Figure 2) used two cylindrical quart tubes to construct the absorption bulb, thus limiting the dead space to as small as 50 cc. All the gases, used H_2, Ar, and He, had a purity of over 99.99%. The induction heating method could control the temperature at ±1 °C. The samples of aluminum were about 300 g, and the minimum absorption time was 10 min.

Though in the recent studies on H solubility, most researchers used the direct measurement technique, the indirect was still used. Eichenauer et al. used the isothermal absorption/desorption technique in the early 1960's [10]. In this method, a sample was first allowed to absorb H from the gas phase and when the absorption was completed, the H was desorbed from the sample isothermally into a low pressure system for measurement. For the transfer from the H absorption to the desorption, the method used in this study was to evacuate the H_2 gas from the absorption vessel rapidly, and when the evacuation reached the required level, to connect the vessel to the low pressure gas collection system immediately. Suddenly applying a vacuum to liquid aluminum causes H to nucleate within the bulk of the melt and subsequently may lead to some H loss during the evacuation. In order to compensate the H loss, corrections were made in this study by applying empirical "velocity constants" in the calculation. The accuracy of this method is considered to be largely dependent on the corrections. The H loss is apparently inevitable in this method and the quantity of the loss can be affected by the vacuum pressure, duration of evacuation, melt temperature, and H content, composition, and condition, which is difficult to assess. In addition, the values obtained using this method were considerably lower than those from the direct absorption method. Those factors made the data from this method questionable and not widely accepted.

1.2.2 Measurement of H Solubility in Aluminum Alloys

Because of the large numbers and the complexity of aluminum alloys which may contain many elements with different concentrations, a systematic study of the effects of the elements and their interactions on the H solubility in the alloys would be very difficult by experiments. However, this study is essential for practical use. To evade the difficulty with experiments, the approaches that have been used so far are first to study simple systems, like X-H (X represents an element) and Al-H-X systems. Based on the results from these simple systems, some thermodynamic data can be derived and from this information the H solubility for more complex systems can be calculated. Though some work was conducted in this way, the published information for complex alloys are still limited.

As early as the 1930's, Baukloh et al. studied the effects of Cu and Si additions on the H solubility in aluminum [4, 11]. It was reported that the presence of up to 6% of these elements decreased the solubility quite rapidly, with a definite minimum noted at 6 w% for both Cu and Si, although no reason was apparent for these minima. Opie et al. studied these effects again while measuring the H solubility in pure aluminum [6]. They also found that both Si and Cu decreased the H solubility, the effect of Cu being considerably greater than that of Si. However, in contrast to the previous evidence, no minima were found over the composition ranges investigated (up to 50% Cu and 18% Si). Cu additions caused the solubility to decrease up to the composition of the intermetallic compound $CuAl_2$, which occurred in the composition range of 52.3 to 54.7% Cu. From their results the following equations were derived, which related the solubility and temperature.

Alloy	Solubility Equation	
Pure Al	$\text{Log } S_0 = \frac{-2550}{T} + 2.62$	(5)
2% Cu	$\text{Log } S_0 = \frac{-2950}{T} + 2.90$	(9)

4% Cu $\text{Log}\, S_0 = \frac{-3050}{T} + 2.94$ (10)

8% Cu $\text{Log}\, S_0 = \frac{-3150}{T} + 2.94$ (11)

16% Cu $\text{Log}\, S_0 = \frac{-3150}{T} + 2.83$ (12)

32% Cu $\text{Log}\, S_0 = \frac{-2950}{T} + 2.57$ (13)

2% Si $\text{Log}\, S_0 = \frac{-2800}{T} + 2.79$ (14)

4% Si $\text{Log}\, S_0 = \frac{-2950}{T} + 2.91$ (15)

8% Si $\text{Log}\, S_0 = \frac{-3050}{T} + 2.95$ (16)

16% Si $\text{Log}\, S_0 = \frac{-3150}{T} + 3.00$ (17)

Anyalebechi et al. studied H solubility in liquid binary Al-Li alloys in stet [12]. The apparatus used was basically the one they used for determining H solubility in pure aluminum (see Figure 5) [7]. In this apparatus a lid was used to cover the crucible to protect the silica tube from the Li attack. Because Li is volatile and reactive to silica, without the lid protection the silica would develop microcracks and become permeable to both H_2 and the reference gas He before the measurement could be completed. Even if the lid cover was not used, the Li evaporation could still cause some measurement error. The results obtained from their experiments for Al-1%, 2% and 3%Li binary alloys for the temperature range of 913 to 1073 K (640 to 800 °C) and pressure 53 to 107 KPa (0.52 to 1.06 atm) were given by:

Al-1%Li $\log\frac{S}{S^o} - \frac{1}{2}\log\frac{P}{P_o} = \frac{-2113}{T} + 2.568$ (18)

Al-2%Li $\log\frac{S}{S^o} - \frac{1}{2}\log\frac{P}{P_o} = \frac{-2797}{T} + 3.329$ (19)

Al-3%Li $\log\frac{S}{S^o} - \frac{1}{2}\log\frac{P}{P_o} = \frac{-2889}{T} + 3.508$ (20)

The results indicate that the H solubility in the liquid Al-Li alloys is higher than that in pure aluminum and increases with increasing Li content.

Anyalebechi also reviewed and analyzed the data of H solubility in liquid pure aluminum (Al-H) and aluminum alloys (Al-H-X) in the experiments reported previously [13]. Based on the data, the effects of alloying elements on the solubility and thermodynamic behavior of H in liquid aluminum were analyzed in terms of interaction parameter. Figure 6 shows the data collected from the literature [6, 12, 14-18]. The data and analysis revealed that isothermal H solubility in liquid Al-H-X alloys at H_2 partial pressure of 101.3 Kpa (1 atm) decreases with an increase in Cu, Si, Zn, and Fe levels, but increases with an addition and rising levels of Mg, Li, and Ti. Within the reported temperature and composition ranges, all of the Al-H-X alloys he examined are endothermic occluders of H. That is, H solubility increases with an increase in temperature. Anyalebechi's study [13] was aimed to predict H solubility in the more complex, but commercially important, multicomponent aluminum alloys through the interaction parameters obtained from the simple alloy systems. Besides the elements mentioned above, it was also reported [19] that an Mn addition decreased and a Ni addition increased the H solubility in liquid aluminum.

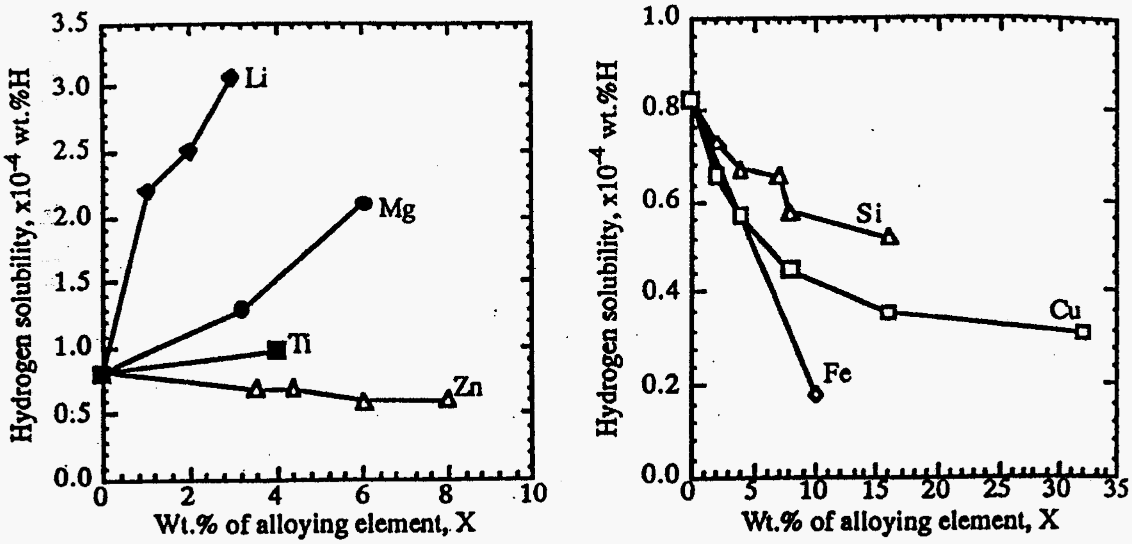

Figure 6. Reported effects of alloying elements on hydrogen solubility in liquid aluminum at 973 K (700 °C) and 101.3 Kpa (1 atm) hydrogen partial pressure [7].

Based on the investigation of the effects of composition on the H solubility in aluminum alloys conducted until 1970's, Hess [20] gave an empirical equation:

$$S\ (\mathrm{ml/100g}) = [1.23 - 0.0733\ (\%\mathrm{Cu}) - 0.033\ (\%\mathrm{Si}) + 0.0489\ (\%\mathrm{Mg})]\ (T - 585)\ (0.00606) \qquad (21)$$

where T = Temperature, °C.

This information was later used in developing the H measurement device, Alscan [21]. For foundry alloys, the values of H solubility *S* needed in using the Alscan anallyzer were calculated by:

$$S = S'_o \times \sqrt{P} \times CF(T) \times CF(A) \qquad (22)$$

where S'_o is the H solubility in pure aluminum at 700 °C and H_2 partial pressure of 1 atm, CF(T) is a correction factor for melt temperature, both S^1_o and CF(T) are derived from Ransley's work, and CF(A) is a correction factor to account for alloy composition. It was considered that in the foundry alloys only Si, Cu, and Mg had a significant effect on the H solubility. For calculating the CF(A), initially Hess' data was used. However, it was found that Hess' data, which was obtained mostly from wrought alloys, overcorrected for highly alloyed foundry alloys. Having reanalyzed Hess' data, the CF(A) for using the Alscan device in foundry alloys was modified as:

$$\log CF(A) = 0.0170\ \%Mg - 0.0269\ \%Cu - 0.0119\ \%Si \qquad (23)$$

A theoretical analysis of H solubility in liquid aluminum alloys was also conducted by Lin and Hoch in the later 1980's [22]. In their analyses, the thermochemical model, developed by Hoch and Arpshofen [23, 24], was adopted to describe the solution behavior of binary and ternary aluminum alloys. By applying this model, the thermodynamic properties of the Al-H, Cu-H, Mg-H, Li-H, Al-Cu, Al-Si, Al-Mg, Al-Li, Al-Li-H, Al-Cu-H, Al-Mg-H, and Al-Si-H systems have been calculated. This model offers the possibility of applying the binary parameters in evaluating the thermodynamic properties of the corresponding ternary system without any measurement in the ternary system. The H solubility in aluminum alloys containing Cu, Li, Mg, and Si calculated in this study showed general agreement with the previously published data.

1.2.3 Measurement of H Solubility in Solid Aluminum

Ransley et al. measured the solubility of solid aluminum in the 1940's, using a saturation, quenching, and subsequent extraction technique. The Ransley experiment has been considered to be the first successful measurement of the solubility of solid aluminum that was reasonably accurate, and is still widely accepted. Figure 7 is the sketch of the apparatus used. The boat in the assembly is the only part which calls for special comment. It consisted of a rectangular frame of special glass, fitted with prongs along each side, which shaped against the inside of the tube; a long rod resting along the bottom of the tube connected this frame to a small sealed-off U-tube containing a length of iron rod in each limb. With a powerful horseshoe magnet the whole boat which carried the specimen could be moved and rotated to move, load and unload the specimen.

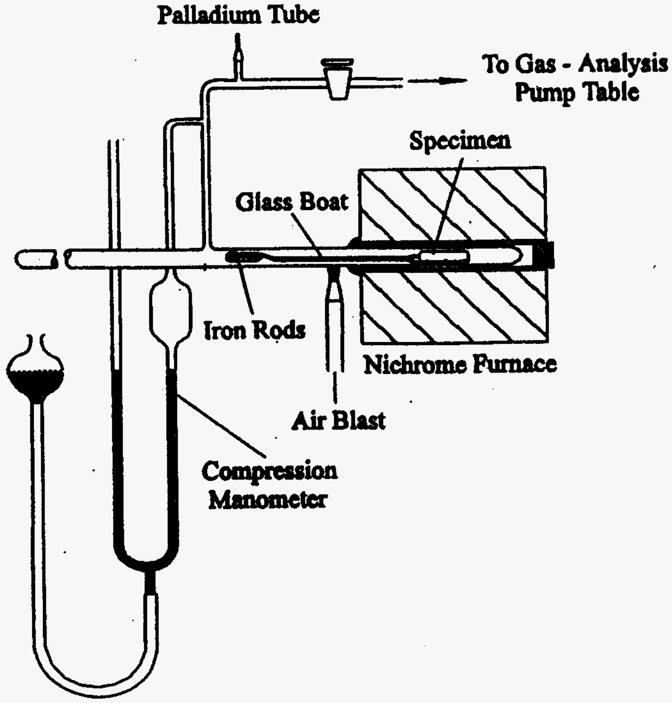

Figure 7. Schematic diagram of the apparatus for determining the solubility of hydrogen in solid aluminum alloys in Ransley et al's experiment [5].

The H_2 gas could be admitted to the system through the palladium tube and the pressure regulated and measured by means of the compression burette. The furnace temperature was controlled at ±5 °C. The specimen was a completely sound cylinder, 12 mm in diameter and 60 mm long, weighing about 18 g.

At the beginning of each experiment the tube and boat were thoroughly degassed at high temperatures (650 - 670 °C) and then the specimen was degassed at the maximum temperature permitted by the conditions of the individual experiment. When the rate of gas evolution was reduced to a negligible proportion, the boat and the specimen were withdrawn from the furnace. The large tap leading to the gas-analysis apparatus was closed and H_2 was admitted to the system via the palladium tube. When the H_2 pressure and the temperature in the furnace were adjusted to the required value, the specimen was re-inserted in the furnace where it absorbed the H. The time necessary for completing the absorption was assessed from the rate of degassing at various temperatures. After the H absorption ceased, the specimen was withdrawn quickly from the furnace into the zone and quenched by an air blast to the tube. The rapid quench retained substantially all the gas dissolved in the metal.

The H_2 was then pumped away and the specimen was tipped out of the boat. The boat was pushed back to the furnace and the boat and tube were baked again at 650 - 670 °C to expel the gas that was absorbed. After the degassing of the boat and tube, the furnace temperature was reduced to the value at which the specimen was to be degassed. At this temperature a careful cut-off test was carried out over a period of 0.5 - 1 hr. to determine the rate of gas evolution from the tube and boat before the specimen was picked up and pushed into the furnace. Finally, the specimen was moved into the furnace, the H was extracted from the specimen and the pressure of the collected H_2 was measured, from which the H solubility was calculated. The H extraction took up to 3 hrs. Since the H content was extremely low and the extraction was a prolonged process, the cut-off test was essential for the data correction. Several pure aluminum samples from different sources and under different treatments were tested. The results were represented by the equations:

$$\text{Log } S_0 = \frac{-2080}{T} + 0.788 \qquad (24) \quad \text{and}$$

$$\text{Log} \frac{S}{\sqrt{p}} = \frac{-2080}{T} - 0.652 \qquad (25)$$

The extrapolated solubility at the melting point (660 °C) was 0.036 ml/100 g metal. The experimental results for the commercial metal were in sufficiently good agreement with those for the super-purity material to suggest that true solubility does not alter appreciably with the variation in purity within the normal limits. Not much information is now available about the effects of elements found in Al alloys on the H solubility in the solid alloys. It was not clearly documented but it may be assumed that the elements that decrease the H solubility in liquid aluminum, such as Si, Cu, Zn, Fe, and Mn, also decrease the H solubility in solid aluminum, and conversely, the elements Mg, Ti, Ni, and Li increase the H solubility in solid aluminum.

In the 1980's, Anyalebechi et al. studied the H solubility in solid Al-Li binary alloys for the temperature range of 473 to 873 K (400-600 °C) and the pressure range of 26,700 to 113,300 Pa (0.26-1.12 atm) [25]. The absorption-quench-desorption technique was used, which was the same as Ransley's. The apparatus used was the same as that used to measure H solubility in liquid aluminum (Figure 5) [7]. The results were given by:

$$\log\frac{S}{S^{o}}-\frac{1}{2}\log\frac{P}{P_{o}}=\frac{-A}{T}+B \tag{26}$$

The values of the constants A and B are:

Al-1%Li	$473 < T < 680$:	$A = 358$,	$B = 0.576$	(27)
	$680 < T < 873$:	$A = 604$,	$B = 0.620$	
Al-2%Li	$473 < T < 740$:	$A = 273$,	$B = 0.597$	(28)
	$740 < T < 873$:	$A = 676$,	$B = 0.767$	
Al-3%Li	$523 < T < 770$:	$A = 615$,	$B = 1.272$	(29)
	$770 < T < 873$:	$A = 830$,	$B = 1.166$	

This study indicates that the H solubility is one or two orders of magnitude greater in these alloys than in pure aluminum and increases with Li content. Thus, it can be seen that Li has an interesting effect. It increases the H solubility in both liquid and solid aluminum alloys, but the increase in the solid is much greater. On freezing, an Al-Li alloy can retain 30-50% of its dissolved H in the solid form. Therefore, Al-Li alloys exhibit a lowered tendency to porosity [19]. The H solubility in these alloys also shows unique temperature dependence. In other alloys, the activity of a given H content diminishes progressively with increasing solubility as the temperature rises, but, for a binary Al-Li alloy, there is an increase in activity corresponding to the abrupt decrease in solubility as the temperature rises above the critical temperature.

1.2.4 Summary

The accurate values of the H solubility in liquid and solid aluminum alloys are essential for understanding and modeling the pore formation in the casting and for developing H measurement techniques. Much research work has been done in this area and many techniques were applied. So far, the direct absorption method has been considered to be the only suitable method for measurement in liquid alloys. Several research groups used the same technique with differently constructed apparatuses. Several research groups conducted the measurements. The results from four groups mentioned above are plotted in Figure 8. Considering the very low values, about 0.9 to 2 ml/100 g Al, and the difficulties encountered in the experiments, these data show a good agreement, especially in the temperature range of 700 to 800 °C. Though the exact H solubility in liquid aluminum at the melting point (660 °C) has not been measured, its value extrapolated from these four experiments is in the range of 0.69 - 0.77 ml/100 g Al. This is the value that is currently widely accepted. However, in their experiments a large discrepancy existed regarding to the H solution rate. Ransley used 18 g specimens and several hours for the H saturation, indicating that the solution rate of H in liquid aluminum was very slow. Opie, Talbot, and

Liu used much larger specimens. Opie's were 105 to 158 g, Talbot's were ~100 g, and Liu's were ~ 300 g, but they all gave only 10 min for the H absorption. (Indeed, the induction furnace technique used by the later researchers produced a stirring effect accelerating the H solution; does it make such a big difference?) Because the H solution rate is important, which needs to be considered in melting and handling the aluminum alloys for reducing the H content, this discrepancy needs to be cleared up.

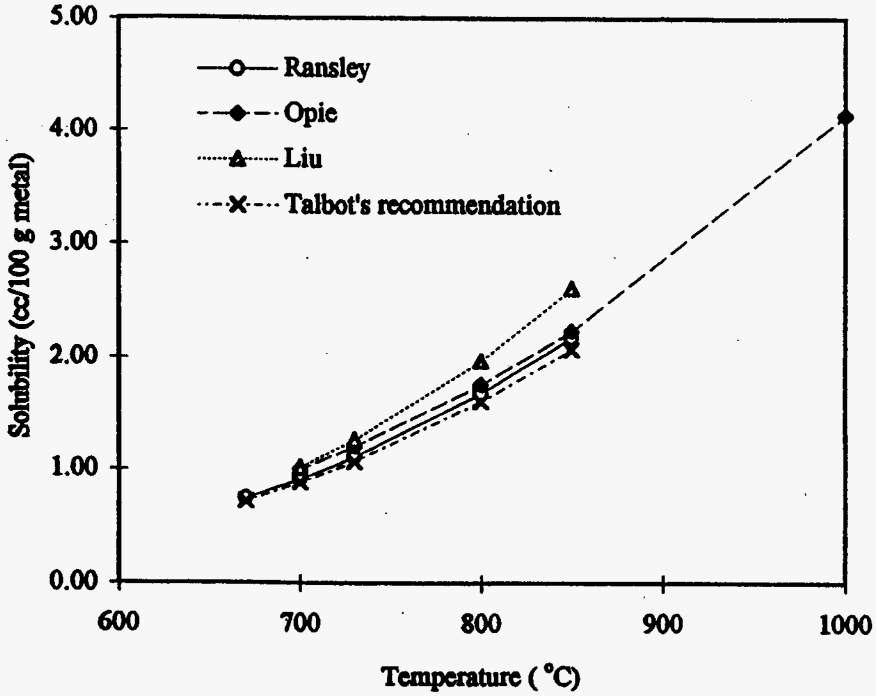

Figure 8. The hydrogen solubility in liquid aluminum as reported by various researchers.

For practical use, the values of H solubility in aluminum alloys are of more significance than in pure aluminum. The effects of some elements on H solubility in simple aluminum alloy systems were investigated. Based on the results of the simple system studies, the thermodynamic properties of H in liquid aluminum and its alloys were studied theoretically, which were used to predict H solubility in the more complex aluminum alloys. However, the results from the theoretical work need to be proved by experiments and are still limited. The information currently available in the published literature is not sufficient to provide a clear, reliable picture about H solubility in commercial alloys. Such information used in practice is provided by empirical equations derived from data for pure aluminum and using correction factors for the composition and temperature.

Ransley and Anyalebechi et al. measured H solubility in solid aluminum and Al-Li alloys in the 1940's and the 1980's, respectively. These results have not been reexamined and, therefore, have not been really challenged. These data are considered to be reasonable and have been accepted. Other than Li, little work has been conducted in examining the effects of elements on H solubility in solid aluminum alloys but this is also the necessary information.

References

1 Röntgen, P. and Braun, H., Metallwirtschaft, 1932, 11, p459.

2 Röntgen, P. and Möller, F., Metallwirtschaft, 1934, 13, p97.

3 Bircumshaw, L. L., Trans. Faraday Soc., 1935, 31, p1439.

4 Bauhloh, W. and Bedjali, M., Metallwirtschaft, 1942, 21, p683.

5 Ransley, C. E., and Neufeld, H., "The Solubility of Hydrogen in Liquid and Solid Aluminum", J. Inst. Metals, Vol. 74, Aug. 1948, p599-620.

6 Opie, W. R., and Grant, N. J., "Hydrogen Solubility in Aluminum and Some Aluminum Alloys", Transactions AIME, Vol. 188, October 1950, Journal of Metals, p1237-1241.

7 Talbot, D. E. J. and Anyalebechi, P. N., "Solubility of Hydrogen in Liquid Aluminum", Materials Science and Technology, Jan. 1988, Vol. 4, p1-4.

8 Liu, H., Bouchard, M., and Zhang, L., "Measurement of Hydrogen Solubility in Liquid Aluminum", Light Metals 1995, Edited by J. Evans, p1285-1291.

9 Liu, H., M. Bouchard, and L. Zhang, "An Experimental Study of Hydrogen Solubility in Liquid Aluminum", JOM, Sep. 1, 1995, Vol. 30, No. 17, p4309-4315.

10 Eichenauer, W., Hatenbach, K., and Perler, A., Metallkd., 1961, 52, p682.

11 Baukloh, W. and Oesterlen, F., Ztsch. Metallkunde, 1938, Vol. 30, p386.

12 Anyalebechi, P. N., Talbot, D. E. J., and Granger, D. A., "The Solubility of Hydrogen in Liquid Binary Al-Li Alloys", Met. Trans. B, Vol. 19B, No. 1, March. 1988, p227-232.

13 Anyalebechi, P. N., "Abnalysis of the Effects of Alloying Elements on Hydrogen Solubility in Liquid Aluminum Alloys", Scripta Metallurgica et Materialia, Vol. 33, No. 8, Oct. 15, 1995, p1209-1216.

14 Ransley, C. E., and Talbot, D. E. J., Ztsch.. Metallkunde, 1955, 46, p378.

15 Stephenson, H., Ph. D Thesis, Brunel University, Middlesex, England, 1978.

16 Grigoreva, A. A. and Danilkin, V. A., Tsvetnye Metally., 1984, 1, p90.

17 Sargent, M., Ph. D Thesis, Brunel University, Middlesex, England, 1989.

18 Vaschenko, K. I., Chernega, D. F., Ivanchuk, D. F.,Vyalik, O. M., and Remizov, G. A., Izv. Vyssh Ucheb Zaved Tsevet. Metally., 1975, 2, p48.

19 Gruzleski, J. E., The Treatment of Liquid Aluminum-Silicon Alloy,

20 Hess, P. D., "An Empirical Equation for Calculating the Solubility of Hydrogen in Molten Aluminum Alloys", Light Metals, 2, 1974, p 591-596.

21 Painchaud, F. and Martin, J. -P., "The New Alscan Analyzer: Easy-to-Use, Reliable, On-line Measurement of Hydrogen in Liquid Aluminum Alloys", Proceedings of 2nd International Conference on Molten Aluminum Processing, Orlando, Florida, Nov. 6-7, 1989, paper 20.

22 Lin, R. Y. and Hoch, M., "The Solubility of Hydrogen in Molten Aluminum Alloys", Met. Trans. A, Vol.20A, No. 4, SEP. 1989, p1785-1791.

23 Hoch, M., CALPHAD, 1987, Vol. 11, p219-224.

24 Hoch M. and Arpshofen, I., Ztsch.. Metallkunde, 1984, Vol. 75, p23-27.

25 Anyalebechi, P. N., Talbot, D. E. J., and Granger, D. A., "The Solubility of Hydrogen in Solid Binary Aluminum-Lithium Alloys", Met. Trans. B, Vol. 20B, No. 4, Aug. 1989, p523-533.

1.3 DETERMINATION OF HYDROGEN CONTENT IN LIQUID ALUMINUM ALLOYS

Over the years, many techniques have evolved for the analysis of H in aluminum alloys and new methods are still being developed. These techniques can be categorized in a variety of ways based on different considerations. In this paper, according to their usage in the practice, these techniques are described in three categories: quantitative laboratory analysis of solidified samples, in-situ quantitative analysis and semi-quantitative cast shop methods.

1.3.1 Quantitative Laboratory Analysis

Quantitative Laboratory Analysis of Solidified Samples

Ransley Sub-Fusion Method - The vacuum sub-fusion extraction technique was developed by C. E. Ransley, R. Eborall, and D. E. J. Talbot during 1945-55 [1]. It is often simply called "The Ransley Method". Since this method was invented, it has been considered and used as a reference technique against which the other techniques are calculated or compared, because of its accuracy and stability. Though, many other H measuring methods and devices are now available, the Ransley Method is still in use despite its drawbacks.

This method uses a carefully machined cylindrical sample of given dimensions. The sample is heated under vacuum to a temperature just below the point at which fusion commences. At this temperature H is extracted from the sample through diffusion. The extracted H is collected in a known volume of the equipment and the H pressure is measured using a Mcleod or Pirani gauge, from which the H content is calculated. The apparatus used for this method has been improved in many aspects since it was first established. However, because it is not commercially available, the apparatuses used in different laboratories may slightly differ from one other. Figure 9 shows a schematic diagram of one of the apparatuses [1].

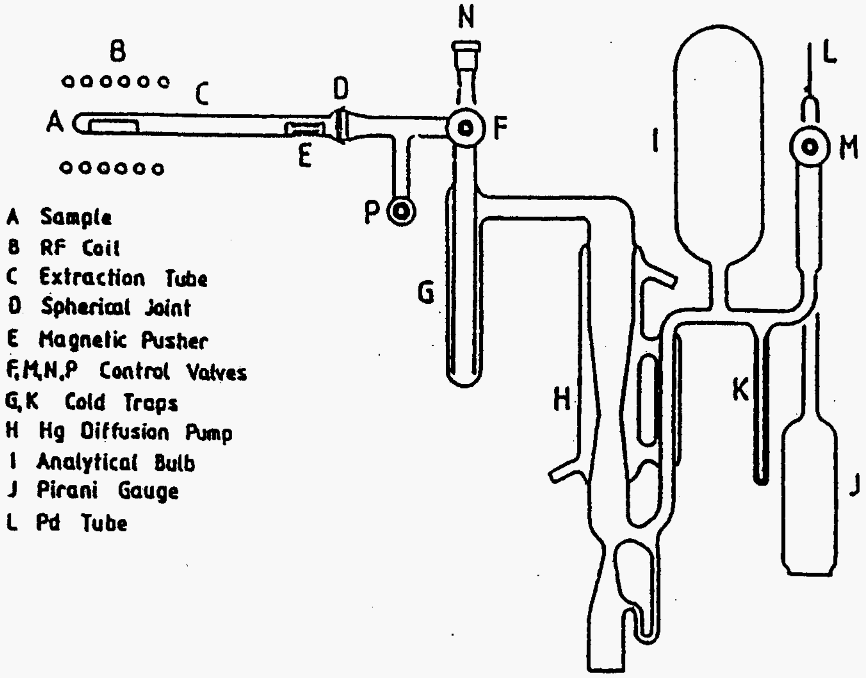

Figure 9. Schematic diagram of Ransley apparatus [1].

One of the complications in the determination of H in aluminum by the sub-fusion method is the surface H, which is generated from surface reactions additional to what is present in the bulk of the metal. The reactions are mainly due to:

(a) Breakdown of hydrocarbons from contaminating oil or grease.
(b) Reaction of adsorbed surface moisture with the metal sample.

The first problem is usually minimized or overcome by dry machining of the sample and avoiding subsequent manual contact. For the second problem a proper surface correction needs to be taken. The solutions can be to minimize the moisture absorbed and/or to measure the amount of surface H generated, which is then subtracted from the total measured amount of H. In the Ransley method this is accomplished by first measuring the total H, then removing the sample from the apparatus, re-machining the surface and replacing the sample in the equipment for the second H determination. The latter is subtracted from the total H to provide an H correction. This presupposes that the surface contamination on the newly exposed surface is identical to that of the original sample and that the new surface is close to or identical to that presented to the instrument during the total H determination.

It has been found that the H values measured by the Ransley method are lower than those calculated by some other methods, such as Telgas, Alscan, or CHAPEL [2, 3]. The results obtained by the Ransley Method could differ by as much as 30% for wrought alloys from H values obtained by Telgas and Alscan measurements [2]. An Experiment conducted by Dupuis et al. showed that the measured H values from the Ransley method were lower than expected from calculation and the difference was attributed to H loss during sampling, mainly during transfer and/or solidification, or to underestimation of the H content in the subsequent extraction [2]. They thought that H rejection during solidification did occur but that actual losses were fairly small. Chen et al. considered that the cooling power of the sampling mold was not sufficient to hold the H in forced solution during the solidification, especially at high H content [3]. However, in their experiments there was no direct evidence that could support this argument, because there may be some other factors responsible for the lower values measured by the Ransley method. If there were H loss during transfer and/or solidification, the metal transfer time and cooling rate would affect the measured values. Dupuis et al. measured the H content from the samples taken from a DC cast full size ingot (660 x 1320 mm) of alloy AA5182 and showed that the H concentrations near the center of the ingot were approximately 15% lower than those in the rest of the ingot [2]. Because the cooling rate in the ingot was estimated to be 0.5 - 1.0

°C/s near the center and 10 °C/s near the surface, it was much slower than in the Ransley mold, and it was also found that except near the center of the ingot, the H concentration did not vary significantly and the average H concentrations in the rest of the ingot were equivalent to the corresponding Ransley mold samples. In addition, the experiments using the Ransley mold samples showed that the cooling rate varied by changing the mold temperature at 35 - 410 °C, and the sample location did not affect the measured H content values [2]. Rayís experiment, which used Ransley molds and studied the effects of the mold and sampling technique on H content [4], showed that higher H levels seemed to be associated with a hotter mold. The H increase was attributed to the slower cooling rates which can lead to increased shrinkage porosity and gas entrapment. The experiment also showed that a reasonable variation in melt temperature (tested at 1240 - 1300 °F (671 - 704 °C)), a sample transfer time as long as 15 s, and sample location did not significantly affect the measured H level. Thus, whether there is H loss during sampling in the Ransley method cannot be concluded from these experiments.

The lower H values measured by the Ransley method may be attributed to H not being completely extracted from the sample. An experiment was conducted which added an additional extraction time of 210 - 240 min over the standard extraction time of 90 - 120 min. It was found that an additional quantity of H was measured for this extended period, which was significant and represented 15-33% of the total H measured during the normal extraction period [2]. (Even through long time extraction a non-zero value of H content can often be obtained by other methods from the sample after a Ransley determination.) No definite explanation for this is universally accepted. Possible reasons were proposed to be: H is more strongly bound in the metal than the conventional physically entrapped H. Talbot [5] studied and defined both the physical and chemical traps for H. For example, the chemical traps can be hydrides, such as zirconium hydride and sodium hydride. Evidence for the existence of these hydrides was presented by Konar [6] and Varhegyi et al. [7] The latter also demonstrated the slower release of H from the metal and suggested a method for its determination. If this is the case, it means that the H content measured in the surface correction process also contains some bulk H and the final H content is undermeasured. That is, some chemically bound H can not be detected, but this kind of H can also produce deleterious effects, such as forming porosity during rolling [8]. In addition, during the heating process, volatile alloying elements may build a film of condensation on the wall of the quartz tube. This film could store some of the H extracted from the sample.

Though the great stability of this technique is well recognized, its consistency is still a matter of concern. The extensive manipulations involved in sampling and sample preparation can be the source of significant variability in the results. It was found that consistency between duplicate Ransley samples was reduced at higher mold temperature (tested at 200 - 1000 °F (93 - 538 °C), poor consistency between duplicate samples can result from turbulent pouring into the mold, and the mold condition can affect the flow of metal into the pin area [2]. Chen et al. contributed the inconsistency to H segregation in Ransley samples [3]. Round robin analyses between different laboratories (on the same set of standards) showed that results obtained may vary significantly from laboratory to laboratory [2]. The variations were especially large for alloys containing volatile elements, such as Zn and Mg, but they remained significant even for pure metal. The temperature at which the extraction is performed, the time allowed for the extraction and the type of heating are the principal reasons causing the discrepancies between different sites. In addition, in the surface correction operation the assumption of parity between surface quality and contamination before and after re-machining is illogical, especially when there is extensive shrinkage porosity in the alloy, as in AA-7075 alloy. Here, re-machining of the surface may produce a whole new distribution of cracks and fissures compared to that presented to the apparatus for the total H determination

The principal advantage of this method is its accuracy. It has been reported that the standard deviation of internal precision for the Ransley method is generally 0.02 ml/100g. The major drawbacks are its long processing time and, consequently, its cost. A typical extraction requires about 3.5 h. This can be doubled if an individual surface correction factor is required for a particular sample. Besides requiring costly laboratory equipment and time, this technique must be operated under strict procedures by trained personnel and be maintained rigorously if consistent results are expected. Therefore, despite accuracy, its time-consuming nature and high cost limit its application in on-line control on the shop floor. However, it is used widely in the wrought alloy industry and research.

Quantitative Laboratory Analysis by Remelting Samples

Nitrogen Carrier Fusion Methods - LECO RH and Ithac Devices

The development of these two devices was based on the work of Degreve [8]. In this method a cylindrical sample (0.001 - 20 g used in LECO RH-402) is placed in a graphite crucible and melted in a stream of nitrogen (carrier gas) [9]. The H is evolved from the melt, mixed with the nitrogen, and carried downstream. The H is then detected and measured by a catharometer through measuring the thermal conductivity of the gas mixture. The measuring principle is based on the fact that the thermal conductivity of H is approximately seven times that of nitrogen gas. Figure 10 shows the simplified gas flow diagram of the apparatus RH-402 [9].

Two major factors affecting the measuring accuracy are the ingress of moisture into the nitrogen gas carrier and the surface H. The moisture may come from two sources: the carrier gas and the hydroxyl ions in the silica network of the quartz tube in which the sample is melted. During fusion, spurious H can be produced by the reaction of water and metal vapor, and water and H may react with carbon producing carbon monoxide and methane. The water and its reacting products will change the thermal conductivity of the carrier gas. Table 1 shows the thermal conductivity of various gases relevant to the fusion process. Oxygen may react with the graphite of the crucible, producing carbon monoxide, but its presence in a small amount would not seriously affect the results because the thermal conductivity of either oxygen or carbon monoxide is close to that of nitrogen. Water and carbon dioxide would lower the reading of the catharometer, because their thermal conductivity is below that of nitrogen. The lower thermal conductivity of the methane than that of H would make the H content undermeasured.

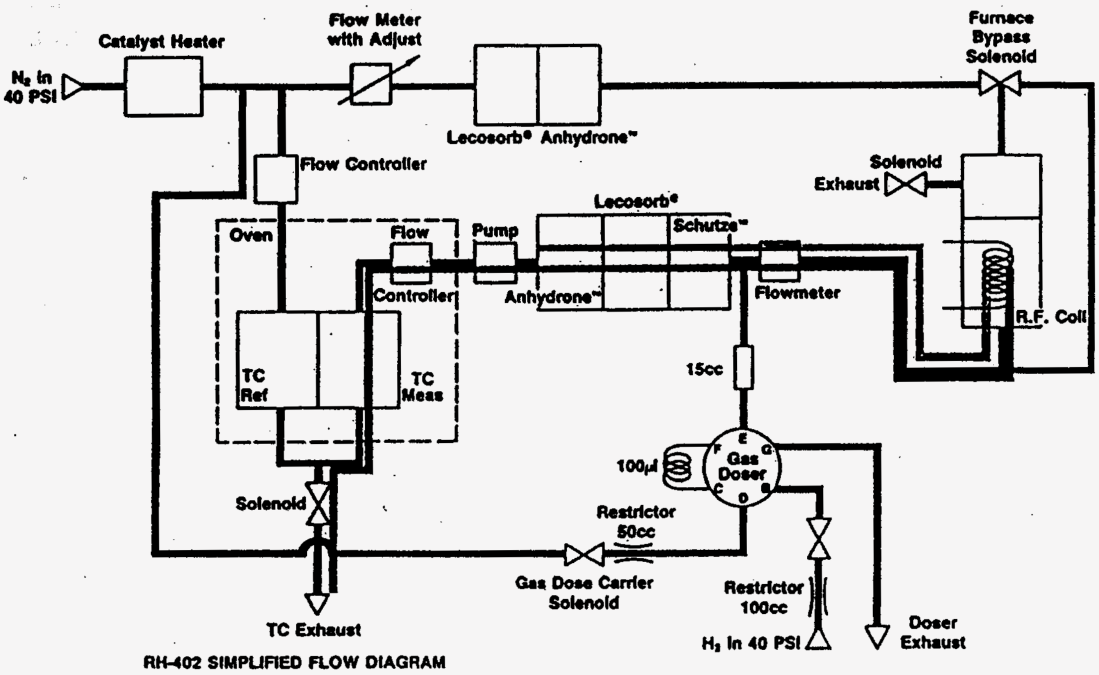

Figure 10. LECO RH-402 simplified gas flow diagram [9].

Table 1. Thermal conductivity of gases at 48.9 °C [10]

Gas	Thermal Conductivity cal/s·cm^2·(°C/cm) x 10^{-6}
Nitrogen	65.71
Oxygen	68.19
Water	46.70
Methane	89.28
Carbon Monoxide	63.89
Carbon Dioxide	43.81
Hydrogen	471.11

In this technique the atmospheric moisture is minimized by drying the carrier gas through magnesium perchlorate and a molecular sieve. With this arrangement the dew point of the carrier gas can be lowered to approximately -60 °C. At a dew point of -78 °C, the interference caused by the water reaction will be less than 0.01 ml/100g. To avoid picking up moisture from the atmosphere, the operation should ensure that the exposure time of the furnace to the air be minimized, for example when the furnace is opened for introducing the specimen. It is considered that the problem related to the hydroxyl ions may not be serious, because the reaction of the hydroxyl ions with metals is controlled by the diffusion rate of the hydroxyl ions in the silica network of the quartz tube, which in turn depends on the temperature. In this method the quartz tube is not directly heated and does not get very hot. Accordingly, there is some uncertainty about the extent of this reaction, but if it does occur, then evidently the H will be overmeasured.

The problem of surface H is generally treated by preheating the specimen. It was considered that the surface H could be eliminated by heat treatment of the specimen to 400 to 500 °C before melting [11, 8]. However, experiments showed that different preheating procedures, e.g., heating to a temperature directly or stepwise, resulted in different surface H readings. Moreover, it was found that the specimen could be over or under heat-treated resulting in the bulk H being much lower or higher than that obtained from a Ransley analysis. The main problem is that surface H is evolved at temperatures close to the melting range of some alloys. This suggests that the surface treatment is critical to the accuracy of this method.

With adequately dried carrier gas and appropriate surface treatment, the accuracy of LECO RH-3 can be approximately at the same level as that of the Ransley method, 0.02 ml/100g. However, for some alloys, in higher H concentration ranges the differences between the two methods become significant. The accuracy of LECO RH-402 is 1% relative with sensitivity of 0.001 ppm (0.0009 ml/100g). The measured values are higher with the fusion method than the sub-fusion method. The reasons for this were suggested to be the extensive shrinkage porosity, its nonuniform distribution and the rate of H release. The voids can act as traps for H and water vapor when they are exposed to the surface. The entrapped water vapor may escape during the slow heating in the sub-fusion method, but it has little chance to escape in the fusion method, because of the fast heating. Some strongly bound H, which may not be extracted during the sub-fusion process, can be expelled in the fusion method.

The main difference between the *Ithac* and *LECO RH* instruments, taking Ithac-02 and LECO RH-3 as examples, is that the latter is provided with a loading head for the introduction of the sample into the equipment. The loading head permits the sample to be stored in a cavity, which has been purged with dry nitrogen gas and sealed, prior to the introduction of the sample into the graphite crucible and the subsequent fusion. In this way the baking out of the crucible and subsequent fusion can be accomplished without opening the apparatus at any stage of the analytical cycle. As a result, it avoids bringing atmospheric moisture into the furnace and contaminating the carrier gas. With the Ithac-02 device it is necessary to open the furnace for placing the sample after baking out the furnace.

This method is much faster than the sub-fusion method. A complete analysis by this method takes approximately 20 min, and the fusion/analytical cycle is only approximately 3 minutes. It has a satisfactory accuracy for some alloys, but generally it is not always as accurate as the sub-fusion method. Its equipment is costly and it has strict requirements for sample preparation and operation. Besides, like the Ransley method, it must be operated under strict procedures by trained personnel, maintained rigorously, and used mainly in laboratories.

Vacuum Fusion Method - Initially, the vacuum fusion method was developed for ferrous alloys to determine the gaseous elements, oxygen, nitrogen, and H, simultaneously [12]. It allows a specimen to be melted under vacuum and measures the increase in the gas pressure in the vacuum chamber. The increase in gas pressure results from the liberation of contained gases accompanying melting of the specimen and, therefore, can be converted to the gas content. This method was first used to determine H content in aluminum alloys in the early 1940is. By that time this method had been used successfully and was generally accepted as the standard method for ferrous alloys. At the same time, most of the attempts of estimating the H in aluminum alloys had been based on the extraction of the gas, at high temperature and in a vacuum, from the metal in either the solid or the liquid state. These methods were still under development and all the recorded data had been rendered suspect by uncertainties in the "black" corrections from the refractory parts of the apparatus [12]. As a result, the vacuum fusion method could be considered the first feasible method for determining H content in aluminum alloys. However, later the Ransley extraction method succeeded and gained popularity because of its accuracy and other advantages. Since then there has been no evidence showing the vacuum fusion method being used solely for H determination, but it is still used in related fields, for example, in measuring the total gas content in die castings.

The early vacuum fusion apparatus for aluminum alloys was the one built for ferrous alloys but operated at lower temperatures [12]. Recently, a vacuum fusion system was constructed by Gordon et al., which was used in their study of the occluded gas content in the die castings, including both the entrapped air and dissolved gases. Coupled with gas chromatography, this system could also identify the source of the contained gases. The schematic diagram of this system is shown in Figure 11 [13]. It consists of a vacuum pump, a chamber in which the sample may be melted, a pressure gauge, and a gas collection system. The gas collection system includes two gas collectors, one for collecting a sample of gases present in the melt chamber prior to melting of the sample and the other for collecting the gases after melting of the sample.

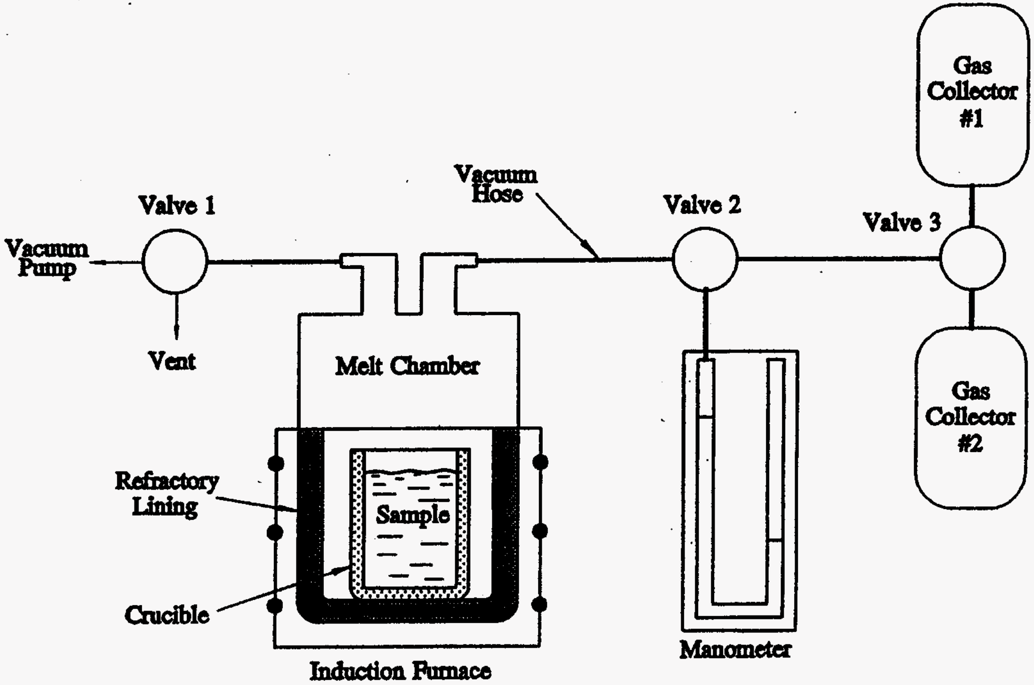

Figure 11. Schematic diagram of a vacuum fusion device [13].

The specimen has to be thoroughly cleaned, dried and carefully weighed before being placed in the crucible. After the specimen is placed in the crucible and the entire system is properly assembled, the determination of gas content proceeds in the following three steps.

(a) *Determination of the volume of the melting chamber* First, vacuum the whole system, including the melting chamber and the two gas collectors, to a sufficient level, and record the pressure, P_{GC} indicated on the manometer. Second, to disconnect both of the gas collectors from the vacuum system, further vacuum the melting chamber to an even lower level, disconnect the vacuum pump from the system, and record the pressure of the melting chamber, P_{MC}. Then reconnect the two gas collectors to the system and record the system pressure P_E. All these measurements are conducted at room temperature T_O.

Based on the measured values P_{GC}, P_{MC}, and P_E, and the known volumes of two gas collectors V_{GC} (=V_{GC1} + V_{GC2}), the volume of the melting chamber, V_{MC}, can be calculated.

(b) *Operation for gas content measurement* At room temperature, vacuum the whole system for a sufficiently long time to a low pressure level, disconnect the vacuum pump and maintain the obtained vacuum in the system, make sure there is no leak, and record the system pressure, P_O. Turn on the furnace to start melting the specimen, and just prior to melting of the specimen, record the system pressure, P_E. Disconnect both of the gas collectors from the melting chamber. Melt the specimen and record the chamber pressure, P_{MELT}. Then, reconnect one of the gas collectors to the melting chamber to collect the gases evolved from the molten metal.

(c) *Calculation of the gas content and identification of the gas species* According to the measured values of P_O, P_E, and P_{MELT}, the known values of V_{GC1}, V_{GC2}, and T_O and the calculated V_{MC}, assuming that the gases are "ideal" and the temperature in the melting chamber is not affected during melting, the temperature of the melting chamber, $T_{GAS,}$ and the volume of gas evolved upon melting of the specimen, V_{GAS}, can be calculated. Since the weight of the specimen is known, the gas content of the specimen (ml/100g) can be calculated. The gases in the two gas collectors, one containing the indigenous gas and the other containing the gases evolved upon melting of the specimen, are analyzed by the gas chromatography for the identification of the gas species present.

The method used by Gordon et al. does not need a special specimen [13]. The specimen can be sectioned from any product and from any location of the product to be analyzed, as long as it fits in the crucible. Its operation is relatively simple and the results are derived from only a few pressure measurements. The vacuum fusion unit itself (not including the gas chromatograph) is relatively inexpensive to construct and operate. This method measures the total gas content evolved, both dissolved and entrapped in the specimen, but not any special species. This is one of its advantages, that is, it can be used for the H determination of aluminum alloy where H is the only gas dissolved when there are no entrapped gases, as well as for the determination of other gases in other alloys. However, this is also one of its drawbacks; it will not be accurate to measure a special gas when other gases are dissolved or entrapped in the specimen, because the gas chromatography can only identify the species of the gases present but not give a quantitative measurement.

The vacuum fusion method uses a solid sample and needs to run at a high temperature to melt the sample. Thus, the sample surface H and the evolution of gases from the crucible and tubes of the apparatus may cause errors and need to be treated properly. In the early experiments adopting the apparatus for ferrous alloys, great attention was given to degassing the apparatus and the sample surface [12]. The furnace was first heated to a high temperature under vacuum with the sample placed in a proper place beside the furnace for a sufficiently long time. Then the temperature was lowered to the desired value and the sample was moved into the crucible by a magnet under vacuum. In this way the furnace area may be thoroughly degassed, but it is uncertain whether this occurred for the sample surface. When the sample was at a high temperature for long, it may be overdegassed and some dissolved H may be lost, while at a low temperature the surface H may not be removed completely. In Gordon et al's experiments the total gas contents were high in the range of 1.5 to 80 ml/100g, and therefore, the error caused by the sample surface and the furnace may consist of only a small portion of the total gases. However, when measuring only H, it would be a serious problem. Because there is very limited information about its use in H measurement in aluminum alloys, the accuracy of the vacuum fusion method is unknown compared with the other method. Presumably, it is low. In addition, because the sample needs to be melted under vacuum and it is difficult to be used for alloys containing certain amounts of volatile elements, such as Mg and Zn, there may be reactions between the alloy and crucible and furnace materials. Moreover, this method is time-consuming, taking several hours to conduct a measurement.

Vacuum Tin Fusion Method - The vacuum tin fusion method was developed in the late 1940's [14]. Before that time the only feasible method for measuring the H in aluminum alloys was the vacuum fusion method, and the Ransley method was still under development. The vacuum tin fusion method was developed in an attempt to solve the problems associated with the vacuum fusion method, mainly in analyzing the alloys containing substantial Mg or Zn, treating the surface H and shortening the operating time. In the vacuum tin fusion method, the sample was dissolved in the molten tin and the H was extracted at a much lower temperature than the melting temperatures of aluminum alloys. Thus, the speed of vaporization of Mg and Zn and the possible reaction between the alloy and crucible and furnace materials could be reduced. By using this method the surface H can also be distinguished.

A schematic diagram of a vacuum tin fusion method is shown in Figure 12 [15]. It consists of three sections: (1) furnace where H is extracted; (2) a unit collecting and measuring the evolved H; and (3) a device for analyzing the collected gas for H. The furnace section is a T-shaped borosilicate glass tube. In its vertical portion, about 200 g of tin was heated in a crucible. The horizontal portion was used for storage and preheating of the sample. In this portion a steel pusher for moving the sample was also stored. In operation, the system was first evacuated and the tin was melted for degassing, while the sample was preheated. After the tin bath was degassed, the sample and the steel pusher were pushed into the bath by a magnet. Dropping the pusher into the bath was done to submerge the sample in the tin bath and facilitate the stirring of the molten tin. Pressure of the evolved gas was measured with a McLeod gauge in the collection section. The tin bath was occasionally stirred by moving the still pusher up and down by the magnet. When the rate of gas evolution subsided to that of the blank, the gas was pumped from the fixed volume into the heated palladium tube allowing the H to diffuse out. When the palladium tube had cooled to room temperature, the residual gas was pumped back to the original calibrated volume and the pressure was read on the McLeod gauge. The difference between the original volume of gas collected and the residual gas represented the volume of H evolved from the sample. For different alloys different preheating temperatures needed to be used. Most aluminum alloys were preheated at 525 °C (980 °F), but the alloys containing substantial amounts of Mg or Zn were preheated and dissolved at 500 °C (940 °F) or lower, since rapid vaporization of Zn and Mg occurs above this temperature.

To distinguish the amounts of H absorbed on the sample surface and dissolved in the bulk sample, three measurements could be conducted from three identical samples. The first sample was analyzed for the total H content from the "as-received" sample. The second sample was preheated for 4 hours at 500-525 °C (940-980 °F) in a vacuum to remove the entire surface H and nearly all of the dissolved H. Then without exposing it to the atmosphere the sample was analyzed. The value obtained was the residual dissolved H. The third sample was also preheated for 4 hours at 500-525 °C (940-980 °F) in a vacuum, as for the second sample, but the sample was then exposed to the atmosphere, reabraded in the same way as in the final step of the sample preparation, and analyzed. The difference between the values obtained from the second and the third samples were the amount of surface H. The amount of the dissolved H could be calculated from the total amount of the H value obtained from the first sample and the surface H.

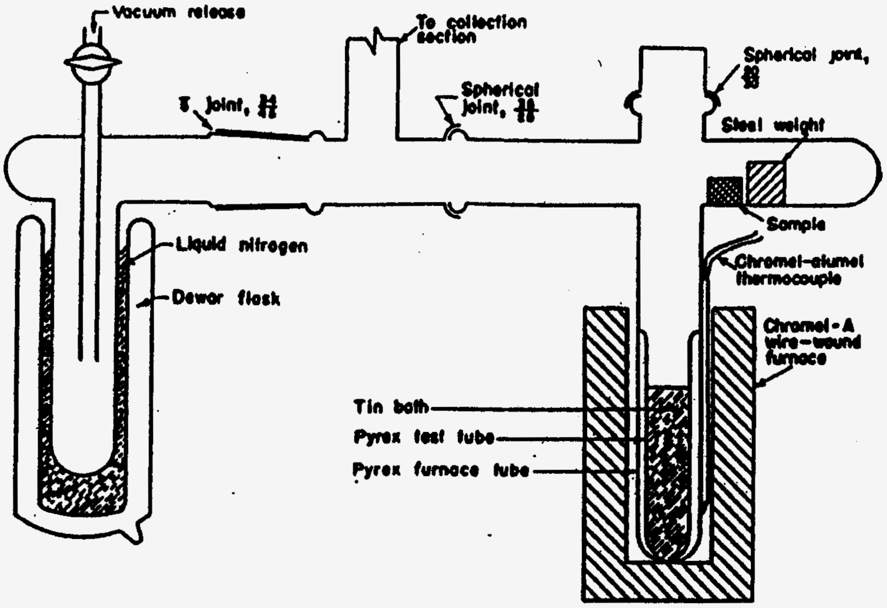

Figure 12. Schematic diagram of a tin fusion apparatus [15].

Though this method was better than the vacuum fusion method in analyzing alloys with higher Mg or Zn, treating surface H, and reducing the operating time, its accuracy was still low, which was reported to be 0.1 ml/100g. This level of accuracy was not suitable for the alloys with low H contents. In addition, it was still a time-consuming process. Maybe for these reasons this method did not survive when later techniques emerged.

1.3.2 In-situ Quantitative Analysis

Telegas and Alscan Analyzer **-** The telegas technique was developed by Ransley, Talbot, and Barlow in 1958 and it is now marketed by Alcoa. The Alscan analyzer was developed by Alcan based on the same principle as the Telegas uses.

The basic principle for the Telegas and Alscan methods is the closed-loop gas recirculation technique. A small amount of carrier gas (such as nitrogen, argon, or helium) is brought in contact with the molten aluminum alloy by, and recirculated through, a ceramic probe, which is submerged in the molten alloy. The H diffuses into the recirculating carrier gas until it has reached its equilibrium pressure to the monatomic H content of the melt. At this equilibrium condition, according to Sievert's law,

$$[H] = S_o \cdot \sqrt{P_{H_2}} \qquad (30)$$

where: is the H partial pressure over the melt;
S_o is the H solubility in the alloy under 1 atm of H_2 gas (ml/100g); and
$[H]$ is the concentration of H in the melt (ml/100g). At equilibrium, $[H]$ equals the solubility, S, corresponding to the H partial pressure P_{H_2}.

The H_2 pressure, P_{H_2}, in the carrier gas can be measured using a gas thermal conductivity sensor (katharometer - a hot wire (or film) detector), as in the Ithac-02 and LECO RH-3 methods. Thus, if S_o is known, $[H]$ can be calculated. However, because S_o is a function of metal composition and temperature and generally the function is unknown, $[H]$ could not be calculated from this equation directly. To overcome this obstacle, in the Telegas a factor, k, called Telegas correction factor, was empirically determined. This factor is the ratio of the H solubility of the aluminum alloy to the H solubility of the pure aluminum for the alloy to be measured [16, 17]. Based on this information the relationship between [H] and the temperature, alloy, and P_{H_2} is established.

In the case of the Alscan analyzer, Equation 30 is modified as [18]:

$$[H] = S_o' \cdot \sqrt{P_{H_2}} \cdot CF(T) \cdot CF(A) \qquad (31)$$

The Equation 31 is shown in the previous section as Equation 22, where: $[H]$ equals the H solubility, S, at partial H pressure P_{H_2} at equilibrium. S_o'

is the solubility of H in pure aluminum at a reference temperature taken to be 700 °C. S_o' can be measured and is available; $CF(T)$ is a correction factor for metal temperature, which can be derived from the known solubility-temperature curves for pure aluminum [19], and $CF(A)$ is a correction factor for metal composition.

Alcan [20] developed the following equation for calculating the $CF(A)$, which is based on Hess' work [21] and claimed to be appropriate for all foundry alloys.

$$\log CF(A) = 0.0170\ \%\mathrm{Mg} - 0.0269\ \%\mathrm{Cu} - 0.0119\ \%\mathrm{Si} \qquad (32)$$

The Equation 32 is the same as equation 23 shown in the last section. Thus, by knowing the alloy composition, the temperature and measuring P_{H_2}, $[H]$ can be calculated.

Basically, both the Telegas and Alscan analyzers consist of a gas recirculating system including a changeable, consumable probe, a sensor (thermal conductivity detector) and a data display. The probe houses the open section of the carrier gas recirculating system, where the gas contacts the molten metal.

The Telegas uses as the carrier gas. In the early model of the Telegas the device displayed the reading of the gas thermal conductivity sensor, which was proportional to the P_{H_2}. The device itself did not measure the temperature of the melt, which was measured separately. Having obtained the meter reading and temperature, the operator could find the H content in the melt by referring to a set of tables in the manual, which related the H content to the alloy, temperature and instrument meter reading. This method has been used effectively on the shop floor for many years. This kind of device should be simple and inexpensive; however, it was bulky and the manual task of converting the meter reading and the temperature measurement to the H content was cumbersome and error-prone. A new version of Telegas, Telegas II, has been developed recently. A schematic diagram of the Telegas II is shown in Figure 13. The Telegas II is a self-contained instrument, which could measure, calculate, and display and/or print the H content directly. It is also compact, portable, and easier to use than the original Telegas.

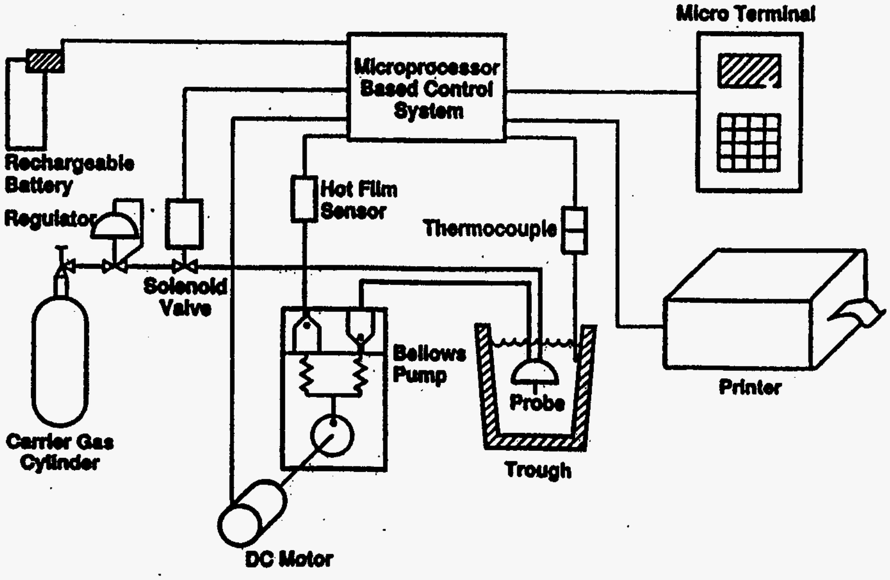

Figure 13. Schematic diagram of Telegas II [16].

Figure 14 shows a schematic diagram of the Alscan [22]. In the Alscan analyzer, like in Telegas II, both the P_{H_2} values and the temperatures are measured and the $[H]$ value is computed automatically by the built-in microprocessor with special software. The correction factors $CF(T)$ and $CF(A)$ are calculated according to the measured temperature and the alloy composition, which is input by the operator, and then the $[H]$ value is calculated, displayed and/or printed. The software of the Alscan analyzer applies to three carrier gases, nitrogen, argon and helium. Thus, the operation of this device is simpler. It is also claimed that the sensor is implemented in a proprietary manner, which renders the operation highly accurate independent of ambient temperature variation.

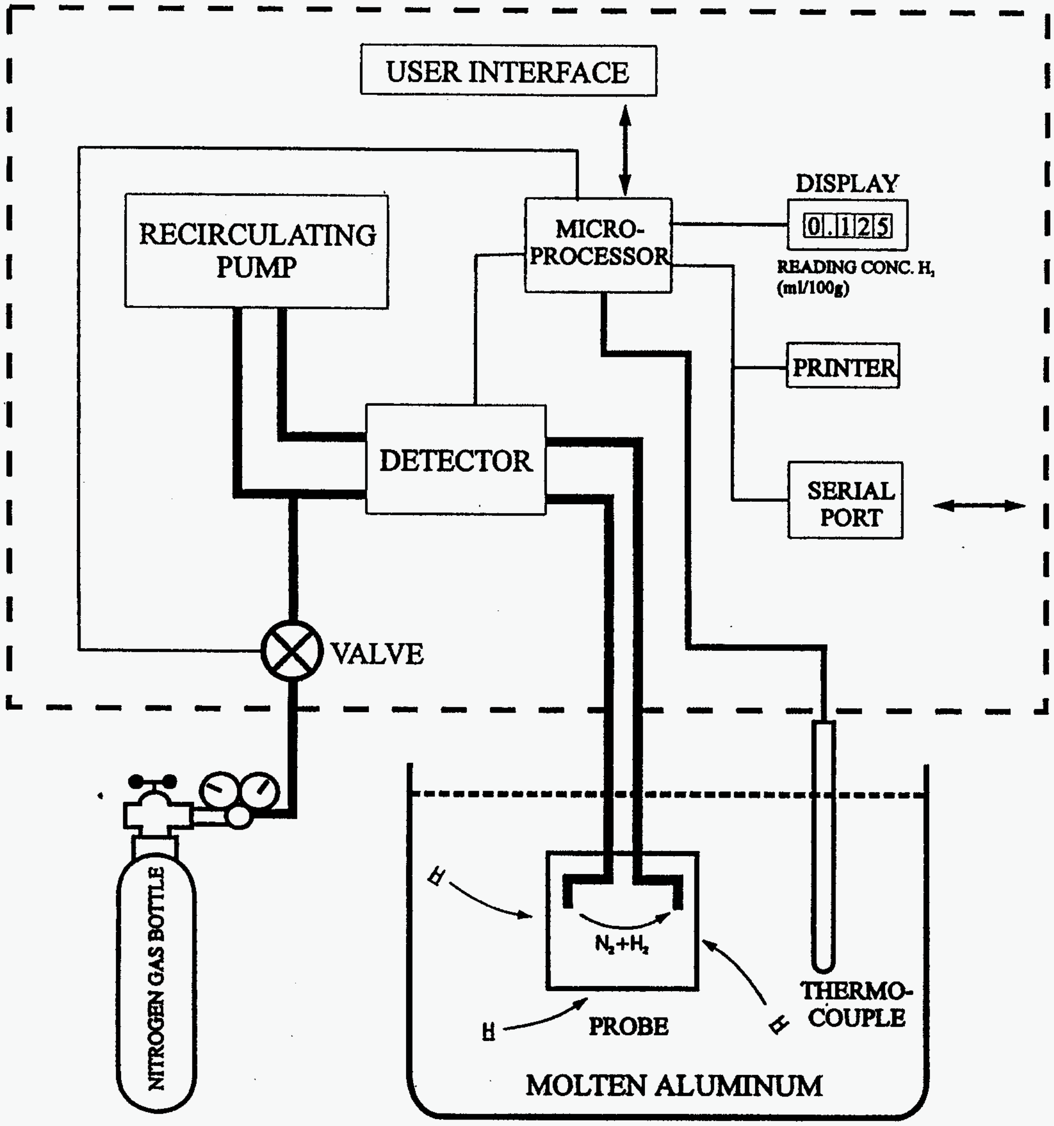

Figure 14. Schematic diagram of Alscan [22].

Figure 15 (a) and (b) show schematic diagrams of Telegas and Alscan probes, respectively. In the Telegas the probe consists of a hood and two tubes, outlet and inlet tubes, of the carrier gas recirculating system. The hood is made of ceramic and the metal tubes are embedded in a ceramic tube. During the operation work the probe is inserted in the melt. Under the hood the outlet tube bobbles a small amount of the carrier gas continuously into the molten metal, where the H diffuses from the molten metal into the gas bobbles. The gas bobbles are collected by the hood and led into the inlet tube to recirculate. The probe should be placed in the melt vertically to ensure no gas escapes. Since the hood and tubes are submerged in the melt, thermal shock and the possible blockage of the gas tubes caused by the metal penetration limit the probe's serving life, which in turn adds cost to the operation. Grusleski et al. found that the blockage of the gas tubes was more severe in modified than in other alloys [23]. The reasons for this were not identified, but because it occurred mainly after modification, it was likely caused by the intermetallics formed by modification treatment. It was reported [23] that some blocked probes could be cleaned and recycled. This could be done by suspending the probe vertically in a furnace at 740 °C and using compressed air to blow out the capillaries. Obviously, recycled probes had a shorter life than new ones.

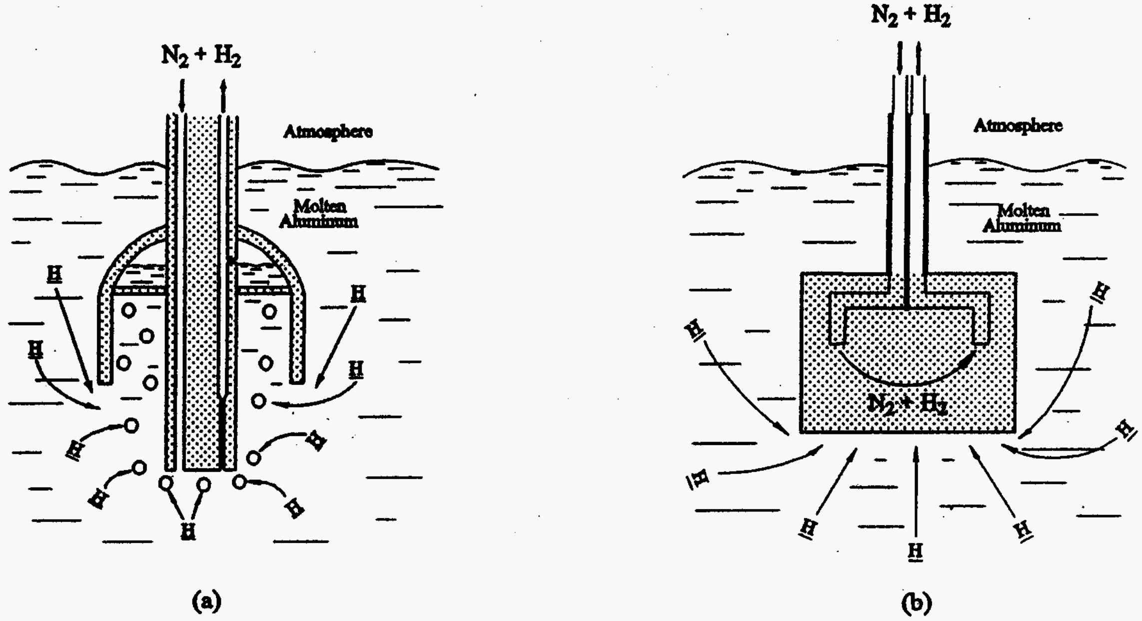

Figure 15. Schematic diagrams of (a) Telegas probe and (b) Alscan probe.

The ALSCAN analyzer uses a "disposable" probe. It consists of a small piece of open pore ceramic, in which two capillary metal tubes, the outlet and inlet of the carrier gas, are embedded. The pore size of the probe material is large enough to allow good gas circulation but small enough to prevent metal penetration. In this manner, the ceramic piece simply serves to physically locate a stationary gas bobble inside the molten metal. At the interface between the open pores of the ceramic piece and the molten metal the gas/liquid H exchange takes place.

The open pore structure enhances the thermal shock resistance of the ceramic. The metal tubes embedded in the ceramic piece do not contact the melt, and the section of the metal tubing, which contacts the melt, is protected by a thin ceramic coating. It was reported that with this structure the probe was simple, inexpensive, and very robust. It had no tube blockage and no thermal shock to worry about. It could be directly inserted into the melt without any preheating. Moreover, it could be operated at any convenient angle, even in very shallow metal, as long as the ceramic portion of the probe can be submerged totally in the melt. It is also claimed that this structure avoids a possible error associated with Telegas. When using Telegas some gas bobbles left in the melt from the degassing operation may be collected by the carrier gas bobbles and the hood, leading to unstable or undervalued results. This does not happen to the Alscan analyzer. The Alscan analyzer is also equipped with a defeatable stirring device, which refreshes the probe/metal interface providing for a fast response time and good reproducibility. As a result, this process normally requires approximately five minutes for the H equilibrium between the carrier gas and the metal, but a ten minute operation is recommended to insure good reproducibility. It was reported that the average variability was 0.02 ml H_2/100 g under actual production conditions including temperature variations. Under more favorable conditions, e. g. in a hot but stagnant melt, the reproducibility was 0.01 ml H_2/100 g. In the late 1980's the average lifetime of the Alscan analyzer was on the order of five to eight hours cumulative in metal or five to eight distinct dippings.

Compared to the sub-fusion and fusion techniques, Telegas and Alscan both are much faster in quantitatively determining the H content of aluminum alloys. It takes about 10 to 20 min for one determination and, therefore, they can be used for on-line control. Reportedly, they have a high accuracy. However, it is generally considered that their accuracy is not always as high as that of the sub-fusion method while it is higher than that of the reduced pressure test, which will be discussed below. They also have higher operation costs because of the costly and venerable prove.

A set of data presented by Sigworth [24] showed the Telegas instrument was not suitable for measurements at low temperatures. The possible reason for this, he proposed, was the freezing of metal inside the probe at low temperatures caused by the cold recirculating gas. Because the recirculating gas in Telegas is a small amount and contacts a volume of the metal within the reversed probe cup, it would be susceptible to the loss of gas bubbles in a fast flowing metal stream, and/or to the catching of microbubbles of gas used for the degassing operation, thus giving low readings. It was reported [2] that Dokken and Pelton identified a more fundamental problem, called the "chimney effect," affecting the performance of the Telegas probe. This "chimney" was described as being present along the porous insulating layer of material on the outer surface of the probe which was applied to protect the underlying ceramic against thermal shock failures. Dupuis et al. verified this effect with an experiment [2]. Two Telegas probes were used to measure the H content in a melt of pure aluminum at 700 °C contained in a tightly insulated vessel under controlled atmosphere. One probe was used normally. Around the ceramic tube of another probe a glass tube was inserted into the melt with the other end being open to air. This glass tube connected a small surface area of the metal around the probe tube to external ambient atmosphere and would not affect the H content in the melt. The probe with the glass tube showed the "chimney effect." The H content measured using this probe showed about 14% less than the probe normally used for tested gas mixture in the vessel. The underestimation of H content caused by whatever reasons in the Telegas may be corrected in some way. Studying the charts provided with the Telegas instrument, Dupuis et al. found that the H solubility value used for the instrument was larger than standard. This larger solubility value would partially offset the underestimation, but it was considered insufficient.

CHAPEL or DPM - This is a direct H partial pressure measurement technique that was developed in Germany in the 1980ís. It is called CHAPEL (short for Continuous Hydrogen Analysis by Pressure Evaluation in Liquids) [25, 26] or DPM (short for Direct Pressure Measurement) [27, 24]. Figure 16 shows a schematic diagram of apparatus using this technique. A porous probe consisting of a graphite disc is affixed to the end of an impermeable ceramic tube and placed in the aluminum melt. The probe and tube are connected to a pressure measurement instrument and this assembly is connected to the vacuum system through valves 1 and 2. In the measurement process, the space inside this assembly is first evacuated. When evacuation is complete, valves 1 and 2 close. Under the low pressure the H dissolved in the melt diffuses from the melt into the space inside this assembly, where, consequently, the gas pressure rises. When the H diffusion reaches equilibrium, H_2 gas pressure is recorded by the measuring sensor. According to the H gas pressure, the volume of the space inside the assembly, and the melt temperature, the H concentration in the melt can be calculated.

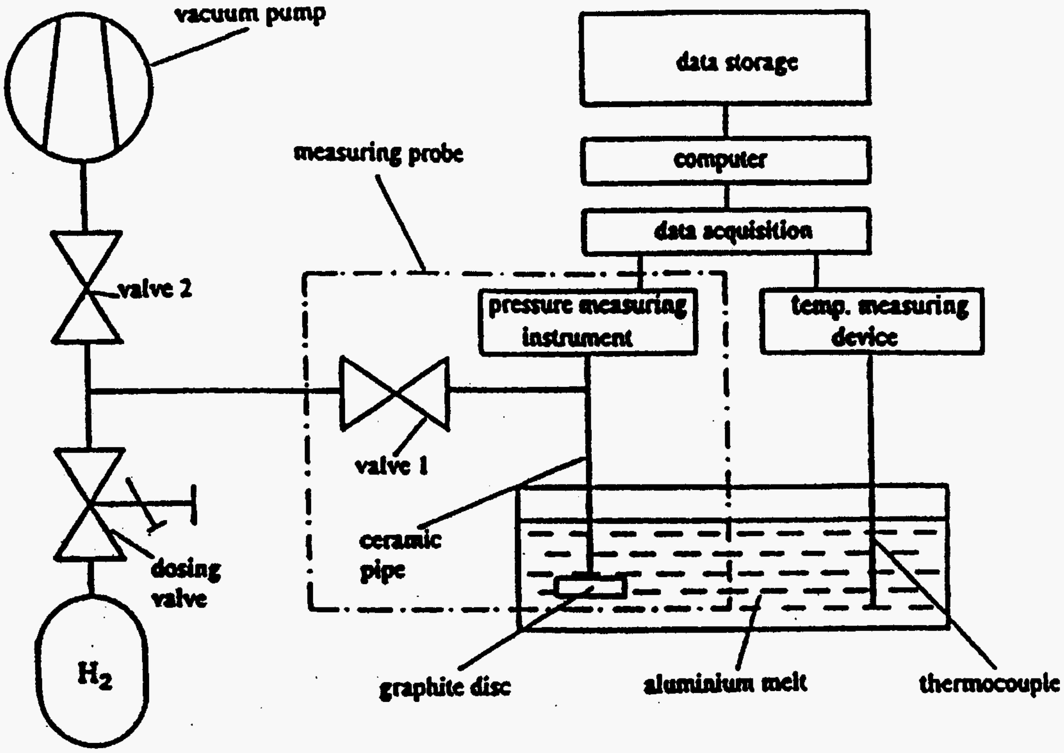

Figure 16. Schematic diagram of CHAPEL device [26].

Obviously, it is a simple and straightforward technique. Actually, when a H measurement device was first developed about 40 years ago, Ransley tried this method but abandoned it as being impractical. Since then numerous advances have been made in instrumentation and electronics, which make the method feasible. A key component in the apparatus using this method is the probe, where the H diffusion from melt to measuring space is taking place. The probe material must have a porous structure, so that gas may easily diffuse from the melt through the walls of the probe into the measuring volume. The pores must also be sufficiently small, and the material non-wetting with aluminum, so that capillary forces will prevent the liquid metal from entering the apparatus. Thus, the porous probe, which is made of graphite at present, acts as an “artificial bubble” with respect to the gas phase. When the probe is first placed in the melt, 20 to 60 min are required for equilibrium, depending on the design of the apparatus and probe employed. The response time could be reduced by reducing the measuring volume and increasing the permeability of the probe. By doing so, the best response time obtained was 20 min. To further expedite this process, a doping technique is adopted. A H bottle is connected to the system by a doping valve, which can admit a small, controlled amount of H into the measuring space. The added H increases the H pressure in the measuring space and therefore shortens the time required to reach equilibrium. The doping technique allows equilibrium to be reached in a few minutes. Once equilibrium is reached in the measuring probe, the system continuously monitors the H change in the melt. Readings can be validated at any time during continuous monitoring by doping the probe. For validation, the probe is temporarily evacuated and doped with pure H to approximately the original value. The reading is confirmed if the new value is roughly equal to the previous measured value after a few minutes have elapsed. During several years' development the early laboratory device has undertaken several improvements in accuracy, reliability and durability and been automated. The CHAPEL device has recently been commercialized and used in production [26].

This method and the operation are exceedingly simple. In its operation only the doping process needs more attention. With the computer-aided automated apparatus, a specially trained operator is not necessarily required. Because it has a rugged probe insensitive to thermal shock, it can be used for spot measurement or used continuously for a long time. For example, a test assembly consisting of a graphite probe and an alumina tube was used continuously for several weeks without deterioration in the assembly and readings could be obtained as long as the temperature was less than 800 °C [24]. The experiments suggest that the cost of operation would be significantly less than with its currently used counterparts. Sigworth [24] presented a set of data showing the accuracy of the DPM, which was compared with the Telegas measurements. At high temperatures the agreement between the two sets of readings was good: to within 0.01 ml/100g. At low temperature the discrepancy was higher: on the order of 0.04 ml/100g. At high gas contents the DPM probe gave consistently higher readings, whereas the opposite occurred at lower gas contents. The difference in readings between the two instruments occurred primarily as the temperature approached the melting point, where a large disagreement occurred. The pressure of the DPM readings increased from 14 to 60 mbar as the temperature dropped from 800 to 670 °C. The pressure dropped as the melt was heated once again. This change was reversible. The reason for the pressure-temperature dependence is governed by Sievert's law (see Equation 30). For the melt with a given H content, [H], at equilibrium the square root of H partial pressure, $\sqrt{P_{H_2}}$, is inversely proportional to the H solubility, S_o, in the melt. The H solubility in the melt, S_o, is temperature dependent (see Equations 4, 5, 7, and 8). When temperature increases, the H solubility increases. So, when the temperature increases the H_2 partial pressure decreases for a given H content. Calculation from the H_2 pressure readings in the DPM gave a constant H content value. This means that the results obtained from the DPM are not affected much by the temperature variation within the tested range.

However, the Telegas technique did not give the same results. Sigworth's data suggests that at higher temperatures the DPM and Telegas both work well, but at lower temperatures the DPM works better and could give more accurate readings than Telegas. The possible reason for this is that in the DPM there is no metal freezing inside the probe at lower temperatures, which may happen for Telegas because of the cold recirculating gas. The commercial DPM apparatus could measure gas pressure 0 - 200 Torr, which corresponds to the total effective range of pressure in normal melting practice, and give readings of gas content in the range of 0.05 - 0.5 ml/100g. The temperature compensation of the sensor and the related amplifier limited the absolute level of accuracy to about 0.25%. Consequently, the absolute accuracy of the pressure measurement over the range is about 0.5 Torr. At higher gas contents this error is insignificant, but it is an important part of the total pressure at low gas contents, considering that the equilibrium pressure at 0.05 ml/100g is 1.3 Torr. For low gas contents, it could be possible to use a different sensor or amplifier to give readings in the range of 0 - 40 Torr with a higher accuracy. The main operating problem observed during trials is with the fluxes in the melt. Molten salts of the fluxes penetrate the porous probe or "artificial bubble". This destroys the probe and makes meaningful measurements impossible, so this apparatus cannot be used where salts are present. Because it is still a new method, the data from practical use are limited.

Electrochemical Method

Electrochemical Probe - Gee et al. worked on an electrochemical method in the middle 1970's [28]. By that time solid electrolyte probes had been used for the instantaneous determination of oxygen in steel and copper and in the measurement of sodium content of molten aluminum alloys. Gee et al's work was an examination of using this technique for H measurement in aluminum alloys.

In a cell consisting of two electrodes in an electrolyte, the equilibrium electrical potential, E, measured across the electrode/electrolyte interfaces and the chemical potentials of species *i* at the two electrodes, μ'_i and μ''_i have the relationship:

$$\mu'_i - \mu''_i = -zFE \tag{33}$$

where F is the Faraday constant and z is the number of electrons involved in the reversible reaction occurring at the electrolyte interface.

For two gaseous H electrodes, chemical potentials may be replaced by the corresponding partial pressures P'_{H_2} and P''_{H_2} :

$$RT \ln \frac{P'_{H_2}}{P''_{H_2}} = -zFE \tag{34}$$

where R is the gas constant and T is the temperature. This equation indicates that in such a cell, if one of the partial pressures is known or can be measured and zFE , (the electromotive force, *emf*) can be measured, the other partial pressure could be calculated. This cell may be used as an analytical device.

For forming such a cell as a H probe used in aluminum, the aluminum melt containing H will act as the electrode whose H partial pressure is to be measured. Then, for this device to be successful it must find the electrolyte and the other H electrode. It is essential that the electrolyte maintain its properties under the conditions of operation of the system. In particular, it must be thermally stable and be stable in contact with the two electrodes. The other electrode must also maintain the H partial pressure constant. For this electrode to be a H reference, a mixture of a metal with its hydride which would provide a fixed H potential at given temperature would be suitable. Gee et al. constructed such a probe [28], in which a calcium hydride was chosen as the electrolyte and a mixture of calcium and calcium hydride as the other electrode. The equilibrium H pressure over mixture of βCa and αCaH_2 at compositions of 20 to 95 mole pct CaH_2 and in the temperature range of 873 to 1053 K (600 to 780 °C) was given by:

$$\log P_{H_2} = \frac{-9610}{T} + 10.227 \tag{35}$$

Thus, a given temperature in the range the P_{H_2} over the mixture of calcium and calcium hydride can be calculated, which is the partial pressure P'_{H_2} in Equation 34. Knowing the P'_{H_2} , the equilibrium H pressure of the melt, P''_{H_2} , can be calculated from Equation 34 when *emf* is measured. According to Equation 3, the relationship between the H solubility of pure aluminum and the temperature and the corresponding H gas partial pressure established by Ransley et al. [19], the H solubility can be calculated for the P''_{H_2} . This value will be the H content to be measured. The equation for calculating the H solubility can be derived by substituting Equations 35 and 30 into Equation 34, giving:

$$\log S = \frac{-zFE}{4.606RT} - \frac{7565}{T} + 6.47 \tag{36}$$

For alloys, like in Telegas or Alscan, composition correction factors can be used in the calculation. By using this method the variables needed to be measured to determine the H content are the temperature and the *emf* (*zFE*). The schematic diagram of Gee et al's probe and lance is shown in Figure 17. The outer steel casing of the lance provided the connection for the aluminum electrode. The probe was connected to the lance central steel rod that was insulated by ceramic tubes. The coaxial construction prevented *emf* pickup from external sources. The *emf* from the probe was measured on a Keithley 610 C electrometer. The temperature was measured separately.

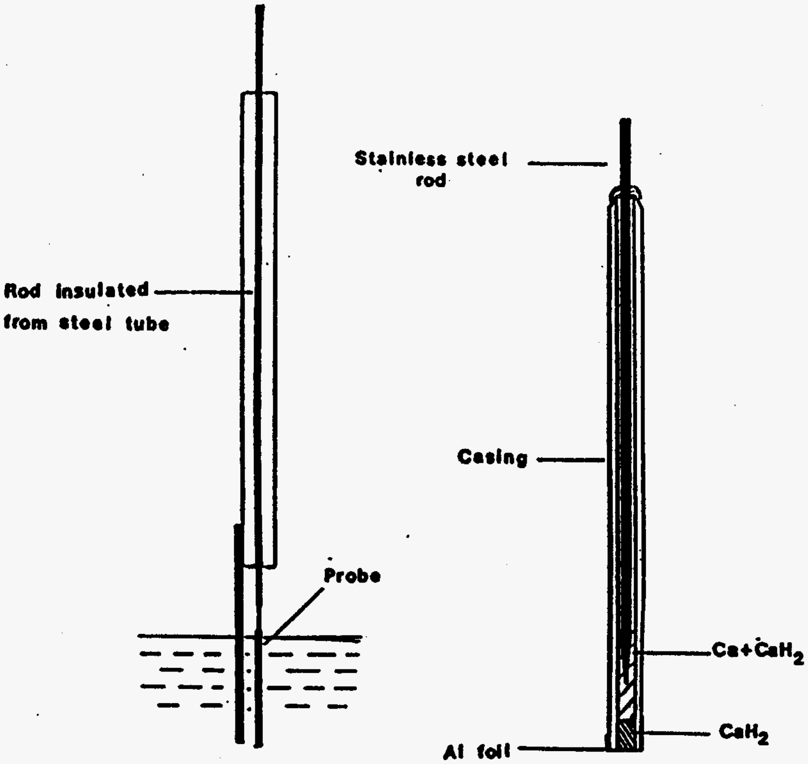

Figure 17. Schematic diagram of electrochemical H determinator [28].

If there is a reliable probe the operation of this method will be very simple. A steady *emf* could be established in 2-3 min and, therefore, this method gives virtually an instantaneous reading. The results obtained in Gee et al's tests were said to be in good agreement with the vacuum sub-fusion method. However, the thermodynamic stability of the probe materials was not satisfactory, resulting in a short life of the probe or unstable readings. It was not seen that this method underwent any further development or use in practice, and, therefore, information about it is very limited and its accuracy is unknown.

Notorp Instrument - Gallo mentioned the Notorp instrument in a paper about successfully using it in a degassing practice [29]. No detailed information has been found about this instrument either in Gallo's paper or from other available sources. Based on a description of its operating principle briefly mentioned in Gallo's paper, this instrument may be categorized to be one of the electrochemical devices. It said that the Notorp equipment combines Sievert's law and a H concentration cellular sensor [30]. The construction of the sensor is made using a non-porous proton conducting ceramic which is plated with a layer of porous platinum mounted in the end of a high density tube. It uses a mixture of 1% H_2 gas and 99% Ar as reference gas. The instrument is also provided thermocouple - electrode assembly which provides the temperature measurement required to solve the Sievert equation. This equipment was developed in Japan and the Foundry System International was the first successful user in the U. S.

H-Strip and Diffusion Tube Methods [31] - The H-strip and diffusion tube methods both were developed for Mg and its alloys. As mentioned earlier, the volatile nature of Mg adds some difficulties in H measurement for alloys containing substantial Mg. Therefore, some methods suitable for H measurement in aluminum and its alloys, like vacuum fusion, do not work well for Mg and its alloys and vice versa. The difference between H content in Mg and aluminum may be the main factor why some methods are suitable for use in Mg but not in aluminum. Mg has a much higher H solubility than aluminum and, subsequently, Mg and its alloys generally contain more H than aluminum and its alloys. So, an error produced by a method can be relatively small for Mg and its alloys but it could be large for aluminum and its alloys. It is a matter of the accuracy. In principle, a method that works well for Mg has no reason not to work for aluminum. These methods are briefly introduced here as methods which have been proposed and investigated and which may become feasible for aluminum as their accuracy improves.

The H-strip method was first introduced for the measurement of H in molten Mg by Bakke et al. [32]. Figure 18 shows the principle of this method. A steel tube is used to restrict a known quantity of melt. H is extracted from the sample by gas purging. The purged gas is continuously sampled and H is measured with a gas chromatograph. The advantage with this method is that the measurement is direct. However, it is time and labor consuming and the reproducibility was reported to be about ±15% for H contents of 15-60 ppm (~16.7-66.7 ml/100g). The accuracy, about ±2.5-10 ml/100g, is apparently not suitable for aluminum and its alloys. The inaccuracy was considered partly due to the pickup of H through the steel walls of the probe.

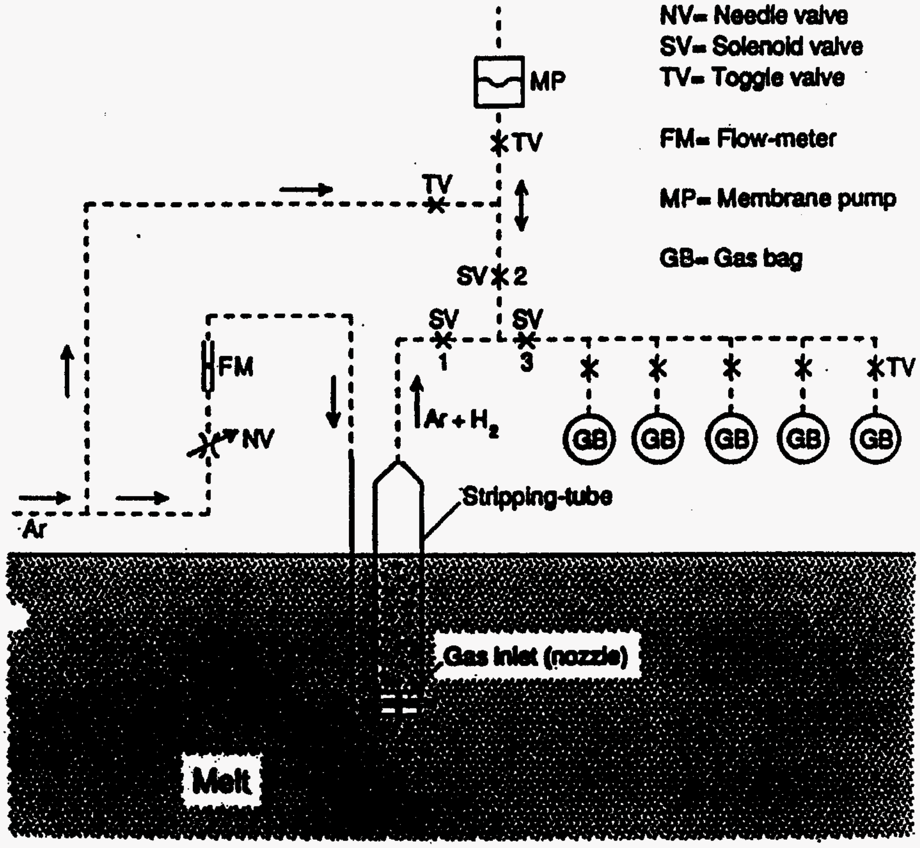

Figure 18. Flow scheme of H-strip method [32].

A technique, called Dip-in Probe Technique, was developed for aluminum and its alloys by Russian scientists Vaschenko et al. [33]. According to its principle described by Anyalebechi, this technique was very similar to the H-strip method [17]. In the dip-in technique, H was extracted from a melt sample of a known size contained in a compartment of a probe. The probe was immersed in the melt to a depth of 300 mm. The melt sample was drawn into a part of the probe and isolated from the environmental melt by a gas seal. Ar carrier gas was circulating into the melt sample, and the H evolved from the sample into the carrier gas was measured by an integrating gas analyzer. It was reported that the analysis took 4-10 min with a sensitivity range of 0.03-1 ml/100g and accuracy for Al-Mg alloys was 0.01-0.02 ml/100g. Information about this method is limited and it is not seen in development or practical use in aluminum and its alloys outside Russia. Because of the similarity in principle, this method presumably should have some operating problems similar to the H-strip. Its surprisingly high accuracy over the H-strip method may be attributed to different probe material and/or some advancement in this method, but more evidence from independent sources is needed for the accuracy to be verified.

The diffusion tube method was developed by Bakke et al. to overcome the operating problems with their H-strip method. Figure 19 shows the principle of this method [31, 34]. It is based on the diffusion of H through a steel tube immersed in the melt. The H diffusing through the steel tube is brought to the measuring device, katharometer, carried by Ar. The katharometer gives a constant value for H, which can be converted to the H concentration in the melt. The advantage is that the instrument can be used for the continuous supervision of the melt. Disadvantages are that the measurements strongly depend on the diffusion rate of H through the steel walls and the contact area between the tube and melt. Also because the values reported for diffusion of H in steel show some disagreement and depend on temperature, the apparatus may be difficult to use routinely. Especially for a melt with low H content, as in aluminum, the small difference in the H concentration between the inside and outside of the steel tube would make the measured value too low with a large error.

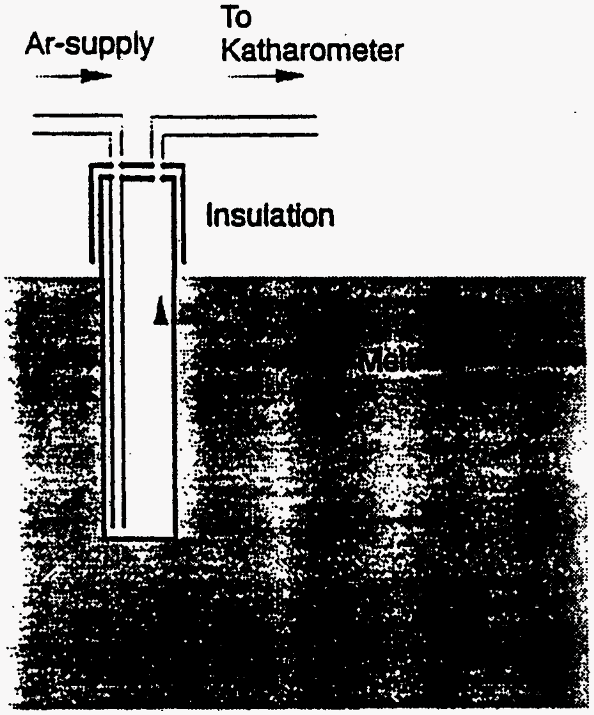

Figure 19. Principle of diffusion tube [31].

1.3.3 Semi-quantitative Techniques

Reduced Pressure Test (RPT) - Reduced pressure test (RPT) is also called vacuum solidification test or Straube-Pfeiffer test. Figure 20 shows a schematic diagram of the RPT unit. In this test a small amount of molten aluminum alloy sample is allowed to solidify under controlled reduced pressure and the gas content is estimated or determined by observing the solidification behavior of the specimen or by density measurement or porosity analysis of the solidified specimen. This method was first employed in the 1920's and has been developed ever since. In the early stage of its development it was only used for qualitative estimation of the quality of the molten alloy. Now it is a semi-quantitative method for measuring H content and is widely used in the aluminum industry.

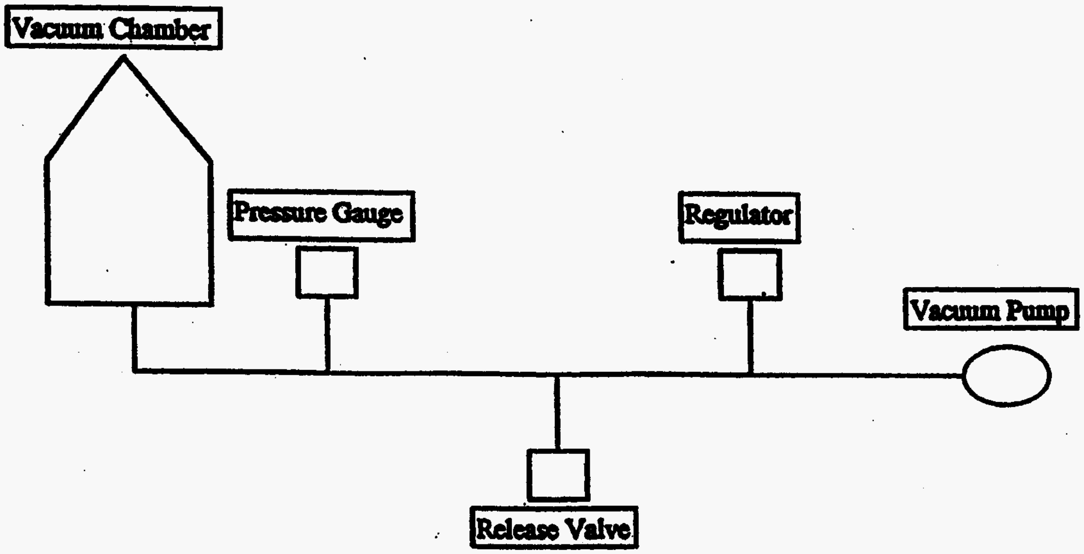

Figure 20. Schematic diagram of reduced pressure test device.

As mentioned in Sections 1.1 and 1.2, H solubility in liquid aluminum and its alloys is much higher than that in their solid, and the dramatic solubility change may result in the formation of pores during the alloy solidification. During the formation and growth of the gas pore in the melt, the gas pressure inside the pore should at least be equal to the external pressure. For a stable pore,

$$p_g = p_o + \rho_L g_r h + \frac{2\sigma_{gL}}{r} \qquad (37)$$

where the term on the left side of the equation, P_g, is the total gas pressure inside the pore; the terms on the right side of the equation are the external pressure, which include P_o (the ambient pressure), $\rho_L g_r h$ (ρ_L is density of the liquid metal, g_r is gravity and h is the distance from the pore to the melt surface; together they constitute the metallostatic pressure head), and $2\sigma_{gL}/r$ (the pressure on the pore resulting from the pore-melt interfacial energy σ_{gL}, r is the pore diameter). In the aluminum alloys only H can dissolve to a significant extent, so the gas in the pore can be considered to be a single species. Thus, in the aluminum alloys the P_g at equilibrium with the dissolved gas in the surrounding metal can be calculated according to the thermodynamic relation:

$$\%\underline{H}_L = K_L^{'}\sqrt{P_{H_2}} \qquad (38)$$

where $\%\underline{H}_L$ is the weight percent of H dissolved in the liquid metal, and P_{H_2} is the H partial pressure in the pore. K'_L is constant, which depends on alloy composition and temperature, and generally increases with the increase of temperature. Since H_2 is the only gas in the pore, the P_{H_2} should be equal to P_g. According to Equation 37, for the formation and growth of a pore P_g should be greater than P_o, that is, P_{H_2} should be greater than P_o. Therefore, to facilitate the gas pore formation and growth the means can be increasing P_{H_2} and/or decreasing P_o. In the conventional solidification, the ambient pressure, P_o, is constant, at one atmosphere pressure. The pore formation and growth, as described above, are due to the increase of P_{H_2} caused by the enrichment of H in the remaining liquid and to the decrease of K'_L caused by the temperature decrease. When the solidification occurs under reduced pressure the decreasing P_o facilitates the formation and growth of the pore, leading to the pore formation at a higher temperature and lower fraction solid or even in full liquid or at lower H content than that under one atmosphere pressure. This effect of reduced pressure can also be seen from Equations 3, 6, 18, 19, 20, and 22. The H solubility, S_o, in the liquid metal decreases with the decrease of H gas partial pressure and temperature. Since, when melt is under reduced pressure, the H gas partial pressure above it is reduced accordingly, a certain H content which is initially below the H solubility at ambient, 1 atm, pressure may become higher than the H solubility under the reduced pressure. This may result in the pore formation at a higher temperature. Consequently, more H can be released from the liquid metal under reduced pressure. In addition, the volume of the pore is expanded. For example, according to Boyle's law, if 0.1 atmospheric pressure is used, the volume occupied by the gas precipitated from the melt is magnified by a factor of 10 comparing with at one atmospheric pressure. If all the pores are maintained in the metal during the solidification, a greater level of porosity will result. In this manner the effects of dissolved H on porosity and density are magnified by the reduced pressure, and thus the accuracy of using porosity or density values to evaluate the H content can be enhanced. The RPT was developed on the basis of these phenomena.

Generally, the following characteristics that occur occurred in the RPT are used to evaluate the H content:

1. Surface movement of the specimen;
2. Porosity content in the specimen;
3. Density of the specimen; and
4. The pressure at which the first pore is formed in the melt.

Based on different characteristics various versions of RPTs have been developed. These methods can be broadly classified as a conventional (basic) test with modifications.

Conventional Reduced Pressure Test - In the conventional test the specimen is allowed to solidify at a constant, predetermined reduced pressure and the H content is determined by observing or analyzing the solidified specimen. The following three methods are generally used in the H determination.

The surface of the specimen may move during solidification because its volume increase caused by the porosity formation and the pore expansion under low pressure. Visual observation through a viewing window or a transparent hood of the vacuum chamber during solidification or observation of the surface shape of the solidified specimen gives the indication. Surface moving up and/or gas bubbles coming to the surface indicate the presence of H. The more gas dissolved in the original melt and the lower the pressure, the more severe the surface moves up and the more gas bubbles come to the surface, resulting in a puffed specimen with a convex surface. When only a little or no gas is dissolved in the melt, there are no gas bubbles observed, the surface does not move up and may be depressed a little because of shrinkage, and the solidified specimen has a concave surface. This visually interpreted test is simple and fast. It can only give a rough estimation of the H content in the melt on a comparative basis. However, by setting a standard for fixed pressure this test can serve as a very good acceptance test for routine quality control and has been widely used.

Attempts were made by H. V. Sulinski et al. [35] to quantitatively measure the H content based on the specimen surface movement. An apparatus was designed to precisely measure the liquid (specimen surface) displacement, which was related to the H content, through converting the displacement to the density of the specimen. While this method was rapid, its accuracy was limited to ± 0.02 g/cm^3 (density), and the need for this special apparatus impeded its acceptance for production foundry use. With the advances in the technique of precisely measuring the displacement of a moving substance, this idea may be worth trying again.

Obviously, the porosity level in a specimen is related to its gas content. Because H is the only gas that can be substantially dissolved in the aluminum alloys, if the volume of porosity in the specimen can be measured, the H remaining in the solid is known and no H escapes from the melt during solidification, the total H content in the metal will be able to be evaluated. In controlled conditions the H loss can be eliminated, and the amount of the dissolved H in solid can be kept at a fixed level and it is generally small; thus, the porosity level will be the only variable needed for assessing the total H content. The porosity level can be measured in several ways.

- *Visual Observation* The simplest approach is to cut the sample in half on the transverse plane and examine the cut surfaces. For determining the porosity level a photographic standard has been set up for comparison. According to the porosity level the H content can be estimated.

- *Metallographic Analysis* In this analysis, the sample halves are polished to better delineate the porosity. This method can reveal the fine pores, which could be masked by the saw marks developed in the cutting process. On the polished surface an image analysis technique can be utilized to measure the porosity precisely.

- *Radiography and Ultrasonic Techniques* These methods can provide some quantitative information about the porosity in the specimen. However, using x-ray and γ-radiography requires special equipment and the process is not economical in terms of the time consumed in preparation of the radiographs and measurements [36]. The effort to use ultrasonic techniques has led to the formation of a special method for the H determination [37], which will be discussed separately. The ultrasonic technique is a promising method for measuring porosity; however, its use in the RPT was not reported.

- *Volume Measurement* If the volume of the solidified specimen can be precisely measured, the difference between the measured volume and porosity free volume of the specimen will be the porosity level. The porosity free volume can be calculated from the weight and density of the specimen. This method was not used in conventional RPT; however, a similar method was used in the Density Measurement Techniques.

The visual observation of a cutting specimen is widely used in production for quality control because it is simple and fast, but it can only give a rough estimation. Among all the available methods, the image analysis is the only one that can provide an accurate porosity level from the measured surface. However, it needs sophisticated equipment and is time consuming and its measured surface may not be representative of the bulk of the specimen. Therefore, the image analysis method is only suitable for use in research. Since a fast, accurate method is not available in measuring porosity for the reduced pressure process, the determination of the H content in this process relies mostly on density measurement.

Basically, density measurement is another way to determine the porosity level, which can be quantitative and faster than image analysis. Generally, density measurement is calculated by:

(1) *Gravitometer* Lipson et al. developed a gravitometer for this specific application [38, 35]. This apparatus consists of a cylinder which contains two immiscible liquids, the lighter liquid floating above the heavier liquid. Mercury and ethyl alcohol are used. A specimen submerged in the alcohol will float upon the surface of the mercury. The density of the specimen is calculated from the relative displacements occurring in each liquid. It permits determination of the density of aluminum specimens within 30 seconds with the reproducibility of ± 0.02 g/cm^3.

(2) *Archimedes' Method* [39] The density is calculated from the weight difference of the specimen weighed in two different media, for example, in air and in a liquid, such as distilled water or ethyl alcohol. The procedure follows the Standard Test Method for Density of Glass by Buoyancy (ASTM Standard C-893).

The determination of H content through density measurement can be done in various ways.

(1) To compare the measured density value with preset or predetermined standards. This method can be fast, but the standards need to be prepared for various conditions. This renders difficulty for practical use. The comparison can also be performed on a series of specimens taken at different stages in a process. Though this does not give quantitative H values, it can

serve as an indication for process performance, such as in degassing.

(2) To calculate the gas volume in the specimen directly from the measured density of the specimen and the standard density of a porosity specimen. The standard density can be calculated from the alloy's composition or measured from a porosity free specimen. The porosity free sample can be obtained from a well fed casting or by HIP. The derivation of the formula is as follows [38]:

Let D = Density of measured specimen

D_o = Density of porosity free specimen

$$D = \frac{\text{weight}}{\text{volume}}$$

$$\frac{1}{D} = \frac{\text{volume}}{\text{weight}} = \frac{\text{volume(metal)} + \text{volume (gas)}}{\text{weight(metal)} + \text{weight (gas)}}$$

Since the weight of the gas can be neglected,

$$\frac{1}{D} = \frac{\text{volume(metal)}}{\text{weight(metal)}} + \frac{\text{volume(gas)}}{\text{weight(metal)}}$$

$$\frac{\text{volume(gas)}}{\text{weight (metal)}} = \frac{1}{D} - \frac{1}{D_o}$$

$$\frac{\text{ml gas}}{\text{100g metal}} = 100\left(\frac{1}{D} - \frac{1}{D_o}\right) \qquad (39)$$

Suppose the gas which forms the voids in the specimen is precipitated under pressure P (mm Hg) at the freezing temperature of the tested alloy T (°C), the volume of gas at standard conditions of pressure and temperature (STP) can be calculated in accordance with Boyle's and Charles' laws,

$$\text{volume(STP)} = \frac{P}{760} \cdot \frac{273}{273+T} \cdot 100\left(\frac{1}{D} - \frac{1}{D_o}\right)$$

$$\frac{\text{ml gas(STP)}}{\text{100g metal}} = \frac{P}{7.6} \cdot \frac{273}{273+T} \cdot \left(\frac{1}{D} - \frac{1}{D_0}\right) \tag{40}$$

The density measurement by gravitometer is not accurate and the measurement by weighing specimens is time consuming. The effort to overcome these problems resulted in some modified reduced pressure testing methods, which will be discussed later.

The gas content calculated by density or porosity measurement in the RPT can be the true (total) gas content in the metal only if:

(1) The solid solubility of H is negligible and all the gas originally dissolved in the liquid is expelled during the test.
(2) None of the gas precipitated from the specimen is lost.
(3) The voids in the specimen contain gas at the pressure equal to the sum of the reduced pressure in the system plus the metallostatic head. That is, the shrinkage does not contribute to the void formation.
(4) The gas (void) free density of the metal is accurately known.

These conditions can be roughly met in common RPTs for the following reasons:

(1) The equilibrium solubility of H in solid aluminum is small, being approximately 0.012 ml/100g at the common test pressure, e.g., 80 mm Hg.
(2) The experiments showed that the total void volume varied with the gas pressure over the specimen, as predicted by Boyle's Law [38], and the gas holes were uniformly distributed in the sectioned specimen [35]. These are two evidences showing no appreciable tendency for gas bubbles that float to the specimen surface to escape. However, a study [38] showed that there was a loss of H under reduced pressure. This will be discussed below.
(3) The commonly used specimen design, the truncated cone with larger end up in the conventional RPT, ensures no shrinkage of voids in the specimen. In addition, no voids detectable in the specimen of very low gas content is also an evidence of the absence of the shrinkage effect.
(4) The effect of the variation of the density caused by the alloy chemistry is reduced by a factor P1/P0 (P1 - reduced pressure; P0 - normal ambient pressure, 1 atm) in the RPTs (about 10 times at commonly used reduced pressure) according to Equation 40. This makes the effect of the density variation negligible.

Pressure: The sensitivity of the RPT depends, to a large extent, on the pressure used. In practice, various pressures, ranging from 1 to 100 mm Hg, were used successfully in different conditions [40, 41]. When the test is used on a qualitative basis for low gas content alloys, it is necessary that a low solidification pressure be used to satisfy the required sensitivity. For example, tests for melts processed to meet premium casting requirements, that is, maximum freedom from both H and inclusion, should be conducted at a maximum pressure of 5 mm Hg. At this low pressure, the information provided by observation of the specimen's solidification behavior is considered superior to that obtainable from the solidified specimen. Subsequent determinations of specimen density may provide a convenient and supplemental numerical rating of melt quality. However, with lower pressure the volume of gas lost from the specimen is increased. By employing a density measurement to provide quantitative data, it was found that approximately 1/8 atmosphere provides sufficient sensitivity for most foundry test purposes, as in the melt-acceptance test where extremely high-quality metal is not required [41]. This permits a workable degree of sensitivity for purposes of density measurement without excessive gas loss from the specimen.

Rosenthal et al. studied the effect of the pressure on the measured values of the gas content [38]. The gas content of the same heat of alloy was measured under atmospheric pressure and reduced pressure and at different temperatures and holding times by density measurement. It was found that the gas contents calculated from the atmospherically solidified specimens were consistently higher than the gas contents calculated from the reduced pressure sample, and that at higher levels of gas content, the divergence of the data was greater than that at lower gas contents. It was considered that the difference was due to the loss of gas from the specimens solidified at reduced pressure. Considering the gas loss at reduced pressure, correction factors were introduced and derived experimentally for various gas contents.

Pouring temperature: The sampling temperature is not critical but must be high enough to avoid any solidification prior to the attainment of the desired vacuum. Temperatures in the range of 1250-1400 °F (676-760 ° C) are commonly used. High pouring temperatures are undesirable for alloys that contain considerable sodium, cadmium, zinc or magnesium, because these elements may boil out under reduced pressures and give false indications of H in the vacuum density test. Losses of cadmium and zinc cause low density values, whereas losses of sodium and magnesium have the opposite effect. Low density will result also if bubbles of the vapor of these elements are trapped in the specimen [41].

Inclusions: A major factor which may affect the capability of the RPT in measuring H content has been the amount of inclusions in the melt. It has been well established that inclusions can act as nucleating sites facilitating the H bubble formation. Therefore, it has been considered that the RPT actually reveals the combining effects of both H and inclusions. Several studies were reported to show this effect [24, 17]. Experiments they referred to showed that the same heat of melt behaved differently before and after filtration in RPT. In the filtered melt much less porosity was produced than in the unfiltered melt. The effect of inclusions on the porosity level was evident. The reasons for the increase of porosity can be that the large amount of gas bubble nuclei created by inclusions lead to the formation of a large amount of pores, or the high pore density in the melt reduces the average distance that the H needs to diffuse to the pore. Also, these pores may start to form at a higher temperature during metal solidification than those formed in the melt with fewer inclusions, and thus these pores have a longer time to grow.

However, to what extent do the inclusions affect the porosity level in the RPT? Can this effect be minimized, separated, or corrected? Inclusions only create nucleating sites but do not change the H content in the melt or the H solubility in the solid metal. The only way by which inclusions increase the porosity level is to reduce the supersaturated H in the solid solution in the specimen. As mentioned in Section 1.1, experiments and calculation showed that in conventional casting the H content that may be tolerated before the onset of porosity is of the order of 0.05-0.08 ml/100g at a cooling rate of 0.1-20 °C/s. In this case, the amount of the supersaturated H can be estimated. According to Equation 25, the H solubility in solid aluminum is dependent on the H partial pressure. From Equation 37 it can be seen that during pore growth in castings the H pressure within a pore is approximately equal to the ambient pressure, because the melt is shallow and the pore has sufficiently large size. This means that the H solubility in the bulk of solid aluminum is dependent on the ambient pressure. At 1 atm it is approximately 0.036 ml/100g at solidus and the amount of the supersaturated H can be of the order of 0.014-0.044 ml/100g. This would be the maximum amount of H the inclusions can act on. In the RPT, the sample solidifies at a slower cooling rate to allow the pores to develop. This would reduce the amount of H for inclusions to act on. The effect of the reduced pressure is not clear. It decreases the H solubility in the solid, which may provide more H for inclusions, but it also facilitates the pore nucleation and growth which would allow less H for the inclusions. Attempts have been made to evaluate the effects of inclusions on the porosity quantitatively, but no reliable data were reported. However, to use the RPT quantitatively in the H determination, these effects should be made clear.

Vibration: acts like the inclusions which may help to nucleate H bubbles and may render a false indication of metal density. Therefore, the vibration during the test should be kept constant or to a minimum.

Testing cup design: To retain gas within the specimen, consideration should be given to the geometry of the sampling cup. The ratio of free surface area to the volume of the specimen should have an important bearing on the gas loss which occurs.

Recently Laskowski et al. conducted a Gauge Repeatability and Reproducibility Analysis (R&R) on the RPT to evaluate the effectiveness of this method [42, 43]. The independent variables investigated in their study were initial H content, solidification pressure, cooling rate, degree of vibration, the alloy's freezing range, melt contamination, and operators. The analysis indicated that there was a high degree of variability in the RPT results obtained by different operators. Considerable variability also occurred with the same operator. An acceptable %R&R was only achieved at a fast cooling rate. However, using a fast cooling rate would be an inappropriate practice in the RPT, because it reduces H release from the melt, which is against the purpose of reducing pressure. The unacceptable degree of variability was obtained under all other conditions investigated. The accuracy of the RPT in determining the H content was studied by comparing the RPT results with the Telegas measurements. It was found that they were not compatible. The results of this study indicated that the conventional RPT although, it can be used as a melt quality acceptance guide, is not suitable for quantitatively evaluating the H content in aluminum alloys. To use the RPT quantitatively in determining the H content in aluminum alloys, much advancement and/or improvement of the existing method and equipment are needed.

Conventional RPT has been widely used in the aluminum industry. It is simple, inexpensive and versatile. Because it has different ways to show the existence and quantity of H, it has served a variety of purposes in production and research, such as quality control, H detection and measurement. It has a workable accuracy for many applications. However, its accuracy is generally lower than some of the other methods, such as the sub-fusion and the fusion methods and Telegas etc. Since in the quantitative analysis the density or porosity measurement needs prolonged time, this method has been mostly used qualitatively. The porosity level produced in RPT depends not only on the H content but also on the amount of inclusions. This has been considered as a major factor affecting the accuracy of the RPT. However, it makes this apparatus unique tool to measure the combining effects of both H and inclusions for quality control.

Modified Versions of Reduced Pressure Test

Constant Volume Specimen Reduced Pressure Test - This method was developed in the 1950's by Sulinski et al. [35] for quantitatively determining the gas content in an aluminum alloy melt. The gas content is determined by a single weighing of a constant volume specimen solidified at reduced pressure.

It uses a constant volume specimen cup. The usage of the constant volume is to simplify the density measurement of the specimen. In Sulinski et al's device [35], a 20-cc specimen was used, which was made with a resin bonded shell mold with a knock-off plaster riser and gating system of special design. The mold assembly was partially embedded in brass shot to seal the mold and to provide a heat sink. This design and arrangement enables close control of as-cast specimen volume and eliminates shrinkage pores in the specimen through providing directional solidification and good feeding.

The testing procedure is as follows: After the mold assembly is poured, the pouring basin is immediately removed, and the vacuum chamber is closed and evacuated to 80 mm Hg. Four min later the vacuum is released and the mold is removed. After the riser segment of the casting is knocked out, the top surface of the specimen is carefully ground flat to avoid introducing an error due to an irregular fracture. The sample thus obtained is then weighed on an analytical balance. The volume of gas in the specimen at standard conditions of pressure and temperature (STP) is calculated from the measured weight of the specimen and the standard density of the tested alloy according to the equation:

$$\frac{\text{ml gas(STP)}}{\text{100g metal}} = \frac{P_1}{P_0}\cdot\frac{T_0}{T_1}\cdot 100\left(\frac{W_1}{V_1}-\frac{1}{D_0}\right) \qquad (41)$$

where W_1 = measured weight of RPT specimen
D_0 = standard density of the tested alloy
V_1 = volume of the specimen, 20 cc
T_0 = 273 K
T_1 = solidus temperature of the alloy
P_0 = atmosphere pressure, 76 mm Hg
P_1 = solidification pressure (reduced pressure during the test plus metallostatic pressure).

In practice, the gas content is found directly from a weight-gas content curve plotted based on the above equation.

A similar approach was investigated recently by LaOrchan et al. [44], in which a riser was incorporated on the reduced pressure sample to simplify the test. The riser was used to produce a sample of constant volume once the riser was removed. In addition to the riser, a calibration curve for each alloy-melt treatment combination was suggested to relate the weight of the solidified sample to the actual amount of H in the liquid alloy. The calibration curve was produced using an independent H measurement method such as Telegas.

Compared to the conventional RPT, this method simplifies and expedites the density measurement with an acceptable accuracy, but it needs a specimen mold of special design. A constant volume sample would eliminate the need to measure the sample density by weighing the sample in both air and a liquid, which can reduce variability in the RPT. The use of the calibration curve should minimize the variability due to variations in the alloy freezing range and metal treatment process, particularly those that may influence the melt contamination level, e.g., melt filtering. In Sulinski et al's device [35], by controlling the specimen volume at exactly 20 ml, the conversion from weight to density could be readily performed by a single mental computation. The standard volume and density deviation obtained by this design was 0.028 ml and 0.003 g/ml, respectively, which were equivalent to a gas content error of 0.002 ml/100g metal (STP).

SEVERN Analyzer - The SEVERN Analyzer was developed in the UK and uses a constant weight specimen. The constant weight of molten aluminum alloy, 100g, is placed in a vacuum chamber of known volume and the pressure is reduced to a predetermined level. The chamber with the liquid sample is then isolated from the rest of the environment and the sample is allowed to solidify. In the course of solidification, the released H develops a gas pressure, which is measured by a Pirani gauge. The Pirani gauge is carefully calibrated using known volumes of H gas. The measured gas pressure is then converted to a digital readout of H content [45, 46].

According to its operating principle, it seems that it is a simple, fast process. Because a known weight of metal, 100g, is used, the readout, which can be obtained upon the completion of the solidification, is or can be easily converted to the required H content. It was reported that this method was capable of detecting a H level of less than 0.10 ml/100g. To ensure reasonable accuracy, this method needs an accurate weight measurement of 100g liquid metal, a means to control the solidification rate to extract all the H which should be extracted out of the specimen, and a way to prevent or correct the H loss during the initial vacuum build-up.

Initial Bubble Test - The initial bubble test, also called first bubble test, was first proposed in the late 1940's [47] and used for practical purposes in the early 1960's [48]. The test involves maintaining a small sample of an aluminum alloy in the molten state while the pressure over the sample is slowly reduced. At a certain pressure below one atmosphere, bubbles of gas will nucleate and break through the surface. The pressure and the temperature at which the first bubble is observed are noted and used to determine the H content of the melt.

As can be seen in Equations 3, 6, 18, 19, and 20, the H solubility, S, in molten aluminum alloys varies with temperature, T, and the H partial pressure, P_{H_2}, according to the relationship:

$$\log S = 0.5 \log P_{H_2} - \frac{A}{T} + B \qquad (42)$$

where A and B are positive constants for a given alloy.

Consider that a sample of an aluminum alloy is held at a temperature T_o (the subscript, o, represents the observed value) and contains a certain amount of H, $[H]$, and when the pressure above the melt is reduced to the value P_o the first bubble is observed. At this moment the $[H]$ should be equal to the H solubility, S, at the T_o and P_o. The relationship between the S and P_o and T_o is governed by the Equation 42. Thus, for an alloy, if the A and B values are known, by measuring P_o and T_o at the moment the gas bubble starts to appear, the S can be calculated. Furthermore, if T_o can maintain constant, the S can be directly related to the P_o. Another approach is to obtain chill cast specimens corresponding to each set of values T_o and P_o. The H content of these specimens is then determined by another method, like the vacuum subfusion. Thus, the relationship between the S, that is $[H]$, and P_o and T_o can be established.

However, the A and B values are only known for pure aluminum and a few simple alloys, as shown in Equations 3, 6, 18, 19, and 20. For commercial alloys they are not available and are difficult to obtain. The second approach is also impractical, because of numerous T_o and P_o combinations involved.

In the practical use of the initial bubble method, a combination of these two approaches is used. Since for a given gas content and a temperature above the liquidus, the following expression can be derived from Equation 42:

$$\sqrt{P}\, e^{-\frac{k}{T}} = \text{constant} \qquad (43)$$

where

$$k = \frac{A}{\log e} \qquad (44)$$

Therefore, $$\sqrt{P_o}\, e^{-\frac{k}{T_o}} = \sqrt{P_r}\, e^{-\frac{k}{T_r}} \qquad (45)$$

where P_r and T_r are the reference pressure and temperature, respectively. The reference temperature, T_o, is chosen as 670 °C (1238 °F) for practical use. It can be seen that for the given reference temperature, T_o, a knowledge of the constant A only is sufficient to calculate the corresponding P_r for any set of observed pressure and temperature, P_o and T_o, by the equation:

$$P_r = P_o\, e^{2k(\frac{1}{T_r}-\frac{1}{T_o})} \qquad (46)$$

The A values found in Equation 46 for pure aluminum and the binary Al-Cu (up to 32%Cu) and Al-Si (up to 16%Si) alloys are in the range of 2550 to 3150. The corresponding k values calculated from Equation 44 are in the range of 5872 to 7253. Calculations show that the variation of k within this range had relatively small effect on the values of $\sqrt{P_r}$, and thus, 6355 is chosen as a reasonable value of k for the application to commercial aluminum alloys.

Now, the value $\sqrt{P_r}$ can be calculated when the values of P_o and T_o, at the moment the first gas bubble appears, are measured. If a relationship between the $\sqrt{P_r}$ and S can be established, the S can be determined. As mentioned above, this $\sqrt{P_r}$ vs S relationship can be calculated from Equation 42 or determined by experiments. This relationship can be calculated only for a very few simple alloys, whose A and B values are known, this relationship can be calculated, and for commercial alloys it is established through the initial bubble tests. In the experiment, a set of specimens is obtained by chilling the melt, from which the bubble forms at T_o and P_o. For each specimen, the value $\sqrt{P_r}$ can be calculated from the measured T_o and P_o, and its corresponding H can be determined from the chilled specimen by another method, like the vacuum subfusion.

The apparatus mainly consists of a small crucible for holding the molten sample, a heater, a vacuum system including a pump, valves, and a manifold, a thermocouple, a pressure gauge, a cover with a glass viewing port and an instrument cabinet. The molten alloy sample is transferred into the crucible by a small ladle. The cover is placed over the heater that introduces the thermocouple into the sample. The heater keeps the sample at a temperature, which will eventually rise to approximately 670 °C (1238 °F), and then the vacuum pump is switched on. The rate of pressure decrease is controlled at about 5 - 10 Hg/sec. While the pressure is being reduced, the specimen surface is observed with care. At the point that the first gas bubble is observed, the pressure and temperature are immediately noted, which are the observed P_o and T_o. A further reduction in pressure will usually produce more bubbles to confirm the original observation. The pressure is then returned to atmosphere.

It is a fast method for a quantitative measurement of H content in aluminum alloys. An individual determination can be made in approximately 2 mins. However, the determination of the first bubble appearance involves some degree of subjectivity. The first gas bubble may not be the H gas bubble, which may result from the air entrapped in dross adhering to the surface of the crucible. In addition, as for the Straube-Pfeiffer method, the formation of the first bubble is not only determined by the H content, temperature, pressure, and alloy composition, but also depends on the nucleation conditions of the gas bubble, such as levels and natures of exogenous particles, the crucible materials and its surface condition, and the degree of vibration. All these factors lead to occasional spurious results. Because of this at least three measurements on each melt should be made. Consequently, its accuracy is relatively low and was reported to be within ± 0.05 ml/100g. It was reported [45] that this method was quite popular in Europe and, to a lesser degree, in the U. S. Some fairly sophisticated equipment has been commercially available but expensive. In the 1980's a quote for the top of the line unit was in excess of $25,000.

A process similar to the first bubble test was used by Alcoa as an acceptance test for high quality castings [41]. The evaluation of the melt quality was conducted by observing whether gas bubbles were evolved from a sample during solidification under reduced pressure. A pressure of 2 - 5 mm of mercury was employed to facilitate bubble emission. No emission indicated high-quality metal, whereas bubble evolution was evidence of a need for further treatment to improve quality. The observation of the site and time of the bubble formation was also interpreted relative to vacuum application and complete solidification. Bubble formation immediately following vacuum application was indicative of inclusions in the sample. The number of sites from which bubbles evolved further indicated the level of inclusion contamination. While inclusion level may be generated in this manner, an accurate assessment of the level of H present was not possible when early bubble formation occurred because of the presence of inclusions. The appearance of bubbles when solidification was nearly complete disclosed high H content in the absence of inclusions. If no bubbles were observed through complete solidification, an absence of inclusions and low H were indicated.

Ultrasonic Attenuation Measurement Method

Ultrasonic techniques have been used successfully to detect irregularities such as inclusions, porosity, and cracks in ferrous and nonferrous alloys. In the early 1980's, M. Thiagarajan et al. [37] made an effort to use this technique to measure the gas content in aluminum alloys on the shop floor. In this method, the gas content is determined by measuring the porosity levels from an as-cast specimen using ultrasonic attenuation measurements.

Thiagarajan et al's study [37] found that for a given alloy, the percentage (%) attenuation of ultrasonic waves increases in a linear manner with increasing porosity content. The % attenuation is defined by the equation:

$$\%\ \text{attenuation} = 100 \cdot \left(1 - \frac{\text{attenuation in measured specimen}}{\text{attenuation in porosity free specimen}}\right) \qquad (47)$$

In the pulse-echo technique used in Thiagarajan et al's study, the attenuation is calculated by:

$$\text{attenuation} = 20 \cdot \log \frac{HT_2}{HT_1} \qquad (48)$$

where HT_2 and HT_1 are the height of successive multiple echoes.

Since the porosity level in the aluminum alloy specimen is directly related to the H content, the relationship between the H content and the % attenuation can be established.

A barium titanate probe of 0.8 MHz frequency was used throughout Thiagarajan et al's investigation. Castor oil was used as a couplant, and the couplant layer thickness and the pressure on the probe were maintained constant in all the experiments. It was essential that the specimens have a smooth surface without any surface defects. Two kinds of specially designed specimens were used, one for the porosity-free specimen and another for the porosity detection.

Three commercial aluminum alloys, Al-12%Si (LM6), Al-3%Cu (LM4), and Al-7%Si0.4%Mg (LM25), were investigated. It was found that the increases in ultrasonic attenuation for one percent increase of porosity level (called "Attenuation Index") were different for different alloys. It was 1.083 for LM6 alloy, 0.444 for LM4 alloy, and 0.0847 for LM25 alloy. An alloy having a low value of Attenuation Index, like LM25 alloy, would not show an appreciable variation in attenuation value when the porosity level varies. It suggested that gas content could be determined more accurately in LM6 and LM4 alloys than in LM25 alloy.

For practical use on the foundry floor, Thiagarajan et al. provided charts relating the % attenuation to the porosity level and H content for tested alloys and a chart relating the echo heights ratio to the % attenuation. Thus, by knowing the echo heights, the % attenuation and, subsequently, the H content can be determined.

It was claimed that this was a simple and fast method. The time for a measurement of H content with the help of provided charts was about 5-10 mins from the time the melt was poured into the mold. However, there were two limitations: a skilled operator was required to determine accurately the values of echo heights, and the sensitivity was low for some alloys. The practical application of this method has not been reported in the published literature.

The accuracy and the reproducibility of this method were not disclosed. Its accuracy could be affected by the fact that ultrasonic techniques have difficulty distinguishing porosity and other defects in the specimen, but the accuracy of this method could be improved by magnifying the porosity. This suggests that combining the reduced pressure solidification and ultrasonic measurement technique is worth of investigation.

References

1 Wood, G. C., Anyalebechi, P. N., and Talbot, D. E. J., ìA New Technique for Determining the Hydrogen Content of Aluminum and its Alloys by Vacuum Hot Extraction," International Seminar of Refining and Alloying of Liquid Aluminum and Ferro-Alloys, Aug. 26-28, 1985, Trondheim, Norway.

2 Dupuis, C., Wang, Z., Martin, J-P., and Allard, C., ìAn Analysis of Factors Affecting the Response of Hydrogen Determination

Techniques for Aluminum Alloys," Light Metals, 1992, TMS, Edited by Euel R. Cutshall, p1055-1067.

3 Chen, X. G., Klinkenberg, F. J., Engler, S., Heusler, L., and Schneider, W., ìComparing Hydrogen Testing Methods for Wrought Aluminum," JOM, Aug. 1994, p34-38.

4 Ray, L. D., ìFactors Affecting the Hydrogen Content of Aluminum Samples Cast in A Copper Chill," Light Metals, 1989, TMS, Edited by Paul G. Campbell, p825-830.

5 Talbot, D. E. J., "Effects of Hydrogen in Aluminum, Magnesium, Copper and Their Alloys," International Metallurgical Reviews Vol. 20, 1975, p166-184.

6 Konar, J. and Banerjee, N. G., "Vacuum Heating Hydrogen Determination in the Aluminum and Aluminum Alloys," N.M.L. Tech. J., Vol. 16, Feb.-May 1974, p18- 19.

7 Varhegyi, G. et. al., "Method for the Determination of Hydrogen Content of Aluminum or Aluminum Alloys," Hungarian Patent 18,441, Jan. 12, 1978.

8 Degreve, F. and Jardin, C., "New Methods for the Determination of Hydrogen Content of Aluminum and Its Alloys, Part II Rapid Determination by the Nitrogen Carrier Gas Fusion Method," Met. Trans. B, Dec. 1975, 6B, p545.

9 Technical Information, ìRH-402 and RH-404 Hydrogen Determinators," LECO® Corp., 1990.

10 Handbook of Chemistry & Physics, 51st Edition, 1970-1971, Chemical Rubber Co.

11 Simesen, C. J. and Lauritzen, J. L., "Analysis of Hydrogen in Aluminum- Magnesium Alloys," Aluminum, 56, Jahrg., 1980, 2.

12 Sloman, H. A., ìVacuum-Fusion Method for Determine Gases in Non-Ferrous Metals," Engineering, 1945, Vol.160, p385, 405-406, 419-420.

13 Gordon, A. W., Meszaros, G. A., Naizer, J. P., Gangasani, P. R., and Mobley, C. E., Comparison on Methods for Characterizing Porosity in Die Casting, Report No. ERC/NSM-C-91-51, Aug. 1991.

14 Carney, D. J., Chipman, John, and Grant, N. J., AIMME Trans., 1950, Vol. 188, p397-403.

15 Griffith, C. B. and Mallett, M. W., ìDetermination of Hydrogen in Wrought Aluminum Alloys," Analytical Chemistry, 1953, Vol. 25, p1085-1087.

16 Anderson, D. A., Granger, D. A., and Avery, R. R., ìThe Alcoa Telegas II Instrument," Light Metals 1990, Edited by Christian M. Bickert, p769-773.

17 Anyalebechi, P. N., ìTechniques for Determination of the Hydrogen Content in Aluminum and Its Alloys," Light Metals, 1991, edited by Elwin Rooy, p1025-1046.

18 Painchaud, F. and Martin, J.-P., “The New AlSCAN Analyzer: Easy-to-Use, Reliable, on-Line Measurement of Hydrogen in Liquid Aluminum Alloys,” Proc. of 2nd International Conference on Molten Aluminum Processing, Orlando, FL, Nov. 6-7, 1989, paper 20.

19 Ransley, C. E. and Neufeld, H., “The Solubility of Hydrogen in Liquid and Solid Aluminum,” J. Inst. Metals, 74, 1948, p599-620.

20 Doutre, D. and Dewing, E., <u>Internal Report</u>, Alcan International Ltd, Kingston Research and Development Center, 1989.

21 Hess, P. D., “An Empirical Equation for Calculating the Solubility of Hydrogen in Molten Aluminum Alloys,” Light Metals, 2, 1974, p591-596.

22 Technical Information, ìAlscan™ F,” BOMEN Hartmann & Braun.

23 Gruzleski, J., Handiak, N., Campbell, H., and Closset, B., ìHydrogen Measurement by Telegas in Strontium Treated A356 Melts,” AFS Trans. 1986, Vol. 91, p147-154.

24 Sigworth, G. K., ìA Novel Method for Gas Measurement in Aluminum,” Light Metals, 1993, Edited by Subodh K. Das, p981-989.

25 Chen X. G. and Engler, S., “Measuring Hydrogen Content in Molten Aluminum Alloys Using the CHAPEL Technique,” Cast Metals,Vol. 6, No. 2, p99-108.

26 Chen, X. G., Klinkenberg, F. J., and Engler, S., ìOptimization of the Impeller Degassing Process through Continuous Hydrogen Measurement,” Light Metals, 1995, Edited by J. Evans, p1215-1222.

27 Sigworth, G. K. and Engh, T. A., Met. Trans. B. 1982, Vol. 13B, p447-460.

28 Gee, R. and Fray, D. J., ìInstantaneous Determination of Hydrogen Content in Molten Aluminum and Its Alloys,” Met. Trans., B, Sep., 1978, Vol. 9B, p427-430.

29 Gallo, R., ìMeasurement of Hydrogen Content in Molten Aluminum Alloys Using Crucible and Reverberatory Furnaces for Sand and Permanent Mold Castings,î Proc. of 4th International Conference on Molten Aluminum Processing, Orlando, FL, Nov. 12-14, 1996, p209-225.

30 Technical Information of TYK R&D Center, ìHydrogen Sensor for Molten Aluminum Alloys,” TYK Corporation, Japan, 1992, p1-10.

31 Φvrelid, E., Engh, T. A., and Φymo, D., ìMeasurement of Hydrogen in Liquid Mg Alloys,”

32 Bakke, P., Lauritzen, J. L., Engh, T. A., andΦymo, D., ì Hydrogen in Magnesium, Absorption, Removal, and Measurement,” Light Metals, 1991, Edited by Elwin Rooy, p1015-1023.

33 Vaschenko, K. I. et al, Liteinoe Proizvodstvo, 1971, No. 6, p21-.

34 Bakke, P., ì Measurement and Removal of Inclusions and Hydrogen in Magnesium,” Dr. ing. Thesis, The Norwegian Institute of Technology.

35 Sulinski, H. V. and Lipson, S., "Sample for Rapid Measurement of Gas in Aluminum," AFS Trans. Vol. 67, 1959, p56-64.
36 William, D. K., AFS Trans., 63, p736.
37 Thiagarajan, M. and Mallya, U. D., "Evaluation of the Gas Content of Molten Aluminum Alloys," AFS Trans., 1981, p495-500.
38 Rosenthal, H. and Lipson, S., "Measurement of Gas in Molten Aluminum," AFS Trans. Vol. 63, 1955, p301-305.
39 Brodkey, R. and Hershey, H., Transport Phenomena - -A Unified Approach, McGraw-Hill Book Co., 1988, p316-319.
40 Dardel, Y., "Hydrogen in Aluminum", Trans. AIME, Vol. 180, 1949, p273-286.
41 Rooy, E. L. and Fischer, E. F., "Control of Aluminum Casting Quality by Vaccum Solidification Test", AFS Trans., 1968, Vol. 76, p237-240.
42 Laskowski, J., M. S. Thesis, 1995, Worcester Polytechnic Institute.
43 Laskowski, J., D. Apelian, and Makhlouf, M., ìOptimization of the Reduced Pressure Test,î Proc. of 4th International Conference on Molten Aluminum Processing, Orlando, FL, Nov. 12-14, 1996, p248-260.
44 LaOrchan, W., Chen, X., and Gruzleski, J., ìA Qualified Reduced Pressure Test,î AFS 99th Casting Congress, 1995.
45 Acklin, T. E. and Davidson, N. J., "The Measurement of Gas in Molten Aluminum Casting Alloys," Proc. of 2nd International Conference on Molten Aluminum Processing, Orlando, Fl, Nov. 6-7, 1989, paper 19.
46 Hilton, D. A., ìMeasurement of Hydrogen in Molten Aluminum Alloy Using a Quantitative Reduced Pressure Technique," International Molten Aluminum Processing, AFS, Des Plaines, IL, 1986, p381-394.
47 Metal Technology, 15, 1, 1948.
48 Neil, D. J. and Burr, A. C., 'Initial Bubble Test for Determination of Hydrogen Content in Molten Aluminum," AFS Trans. Vol. 69, 1961, p272-275.

1.4 HYDROGEN REMOVAL

Reducing H content in the aluminum alloys can be accomplished through two approaches: by preventing H from being absorbed and by removing the H already absorbed in the alloy. To identify the sources and prevent the H absorption can be a very effective and economic way to reduce the H content in the alloy and it does not cause the problems, like forming inclusions and element loss etc., which may occur in some H removal processes. Therefore, proper melting practices that can minimize H absorption are always highly recommended. The prevention of aluminum alloy contamination, including H absorption, like using inert gas or proper salt flux protection, is studied as a separate task in this project. The present contribution focuses only on the H removal.

1.4.1 Categories and Mechanisms of Hydrogen Removal

In all the H removal techniques currently used, the depletion of H from melt is accomplished by the H diffusion in the melt and transfer (interfacial diffusion) from melt to the contacting gas or vacuum. The simplest method is natural outgassing, which is accomplished by to holding the melt at a lower temperature for some time. The second method is vacuum degassing that is achieved by creating a vacuum environment over the melt. The third is bubble degassing which is done by introducing H-free gas bubbles into and having them go through the melt.

Many factors can influence the H removal efficiency. These factors can be: alloy type, melt temperature, initial alloy H content, treatment gas type and flow rate, treatment gas/metal contact time, equipment efficiency, and external environmental conditions. Each of these factors functions through influencing one or some of the following aspects of the H diffusion and transfer.

1 The difference between the H partial pressure inside the gas or vacuum, which contacts the melt, and the corresponding equilibrium H partial pressure of the melt contains the H. This H partial pressure difference is the driving force for the H removal in almost all of the H removal techniques.
2 The H diffusion coefficient in the melt.
3 The melt/gas or vacuum interfacial conditions and, consequently, the H transfer coefficient through the interface.
4 The diffusion distance, that is, the mean distance that H has to travel from the melt to the melt/gas or gas/vacuum interface, and time allowed for the diffusion.

The H diffusion coefficient in the melt is affected by the alloy composition and temperature, and the H transfer coefficient through the interface is affected by the interfacial condition that depends on alloy composition, temperature and the gas type. It is essential for the H removal that the H partial pressure inside the gas bubbles or the environment is lower than the equilibrium H partial pressure of the melt. The larger the difference, the greater amount of H and the faster it can diffuse to the contacting gas. For a given alloy, the equilibrium H partial pressure, P_{H_2} of the melt depends on its H content, $[H]$ which is equal to the solubility, S, at equilibrium, the melt temperature, T, the standard H solubility in the liquid alloy, S_o, as expressed by the equations:

$$\sqrt{P_{H_2}} = \frac{[H]}{S_o} \quad (49)$$

and

$$\log S_o = \frac{A}{T} + B \quad (50)$$

Equation 49 is the same as Equation 30, and Equation 50 represents the Equations 4, 5, 7, 8, and 9 through 17, where A and B are constants. Values of A and B depend on the alloy composition. For pure aluminum and some simple aluminum binary alloys they have been determined as shown in Equations 4, 5, 7, 8, and 9 through 17. The difference in A and B values indicates that different alloys may behave differently in the H removal. It can be seen from Equations 3 and 4 that, for a given alloy with a given H content, when T increases, the S_o increases and the P_{H_2} decreases. In other words, it says that for a given H content in a melt its equilibrium partial H pressure is higher at lower temperatures. Thus, thermodynamically, for a given metal/gas system, lower temperatures favor H to diffuse from metal to gas, and higher temperatures favors the absorption of H by the metal from the environment. For example, plant data [1] showed that a 25 °C increase in furnace temperature generally results in an increase of 0.04-0.05 ml/100g.

Natural Outgassing

Natural outgassing is feasible only when the H partial pressure is sufficiently low and there is a minimum of H sources in the environment. When using this technique, lowering the temperature increases the equilibrium H partial pressure of the melt and thus increases the partial pressure difference. This method is simple and does not need capital investment, but generally it has a low efficiency and is not always feasible, as in hot humid weather. Its efficiency depends on the moisture level in the air, the H content in the melt, the surface area, and the dross layer on the melt surface.

Vacuum Degassing

In vacuum degassing, the vacuum provides a very low H partial pressure over the melt. This method has a much higher H removal efficiency than natural outgassing. However, it needs sophisticated equipment which works in a high temperature environment. This restrains its use in treating a large volume of melt or in in-line treatment.

Vacuum Stirring

The Vacuum stirring [2] is a traditional vacuum degassing method, which is designed to keep the whole furnace under vacuum or to a reduced pressure while the melt is stirred. Several stirring methods can be used. Figure 21 shows an experimental setup of a vacuum stirring system, in which a graphite propeller stirs the melt.

Dynamic Vacuum System and Vacuum Fluxing System

The Dynamic Vacuum System and Vacuum Fluxing System [3] were developed at Årdal og Sunndal Verk a/s (ÅSV) in the early 1980's for treating aluminum alloys. Figure 22 is the schematic of the Dynamic Vacuum System. This system was evaluated for 99.5%Al and Al-Mg alloys. In the test, a 20 ton melt was transferred to the vacuum furnace through a nozzle under vacuum of 1-10 mm Hg, and the metal was cast after a holding time of 30 mins. For the 95.5%Al, an average of 63% of H was removed and the final H content was about 0.09 ml/100g. The degassing effect of this system was somewhat lower for Al-Mg alloys, and its H removal efficiency was about 56%. The vacuum fluxing system combines the vacuum and porous plug fluxing. The schematic of a large vacuum furnace (50 t) is shown in Figure 23. Three alloys, 99.5%Al, Al-0.5%Mg-0.5%Si, and Al-5%Zn-1.2%Mg-0.3%Cu, were produced and tested in this furnace. The melt was poured into the furnace and alloyed. Then the melt was mixed and refined by 30 mins fluxing of Ar under pressure of 15 mbar. The metal was cast after a holding of about 1 hr. The resulting H removal efficiencies for the three alloys were 31% (from 0.16 to 0.11 ml/100g), 50% (0.24 to 0.12% ml/100g), and 24% (0.17 to 0.13 ml/100g), respectively.

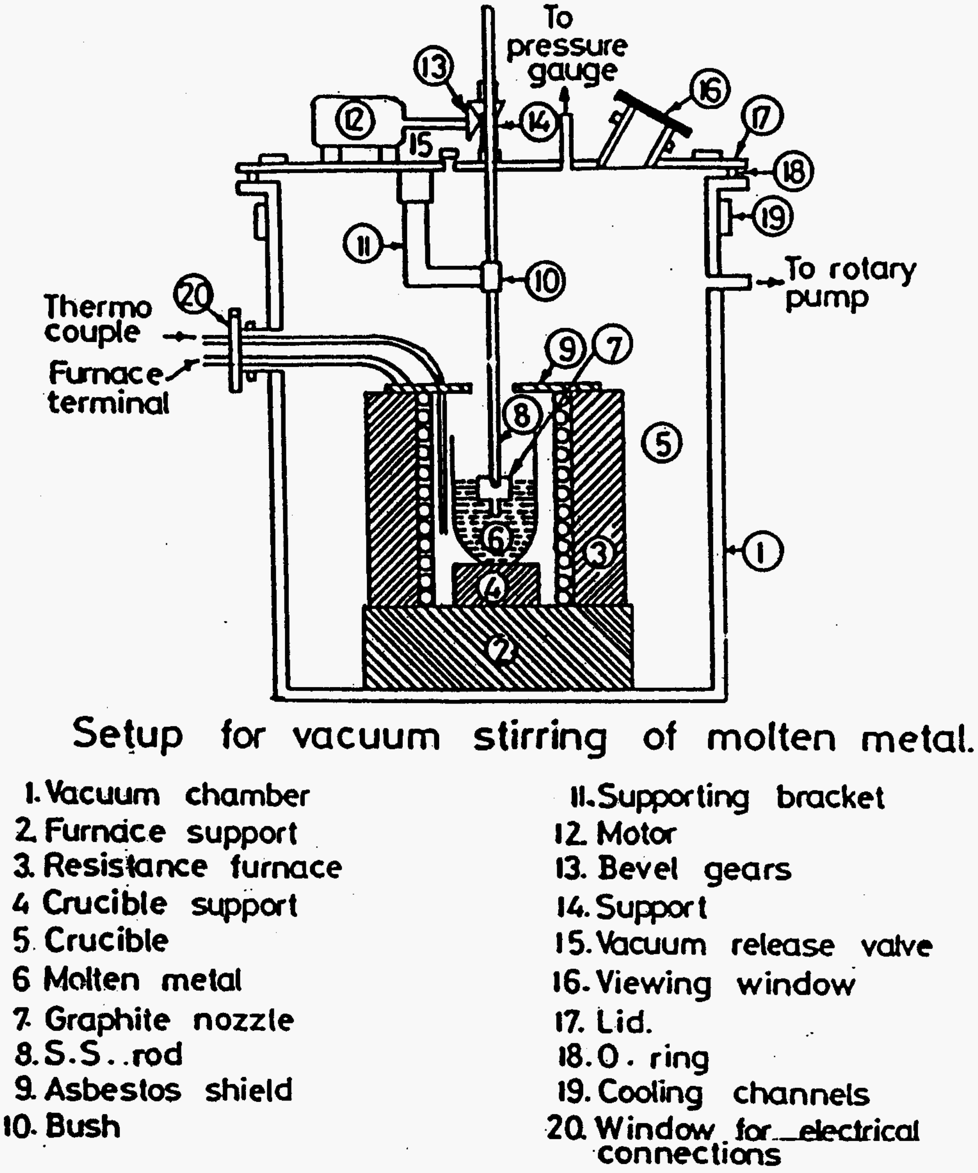

Figure 21. An Experimental setup for vacuum stirring of molten metal [2].

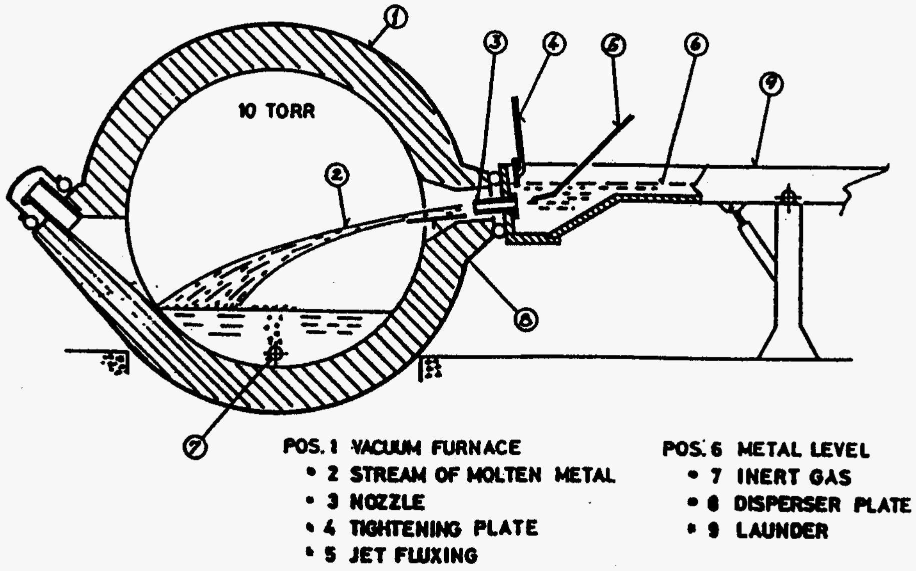

Figure 22. Schematic of Dynamic Vacuum System [3].

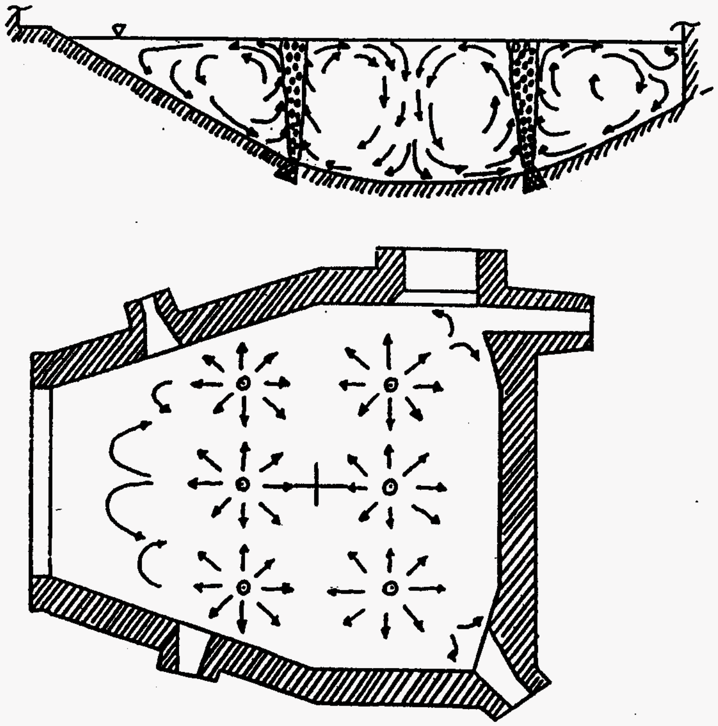

Figure 23. Schematic of Vacuum Fluxing Furnace viewed from the side and above showing the flow pattern [3].

Vacuum Suction Degassing

Vacuum suction degassing [4] is a new vacuum degassing method that is under development. An experimental apparatus using this method for aluminum degassing is schematically shown in Figure 24. The design calls for the immersion of a porous graphite tube into the melt, the graphite tube is made to be permeable to gas and impermeable to the melt, and the inside of the tube is evacuated. Because of the vacuum inside the tube, the H in the melt diffuses into the tube and is sucked out. An experiment conducted in a resistance furnace melting 20 kg aluminum demonstrated its effectiveness, but this method is still in the laboratory testing stage.

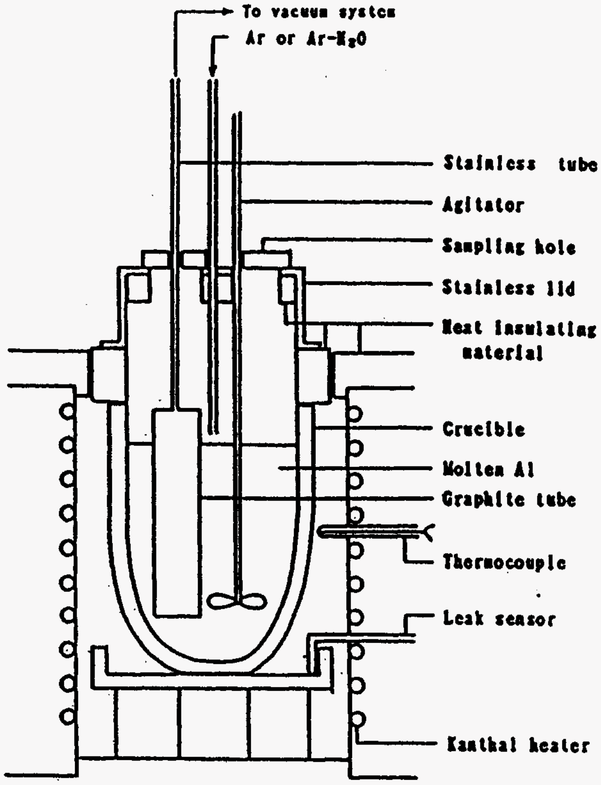

Figure 24. Schematic of the experimental apparatus for aluminum vacuum suction degassing [4].

1.4.2 Bubble Degassing

In bubble degassing, the large number of gas bubbles introduced in the melt provides a very low H content inside the pores, a large gas/melt contacting surface area, and reduced H diffusion distance. Therefore, it is very effective and highly efficient. Intensive research and development work has been devoted to this field in recent years, resulting in various techniques and devices. It has been a major degassing technique and has received increasing interest in the aluminum industry. For this reason, bubble degassing is one of the emphases of this review.

Factors Affecting Degassing Rate

Though many experiments have been conducted, there is still debate on some aspects of the H removal mechanism in bubble degassing. Some researchers [5, 6] consider that the chemical reactions, as when H reacts with Cl_2 forming HCl, may play a role. However, the general consensus is that H removal involves only diffusion in the melt and mass transfer across the metal/gas interface. The factors controlling the H removal rate in bubble degassing can be diffusion through the melt or across the metal/gas boundary, or the rate can be equilibrium controlled [7, 8]. Which factor is dominant depends on the H concentration in the melt, and gas bubble size, density, distribution, movement and surface condition. At higher H concentrations in the melt, the diffusion either in the melt or across the gas/melt interface can be the controlling factor. When there are only a few large gas bubbles in the melt, the mean distance for H traveling to gas the bubbles is long and thus the diffusion in the melt can be the dominant factor. When a large number of small gas bubbles are intimately mixed with the melt or some reacting products form on the gas bubble surface resisting the H transfer, the diffusion across the metal/gas boundary can be the dominant factor. However, when the H concentration in the melt very low, the H removal rate will be equilibrium controlled. This means, in this case, that the H concentration in the gas bubbles and melt is near equilibrium, and the H removal rate is determined by the gas flow rate.

Based on this understanding, several bubble degassing process modelings have been proposed. Because many variables are involved in the process and some important gas and metal properties are not accurately known, the models proposed have to be constructed under some assumptions which more or less deviate from the real conditions. Some models [8, 9] assumed the diffusion across the metal/gas boundary was rate limiting. Some others [7, 10, 11] described the process simply by introducing a reaction constant, through which the H concentration or removal efficiency is related to the initial H concentration, treating time, and gas and metal flow rates. The reaction constant is affected by the process parameters and is measured through experiments. The effects of the process parameters on the reaction constant reveal the role that they play in the H removal.

Major Process Parameters

In bubble degassing, the bubble size, density, distribution and movement as well as the species of the treatment gas are the important factors influencing the process efficiency. For a given gas flow rate, the smaller the bubbles, the greater the surface contact area between the gas and the melt and the shorter the H diffusion distance. For example, for a given volume of gas introduced and uniformly dispersed in the melt, when reducing the diameter of the gas bubbles from 15 mm to 5 mm, the number of gas bubbles is increased by a factor of 27 and the diffusion distance reduced by 4 [12]. In addition, the smaller bubble has a lower floating velocity, which increases the traveling time of gas in the melt and allows more H to diffuse into the gas bubbles. Consequently, the gas consumption can be reduced. Also, small, slowly traveling bubbles may produce gentle convection in the melt, which makes an intimate mix of the gas bubbles and the melt. From the H removal point of view, the best bubbling condition should be large numbers of small bubbles intimately mixed with the melt and floating up slowly. However, very small bubbles may not be appropriate, because they have a very low rising velocity; some may not float up to the melt surface before casting and can be entrained in the castings as porosity. Some researchers consider [13] that the uniform dispersion of gas bubbles throughout the entire furnace is not strictly necessary to improve the efficiency; the melt circulation is more important. Anything that can increase melt circulation will significantly increase the rate of impurity removal. Though the reaction of H and Cl_2 in the melt is debatable, the reaction between aluminum or the alloying elements and some treatment gases may occur. The resulting products may deposit on the bubble surface as barrier to mass transfer. Generally, increasing the gas flow rate increases the H removal efficiency. However, for a given bubble size, the efficiency falls rapidly after the gas flow exceeds a critical value. A study of the in-line treatment [14] indicated that the critical flow rate occurs when approximately half the volume of the reactor is occupied by rising gas bubbles. Further increases in gas flow reduce the volume available for metal flow so that the melt exposure time falls off. Still further increases in gas flow lead to the situation where the metal flow is choked and the reactor will overflow. Accordingly, the ideal conditions in bubble degassing should be:

1 A proper degassing agent, which should be dry and contain no or very low H. It should not react with the alloying elements to avoid their losses, but can react with the H forming stable compounds. The compounds produced in the reaction should not form a barrier to the H diffusion.
2 An appropriate gas introducing device. This device should be able to produce a desired quantity of small bubbles, generate adequate

circulation of the bulk melt, which can distribute and intimately mix the gas bubbles with the melt, and in in-line treatment, generate a counter current melt-gas flow. This device should not produce any surface turbulence, because violent turbulence of the melt may facilitate the alloy oxidation, H absorption, and inclusion entraption.

3 Low degassing temperatures.

Increasing the degassing time generally decreases the H content in the melt. However, the efficiency of the H removal decreases with the treatment time, because lowering the H concentration in the melt reduces the H partial pressure difference. If the treatment time is sufficiently long under given conditions, eventually equilibrium will be reached where the H depletion rate due to degassing and the rate of the H absorption from the atmosphere become the same. The H content at this point is the minimum that can be achieved for the given conditions. During bubble degassing, some H can also diffuse through the melt surface into the atmosphere. Simensen [15] estimated in some cases 85% of H was removed by the gas bubbles and 15% diffused through the bath surface. This figure may vary significantly depending on the melt surface area, weather and process parameters.

Degassing Agents

The oldest, and most traditional degassing agent is Cl_2. The Cl_2 can be introduced into the melt as gas or by adding solid hexachloroethane tablets, which react with aluminum producing Cl_2 gas. In practice, Cl_2 has generally been considered to be the most effective aluminum cleaning agent. This is mainly because not only can Cl_2 remove H, but it is more effective in removal of alkaline elements, Na, Li and Ca, and inclusions than the other gases. The universally accepted explanation for the high level of effectiveness of Cl_2 in degassing is that, in the melt, Cl_2 reacts quickly with aluminum forming aluminum chloride [16].

$$2Al + 3Cl_2 = 2AlCl_3 \qquad (51)$$

Aluminum chloride is a gas at temperatures above 190 °C (374 °F) and initially the H content in the $AlCl_3$ gas bubbles is virtually zero. However, there have been some contradictory opinions about the other reasons. For example, as mentioned earlier, whether there is a chemical reaction between the H and some elements in the degassing agent or the melt is debatable. Some researchers [5, 6, 10] believe Cl_2 reacts with H forming HCl in the bath, which keeps a low H partial pressure in the bubbles and thus favors the H removal. But others [7] claim that H does not react with Cl_2 in the melt; therefore, for H removal there is no thermodynamic advantage for the use of Cl_2. Some researchers [9, 17] think that the formation of Cl-containing salt film on the gas bubble surface, especially, the formation of magnesium chloride in Mg-containing alloys, increases the resistance to interfacial mass transfer. In this sense, the Cl_2 may be not a good degassing agent for some alloys. But, some others consider that in industrial practice the Ar and N_2 distribution systems always contain traces of O_2 or humidity, the presence of which passivates the gas/melt contact surface with oxide films. These films present resistance to the mass transfer. Chlorine can prevent the passivation and thus decrease the resistance. So, the addition of Cl_2 (or other halogen-containing gases) to the treatment gas is claimed to improve degassing [18].

Though it is very effective in degassing, industry has been very cautious about the use of Cl_2. Cl_2 is a dangerous gas because $AlCl_3$ is very reactive, and once $AlCl_3$ reaches the atmosphere it forms hydrochloric acid in the form of gas, a corrosive and toxic gas. In addition, the use of Cl_2 certainly has some other detrimental effects. For example, the presence of Cl_2 produces liquid $MgCl_2$ droplets in Mg-containing alloys. The quantities of Cl_2 required for effective in-line treatment may lead to a number of problems related to the generation and entrainment of these liquid $MgCl_2$ droplets [19]. The problems can be black oxide patches and related defects in alloys with medium and high Mg contents, excessive dross build-up, and salt inclusions. For foundry alloys, Cl_2 may lead to some loss of modifier elements (Na, Sr) [20].

Another traditional degassing agent is dichlorodifluoromethane (CCl_2F_2, commonly known as Freon-12 or Halocarbon). It is effective in degassing, but, though not as toxic as Cl_2, it has detrimental effects on the ozone layer in the atmosphere. Extensive efforts have been made in research and development of environmentally acceptable degassing agents, resulting in many substitutes for Cl_2. Now, nitrogen, argon, and sulfur hexafluoride (SF_6) are commonly used [19, 21]. A proprietary gas, AGA MIX 14 [16, 22] has also been developed and used. As a result, the use of Cl_2 has been reduced substantially and the use of solid hexachloroethane tablets is also declining rapidly due to the evolution of toxic fumes and its inefficiency. When used as degassing agents, these gases show some effects on the characteristics of the dross. Nitrogen has been shown to produce a very wet dross (containing a substantial amount of molten aluminum), resulting in a large amount of metal loss [23]. The driest dross is created by halogen-containing gasses [23]. The addition of Cl_2 in the N_2 can make the dross drier [19]. Moreover, all these gases are not as effective as Cl_2 in degassing. So, when other gases are used, a certain amount of Cl_2 is often added. The amount of Cl_2 added is generally based on concerns other than H removal.

Different treatment gases may have different effects on the H removal. The different results can be attributed to differences in the bubble size, H content in the gas, and the possible reaction with the alloy. The gas dispersing method determines the size of gas bubbles, melt condition, and the gas property. It was reported [16] that the only gas characteristic that can change the bubble size is the surface tension. However, opinions about how the bubble size is affected by the surface tension are contradictory. One study [16] implies that higher surface tension favors smaller bubbles. It says that the gas bubbles tend to agglomerate during flotation forming larger bubbles; for a given melt the gases with higher surface tension are more resistant to the reagglomeration and maintain the smaller bubble size for a longer time and over a longer travel distance. Another study [21] claims just the opposite, saying that lower surface tension results in smaller gas bubbles.

Peterson et al. carried out a fundamental study of the effects of various gases and gas combinations on the removal of H and light metals [10]. Two inert gases (Ar, N_2), two bi-gas mixtures (N_2-Cl_2, Ar-Cl_2), and two tri-gas mixtures (N_2-CO-Cl_2) were tested for several alloys. It was found that the tri-gas combination removed H at the fastest rate. The bi-gas mixtures produced a slightly lower rate. The inert gas was effective, but not as efficient as the reactive (Cl_2-containing) gases. The opposite result was obtained from another experiment. It was reported [9] that in the Alcoa 622 Process the addition of Cl_2 to an inert gas decreased the H removal efficiency. This discrepancy may be attributed to the different experimental conditions, but it shows that the role of adding Cl_2 in the other gases for the H removal is not very clear or the effect, if any, is not significant. Data in a study of the use of SF_6 gas [19] showed that the use of Cl_2 alone or a mixture of Cl_2 and SF_6 did not change the H removal performance appreciably. However, the use of SF_6/Ar mixtures resulted in a 20% reduction in the H removal efficiency. The change in the degassing performance may be attributed to the modification of physical/chemical properties of the gas bubble surface caused by the components of the gases. It was also reported [22] that the components of AGA MIX 14 increase the rate at which H can diffuse through the boundary layer between the bubbles and the melt.

Devices

The simplest device, and the one that was the earliest used, for introducing gaseous agents into the melt for H removal is the lance or wand. It is effective but not efficient. In order to obtain high efficiency, efforts have been concentrated on developing a device which has the desired features mentioned earlier, that is, it can produce fine gas bubbles, move the bubbles in the proper fashion, disperse the bubbles properly in the melt, and at the same time keep a quiet melt surface. In addition, it must have good engineering, be low in cost, and fit the working space and special requirements. A great deal of theoretical analyses, modeling, physical simulations, laboratory and production tests have been conducted, and these have resulted in a variety of degassing devices that are used commercially. All these devices can be divided into batch (furnace or crucible treatment) and in-line systems based on the treatment location. The heart of all these systems is the reactor and the gas bubble generator, such as the like porous plug, or rotor, which directly influence the H removal efficiency. The in-line system generally has a high efficiency. This is because it has the specially designed reactor(s), which usually has a deep bath to increase the gas/melt contact time and can be constructed with components, like baffle plates, stream breakers or ribs, to create the desired metal and gas flow patterns. To enhance efficiency the in-line system can be made as a multi-stage system or it can contain a multiple gas bubble generator, like rotors, in one stage. In addition, the treatment can be conducted just before casting, thus minimizing the H reabsorption after degassing. Because of its high efficiency, the in-line treatment can reduce the treating time, the quantity of gas usage, and consequently, reduce dross generation, melt loss, and energy consumption, and thereby improving productivity. The disadvantages of the in-line system are the need for the sophisticated device, high cost, heat loss in the process, and the space needed for installation which sometimes prohibits its use with the existing melting equipment. In addition, the quality of the metal output in in-line treatment is proportional to the metal input, thus making it difficult to keep the metal quality constant, and therefore, melt pretreatment may be needed. Furnace degassing is usually used for melt pretreatment. Furnace or crucible degassing is also used for final degassing, especially in foundries. The devices used in the furnace and crucible treatment are generally less sophisticated than in-line equipment, therefore inexpensive, and may not need a large space for installation. However, because the furnace design places top priority on good heat transfer, the melting furnace generally has a shallow bath with a large surface, which is not favorable for the melt/gas reaction. Therefore, furnace degassing is, though effective, not efficient.

In both in-line and furnace systems the desired gas bubble density and size are produced by the gas bubble generating device, which, associated with the reactor, also distributes the bubbles and mixes them with the melt. Many bubble generating methods have been developed and used, which can be classified as porous plug fluxing, rotary gas dispersing, high velocity jet, jet fluxing as well as lancing. The unique features of the major degassing systems and some typical gas bubble generators and their performing characteristics are summarized below.

Lance or Wand

The lance or wand is simple, inexpensive, flexible for use in furnaces of any shape and size is very easy to lower or retract from the furnaces. It has no rotating part, does not need external power to operate and can take the rough handling of the shop floor. The only serious problem is that the bubbles formed are large and cannot be distributed well in the melt, leading to a low H removal efficiency. However, despite their low performance and that rotary degassing is making inroads into small cast shops, plain lances still play an important role in the primary as well as foundry industry.

Helical Plug Lance (HPL)

A number of methods have been tried to improve the efficiency of the lancing practice and still essentially preserve its major benefits. The simplest of these methods is to modify the lance itself, which can be to add small porous elements at its end or to modify to the extremity of the lance in order to induce high-speed gas movement. Practical considerations related to difficulties in lance fabrication (hence increased costs), lance erosion and plugging, in addition to very limited gain, have kept most of these approaches from obtaining wide acceptance [24]. Among many attempts, a helical plug lance (HPL) was developed with some success [25]. It uses a special plug that was designed to be adaptable to the most commonly used lances. Compared with the plain lance, HPL has the following features: (1) gas is discharged through multiple outlets, (2) high momentum jets are produced which break up the gas into finer bubbles, and (3) radial tangential momentum is provided to each jet keeping fine bubble clouds away from the lance, thus producing an increased dispersion area. Tests demonstrated that HPL produced a few order of magnitude increases in the interfacial area, and its H removal efficiency was much superior to the plain lance and also higher than the porous plug at high flow rates where the porous plug efficiency started decreasing. Though HPL has shown strong potential in improving the efficiency of present lancing practice, its efficiency is still not satisfactory.

Lance Flux Injection

A lance is also used in the Lance Flux Injection method for H removal. It uses a carrier gas, N_2 or Ar, which is mixed with specially formulated halogen-containing powdered salt flux blends and injected beneath the metal surface through a lance. Figure 25 shows the layout of a lance flux injection system [23]. It was reported [23] that a relatively small addition of flux (typically 2 lb per 1000 lb metal) reduced the overall degassing time and costs. It was considered that the small addition of halogen gas released by the flux doubled the mass transfer coefficient of the H. This method could offer a degassing time similar to when is used, without the environmental concerns of using Cl_2.

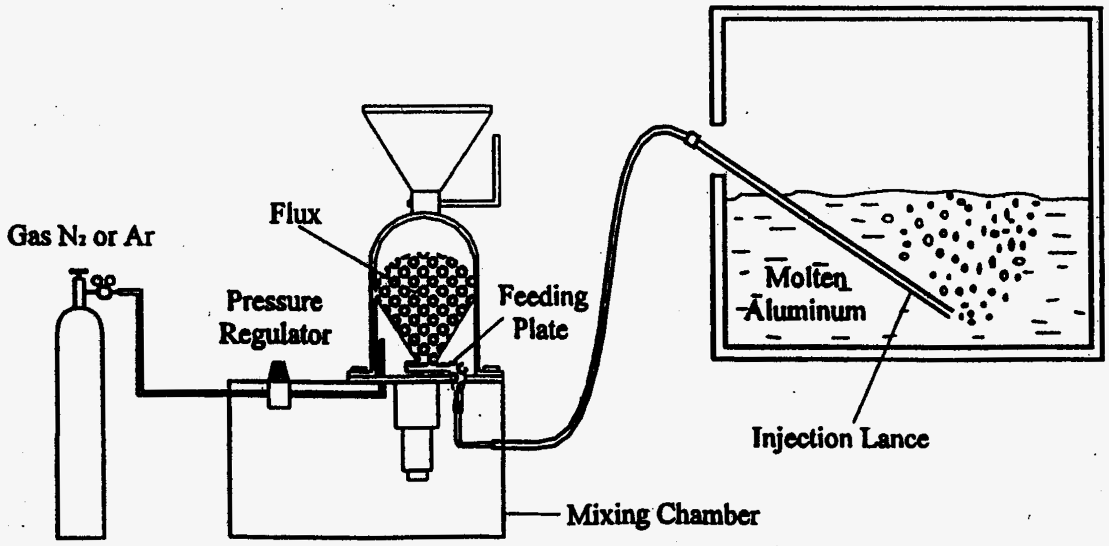

Figure 25. Layout of flux injection process [23].

Porous Plug Fluxing

In porous plug fluxing, porous plugs are installed in the bottom of the furnace or trough. The fluxing gas is introduced and dispersed in the porous plug and then forced upward to exit from its face into the melt. The early use was in flux box and small applications [26]. In the 1980's it started to be used on an industrial scale in both in-line and furnace aluminum alloy treatment. The porous plug fluxing can also incorporate with other techniques for alloy treatment, like combining with a vacuum as in vacuum stirring fluxing mentioned earlier or with deep bed filtration. The porous plug fluxing is considered [27] to be able to produce small gas bubbles but produces less ideal melt circulation and melt/gas mixing. It is generally effective in low rate or batch mode application.

Furnace Porous Plug Fluxing

Furnace porous plug fluxing [5, 26] was applied to furnaces in the late 1980's. Reynolds Metals Company equipped each of their five, 25" deep, 32 foot diameter, top charged, 240,000 lb smelters with 16 porous plugs and for each of their six, 48" deep, 225,000 lb, tilting holding furnaces with 23 porous plugs in a 100 million pound per month EMC ingot casting facility at its Alloys Plant in Muscle Shoals, Alabama. The key to this technique was the porous plug. The core of the plug used in the Alloys Plant facility is a pressed and fired version of Narcon A94 material. Its final shape is a dense aluminum-resistant unit with a texture much like that of a common high alumina brick. The porous characteristic is derived from grain size engineering and pressing techniques. The critical part of the plug assembly and installation is its seal and air tightness, which have to ensure the upward surface of the plug core being the only gas exit. This facility has been successfully operated for production of can stock alloys 3104 and 5182 since 1990. The plugs are durable with a life of probably 3 to 4 years. It was reported that this technique improved the efficiency of H removal and reduced significantly the holder fluxing time. Tests indicated H levels in the bath immediately following fluxing to be reduced up to 50% compared to levels achieved by the standard fluxing wand practice. In the holders, 225,000 lbs of metal can be degassed to 50% of the preflux gas levels in less than one hour using gas flow rates of less than 0.5 scfm per plug. It also lowered the Cl_2 content of the fluxing gas, consequently reducing emission, substantially reducing and improving dross, eliminating temperature stratification and easing the operation.

Porous Trough Fluxing [1, 28]

In the later 1980's, Alcoa and C. E Eckert applied porous plug fluxing in in-line treatment. In this system the metal transfer trough is used as a fluxing reactor, as shown in Figure 26. The bottom of the trough is lined with refractory diffusers that uniformly disperse fluxing gas as small bubbles through a flowing metal stream. The trough is covered with an electrically heated sealed lid to preheat the unit. One of the purposes of developing this system was to overcome some problems associated with the rotary degassing devices. In in-line rotary degassing, usually there is a resident volume of molten metal in the tank reactor. This pool of melt must be flushed for alloy changes which results in a significant scrap loss and production downtime for each metal change or that require continuous low speed stirring and heating and periodic skimming during idle operation. The porous trough fluxing system is a full drainable unit requiring no downtime or scrap loss during alloy change. It was found that, for low metal flows less than 1.5 cm/s and a low range of gas velocities, the gas entering the melt through each diffuser pore forms a bubble column that is displaced downstream by the metal flow. The water model demonstrated that as the metal velocity increases, the bubbles are sheared off from the diffuser before they can coalesce with adjacent bubbles. As the metal velocity increases further, bubble coalescence occurs due to gas-liquid turbulence. With an increasing gas flow rate for a given metal flow, the bubble impingement at or near the surface of the diffuser is likely. By assuming the mass transport to be the limiting process, calculations from plant data discovered a loss of bubble surface area with increasing gas and metal flow rates. The factors affecting bubble surface area are believed to be coalescence due to gas flooding at the diffuser surface and gas impingement in eddies due to metal turbulence from an increasing metal flow rate. It is reported that this method has achieved low metal H levels in a broad spectrum of alloys. Although this method needs higher diffuser Ar flows compared with Alcoa A622, its overall treatment cost is still lower.

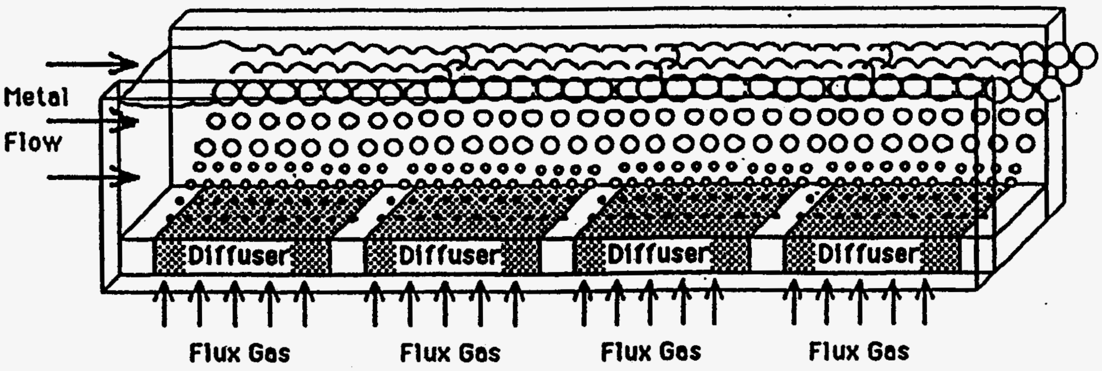

Figure 26. Schematic of porous trough diffuser [1].

Metaullics Degassing Multicast Filtration System (DMC)

The DMC was developed by Metaullics Systems in the middle of the 1980's [29]. The DMC system combines degassing and filtration in a single in-line unit. A schematic of this system is shown in Figure 27, which consists of a heated box with separate chambers for degassing and filtration. The degassing chamber is equipped with a special design porous plug (AL Clean) produced by NARCA, which provides a fine bubble size (6 - 12 mm diameter) and good mixing in the degassing chamber. The plug is used both for degassing and also for backflushing the filter element to extend its life. It is claimed that it is effective in H removal and, because degassing and filtration are combined in one unit, this system has a compact size and low cost. An early DMC unit was successfully used at the Nichols-Homeshield. The H reduction was consistently at 60 - 70%. Absolute H removal was typically from over 0.30 to below 0.11 ml/100g, even as low as 0.06 ml/100g.

DUFI, Alcoa 469 and FILD Systems [30]

All these systems function in a similar way to the Degassing Multicast Filtration System. The DUFI System was developed by Alusuisse. It includes a filter bed of petroleum coke and porous media, which generates a counter-current flow of gas bubbles. The Alcoa 469 System consists of dual filter beds of tabular alumina balls and aggregate and porous media to generate gas bubbles. The FILD System was developed by British Aluminum. It uses a perforated tube to produce gas bubbles and its filter bed is made of tabular alumina balls coated with salt.

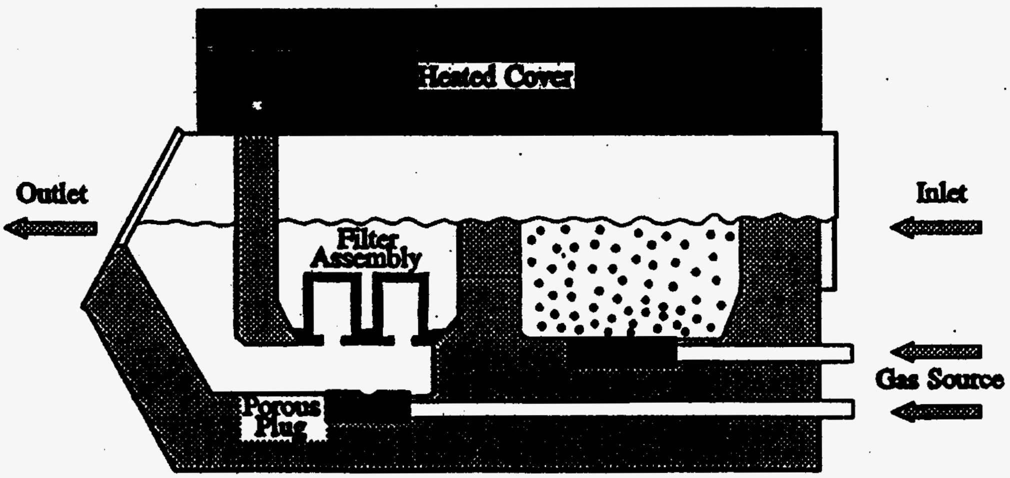

Figure 27. Schematic of Degassing Multicast Filtration System (DMC) [29].

Rotary Degassing

The existing rotary degassing system has a number of configurations, including units hung by hoists, floor mount degassing stations, units that are mounted on the external wall of a furnace and mobile units that can be moved from station to station. For each different system, a variety of rotors have been designed, tested, and now many are in commercial use. Almost every system has its own rotor design(s), and so, the rotor is given different names, such as nozzle, impeller, injector, distributor, or dispenser. However, in spite of having different names, all the rotors basically have the same function, and almost all are made of oxidation resistant graphite. During work, the rotor is rotated and the gas goes through the hallow shaft of the rotor and is forced to exit from the holes in the peripheral of the rotor head, forming bubbles as a result of shearing force and dispersing them in the melt. The rotor is very effective in generating fine gas bubbles and dispersing them. The problems are the high maintenance and operating costs and poor durability. Especially in a batch treatment operation, graphite components are invariably subject to oxidation and erosion problems.

Different rotors may work in different ways and have different characteristics. Nilmani et al. studied the performance of four commercial rotors of different designs, as shown in Figure 28 [31]. The tests were conducted in full-scale water model experiments. The oxygen desorption technique was used to simulate the removal of H from the aluminum melt. It was found that the three rotors, A, B and D, gave the same degassing efficiency in water, whereas rotor C could utilize a large amount of gas and thereby obtained a higher efficiency, and the bubble size in a well dispersed system ranged from 3 to 6 mm in diameter. It was also reported that when the rotors were used in molten aluminum, all four had a high efficiency when operating under optimum conditions. Other rotor designs will be discussed below with the pertinent degassing systems.

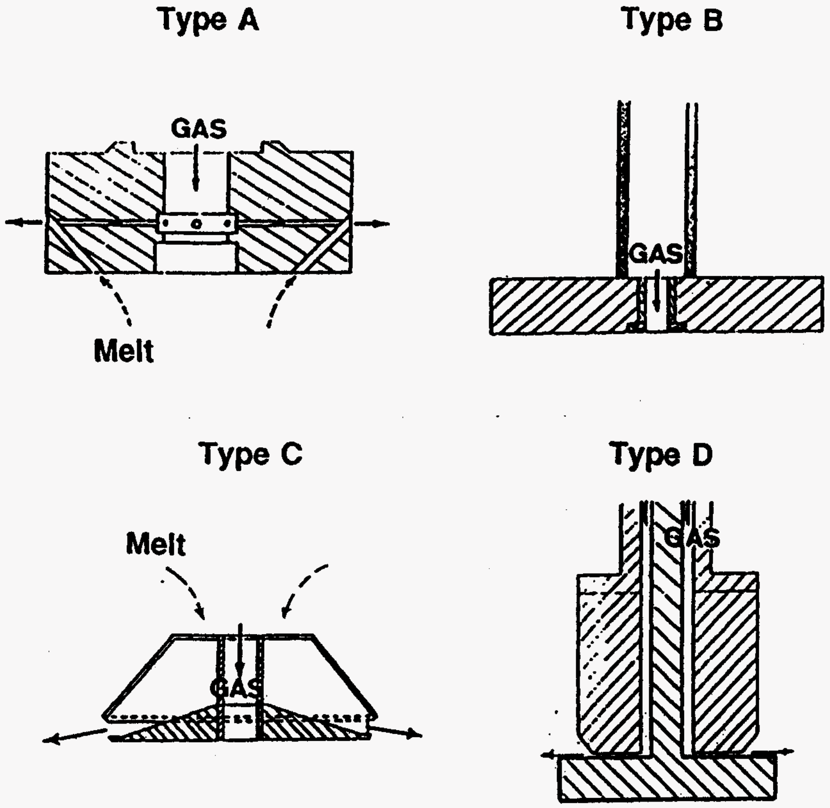

Figure 28. Basic design features of rotors used in the tests [31].

SNIF (Spinning Nozzle inert gas Injection Flotation unit) [7, 32, 33]

The SNIF system was developed by Union Carbide in the early 1970's [32]. It was one of the earliest in-line rotary degassing devices. The early SNIF system was called "T" or "tub" system. A schematic of this system is shown in Figure 29. It consists of a graphite lined cast iron vessel installed in an electric furnace. The SNIF nozzle is a two-piece design consisting of a stationary sleeve (the stator) and a rotating shaft/rotor assembly. The exterior of the rotor is like a straight gear. This two-piece nozzle reduces the undesirable tendency of the melt to vortex, and allows for the use of a stationary seal to control the atmosphere above the melt surface. In the middle 1980's the SNIF "R" (refractory) system was developed which had a compact size and improved furnace life. The SNIF R furnace has a refractory-lined steel shell and a square cross section with one wall consisting of one or more graphite heating element blocks. Multi-stage furnaces have one graphite block for each stage. Various sizes and configurations of R furnaces are designed for different applications. The R-10 has only one nozzle (one Stage) and a capacity of 9 ton/h, while the R-180U has three nozzles (three stages), four interchangeable inlet and/or outlet ports and a capacity of 82 ton/h. The latest version of the SNIF system is the SHEER system introduced in the early 1990's. In the SHEER system a bottom rib is added to the bottom of each stage, and the nozzle is redesigned. The bottom rib stabilizes the metal flow patterns, while the nozzle directs the bubbles down and disperses them evenly throughout the melt. The SHEER nozzle and rib work together to reduce melt agitation, reduce surface splashing, and increase the process efficiency. It was reported [7] that all the SNIF units have capabilities of reducing H to levels of about 0.07-0.08 ml/100g. The National Luxembourg replaced porous plug devices with SNIF R-10 units and obtained consistent H reduction from an average of about 0.25 ml/100g to 0.06 ml/100g. Different versions have different efficiencies, which are affected by metal flow rate, argon flow rate, size and shape of the unit as well as incoming H level. Tests conducted at Kaiser Trentwood verified the staging effects [32], that is, for a given metal flow rate, total gas flow rate, and number of nozzles, the multi-stage system (multi-stage with one nozzle in each stage) has higher H removal efficiency than the one-stage multi-nozzle system. The advantages gained by staging diminish as more (than three) stages are added. However, other evaluations of various SNIF models found [7] that the efficiency was affected by the incoming H level and, therefore, the staging benefits were minimum. When more than one unit was used, it did not make much difference whether they were placed in series or parallel. The implication was that the H removal was dependent upon gas flow and contact time.

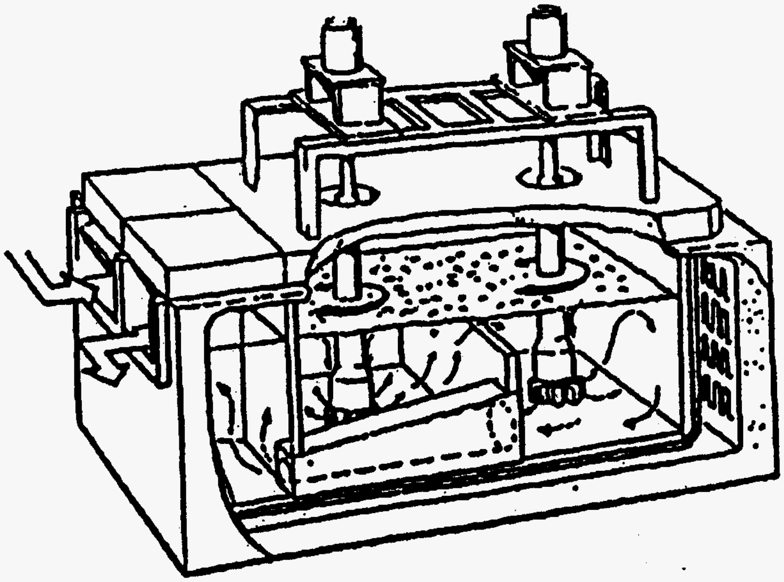

Figure 29. Schematic of SNIF "T" system [32].

Rapid Degassing Unit (RDU) [34, 35, 36]

The early RDU, developed by Foseco, had a single rotor, internally heated compact design, as shown in Figure 30. Its reactor had essentially a circular cross section with a capacity of 2000 lb and was able to treat up to 700 lb/min of metal flow. The design of the rotor (see Figure 30) was such that it pumped simultaneously molten aluminum from the top to the bottom of the unit thus creating a well mixed bath, while shearing the purging gas supply to create fine gas bubbles. A ceramic protection sleeve was incorporated extending over much of the length of the shaft to eliminate the erosion from rotation and to reduce the oxidation. A later version of the RDU has a capacity of 2800 lb and ability to treat up to 1000 lb/min of metal flow, with its improved rotor design, as shown in Figure 31. The rotor has several vanes extending from the shaft to the periphery and dividing the rotor into several compartments, each compartment having an inlet adjacent to the shaft and an outlet adjacent to the periphery of the rotor. Purge gas discharges from the end of the shaft into each rotor compartment while the rotor rotates in the molten aluminum. Molten aluminum entering each compartment of the rotor breaks up the stream of purge gas into tiny bubbles that are then intimately mixed. The performance of the RDU was evaluated at Commonwealth Aluminum. In a unit of 2800 lb, the average H reduction was 37% under the following operating conditions: alloys: 3003 and 3015; metal flow: 570 lb/min, gas flow: Ar 50-52 l/min and Cl_2 2.5 l/min; rotor speed: 225 rpm.

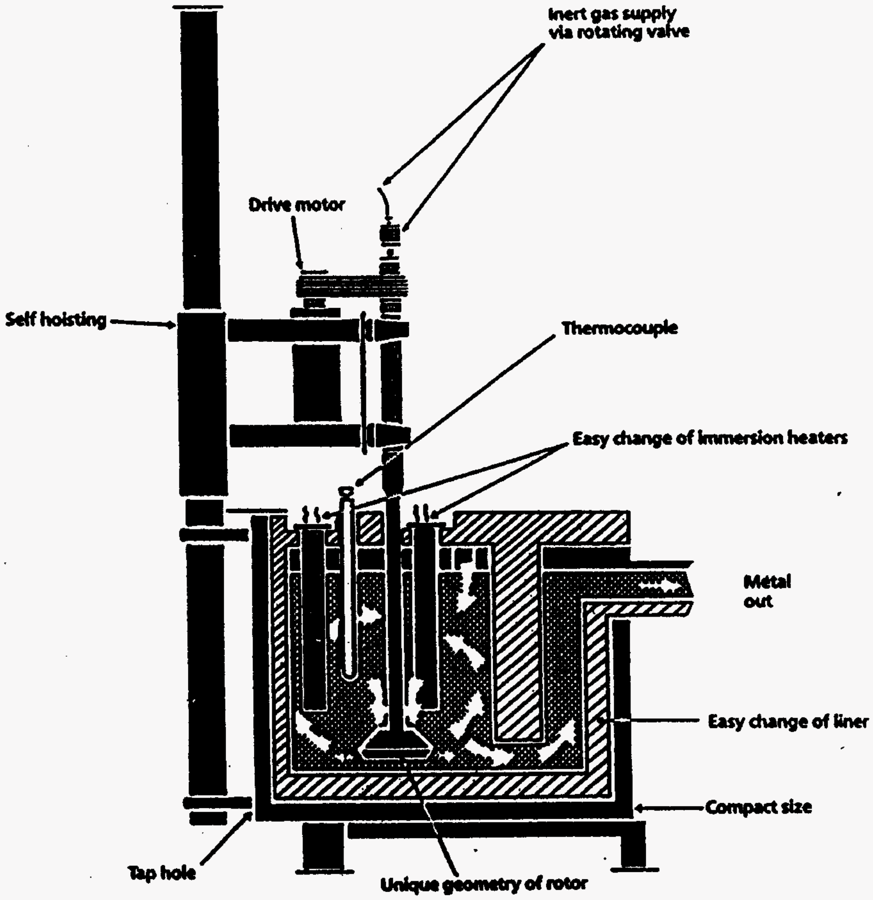

Figure 30. Schematic of Rapid Degassing Unit (RDU) [36].

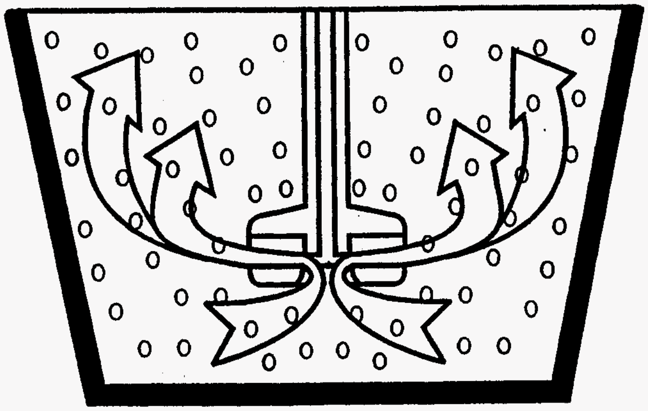

Figure 31. “Hamburger” rotor used in RDU [34].

HYDRO Metal Refining System (HA Rotor Systems) [12, 37, 38]

HYDRO Metal Refining System was developed by Hydro Aluminum, which was reported to have a principle and theory of the gas removal different from other degassing systems. The primary feature of this system is the HA rotor, which is totally cylindrical with no fins, but with a hole at the bottom, as shown in Figure 32. The rotor works like a centrifugal pump that sucks the melt from the hole at the bottom and ejects the melt through peripheral holes in the wall. When metal is forced to flow through the rotor side holes, it contacts the gas which is then broken into small bubbles just outside the holes. Compared to traditional rotors, in terms of gas injection, the HA rotor pumps less metal at a given speed. Thus, this rotor can be run at high speed; for example, a rotor with a diameter of 200 mm can be run at 500-900 rpm. It produces a peripheral speed of 315-565 m/min and pumps approximately 40 tons per hour. The resulting high shearing forces cut the gas into very small bubbles. The size of the bubbles is determined by the shear force but not by the size of the peripheral holes. This ensures that the size of the bubbles remains the same at a constant rotor speed, giving constant and efficient melt cleaning through the entire life of the rotor. The gas bubble dispersion is carried out mainly by melt convection or pumping, and secondly by turbulence. The mixture is described as ideal even if the pumping rate is relatively low. On the other hand, though the rotor produces a very efficient mixing, this mixture only occurs in the lower part of the reactor. The gas flow results in a vertical melt flow in the upper part of the reactor, and the cylindrical shape of the rotor causes little stirring, ensuring very minimum turbulence in this region. The cylindrical shape also produces very little wear and tear to the rotor, giving it a very long operating life. The friction between melt and rotor, through very small, may start the melt to rotate, but a stream breaker can readily stop this rotation.

This system has batch and in-line treatment units and one unit can have one, two, or three rotors depending on the unit capacity. The batch units can be used in either transportable crucible or crucible furnaces and can be either stationary or mobile. The stationary units are used in smaller crucibles of 300-200 kg or in furnaces up to 10 tons. For larger furnaces, the mobile units are preferred, especially when more than one furnace needs to be treated. One rotor is sufficient to treat a furnace with a capacity of 10-15 tons (depending on furnace diameter). For furnaces larger than 15 tons, a twin rotor would be appropriate. In the small crucibles in foundry operations, the treatment time can be 1-2 mins, while the time for a 20-ton crucible furnace can be 30-40 mins. It was reported that one rotor could treat 500 kg/min of foundry alloy for good quality. The H removal efficiency was reported to be 85% for 10 ton alloy with a 30 min treatment. The unit used in in-line treatment can contain 1 to 3 rotors. One-rotor units are generally used up to 20 ton/h, and two and three rotor units are used up to 50 ton/h and 70-80 ton/h, respectively. In the in-line unit the stream breaker in the reactor walls gives optimal metal flow, gas/metal mixing and utilization of the gas. The reactor can be tilted, which makes alloy changing more efficient. Tests were conducted under the following conditions: metal flow rate of 43.5 ton/h, rotor speed of 750 rpm, and Ar flow rate at 150 Nl/min (207 Nl/ton). These tests showed H removal efficiencies in the range of 58% to 71%, increasing with a higher inlet H level.

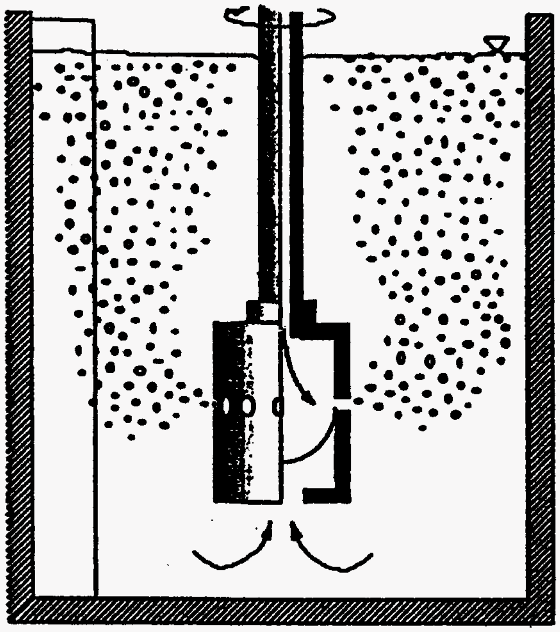

Figure 32. Schematic of the HA-rotor used in HYDRO Metal Refining System [38].

ASV System [39]

The ASV System was developed by Årdal og Sunndal Verk a.s. in the early 1980's, in cooperation with SINTEF in Norway. The system was developed for use in either in-line or batch treatment of liquid metals. A prototype design of a two-rotor reactor of this system for high metal flow rates is shown in Figure 33. Its rotor and a heating element are shown in Figure 34. The rotor design and its working mechanism are very similar to the HA rotor in the HYDRO Metal Refining System, but the ASV System incorporates a heating element. The heating system is based on an electrical arc heating, with or without plasma equipment. A cathode is placed inside the rotor, and the liquid metal is used as an anode. The heat is generated underneath the metal surface, and the energy loss to the surrounding area is therefore relatively small. The temperature in the arc may reach 3000-4000 °C. This would normally cause problems due to the surface evaporation of aluminum. However, it is prevented in this system, mainly by the pumping of the rotor, which gives a constantly replaced anode and a very effective heat transport. Because the heating system is part of the rotor, the rotor can be used in small crucibles or boxes without the need of heating. The experiments and plant experience showed that this system was effective in H removal for aluminum alloys. The batch treatment tests of liquid aluminum in a 2.8-ton induction crucible furnace demonstrated that after 15 and 30 min treatments the H was removed from 0.26 to 0.08 and 0.05 ml/100g, respectively. In the in-line treatment experiments, which were carried out for Al-11%Si and Al-5%Mg-1%Si alloys with the Ar consumption of 300-400 l/t of aluminum, the H was removed from 0.21 to 0.07 ml/100g.

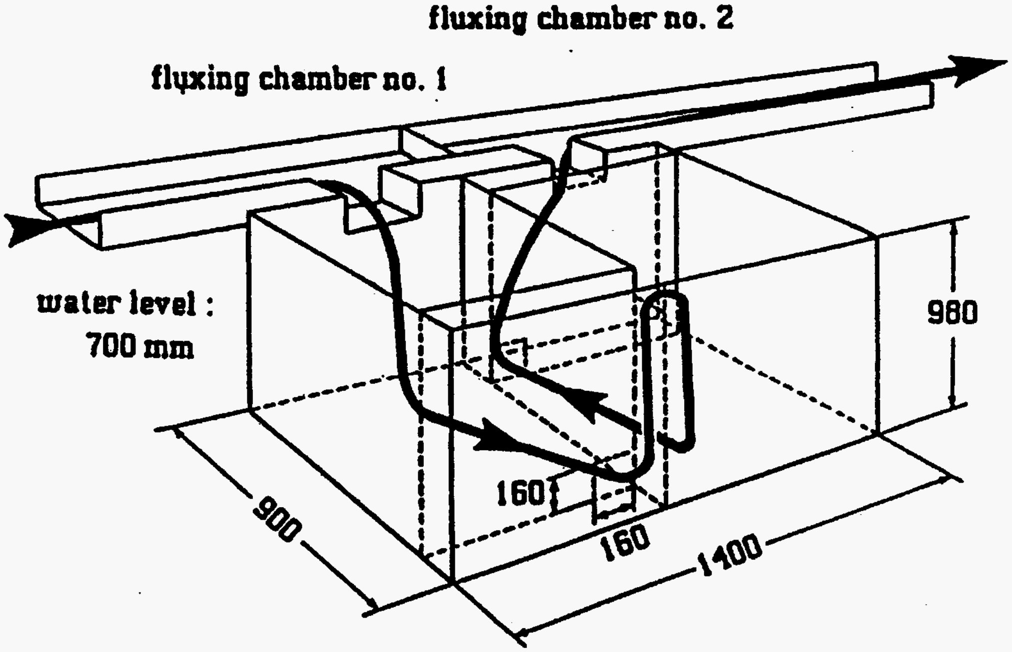

Figure 33. A two-rotor reactor design in the ASV System [39].

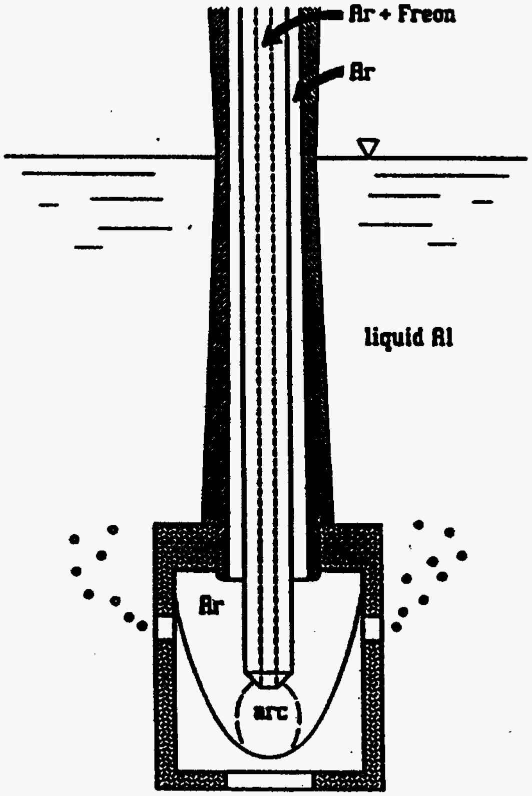

Figure 34. Schematic of the rotor with a graphite cathode in the ASV System [39].

Alcoa 622 (A622) [9, 17]

A622 is an in-line metal treatment process. The reactor of the A622 unit is an isothermal continuous stirred tank containing a rotor. A single stage unit is shown in Figure 35. The unit can be used alone or a set of two, three or four units can be used together. Molten metal typically flows from the holding furnace into a trough section and then into the A622 unit. In a one-stage system or in the first stage of a multiple-stage system, the melt flows downward through the inlet compartment of the reactor. The rotor breaks the fluxing gas into small bubbles that flow up. The melt and the gas form a counter-current flow in this reactor. In some multiple-stage systems a concurrent flow of melt and gas may be used. The melt exits the reactor by passing the channel under a baffle and up through the outlet section of the unit. The melt temperature is usually controlled at 1350 °F (732 °C) with gas-fired immersion heaters or electrical heaters. The typical fluxing gas is a mixture of Cl_2/Ar but other gases are also used. The diameter of the standard rotor is 12 in (305 mm).

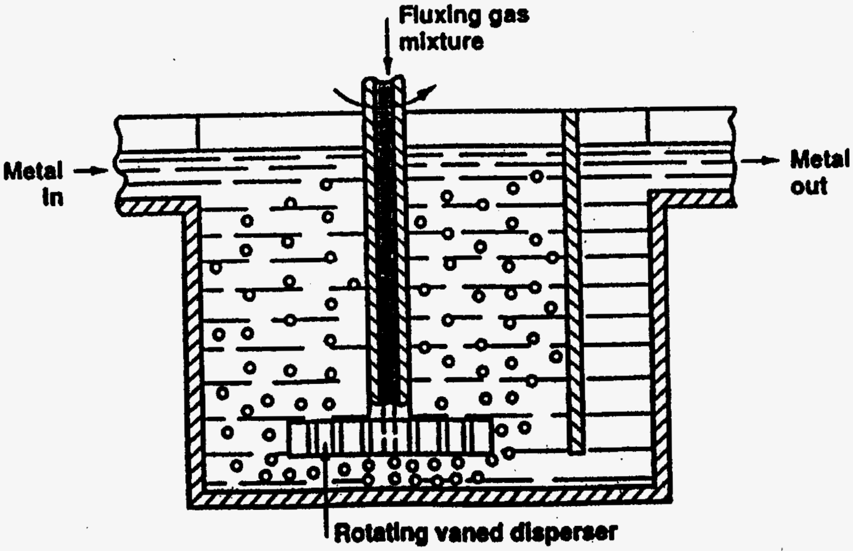

Figure 35. Schematic of one stage Alcoa 622 unit [9].

IRMA Process [11]

IRMA was an early rotary degassing device developed by Pechiney to replace a pipe injector and solid salt for pretreatment in the furnace prior to in-line treatment. An IRMA device may contain several rotors depending on the furnace dimensions. The rotor design is proprietary. The rotors are mounted on a frame where they can be moved up and down for removing from and inserting the rotors into the melt and can be moved along beams by a motorized crane to leave room for other operations. With the IRMA process, the treatment time was reduced by half, the quantity of Cl_2 used was lowered dramatically while alloy quality was improved and metal loss was reduced, as compared to the preceding system.

Alpur Process [20, 40, 41]

The Alpur Process was developed by Pechiney for in-line aluminum alloy treatment. It was first introduced in production in 1982. The principle of the Alpur treatment and its rotor design are shown in Figures 36 and 37, respectively. The rotor has two networks with the same number of pipes, the gas and the liquid metal pipe networks, concurring on the outer cylindrical surface of the rotor. The gas pipe network consists of several pipes of small diameter (1-3 mm). For the normal gas flow in the rotor (3-

10 Nm^3/h) the gas speed at the injection point is greater than 50 m/s. The liquid metal pipes have a larger diameter (8-15 mm) and work like a centrifugal pump. At the concurrent point of the two networks, the metal flow and gas flow mix resulting in a fine dispersion of the two phases along the lateral surface of the rotor. This metal/gas mixture is immediately distributed through blades into the whole melt. The characteristics of a typical rotor are: rotor diameter - 250 mm, pipe number - 8, gas pipe diameter - 1.5 mm, metal pipe diameter - 10 mm, slope angle of the metal pipe - 45°, height of the metal pipe - 80 mm, and number of stirring blades - 4. This rotor can degas up to 12 t/h of liquid aluminum for a gaseous flow rate of 10 Nm^3/h and a rotation speed of 250 rpm. Several series of Alpur units have been developed to match various application conditions, from a low rate of 2 t/h (70 lb/min) or less to a high rate of 90 t/h (3300 lb/min) for use with or without fast alloy change. A unique feature of the Alpur system is the compact design with a tilting tub (reactor) for easy and quick dumping of the unit for alloy change and for more reliable inspection and cleaning. It can have a single or multiple rotors and immersion heaters, which can give a quick heat-up. H removal efficiency was reported to be in the range of 60 to 80 %, consistently reaching final levels of 0.10 ml/100g or less.

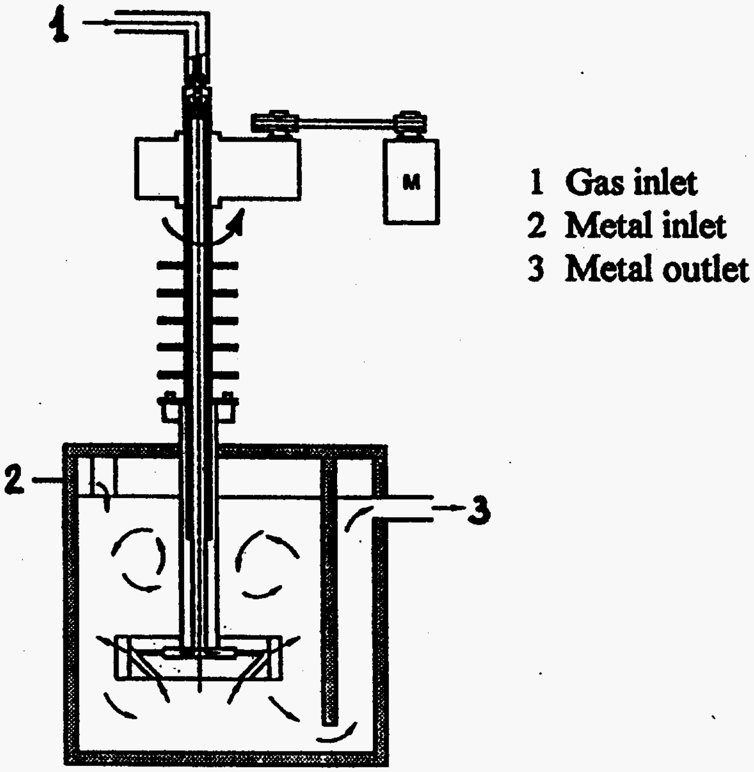

Figure 36. Principal of Alpur treatment [41].

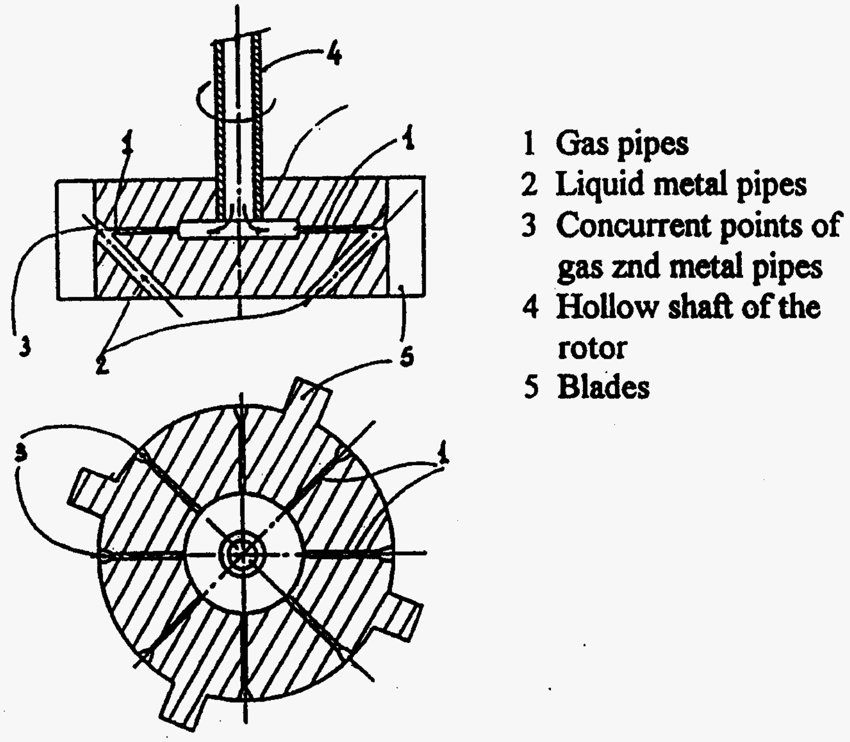

Figure 37. Schematic of Alpur rotor design [41].

GBF System [42]

Showa Aluminum Corporation of Japan developed the GBF degassing system. The schematic of a typical GBF system is shown in Figure 38, which features high speed, specially designed rotor(s) and suitably designed baffle plates. A super rotor design is shown in Figure 39. The rotor is most efficient when the speed varies from 600 to 950 rpm depending on the vessel design, metal volume, and the rotor size (diameter). The diameter of the gas bubbles was observed to be less than 5 mm. The high speed of the rotor is to ensure dispersing a maximum number of fine gas bubbles from as high gas flow rate, which is essential for treating a high metal flow rate. Baffle plates, 2 to 3 of which are placed within the vessel lining, are used to promote the agitation effect in the molten metal and to prevent turbulence or vertex on the metal surface. Several in-line devices of the GBF system were designed, which have either one or two rotors, for treating the metal at flow rates up to 60 tons per hour. The final H content after GBF treatment is typically 0.05-0.12 ml/100g, with the gas (Ar) consumption of 0.20-0.40 l/kg. The rotor life was about 200 hour treatment time.

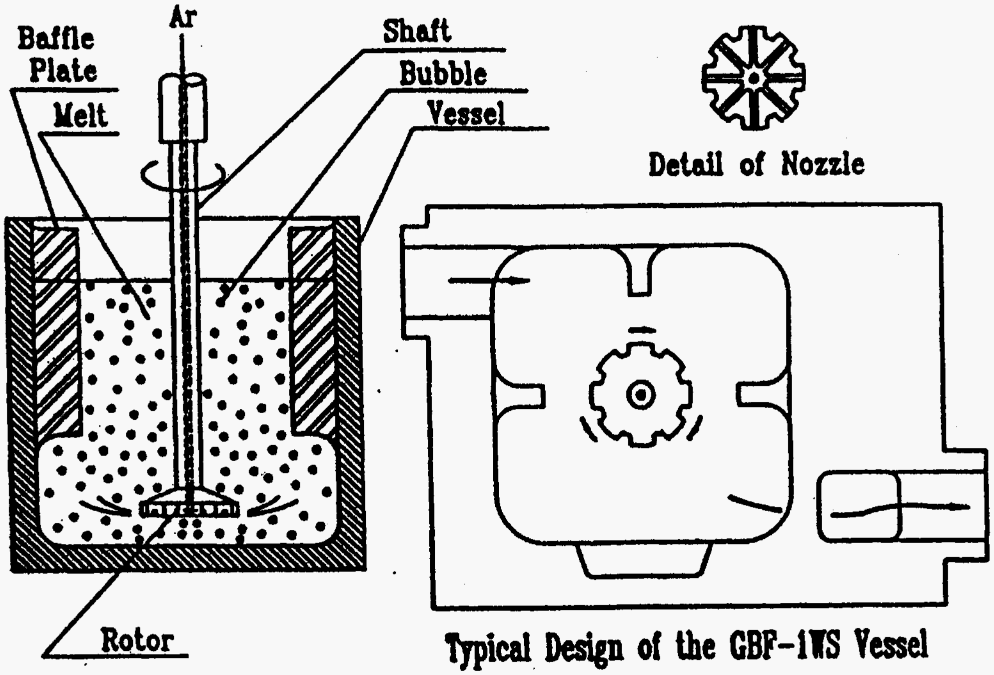

Figure 38. Schematic of the GBF - 1WS vessel [42].

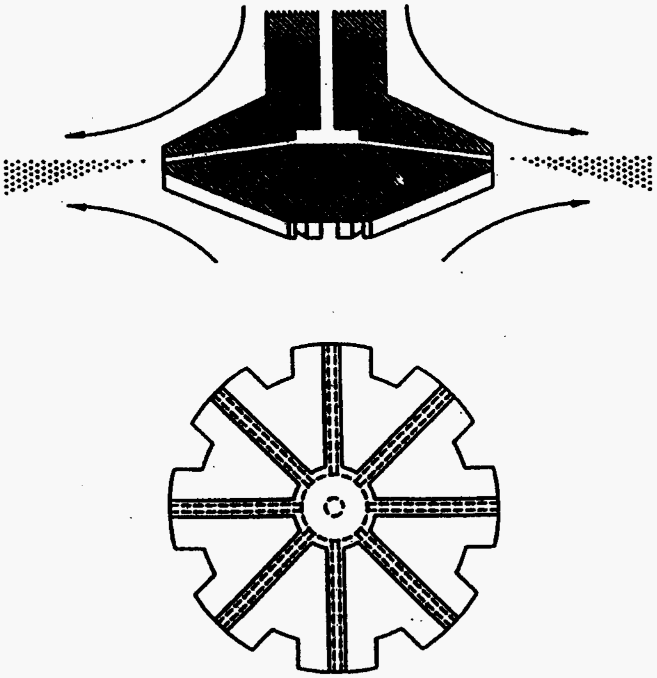

Figure 39. The rotor used in GBF system [42].

Gas Injection Fluxing System (GIFS) [43]

GIFS was an in-house system developed to fit into a limited space, the fluxing bay of the existing holding furnace in Noranda Aluminum. The unit was designed to treat up to 32 tons/h to replace the four lances which were injecting 100% Cl_2. The schematic of the GIFS is shown in Figure 40. It has two simple rotors rotating at about 300 rpm and uses Ar/0.5-2%Cl_2 gas mixture. The measured H removal efficiencies ranged from 50-76% with the outlet H concentrations of 0.15-0.07 ml/100g.

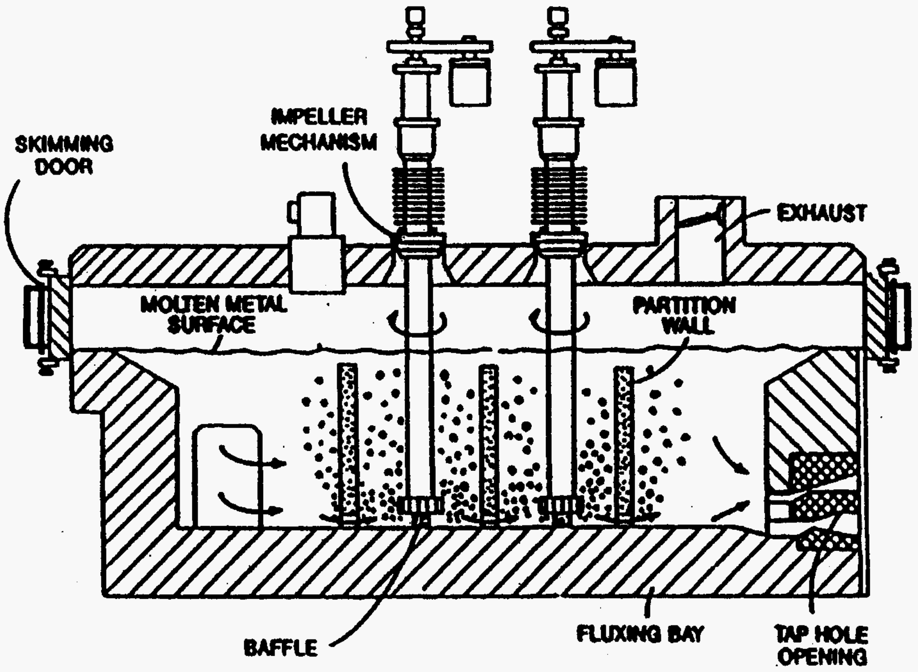

Figure 40. Schematic of Gas Injection Fluxing System (GIFS) [43].

ALCAN Compact Degasser (ACD) [44, 45]

The Alcan compact degasser has been developed in the 1990's. It is a trough-based multi-stage in-line degassing process. The development of this technology was motivated by the need to eliminate metal hold-up between casts and to significantly reduce the floor space requirement, giving the smaller, multi-alloy casting centers access to in-line metal treatment. A schematic diagram of a multi-rotor ACD unit is shown in Figure 41. The device is placed in the trough between the holding furnace and the casting machine. It consists of a series of rotary gas injectors arranged within the trough, each separated by a vertical baffle. The baffles effectively divide the trough into a series of treatment chambers or stages, through which liquid aluminum passes sequentially in a “quasi” plug flow regime. Openings of sufficient area in each baffle allow a metal flow without generating a metallostatic head. This design approach is physically constrained by the low metal depth in the trough available for injection of the treatment gas. The ACD is modular in nature and as such, the number of rotors used depends on the alloy composition and casting rate, the total inert gas flow rate, and to a limited extent, on the trough design. A minimum metal depth of 17 cm must be maintained in the trough during operation. More typically, a metal depth of 20 cm to 25 cm is maintained.

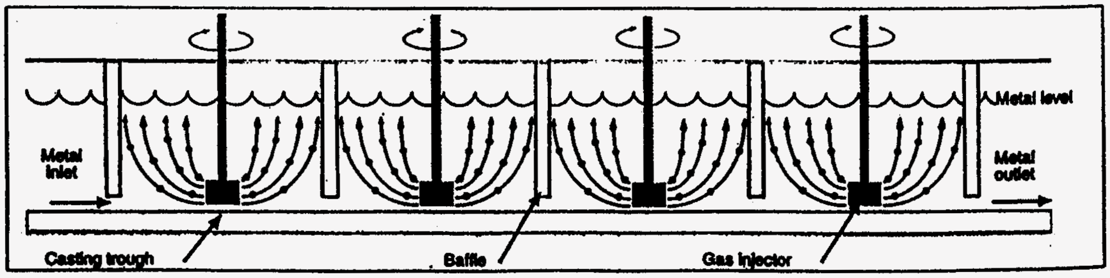

Figure 41. Schematic of Alcan Compact Degasser [44].

Because this degassing unit is confined in a small space and melt residence time is short, in order to maintain a degassing efficiency equivalent to the conventional degassing technology, the approach taken by the designers is to increase the interfacial gas-metal contact area. Because this design can not increase the metal depth and the inert gas flow rate has to be minimized to allow for a small reactor volume without excessive coalescence of the gas bubbles, the approaches left for the designers to increase the gas-metal contact area are to minimize the gas bubble diameter and its rise velocity. The ACD retains gas in melt more effectively than a conventional unit. The effectiveness of maintaining gas in the melt can be expressed by an index, “the volume fraction gas holdup.” During operation, the metal level inside the degasser rises above the metal level in the trough outside the degasser. This level difference is caused by the presence of gas in the metal, and is a direct measure of the volume fraction gas holdup. It is approximately 10 - 15 % for the ACD, while it is typically less than 5% for conventional degassers. This means that the capacity of the ACD in maintaining gas is two to three times that of conventional degassers. Therefore, the ACD can produce equivalent performance in substantially smaller volumes of metal. In addition, the multi-stage design has a considerable impact on the degassing performance.

It is claimed that the ACD can effectively save space. It has no metal hold-up after the cast, eliminating a significant source of metal loss when frequent alloy changes are required. Since there is no molten metal to maintain, no heating system is required, thereby reducing the equipment and maintenance costs of the machine and simplifying its operation. Its modular design can effectively use the length of the trough as the reaction zone. Various ACDs have been used in Alcan. They typically remain at 55-60% H removal efficiency for casting rates of up to 750 kg/min. The ACD also produces less dross, because it is operated with a slight over-pressure of Ar gas and its liquid surface area is approximately 1/10 that of a conventional degasser.

ALCAN Filter Degasser (AFD) [46]

As mentioned earlier, for high gas removal efficiency in an in-line treatment the optimum metal and gas flow conditions should be: (1) the bulk melt has sufficient circulation which can mix the gas bubbles well with the melt, (2) the melt and the gas flows move in a counter current, and (3) no surface turbulence is generated. It is difficult for the conventional rotary degassing unit to meet these requirements concurrently. The ALCAN Filter Degasser (AFD) developed by Alcan is said to be able to achieve all these goals. The schematic of the AFD is shown in Figure 42. Its unique feature is the horizontally oriented, perforated ceramic plate, which divides the reactor into upper and lower sections. On top of the plate a fixed bed of granular ceramic packing is located which forms an intermediate treatment section. During the treatment the metal flows in a downward direction. In the lower section the gas bubbles are generated by the rotor with certain turbulence. The gas bubbles subsequently pass through the perforations of the ceramic plate and the porous fixed bed. This porous fixed bed effectively isolates the turbulence in the lower section, so that no matter how turbulent it is in the lower section, the upper section is always kept quiescent. The quiescent zone allows the incoming metal to distribute evenly across the intermediate treatment section and provides a quiet metal surface. In this way the AFD also effectively separates the contaminated metal at the inlet from the cleaned metal at the outlet and provides an overall metal and gas counter flow. Coalescence of the gas bubbles may occur as they pass through the fixed bed; however, the degree of coalescence is limited by the pore geometry of the bed. On the other hand, the floating velocity of the gas bubbles is reduced and thus the gas-metal contact time is increased. The AFD was successfully used on several different alloys. It was reported that, as a result, it was more efficient than the conventional rotary degassing units. Degassing a metal flow of 30 tons/h by using the AFD only requires one rotor while two rotors are needed in the conventional rotary degassing units. In addition, the AFD can achieve equivalent degassing rates by using typically three to five times less treatment gas.

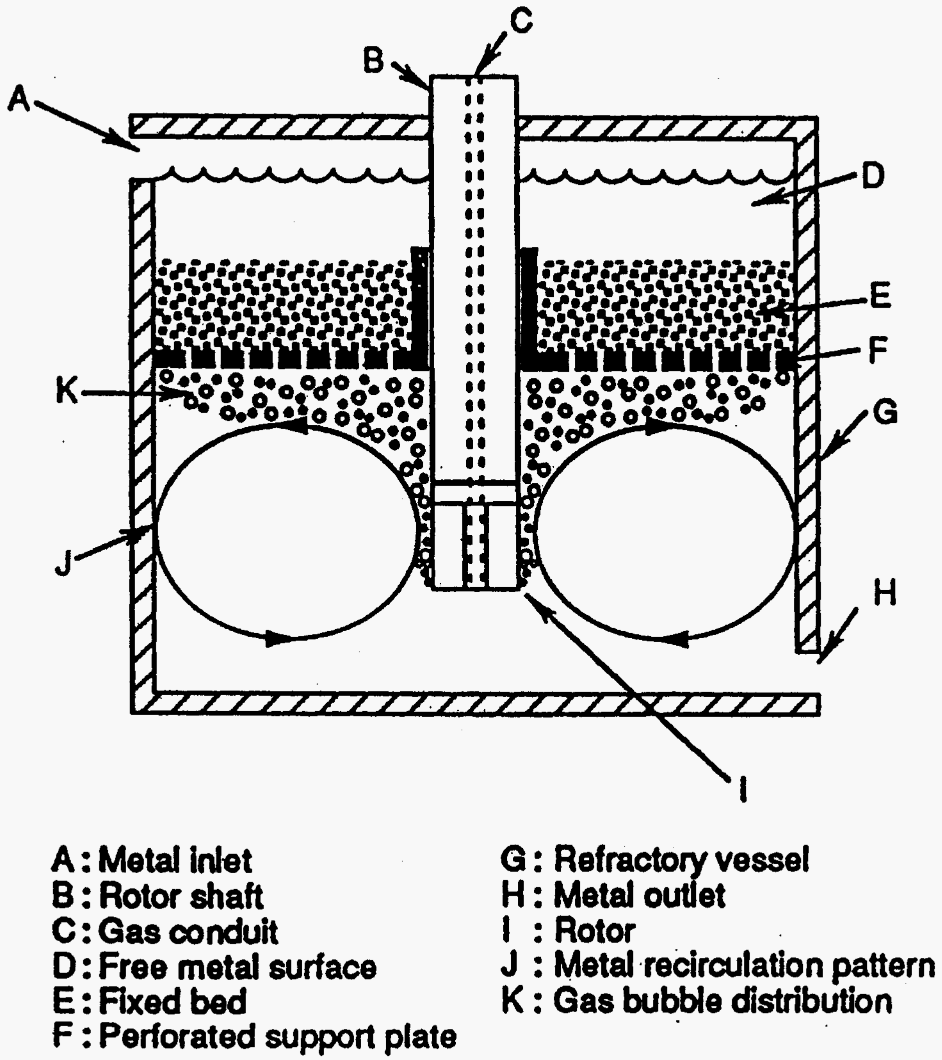

Figure 42. Schematic of the Alcan Filter Degassing In-line Metal Treatment Process [46].

Portable Rotary Degasser (PRD) [47]

The portable rotary degasser was developed by Brumund Foundry. It is a small, portable device suitable for foundries that melt aluminum alloys in small batches. Initially, Brumund Foundry developed the PRD to use on their own 90-lb crucibles and 150-lb bull ladles. Now it has been successfully used on melts from 70 to 300 lbs. The PRD uses an expendable graphite lance/impeller of 24 and 36 ins long for various size crucibles and a variable air motor to drive the rotor. It weighs less than 50 lbs and provided degassing times of 1-3 mins for a melt of 90-150 lbs.

Rotary Degassing and Flux Injection Combination

Rotaflux Process (FI/RD) [23]

The Rotaflux Process is a combination of flux injection and rotary degassing. It was developed by Wedren Flux in the early 1990's. In this system the flux injection unit controls the flow of purge gas mixed with the halogen-bearing salt flux to the impeller shaft and head and controls the total cycle time as well. The most common obstacle when coupling the two units together is the likelihood of flux buildup and choke in the transfer line. This is because the gas flow rate used in the rotary degassing device (averaging 0.5 cu ft per min) is not sufficient to maintain the solid flux powder in suspension. So, a higher gas flow rate, about 0.75 to 1 cu ft per min depending on the flux feed rate, is needed. During the operation, the higher gas flow rate, combined with the halogen gases produced by the flux, quickly overwhelms the rotary impeller head. Thus, the rotary impeller head is operating in an envelope of purge gases, resulting in large gas bubbles, little contact with the molten metal, and lower efficiency. However, it was reported that for a total flux addition of 0.5%, the overall degassing time was reduced by an average of 30% compared with experiments when the flux injection or the rotary degassing methods were used separately and the metal was cleaner.

High Velocity Jet

MINT System [14, 30, 48, 49]

The MINT is an in-line melt treatment system developed by Consolidated Aluminum in the late 1970's. Figure 43 is the schematic cross section of Heated MINT III E. It uses a high velocity jet to generate gas bubbles. In a typical MINT reactor many nozzles are installed on the conical perimeter of the reactor. The bubble formation could be described as the result of an "explosion" of the treatment gas as the turbulent and unstable bubbles formed by a high speed jet at the nozzle orifice burst into the molten metal to form small bubbles. The rising gas bubbles are distributed throughout the reactor by the rotating motion of the molten metal that flows tangentially in at the top of the reactor. The minimum bubble size, about 5 mm for Ar in molten aluminum, can be obtained regardless of orifice size by increasing the gas velocity until an orifice Reynolds number of 10000 is reached. In this way, a large volume of gas can be converted into small bubbles in a very small space and by using multiple nozzles it is possible to get a dense bubble distribution and a high degree of turbulence and consequent high mass transfer rates without any moving parts. Consequently, the MINT unit can be very compact. For example, the reactor capacities vary from 1.6 to 4 lb/lb per min flow rate for SNIF and Alpur, while it is only 0.6 lb/lb per min flow rate for the MINT. The data showed that the average efficiencies of the MINT treatment were over 60%.

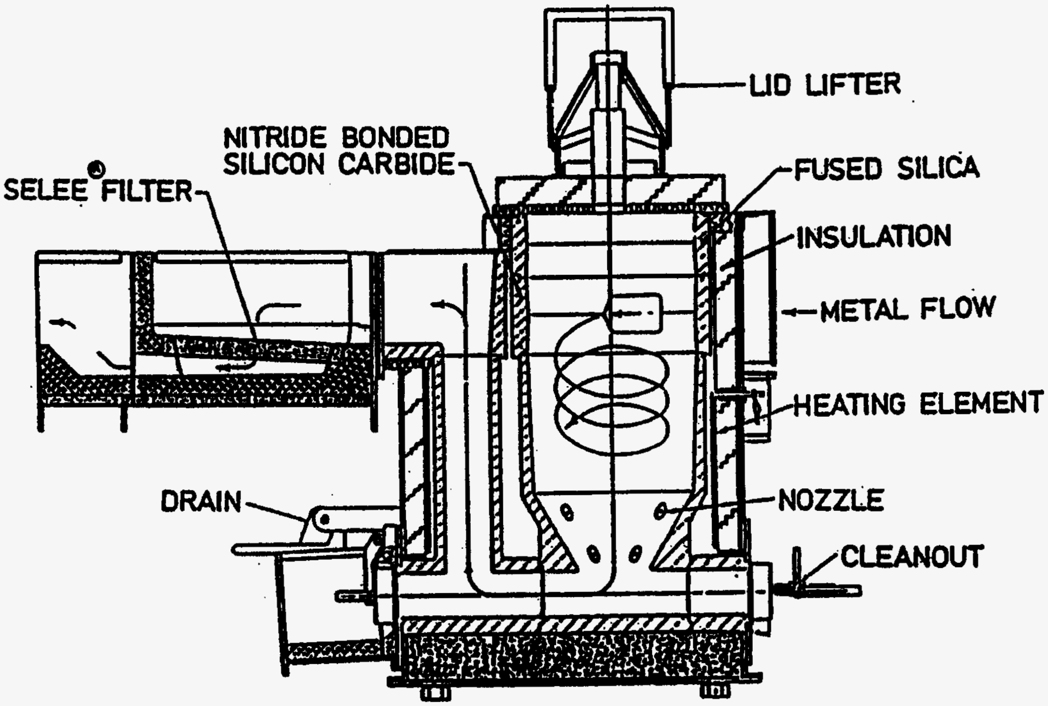

Figure 43. Schematic of Heated MINT III E [49].

Jet Fluxing [24]

The jet fluxing system is a recently proposed furnace treatment device. It requires the use of a subsurface metal pumping system. By proper placement of a single standard lance in front of a jet of metal, for example, as produced by the Alcan Jet Stirrer, it is possible to shear gas bubbles as they are formed and distribute them throughout the metal bulk. It was reported that this system had a high efficiency with substantially less Cl_2 in alkali removal, but there is no data available for its use in H removal.

References

1 Stevenson, D. T., "Porous Trough Fluxing for Hydrogen Removal," Light Metals 1992, Edited by Euel R. Cutshall, TMS, 1991, p1049-1054.

2 Kumar, R., "Liquid State Treatment of Aluminum Alloy Melts," Short Course and Workshop on Aluminum Melt Refining and Alloying -- Theory and Practice, Melbourne, July 10-12, 1989, Edited by M. Nilmani, p11-I2.

3 Aarflot, A., "Development of Melt Treatment," Proceedings of the International Seminar on Refining and Alloying of Liquid Aluminum and Ferro-Alloys, August 26-28, 1985, The Norwegian Institute of Technology, Trondheim, Norway, p360-370.

4 Sano, M., and Hirasawa, M., "Vacuum Suction Degassing - Applications to Degassing of Molten Metals," Aluminum Metal Treatment & Casting, Edited by Nilmani, M., TMS, 1993, p125-135.

5 Guttery, J. R., and Evans, W., "A New Generation of Fluxing in Aluminum Melting and Holding Furnaces," Light Metals 1994, TMS, Edited by U. Mannweiler, p921-927.

6 Peterson, R. D., Wells, P. A., and Creel II, J. M., "Reducing Chlorine Usage in Furnace Fluxing: Two Case Studies," Light Metals 1995, TMS, Edited by J. Evans, p1197-1202.

7 Eister, W. C., and Krumme, W. R., "An Evaluation of a SNIF Unit as an Inclusion Removal and Degassing Device," Light Metals 1991, TMS, Edited by Elwin L. Rooy, p1171-1177.

8 Engh, T. A., and Pedersen, T., "Removal of Hydrogen from Molten Aluminum by Gas Purging," Light Metals 1984, TMS, Edited by J. P. McGeer, p1329-1344.

9 Stevens, J. G., and Yu, H., "A Computer Model Investigation on the Effects of Operation Parameters on the Hydrogen Removal Rate in the Alcoa 622 Process," Light Metals 1992, Edited by Euel R. Cutshall, TMS, 1991, p1023-1029.

10 Peterson, R. D., and Wells, P. A., "The Effect of Fluxing Gas Composition on Removal Kinetics For Hydrogen and Light Metals," Light Metals 1993, TMS, Edited by Subodh K. Das, p891-898.

11 Boeuf, F., and Baud, O., "Rotating Injectors in Casthouse Furnaces," Light Metals 1989, Edited by Paul G. Campbell, TMS, 1988, p815-818.

12 Aarflot, A., "New Melt Cleaning Technology," Light Metals 1991, TMS, Edited by Elwin L. Rooy, p1133-1137.

13 Celik, C., and Doutre, D., "Theoretical and Experimental Investigation of Furnace Chlorine Fluxing," Light Metals 1989, Edited by Paul G. Campbell, TMS, 1988, p793-800.

14 Clumpner, J. A., Dore, J. E., and Hoffmann, W. L., "MINT -- A New Aluminum Melt In-line Treatment System," Light Metals 1981, Edited by Gordon M. Bell, p751-757.

15 Simensen, C. J., “Removal of Volatile Elements from an Aluminum Melt by Gas Fluxing,” Ardal og Sunndal Verk a. s., Norway, 1981.
16 Corns, R. R. and Rack T. P., “AGA MIX 14 Practical Implementation of Aluminum Degassing,” Light Metals 1989, Edited by Paul G. Campbell, TMS, 1988, p783-792.
17 Stevens, J. G., and Yu, H., ”Mechanism of Sodium, Calcium and Hydrogen Removal from an Aluminum Melt in a Stirred Tank Reactor -- The Alcoa 622 Process,” Light Metals 1988, Edited by Larry G. Boxall, p437-443.
18 Hicter, J. M., “Advances in Liquid Metal Treatment,” International Conference on Aluminum-85 (INCAL), New Delhi, India, Oct. 30 - Nov. 2, 1985.
19 Waite, P., and Bernard, D., “Recent Experience with the Use of Sulfur Hexafluoride for Aluminum Fluxing,” Light Metals 1990, Edited by Christian M. Bickert, TMS, 1990, p775-784.
20 Bildstein, J., Lacroix, J., Netter, P., Prevost, P., and Zahorka, G., “Degassing Casting Alloy Ingots Using Alpur System,” Light Metals 1988, Edited by Larry G. Boxall, p431-435.
21 Saha, D., and Fay, D.,”Use of Sulfur Hexafluoride in Aluminum Degassing,” Proceedings of 2nd International Conference on Molten Aluminum Processing, Sheraton World Resort, Orlando, Florida, Nov. 6-7, 1989, paper 22.
22 Corns, R. R. and Rack, T. P., “Production and Laboratory Results Using AGA MIX 14,” Light Metals 1990, Edited by Christian M. Bickert, TMS, 1990, p785-788.
23 King III, S., and Reynolds, J., “Flux Injection/Rotary Degassing Process Provides Cleaner Aluminum,” Modern Casting, April 1995, p37-40.
24 Beland, G., Dupuis, C., and Martin, J. P., “Improving Fluxing of Aluminum Alloys,” Light Metals 1995, TMS, Edited by J. Evans, p1189-1195.
25 Nilmani, M., “A Low Cost Solution to Gas Lancing Problems,” Aluminum Metal Treatment & Casting, Edited by Nilmani, M., TMS, 1993, p117-123.
26 Guttery, J. R., “A Two Year User’s Experience with Porous Plug Fluxing in a Modern Casting Facility,” Light Metals 1993, TMS, Edited by Subodh K. Das, p899-906.
27 Neff, D. V., “Degassing and Cleaning of Molten Aluminum,” Proceedings of 3rd International Conference on Aluminum Processing, Vol. I, May 26-29, 1994, Westin Regina Hotel-Cancun, Q. R., Mexico, p57-72.
28 Eckert, C. E., United States Patent No. 4,714,494 (1987-12-22).
29 Bopp, J. T., Neff, D. V., and Stankiewicz, E. P., “Degassing Multicast Filtration System (DMC) -- New Technology for Producing High Quality Molten Metal,” Light Metals 1987, TMS, Edited by R. D. Zabreznik, p729-736.

30 Clumpner, J. A., Hershey, R. E., and Hoffmann, W. L., "MINT -- An In-line Melt Purification System: Predicting Commercial Performance with Aluminum Alloys," Light Metals 1986, Edited by R. E. Miller, p815-819.
31 Nilmani, M., Thay, P. K., and Simensen, C. J., "A Comparative Study of Impeller Performance," Light Metals 1992, TMS, Edited by Euel R. Cutshall, p939-946.
32 Simmons, S., and Frank, R., "SNIF Aluminum In-line Refining," Aluminum Metal Treatment & Casting, Edited by Nilmani, M., TMS, 1993, p105-115.
33 Davis, R., and Dokken, R. N., "Product Quality Improvements Through In-line Refining with SNIF," Light Metals 1987, TMS, Edited by R. D. Zabreznik, p711-716.
34 Hampton, D. T., Moors, A. W. and Tessandori, J. L., "Review of Operation and Performance of the Rapid Degassing Equipment for Molten Aluminum," Light Metals 1991, TMS, Edited by Elwin L. Rooy, p1159-1163.
35 Walker, G. P., Zeliznak, T. A., and Sibley, S. R., "Practical Degassing With The R. D. U.," Light Metals 1989, Edited by Paul G. Campbell, TMS, 1988, p777-782.
36 Snow, G., Pattle, D., and Walker, G., "R. D. U. -- An Efficient Degassing System for the Aluminum Cast House," Light Metals 1987, TMS, Edited by R. D. Zabreznik, p717-727.
37 Pendersen, T, "Refining Efficiency on Hydrogen, Alkaline Metals and Inclusions in the Hydro Metal Refining System," Light Metals 1991, TMS, Edited by Elwin L. Rooy, p1063-1067.
38 Aarflot, A. O., and Rasch, B., "The Development Process of a New In-line 3 Rotor Metal Refining Unit," Light Metals 1995, TMS, Edited by J. Evans, p1207-1214.
39 Myrbostad, E., Pedersen, T., Venås, K., and Johansen, S. T., "The ÅSV Inline System for Refining of Aluminum," Light Metals 1986, Edited by R. E. Miller, p861-866.
40 Bildstein, J., and Ventre, I., "Alpur Technology -- Present And Future," Light Metals 1990, Edited by Christian M. Bickert, TMS, 1990, p755-763.
41 Hicter, JM. H., "Alpur™ Refining Process," Light Metals 1983, Edited by E. M. Adkins, p1005-1022.
42 Ohno, Y., Hampton, D. T., and Moors, A. W., "The GBF Rotary for Total Aluminum Refining," Light Metals 1993, TMS, Edited by Subodh K. Das, p915-921.
43 Chin, E. J., Celik, C., Hayes, P., Bouchard, P., and Larouche, G., "GIFS -- A Noval Approach to In-line Treatment of Aluminum," Light Metals 1994, TMS, Edited by U. Mannweiler, p929-936.
44 Waite, P, and Thiffault, R., "The Alcan Compact Degasser: A Trough-Based Aluminum Treatment Process. Part I: Metallurgical Principles

and Performance," Light Metals 1996, Edited by Wayne Hale, p1001-1005.
45 Lavoie, S., "The Alcan Compact Degasser: A Trough-Based Aluminum Treatment Process. Part I: Equipment Description and Plant Experience," Light Metals 1996, Edited by Wayne Hale, p1007-1010.
46 Dumont, R., Litalien, M., and Waite, P., "The ALCAN Filter Degasser: A New In-line Metal Treatment Technology," Light Metals 1992, TMS, Edited by Euel R. Cutshall, p1077-1084.
47 Modern Casting, Feb., 1996, Vol. 86, No. 2, p70.
48 English, C. J., and Rogers, D. B., "The Heated MINT III E," Light Metals 1991, TMS, Edited by Elwin L. Rooy, p1165-1169.
49 Heamon, M. L., and Grimm, D. R., "Utilization of the MINT III System and the Electromagnetic Casting Process in the Production of 3004 Alloy Can Body and 1145 Alloy Fine Gauge Foil Stock," Light Metals 1988, Edited by Larry G. Boxall, p349-357.

1.2 Development of a Statistically Optimized Method for the Reduced Pressure Test

Development of a Statistically Optimized Test Method for the Reduced Pressure Test

L. Parmenter
D. Apelian
Worcester Polytechnic Institute
Worcester, Massachusetts
F. Jensen
Palmer Foundry, Inc.
Palmer, Massachusetts

ABSTRACT

The reduced pressure test (RPT) is an inexpensive, foundry floor test that allows the metalcaster to qualitatively assess the cleanliness of a batch of molten aluminum, allowing corrective action to be pursued before defects occur and decreasing the amount of time and money spent on castings with irreparable defects. This study examined various effects: the time elapsed before the sample is placed in the vacuum chamber, the chamber environment, vacuum interruptions, sampling turbulence, crucible preheating, vibration, solidification rate, solidification pressure, sample type, sample size and filtering of the RPT sample. We also examined the reliability of several RPT sample density evaluation methods, including specific gravity measurements, bulk density measurements and comparisons of a sample cross section with classification guides.

The knowledge gained through this comprehensive study of the factors affecting RPT results during sample collection and sample evaluation has been compiled into an optimized test method. We recommend that the prescribed methodology be considered as an industry standard, giving both manufacturers and researchers confidence in the output of the RPT test.

BACKGROUND

Hydrogen in Aluminum Alloy Melts

Hydrogen is the only gas that is appreciably soluble in aluminum and its alloys.[1–8] The variation of hydrogen solubility with temperature in pure aluminum is shown in Fig. 1.[8] Hydrogen gas results from the dissociation of water vapor.[1,3–5] Water vapor may be readily found in the atmosphere, especially on hot and humid days. Due to the presence of water vapor in the atmosphere, a certain level of hydrogen will always enter the melt during melting, transferring and other metal processing steps. Water may also be found on improperly dried charge materials, refractories and foundry tools.

Gas porosity is known to be detrimental to tensile strength, elongation and fatigue strength in aluminum and its alloys.[1,5,8,9] Depending on cooling rate and alloy composition, hydrogen blisters, as well as porosity, decrease resistance to corrosion and crack propagation. Gas porosity can also result in poor surface finish in machined or polished parts.

The Reduced Pressure Test

One of the most commonly used methods for evaluating melt cleanliness in the metalcasting industry is the reduced pressure test (RPT), which is also known as the vacuum density test (VDT), the vacuum solidification test (VST) and the Straube-Pfeiffer Test.[3–5] In the RPT, a small sample of molten aluminum, usually between 100 and 200 grams, is taken from the melt in a metal or ceramic crucible and placed under vacuum.[10]

The sample shown in Fig. 2a is a typical RPT sample, solidified in a simple cup, notched to control sample volume. This type of RPT sample will hereafter be referred to as an "open top" sample. It has been suggested that a riser be added to the sample to eliminate the confounding effects of shrinkage.[3,4] Because the core that forms the riser also determines the size of the sample, a risered sample, such as that shown in Fig. 2b, will hereafter be referred to as a "constant volume" sample.

The absolute pressure in the vacuum chamber is usually between 1 and 100 mm Hg.[5,6] A typical test apparatus schematic is shown in Fig. 3. By reducing the pressure over the sample during solidification, hydrogen bubble nucleation and growth is enhanced, which allows detection of low levels of hydrogen, with a small sample.[5] This enhanced hydrogen bubble formation is due to the decrease in hydrogen solubility with decreasing pressure, according to the law of mass action, given by Equation 1.[8] In its current form, however, the RPT is truly a test for overall melt cleanliness, which is comprised of both oxide/inclusion content and hydrogen content.

$$S = (f \cdot H) / \sqrt{P} \qquad (1)$$

where S = solubility of hydrogen gas in the melt ($cm^3/100$ g)
f = activity coefficient of hydrogen
H = amount of hydrogen gas in the melt ($cm^3/100$ g)
P = pressure of hydrogen vapor over the melt (atm)

Because there are many test parameters that dramatically affect the results of the RPT, the accuracy of the RPT depends highly on the consistent and accurate adherence to a test protocol.[5] Although the RPT has been widely used throughout the aluminum casting industry for approximately 50 years, there has never been a standardization of the test protocol. As a result, each foundry established their own test procedure and a related cutoff point for acceptable metal. To date, it has been highly unreliable to compare RPT results obtained from different facilities.

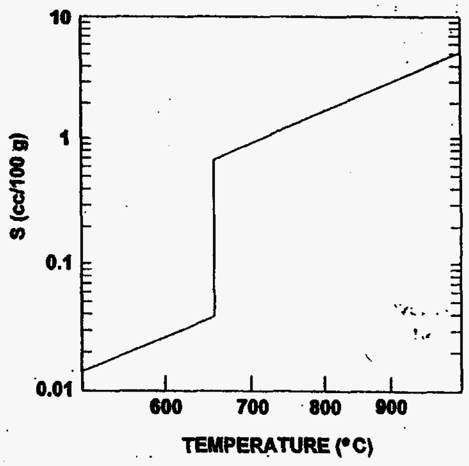

Fig. 1. Solubility of hydrogen in pure aluminum.

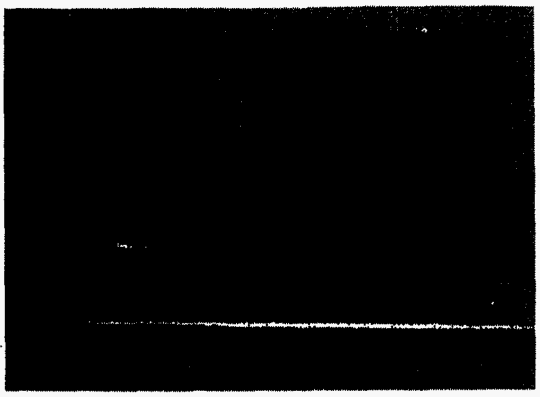

Fig. 2. Typical RPT samples: (a) open top; (b) constant volume.

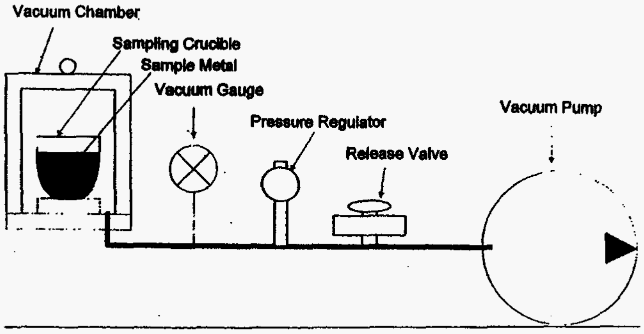

Fig. 3. Typical RPT equipment schematic.

Table 1.
Water Bath Temperature Compensation

Water Temperature (°C)	Water Density (g/cm^3)
$0 \le T \le 7.5$	1.0000
$7.5 < T \le 12.5$	0.9997
$12.5 < T \le 17.5$	0.9991
$17.5 < T \le 25$	0.9982
$25 < T \le 35$	0.9957
$35 < T \le 45$	0.9922
$45 < T \le 55$	0.9881

(adapted from ref. 17)

Although correlation curves between RPT results and Telegas measurements have been developed, these curves are based on a specific test protocol, which has only been partially optimized and may be incomplete.[1,3,4] The R^2 correlation coefficients of these curves are typically between 0.7 and 0.8, indicating that further refinement of the test protocol may be needed. If metalcasters are to use correlation curves to turn RPT results into quantitative hydrogen measurements, it is first necessary to optimize the variables in the RPT procedure and develop correlation curves based on the resulting standard test method.

It is a given that hydrogen and the level of inclusions in the melt are the main two factors that will determine RPT readings. However, for the same level of these two factors, different RPT readings are often obtained. This points to the need for establishing standard procedures. In this work we focused on the variables that may effect RPT results during sampling, such as: sample size, time from sampling to vacuum, vacuum chamber environment, vacuum interruption, solidification rate, crucible preheating, solidification pressure, use of a riser, sampling turbulence, vibration and filtering of the RPT sample.[1–6,11–16]

Density Evaluation Methods

The density of an RPT sample may be determined by weighing the sample in air, then weighing the sample suspended in water.[1] According to Archimedes' Principle, the specific gravity of the sample may then be calculated according to Equation 2:

$$SG_{RPT} = m_{air} / (m_{air} - m_{water}) \qquad (2)$$

where SG_{RPT} = RPT sample specific gravity
m_{air} = mass of sample in air (g)
m_{water} = mass of sample in water (g)

There are some subtleties in this calculation that are frequently overlooked by foundrymen using this evaluation method. Although the scale is usually zeroed before the measurement in air with the weighing jig suspended from the scale, the scale is usually not rezeroed with the weighing jig submersed in water prior to the measurement in water. To truly measure the weight of the sample in water, it may be necessary to perform this second zeroing or compensate for the influence of the basket, as indicated by Equation 3:

$$SG_{RPT} = m_{air} / (m_{air} - m_{water} - c_B) \qquad (3)$$

where c_B = basket compensation factor (g).

The specific gravity of the sample is frequently thought of as equivalent to its density, since the density of water is approximately 1 g/cm^3.[1] However, the density of water changes by about 2% from 40–100F, and is closest to 1 g/cm^3 at 0C (32F).[1,17] It has been suggested that the temperature of the water bath should be regulated, although it seems that measuring and compensating for the naturally occurring temperature should be equally effective (see Eq. 4). It has also been suggested that the water bath should be comprised of frequently changed distilled water to reduce the effects of suspended solids on the water density.

$$d_{RPT} = m_{air} c_{WT} / (m_{air} - m_{water} - c_B) \qquad (4)$$

where d_{RPT} = RPT sample density (g/cm^3)
c_{WT} = water temperature compensation factor or water density (g/cm^3) (see Table 1)

The density of an RPT sample may also be determined by using the bulk density method.[1] First, the sample is weighed. Subsequently, the sample is placed in a known volume of water, and the volume of displaced water is measured. The density may then be calculated as described in Equation 5:

$$d_{RPT} = m_{RPT} / v_{RPT} \qquad (5)$$

where d_{RPT} = RPT sample density (g/cm^3)
m_{RPT} = mass of RPT sample (g)
v_{RPT} = RPT sample volume (ml or cm^3)

For an open top sample, the volume of displaced water must be measured for each sample because the volume of the open top sample varies significantly, even when the side of the sampling crucible is notched to control the sample size. However, for a constant volume sample, the sample volume can be assumed constant, once the volume of the sampling crucible is known.[3,4]

The density of an RPT sample can also be evaluated by sectioning the sample and comparing the sectioned surface to an evaluation guide that shows photographs of RPT samples of known density, which have been sectioned. Stahl Specialty provides examples of such comparison guides with their Gas Tech II RPT tester (Fig. 4).[18]

The sectioned surface can be examined in the as-cut condition, but many pores may be undetectable because of smearing that occurs during cutting. Some foundrymen grind the sectioned surface prior to examination, in an attempt to reveal some of these smeared pores.[1,5] It has also been suggested that a light sandblasting after grinding may further alleviate the smearing problem.[18] It may also be important that proper lighting conditions exist during the examination of sectioned surfaces.

Table 2.
Summary of Statistical Terms

Term	Full Name	Range	Desired Value/Interpretation
GR&R	Gauge Repeatability and Reproducibility	---	1. Study performed to evaluate nondestructive measurement systems 2. Not valid for destructive measurement systems
MSV	Measurement Systems Variance	---	Study performed to evaluate either destructive or nondestructive measurement systems
%EV	Equipment Variation	>0	Low value = more repeatable ie. Less variation in measurements taken by one person
%AV	Appraiser Variation	>0	Low value = more reproducible ie. Less variation in measurements taken by different people
%PV	Part Variation	>0	Low value = more consistent samples ie. characteristic being measured has less variation
%GR&R	Gauge Repeatability and Reproducibility	>0	1. %GR&R<10 to use measurement system quantitatively without further refinement 2. 10<%GR&R<30 indicates measurement system may be used quantitatively after further refinement 3. %GR&R>30 measurement system should be limited to qualitative use
%MSV	Measurement Systems Variance	>0	1. %MSV<60 to use measurement system quantitatively without further refinement 2. 60<%MSV<100 indicates measurement system may be used quantitatively after further refinement 3. %MSV>100 measurement system should be limited to qualitative use
R^2	R Squared	$0<R^2<1$	High value = accurate measurement system ie. Provides good correlation to characteristic as measured by an independent method
S/N	Signal to Noise Ratio	>0	High value = more repeatable ie. Less variation in measurements
Sig/Conf	Significance and Confidence	-- or >90%	1. If value reported, indicates factor to be significant. 2. Magnitude indicates degree of confidence that factor is significant. 3. Only values >90% reported, otherwise -- indicates significance was not shown with greater than 90% confidence.
% C	Percent Contribution	0<%C< 100	1. Indicates relative strength of a significant factor or error term. 2. High value = strong effect

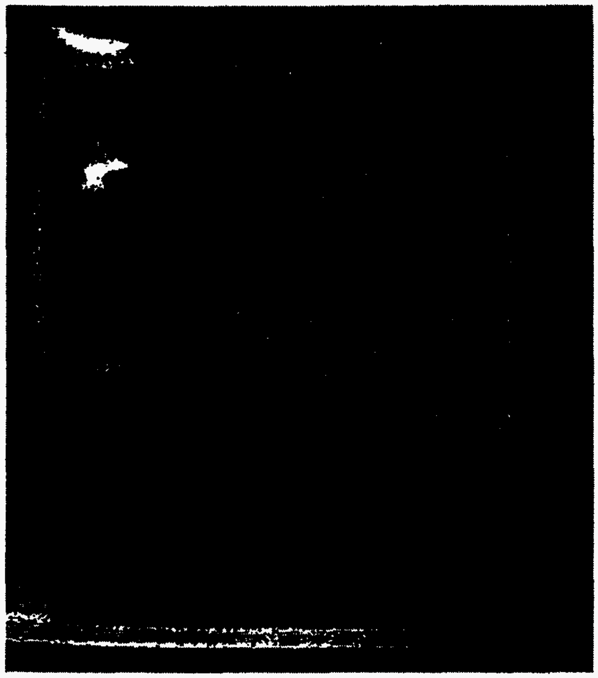

Fig. 4. Comparison guide for evaluating a sectioned RPT sample.

Evaluating a Test Method

There are several statistical tools that may be used to evaluate the robustness of a test method. A summary of the statistical tools and terms used in this study is presented in Table 2.

One method of quantifying the repeatability and reproducibility of a nondestructive measurement system is known as the Gage Repeatability and Reproducibility (GR&R) method.[19,20] To perform a GR&R study, multiple samples are measured multiple times by multiple operators. After performing statistical manipulations on the results for each sample and by each operator, an overall measurement called %GR&R is obtained.

A value of 10% or less indicates that the measurement system exhibits an acceptable level of precision for the particular measurement used for the study. A value of 10–30% indicates that the measurement system is viable, but any changes that could reduce the variability of the measurement system should be investigated. A value greater than 30% indicates that the measurement system is not suitable for this particular application.

It is often overlooked that the GR&R method is limited to use with nondestructive tests. A similar test method called the measurement systems variance (MSV) method has recently been developed for use with either destructive or nondestructive tests.[20] The data collection for an MSV study is identical to that performed for a GR&R study. However, since the test method was designed for the possibility of a destructive test in which a measurement cannot be repeated multiple times on the same sample, "identical" samples are used to obtain the repeated measurements.

The statistical manipulations are very similar to those performed for a GR&R study, producing an overall measurement called %MSV. The major difference between a GR&R study and an MSV study is that, in an MSV study, the data analysis also includes examination of the variation inherent in the so called "identical" samples, which changes the range of acceptable results. A value of 60% or less indicates an acceptable measurement system; 60–100% indicates a viable measurement system; greater than 100% indicates that the measurement system is not suitable.

Signal-to-noise ratios (S/N) are an excellent method for examining the effect of various factors on the repeatability of a measurement.[21,22] S/N values are calculated by manipulating the standard deviation of a set of measurements. Higher values of S/N indicate a lower standard deviation, which, in turn, indicates better repeatability.

It has been demonstrated that RPT densities and hydrogen gas content measured by the recirculating gas method have a reasonably linear relationship.[3,4] It has also been shown that RPT densities and casting porosity have a reasonably linear relationship.[16] This is convenient, since correlation curves for linearly related variables can be developed using linear regression analysis.[21]

R^2, the square of the correlation coefficient, can then also be calculated for each correlation curve, to determine the strength of the linear association between the two variables. The value of R^2 can then be used as an indicator of the accuracy of one variable, such as the RPT, as a predictor of the other variable, such as hydrogen gas content or casting porosity. A value of R^2 close to 1 indicates a strong correlation, and therefore high accuracy, whereas a value of R^2 close to 0 indicates a weak correlation, and therefore very poor accuracy.

A more detailed discussion of these concepts may be found in most fundamental statistics books.[19–23]

EXPERIMENTAL PROCEDURE

All of the aluminum alloy melts tested in this study were prepared from 356 at Palmer Foundry, Inc. of Palmer, Massachusetts. These melts contained up to 30% remelted gates and risers, depending on the daily production schedule, quality requirements and availability of returns. No silicon modification agents, such as sodium or strontium, were added to the melts. All tests were also performed prior to any grain-refiner additions. These melts were degassed to various degrees, depending on the desired gas level for each experiment. Degassing was performed with a gas mixture of 90% argon and 10% chlorine delivered through a portable, air-powered rotary impeller degassing unit.[24]

A test casting with wall thickness varying from 1/2 in. to 2 in. was used to evaluate the amount of porosity that could be seen in a typical casting (Fig. 5). No filters were used in the gating system. Samples measuring approximately 2x2x1/2 in. were cut from the drag surface of the 2-in. wall thickness area of the test castings. These samples were then evaluated for percent porosity by performing Archimedes' Principle measurements, compensated for water bath temperature and basket weight, and using a theoretical density of 2.68 g/cm^3 for 356. Each sample was evaluated three times, and the average of these three readings was reported as the percent porosity.

Hydrogen measurements were performed using an Alscan F.

All RPT samples were collected in a Stahl Specialty Gas Tech II. An APG-M-NW25-SS Active Pirani Gauge was used to monitor absolute pressure in the vacuum chamber rather than using the standard Gas Tech II gauge, which measures relative pressure.

Experimentation was carried out in three phases. Phase One examined the various RPT density evaluation methods. A summary of the evaluation methods and the variations investigated is shown in Table 3.

In Phase Two, the Taguchi Method was used to evaluate the effects of 11 factors and selected interactions on the repeatability and accuracy of the RPT. These factors and their levels are summarized in Table 4. The selected interactions are summarized in Table 5. These factors and interactions were broken into the two matrices described in Tables 6 and 7.

In Phase Three, a confirmation study was performed to evaluate the validity of the results of Phases One and Two.

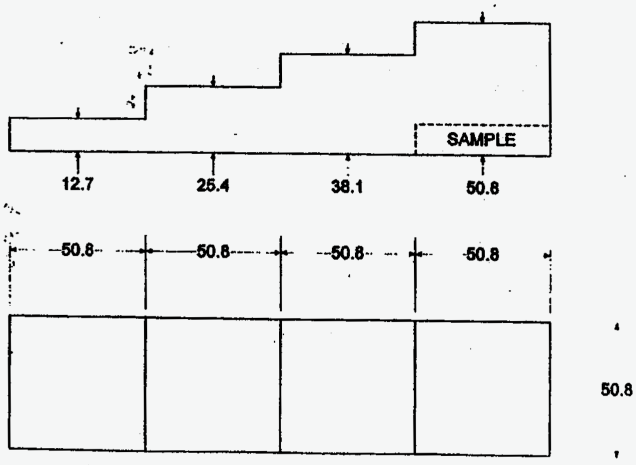

Fig. 5. Test casting configuration (dimensions in mm).

Table 3.
Summary of RPT Density Evaluation Variations

Methods	Factors	Factor Level 1	Factor Level 2
Archimedes Principal	Water bath cleanliness	dirty	clean
Bulk Density • Open Top • Constant Volume	No factors Volume assessment	assumed constant	measured
Evaluation of Sectioned Surface	Grinding to 240 grit 1.75x magnifier lamp	without without	with with

Table 4.
RPT Sampling Factors

Factors	Factor Level 1	Factor Level 2
A: Time to chamber	15 sec	30 sec
B: Chamber environment	preheated	cold
C: Vacuum interruption	without	with
D: Sampling turbulence	low	high
E: Crucible preheating	with	without
F: Vibration	low	high
G: Solidification rate	refractory disc	steel chill
H: Solidification pressure	100 mm Hg	5 mm Hg
I: Sample type	open top	constant volume
J: Sample size	100 g	200 g
K: RPT sample filtering	no filter	15 ppi

Table 5.
Selected Interactions of RPT Sampling Factors

Factors	Description
A x B	Time to chamber x Chamber environment
F x G	Vibration x Solidification rate
F x H	Vibration x Solidification pressure
F x I	Vibration x Sample type
G x H	Solidification rate x Solidification pressure
G x I	Solidification rate x Sample type
G x J	Solidification rate x Sample size
H x I	Solidification pressure x Sample type
H x J	Solidification pressure x Sample size
I x J	Sample type x Sample size

Table 6.
L8 Matrix One of Phase Two

	Factor						
Exp. #	A	B	A x B	C	D	E	J
1	1	1	1	1	1	1	1
2	1	1	1	2	2	2	2
3	1	2	2	1	1	2	2
4	1	2	2	2	2	1	1
5	2	1	2	1	2	1	2
6	2	1	2	2	1	2	1
7	2	2	1	1	2	2	1
8	2	2	1	2	1	1	2

Table 7.
L16 Matrix Two of Phase Three

	Factor														
Exp. #	F	G	F x G	H	F x H	G x H	I x J	I	F x I	G x I	H x J	H x I	G x J	K	J
9	1	1	1	1	1	1	1	1	1	1	1	1	1	1	1
10	1	1	1	1	1	1	1	2	2	2	2	2	2	2	2
11	1	1	1	2	2	2	2	1	1	1	1	2	2	2	2
12	1	1	1	2	2	2	2	2	2	2	2	1	1	1	1
13	1	2	2	1	1	2	2	1	1	2	2	1	1	2	2
14	1	2	2	1	1	2	2	2	2	1	1	2	2	1	1
15	1	2	2	2	2	1	1	1	1	2	2	2	2	1	1
16	1	2	2	2	2	1	1	2	2	1	1	1	1	2	2
17	2	1	2	1	2	1	2	1	2	1	2	1	2	1	2
18	2	1	2	1	2	1	2	2	1	2	1	2	1	2	1
19	2	1	2	2	1	2	1	1	2	1	2	2	1	2	1
20	2	1	2	2	1	2	1	2	1	2	1	1	2	1	2
21	2	2	1	1	2	2	1	1	2	2	1	1	2	2	1
22	2	2	1	1	2	2	1	2	1	1	2	2	1	1	2
23	2	2	1	2	1	1	2	1	2	2	1	2	1	1	2
24	2	2	1	2	1	1	2	2	1	1	2	1	2	2	1

In Phase One and Matrix One of Phase One, the standard Gas Tech II vacuum pump was used to achieve an absolute pressure of 100 mm in the vacuum chamber. In Matrix Two of Phase One, a Rietschle VGC-4 vacuum pump with a single phase motor was used to achieve an absolute pressure of 5 mm in the vacuum chamber, because the standard Gas Tech II vacuum pump was not capable of achieving this vacuum level. The Rietschle vacuum pump was also used to achieve an absolute pressure of 100 mm in the vacuum chamber, which is within the operating range of the Gas Tech II vacuum pump, to avoid confounding the effects of a change in absolute pressure with the effects of a change in pumping rate.

All samples were collected in 08-00050C 100-ml steel crucibles from Fisher Scientific. These cups were notched 3.0 cm from the top for 100-g open top samples and 1.65 cm from the top for 200-g open top samples. These cups were turned down on a lathe 3.0 cm from the top for 100-g constant volume samples and 1.65 cm from the top for 200-g constant volume samples.

The cups were held in the melt until they were cherry red, when crucible preheating was desired. When crucible preheating was not desired, the melt was skimmed with an extra cup and the sample cup was only dipped into the melt long enough to collect the sample.

A CO_2 core was used to create the riser on constant volume samples (Figs. 6 and 7). These cores were baked for one hour at 177C (350F) to eliminate any binding agents that could gas off at the high temperatures encountered during sample collection. A clamping rig was used to allow the collection of constant volume samples with minimal turbulence (Fig. 7). High sampling turbulence was created in both open top and constant volume samples by pouring the RPT sample from a height of approximately 3 to 4 inches.

In both Phase One and Matrix One of Phase Two, a rubber vibration damping pad was placed underneath the RPT tester and the sample platform (refractory disk or steel chill) inside the chamber, in an attempt to achieve low vibration. However, vibration ripples were still visible on the surface of molten samples, indicating that low vibration had not been achieved. In Matrix Two of Phase Two, low vibration was achieved by pulling vacuum on the chamber with an isolated Rietschle VGC-4 vacuum pump located approximately 3 feet from the Gas Tech II, and using the damping pads described previously. When high vibration was desired, the damping pads were removed and the Gas Tech II pump was run as a vibration source. The vacuum chamber was still pumped down using the isolated Rietschle vacuum pump, so that the effects of a change in vibration level would not be confounded with the effects of a change in pumping rate.

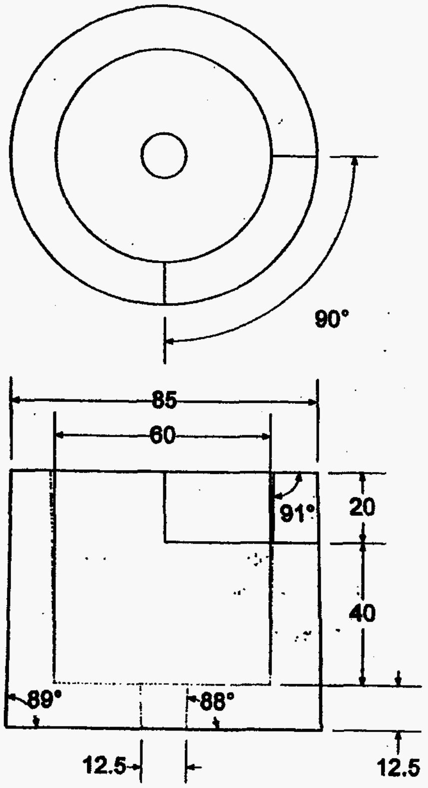

Fig. 6. Schematic of CO_2 core for creating riser on constant volume samples (dimensions in mm).

A throw-away sample was solidified in the RPT tester prior to experimentation when a preheated vacuum chamber was desired. Four different chamber covers were used to allow the use of a cool chamber cover when a cold vacuum chamber was desired.

The refractory disc was replaced with a steel disc when a higher solidification rate was desired.

When filtered metal was desired, the RPT sample was taken by dipping a Dypur filtered pouring cup into the melt and letting the sample pass through the filter into the RPT sampling crucible.

Phase One: Sample Evaluation Methods

Five melts were prepared, then degassed to various degrees to obtain melts that represented the range of melt cleanliness encountered during production at Palmer Foundry. A hydrogen reading, a 100-g open top RPT sample, a 100-g constant volume RPT sample and a test casting were collected from each of these melts. Both RPT samples were collected with minimal turbulence and placed in the vacuum chamber within approximately 15 seconds. The sample was solidified on the standard refractory disc platform under an absolute pressure of 100 mm Hg. The metal sampled was not filtered prior to testing.

The density of each RPT sample was then repeatedly determined by several RPT sample evaluation methods, to compare these sample evaluation methods for GR&R and accuracy. Two operators measured each of the five samples three times for each experiment. A summary of the evaluation methods and the variations investigated is shown in Table 3.

Fig. 7. Riser clamped to 200-g constant volume collection cup.

The GR&R and accuracy of evaluation open top samples by Archimedes' Principle using dirty water was examined, using water that had been sitting in a bucket on the foundry floor collecting dirt long enough to become too murky to see through. The GR&R and accuracy of evaluation of open top and constant volume samples by Archimedes' Principle, using clean water, was examined using fresh tap water.

The GR&R and accuracy of evaluation by the Bulk Density Method with a measured sample volume was examined for both open top and constant volume samples. The GR&R and accuracy of evaluation of 100-g (nominal) constant volume samples by the Bulk Density Method with an assumed volume of 40 cm^3 was also investigated.

The GR&R and accuracy of evaluation of open top samples by the Visual Examination Method was investigated with as-cut samples evaluated on the foundry floor, with as-cut samples under a 1.75X magnifier lamp, with 240-grit ground samples on the foundry floor, and with 240-grit ground samples under a 1.75X magnifier lamp. The GR&R and accuracy of evaluation of constant volume samples by the Visual Examination Method was investigated with 240-grit ground samples under a 1.75X magnifier lamp.

After these results had been analyzed, the GR&R and accuracy of evaluation of open top and constant volume samples under a 1.75X magnifier lamp after a 240-grit grinding operation and sandblasting was also investigated.

Phase Two: Sample Gathering Variables

The Taguchi Method was used to evaluate the effects of 11 factors and selected interactions on the repeatability and accuracy of the RPT. Each of these factors was tested at two levels representing the possible extremes of each factor. These factors and their levels are summarized in Table 4. The selected interactions are summarized in Table 5. These factors and interactions were broken into the two matrices described in Tables 6 and 7.

To evaluate the effects of the Matrix One variables and interactions on the accuracy of the RPT as a hydrogen detection method, 16 melts were prepared over the course of three months. The eight experiments in Table 6 describe the RPT sampling conditions for each of the 16 melts, with each set of experimental conditions occurring twice. The preparation and sampling order of the 16 melts was randomized to minimize the effects of any time-related bias. The Matrix Two RPT sampling variables were all held at Level 1 for all Matrix One experiments.

For each melt, four RPT samples, test castings and Alscan readings were obtained. The first RPT sample, test casting and Alscan reading were taken from the melt, prior to any degassing. The melt was then degassed for five minutes and skimmed before the next RPT sample, test casting and Alscan reading were obtained. This degassing-sampling procedure continued until the melt had been degassed for a total of 15 minutes and four sets of RPT samples, test castings and Alscan readings had been obtained.

The RPT samples were evaluated using Archimedes' Principle with water, and fully compensated for the basket and water bath temperature.

A linear regression analysis of these four RPT and hydrogen content data sets was then performed using Excel V5.0. Hydrogen content in ml/100 g was chosen as the y-series and RPT density in g/cm^3 was chosen as the x-series. The R^2 statistic calculated during the regression analysis was then used as the data value in Matrix One, so that analysis of variance (ANOVA) of this Taguchi matrix would determine the influence of the factors and interaction of Matrix One on the accuracy of the RPT as a hydrogen content measurement.

Similar to the linear regression described earlier, a linear regression analysis was performed with area percent porosity in a 2-in. thick wall as the y-series and RPT density as the x-series. The R^2 statistics from this regression analysis were then used as the data value in Matrix One, so that ANOVA of this matrix would now determine the influence of the factors and interaction of Matrix One on the accuracy of the RPT as a predictor of area percent porosity in a 2-in. thick wall.

To evaluate the effects of the Matrix One variables and interactions (see Tables 4–6) on the repeatability of the RPT, two melts were prepared on consecutive days to achieve two replicates for each experiment needed for Matrix One. In an attempt to minimize the fluctuation of the hydrogen content of these melts throughout the course of the day, both melts were tested without any degassing and the temperature of these melts was held between 1335 and 1355F.

Eight RPT samples were taken from each melt, with the RPT sampling conditions described in Table 6 for Matrix One. All Matrix Two sampling variables were held at Level 1. The eight sets of RPT sampling conditions were randomized to minimize the effects of any time-related bias. This sampling procedure was repeated four times on both of the melts, with a different random order of sampling conditions for each set of eight samples. This resulted in two replicates of four RPT samples for each of the eight sets of RPT sampling conditions, described in Table 6 for Matrix One.

The RPT samples were evaluated using Archimedes' Principle with water, and fully compensated for the basket and water bath temperature.

Each of these sets of four RPT density values was then used to calculate an S/N ratio according to Equation 6. Each of these S/N values was then used as the data value in Matrix One, so that ANOVA of this Taguchi matrix would determine the influence of the factors and interaction of Matrix One on the repeatability of the RPT.

$$S / N = -20 \log S_e \qquad (6)$$

where S/N = signal-to-noise ratio
S_e = standard deviation of the four RPT densities within a trial

The data collected for the repeatability investigation was also used to determine the influence of the Matrix One factors and interaction on the density value obtained by the RPT. The density values of two consecutive sets of eight RPT samples were used as the data values in Matrix One, so that ANOVA of this Taguchi matrix would determine the influence of the factors and interactions of Matrix One on the density value obtained by the RPT. This analysis was performed on all of the consecutive pairs of eight RPT samples, and the analysis with the lowest error contribution was reported.

The procedure for evaluating the effects of the Matrix Two factors and interactions on the accuracy of the RPT as a hydrogen content measurement and as a porosity predictor was essentially the same as those used to evaluate the effects of the Matrix One factors and interaction. The only difference was that 32 melts were prepared over the course of three months so that each of the 16 experimental conditions described in Table 7 occurred twice. The Matrix One factors and interaction were held at their optimized levels, which were determined by the results of the Matrix One experiments.

The procedure for evaluating the effects of the Matrix Two factors and interactions on the repeatability and density value of the RPT was also essentially the same as those used to evaluate the effects of the Matrix One factors and interaction. The only difference was that there were 16 different sets of RPT sampling conditions for Matrix Two, as described in Table 7, compared to the eight sets of RPT sampling conditions described in Table 6 for Matrix One. The Matrix One factors and interaction were held at their optimized levels, which were determined by the results of the Matrix One experiments.

Phase Three: Confirmation Experiments

To evaluate the validity of the results of Phase Two, a confirmation study was performed. Six melts were prepared over the course of three days. Of these six melts, two had not been degassed, one had been degassed for 5 minutes, one for 10 minutes and two for 15 minutes. Once the desired degree of degassing had been performed on a melt, an Alscan reading was taken. The melt was then sampled three times by each of two operators by the three sampling methods described in Table 8. In other words, six RPT samples were taken using Method A, six using Method B and six using Method C, for a total of 18 RPT samples per melt.

Method A represents a completely optimized sampling method based on Phase Two results. Method B represents a more practical version of the optimized test method, which would permit the use of the current high vibration configuration of the GasTech II. Method C represents the worst-case sampling method based on Phase Two results. A test casting was then poured from the melt.

The RPT samples were evaluated using Archimedes' Principle with water, and fully compensated for the basket and water bath temperature.

For each of the three sampling methods, a linear regression analysis of the RPT and hydrogen content data was then performed using Excel V5.0. Hydrogen content in ml/100 g was chosen as the y-series and RPT density in g/cm^3 was chosen as the x-series. Similarly, a linear regression analysis was performed with area percent porosity in a 2-in. thick wall as the y-series and RPT density as the x-series. This allowed for a comparison of the hydrogen and porosity prediction accuracy of each of the RPT sampling methods.

For each of the three sampling methods, an MSV analysis was also performed. This allowed for a comparison of the repeatability and reproducibility of each of the RPT sampling methods.

Table 8.
Phase Three RPT Sampling Methods

Factor	Description	Sampling Method		
		A	B	C
A	Time to chamber	<15 sec	<15 sec	<15 sec
B	Chamber environment	preheated	preheated	cold
C	Vacuum interruption	none	none	none
D	Sampling turbulence	low	low	high
E	Crucible preheating	with	with	without
F	Vibration	low	high	high
G	Solidification rate	refractory disc	refractory disc	refractory disc
H	Solidification pressure	100 mm Hg	100 mm Hg	5 mm Hg
I	Sample type	open top	open top	open top
J	Sample size	100 to 150 g	100 to 150 g	150 to 200 g
K	RPT sample filtering	without	without	without

RESULTS AND DISCUSSION

Phase One

The %GR&R of the variations on Archimedes' Principle for open top samples are shown in Table 9. The hydrogen prediction and porosity prediction accuracy values are given by R^2 (Table 2) and are hereafter represented as H_2 R^2 and 2-in. %P R^2. The values of H_2 R^2 and 2-in. %P R^2 for the variations on Archimedes' Principle for open top samples are shown in Table 10. The results of Student "t" tests performed on the RPT density values generated by each of these variations is shown in Table 11.

The %GR&R of the variations on the Bulk Density Method for open top samples are shown in Table 12. The hydrogen prediction accuracy values (H_2 R^2) and porosity prediction accuracy values (2-in. %P R^2) of the Bulk Density Method for open top samples are shown in Table 13.

Table 9.
GR&R for Variations on Archimedes' Principle to Evaluate Open Top Samples

Experimental conditions	Equipment Variation (%EV)	Appraiser Variation (%AV)	Gauge Repeatability and Reproducibility (%GR&R)
Clean water, whole sample, fully compensated	7.5	7.4	10.5
Dirty water, whole sample, fully compensated	6.8	4.9	8.4
Clean water, *cut sample*, fully compensated	35.7	10.4	37.2
Clean water, whole sample, *incorrect basket compensation*	6.8	8.6	11.0
Clean water, whole sample, *without basket compensation*	7.2	8.5	11.1
Clean water, whole sample, *incorrect temperature compensation*	6.5	9.0	11.1
Clean water, whole sample, *without temperature compensation*	7.1	8.4	11.0

Table 10.
Hydrogen and Porosity Prediction Accuracy for Variations on Archimedes' Principle to Evaluate Open Top Samples

Experimental Conditions	Hydrogen Prediction Accuracy (H_2 R^2)	Porosity Prediction Accuracy (2" %P R^2)
Clean water, whole sample, fully compensated	0.71	0.93
Dirty water, whole sample, fully compensated	0.73	0.93
Clean water, *cut sample*, fully compensated	0.52	0.68
Clean water, whole sample, *incorrect basket compensation*	0.72	0.93
Clean water, whole sample, *without basket compensation*	0.71	0.93
Clean water, whole sample, *incorrect temperature compensation*	0.72	0.93
Clean water, whole sample, *without temperature compensation*	0.72	0.93

Table 11.
Student "t" Test Results for Variations on Archimedes' Principle to Evaluate Open Top Samples

Factor	Confidence Level
No Basket Compensation	99.9%
Incorrect Basket Compensation	90%
No Temperature Compensation	90%
Incorrect Temperature Compensation	99.9%
Dirty Water	–

Table 12.
GR&R for Bulk Density Method to Evaluate Open Top Samples

Experimental conditions	Equipment Variation (%EV)	Appraiser Variation (%AV)	Gauge Repeatability and Reproducibility (%GR&R)
Whole sample, volume measured	91.3	35.6	96.9
Whole sample, volume assumed	0.1	0.3	0.3

Table 13.
Hydrogen and Porosity Prediction Accuracy for Bulk Density Method to Evaluate Open Top Samples

Experimental Conditions	Hydrogen Prediction Accuracy (H_2 R^2)	Porosity Prediction Accuracy (2" %P R^2)
Whole sample, volume measured	0.00	0.00
Whole sample, volume assumed	0.14	0.07

The percent percent Gage R&R (%GR&R) of the variations on evaluation of a sectioned surface for open top samples are shown in Table 14. The hydrogen prediction accuracy values (H_2 R^2) and porosity prediction accuracy values (2-in. %P R^2) of the variations on evaluation of a sectioned surface for open top samples are shown in Table 15.

In summary, open top samples are most repeatably, reproducibly and accurately evaluated by Archimedes' Principle, as long as the sample is not cut. Appropriate basket and water temperature compensation factors will insure that bias is not introduced into the test when the basket is changed or as water bath temperature varies. Water cleanliness was not shown to have any effect on repeatability, reproducibility, accuracy or density values.

The remaining improvements in hydrogen accuracy to reach an R^2 of higher than 0.9 may have to be achieved by optimizing the sampling variables, since the hydrogen accuracy results of all of the reduced pressure test density evaluation method variations fell short of this goal.

Density evaluation of open top samples by the Bulk Density Method was found to be completely unreliable. Density evaluation of open top samples by examination of a sectioned surface was found to be viable when performed on a ground and sandblasted sample under a magnifier light, but was shown to be less reliable than evaluation of an uncut sample by Archimedes' Principle using water temperature and basket compensation.

The %GR&R of Archimedes' Principle, the Bulk Density Method and evaluation of a sectioned surface for constant volume samples are shown in Table 16. The hydrogen prediction accuracy values (H_2 R^2) and porosity prediction accuracy values (2-in. %P R^2) of Archimedes' Principle, the Bulk Density Method and evaluation of a sectioned surface for constant volume samples are shown in Table 17.

Table 14.
GR&R for Variations on Evaluation of Sectioned Surface to Evaluate Open Top Samples

Experimental conditions	Equipment Variation (%EV)	Appraiser Variation (%AV)	Gauge Repeatability and Reproducibility (%GR&R)
As cut, without magnifier light	51.7	40.8	65.9
As cut, *with magnifier light*	38.9	42.3	57.5
Ground to 600 grit, without magnifier light	23.4	17.6	29.3
Ground to 600 grit, with magnifier light	22.3	15.9	27.3
Ground to 600 grit and sandblasted, with magnifier light	22.1	5.8	22.9

Table 15.
Hydrogen and Porosity Prediction Accuracy for Variations on Evaluation of a Sectioned Surface to Evaluate Open Top Samples

Experimental Conditions	Hydrogen Prediction Accuracy (H_2 R^2)	Porosity Prediction Accuracy (2" %P R^2)
As cut, without magnifier light	0.28	0.37
As cut, *with magnifier light*	0.31	0.37
Ground to 600 grit, without magnifier light	0.76	0.60
Ground to 600 grit, with magnifier light	0.78	0.67
Ground to 600 grit and shotblasted, with magnifier light	0.80	0.81

Table 16.
GR&R of Archimedes' Principle, Bulk Density Method and Evaluation of Sectioned Surface for Evaluation of Constant Volume Samples.

Experimental conditions	Equipment Variation (%EV)	Appraiser Variation (%AV)	Gauge Repeatability and Reproducibility (%GR&R)
Archimedes Principle, clean water, whole sample, fully compensated	12.0	1.2	12.1
Bulk Density Method, whole sample, volume assumed	0.8	1.7	1.8
Evaluation of a Sectioned Surface, ground to 600 grit, with magnifier light	26.0	14.5	29.8

Table 17.
Hydrogen and Porosity Prediction of Archimedes' Principle, the Bulk Density Method and Evaluation of Sectioned Surface for Evaluation of Constant Volume Samples.

Experimental Conditions	Hydrogen Prediction Accuracy (H_2 R^2)	Porosity Prediction Accuracy (2" %P R^2)
Archimedes Principle, clean water, whole sample, fully compensated	0.65	0.61
Bulk Density Method, whole sample, volume assumed	0.87	0.61
Evaluation of a Sectioned Surface, ground to 600 grit, with magnifier light	0.77	0.57

The use of an assumed volume with the constant volume samples made the Bulk Density Method the most desirable evaluation method for hydrogen accuracy, indicating that the riser used with the constant volume samples controlled sample volume better than the notch used for volume control of open top samples. The excellent %GR&R and R^2 values indicate that the Bulk Density Method with an assumed volume is the most repeatable, reproducible and accurate method for evaluation of constant volume samples.

Phase Two: Matrix One

The significance, confidence and percent contribution of Matrix One factors on the S/N ratio, hydrogen prediction accuracy, porosity prediction accuracy and RPT density level are shown in Tables 18–21.

The time from sampling to vacuum was found to have a significant effect on the accuracy of the RPT in predicting porosity. Although significance was shown, the relatively low confidence level (90%) and low percent contribution (6%) indicate that the time to vacuum has a weak influence on porosity prediction accuracy compared to the AB interaction and the error term.

The ANOVA revealed that taking about 45 seconds to place the RPT sample in the chamber gave better porosity prediction accuracy compared to placing the RPT sample in the chamber within 15 seconds. This contradicts conventional wisdom, which is that the RPT sample should be placed in the chamber as soon as possible to avoid hydrogen pickup from the atmosphere. It could be argued that 45 seconds to chamber was more representative of the time required to transfer metal from the furnace to the test mold, which would lead to improved porosity accuracy by allowing both the RPT sample and the metal in the hand ladle to be susceptible to hydrogen gains.

It is interesting to note that the time to vacuum was not shown to have a significant effect on the S/N ratio, hydrogen prediction accuracy or RPT density level. The above explanation of the effects of the time to vacuum on porosity accuracy is consistent with an absence of the effect on accuracy of predicting Alscan readings in the furnace, since the hydrogen gain in the RPT sample is occurring after the sampled metal leaves the furnace.

The proposed explanation does, however, seem to be contradicted by the lack of a significant decrease in the RPT density level, since hydrogen pickup in the RPT sample should cause the RPT density level to decrease. This explanation for this apparent contradiction may be that the significance of hydrogen pickup is more easily detected in the R^2 value for hydrogen prediction accuracy than in the RPT density level. At the very least, it has been shown that a slight delay in the transportation of the RPT sample to the vacuum chamber is not detrimental, as previously thought, and may even be slightly beneficial.

The vacuum chamber environment was not shown to have any effect on the S/N ratio, hydrogen prediction accuracy, porosity prediction accuracy or RPT density level.

Vacuum interruption was found to have a significant effect on the porosity prediction accuracy of the RPT. Vacuum interruption was significant with a slightly higher confidence level (95%) and percent contribution (9%) than time to vacuum. The ANOVA indicated that interrupting the vacuum approximately three minutes into the test resulted in a better porosity prediction accuracy than an uninterrupted vacuum.

Vacuum interruption was also found to have a significant effect of the RPT density level. With respect to RPT density level, vacuum interruption was significant with a confidence level of 99% and a percent contribution of 13%. The ANOVA indicated that interrupting the vacuum resulted in a lower RPT density value.

From a purely theoretical point of view, these results suggest that an optimized test method would include interrupting the vacuum approximately three minutes into the sample solidification. However, asking melt supervisors to monitor every RPT sample as it solidifies may not be acceptable in the industrial sector. Instead, an optimized test method might suggest the use of an interrupted vacuum when possible, and provide two sets of hydrogen and porosity correlation curves: one for tests where the vacuum was interrupted and one for tests without vacuum interruption. However, to remain true to the objective of developing a simple optimized test method to be used as an industry standard, it seems wiser and most

Table 18.
Significance, Confidence and Percent Contribution of Matrix One Factors Resulting from ANOVA of S/N Ratios

Factor	Description	S/N Significance and Confidence	S/N Percent Contribution
A	Time from Sampling to Vacuum	–	–
B	Vacuum Chamber Environment	–	–
C	Vacuum Interruption	–	–
D	Sampling Turbulence	97.5 %	27 %
E	Crucible Preheating	95 %	23 %
J	Sample Size	–	–
AB	AxB Interaction	–	–
e	Error	–	40 %

Table 19.
Significance, Confidence and Percent Contribution of Matrix One Factors Resulting from ANOVA of Hydrogen Prediction Accuracy

Factor	Description	H_2 R^2 Significance and Confidence	H_2 R^2 Percent Contribution
A	Time from Sampling to Vacuum	–	–
B	Vacuum Chamber Environment	–	–
C	Vacuum Interruption	–	–
D	Sampling Turbulence	99 %	19 %
E	Crucible Preheating	99 %	25 %
J	Sample Size	–	–
AB	AxB Interaction	99 %	40 %
e	Error	–	14 %

Table 20.
Significance, Confidence and Percent Contribution of Matrix One Factors Resulting from ANOVA of Porosity Prediction Accuracy

Factor	Description	%P R^2 Significance and Confidence	%P R^2 Percent Contribution
A	Time from Sampling to Vacuum	90 %	6 %
B	Vacuum Chamber Environment	–	–
C	Vacuum Interruption	95 %	9 %
D	Sampling Turbulence	95 %	11 %
E	Crucible Preheating	97.5 %	13 %
J	Sample Size	95 %	7 %
AB	AxB Interaction	99 %	38 %
e	Error	–	12 %

Table 21.
Significance, Confidence and Percent Contribution of Matrix One Factors Resulting from ANOVA of RPT Density Levels

Factor	Description	S/N Significance and Confidence	S/N Percent Contribution
A	Time from Sampling to Vacuum	–	–
B	Vacuum Chamber Environment	–	–
C	Vacuum Interruption	99 %	13 %
D	Sampling Turbulence	99 %	49 %
E	Crucible Preheating	99 %	14 %
J	Sample Size	90 %	3 %
AB	AxB Interaction	99 %	12 %
e	Error	–	8 %

pragmatic to suggest that, in all cases, a timer is used to ensure that the vacuum is never prematurely interrupted.

Sampling turbulence was found to have a significant effect on all of the parameters analyzed. The effects of sampling turbulence on the S/N ratio, hydrogen prediction accuracy, porosity prediction accuracy and RPT density level were significant with confidence levels of 97.5%, 99%, 95% and 99%, respectively.

Changes in sampling turbulence accounted for 27% of the variation observed in the S/N ratio. The ANOVA of the S/N ratios revealed that low sampling turbulence improves repeatability. This is most likely explained by the random number and size of oxides that turbulence may have produced in the RPT sample, which then may have resulted in a less repeatable degree of hydrogen bubble nucleation.

Changes in sampling turbulence accounted for 19% and 11% of the variation observed in the hydrogen and porosity accuracy, respectively. The ANOVA of the hydrogen R^2 and porosity R^2 indicate that high sampling turbulence improved accuracy of both hydrogen prediction and porosity prediction. High turbulence may have improved hydrogen accuracy by eliminating the confounding effects of oxide content on the RPT results. In other words, high turbulence may have generated enough oxides so that most of the hydrogen in the RPT sample was able to nucleate and grow as bubbles, regardless of the oxide content in the furnace, thus reducing the sensitivity of the RPT to oxides. High turbulence may have improved porosity accuracy by making the RPT sample more representative of the first metal that splashed down the sprue in the test mold before filling the unfiltered test casting.

The results indicate that there is a tradeoff between repeatability and accuracy when trying to optimize sampling turbulence. This work suggests that two test methods may be needed. For general applications of the RPT where oxide content is thought to be high to moderately low, hydrogen and porosity accuracy may be improved by the ease of hydrogen nucleation, and therefore the RPT could be performed with low sampling turbulence to achieve better repeatability. In applications where oxide content can be measured by an independent test method and is known to be very low, the RPT could be performed with high sampling turbulence to improve the hydrogen sensitivity of the test, with a concomitant sacrifice in repeatability.

Crucible preheating was found to have a significant effect on all of the parameters studied. The effects of crucible preheating on the S/N ratio, hydrogen prediction accuracy, porosity prediction accuracy and RPT density level were significant with confidence levels of 95%, 99%, 97.5% and 99%, respectively. The use of a cold or preheated crucible was responsible for approximately 1/4 of the variation observed in the S/N ratio and hydrogen R^2, and approximately 1/8 of the variation observed in the porosity R^2 and RPT density level. The use of a preheated crucible was found to improve repeatability and accuracy while resulting in a higher RPT density level.

These improvements may have been due to the regulation of a low moisture content in the sample cup's refractory coating. The improvement in porosity accuracy may have also been partly attributable to the similarities between the preheating of a sampling crucible and the preheating performed on the hand ladle prior to pouring each test mold. An optimized test method would include the use of a preheated crucible.

Sample size has a significant effect on the accuracy of porosity prediction and the RPT density level, with a confidence of 95% and 90%, respectively. The percent of variation caused by changes in sample size was low for both porosity accuracy and RPT density level, which indicates that sample size is a weak factor by itself. The ANOVA of porosity accuracy and RPT density level show that a 100-g sample resulted in better porosity prediction accuracy and a slightly higher RPT density level. The effects of sample size and several sample size interactions are studied in more detail in Matrix Two.

The combined effect of time from sampling to vacuum and vacuum chamber environment has the strongest influence on hydrogen and porosity accuracy. This interaction accounted for approximately 40% of the variation encountered in both accuracy analyses. This interaction also had a significant impact on RPT density level, contributing 12% of the variation observed. The ANOVA indicates that an interaction level of A1B1 (less than 15 seconds to a preheated vacuum chamber) and A2B2 (approximately 45 seconds to a cold vacuum chamber) resulted in improved hydrogen and porosity accuracy, as well as a lower RPT density level.

An optimized test method could include either interaction level A1B1 or A2B2. The results discussed above suggest that a longer time to vacuum is preferable in terms of porosity accuracy; accordingly, the interaction should be optimized at level A2B2, which means transporting the RPT sample slowly to a cold chamber. From a practical point of view, however, it is easier to consistently use a preheated chamber than to consistently use a cold chamber, especially when repeated tests must be taken before a melt is approved. Since the time to vacuum had a relatively small effect on the porosity accuracy, the more convenient optimization of level A1B1 is recommended.

Based on the analysis of the Matrix One results, a partially optimized test method was developed and is presented in Table 22. Matrix One factors were then held at their optimized levels for Matrix Two experimentation.

Phase Two: Matrix Two

The significance, confidence and percent contribution of Matrix Two factors on the S/N ratio, hydrogen prediction accuracy, porosity prediction accuracy and RPT density level are shown in Tables 23 through 26.

Vibration was found to have a significant effect on the S/N ratio. The ANOVA indicates that low vibration improves the repeatability of the RPT. This result is expected, since vibration will encourage nucleation of hydrogen bubbles and this will occur unpredictably for uncontrolled vibration. Since all of the commercially available RPT instruments have the vacuum pump mounted on a plate adjacent to the vacuum chamber and would require modification to provide low vibration, the necessity of decoupling the vacuum pump was further investigated in Phase Three. Vibration was not shown to have any effect on hydrogen accuracy, porosity accuracy or RPT density level.

Table 22.
Optimization Results From Matrix One

Factor	Description	Optimized Level
A	Time to vacuum	Less than 15 seconds
B	Chamber environment	Preheated
C	Vacuum interruption	Without
D	Sampling turbulence	RPT as Hydrogen/Oxide Test: Low RPT as Hydrogen Test: High
E	Crucible preheating	With
J	Sample size	See Matrix Two
AB	Interaction of A and B	A1B1

Solidification rate was found to have a significant effect on the S/N ratio and the resultant RPT density level. The ANOVA indicates that a steel chill slightly improves the repeatability of the RPT and increases the density level. It seems that the solidification rate achieved with a steel chill allows the sample to freeze before hydrogen bubbles can form and grow. While this study did not demonstrate a detrimental effect of a steel chill on hydrogen and porosity accuracy, which would be expected according to this explanation, the study performed by Laskowski[16] did show a significant negative impact on hydrogen accuracy. For this reason, the slight improvement in repeatability with a steel chill should be interpreted with caution, and the suggested test method conservatively includes the use of a refractory disc. Solidification rate was not found to have a significant effect on hydrogen or porosity prediction accuracy.

For all of the parameters investigated, solidification pressure was found to have the strongest effect of all of the factors and interactions studied. The ANOVA indicates that using 5 mm Hg improves the hydrogen and porosity accuracy and decreases the density level, but is accompanied by an even more substantial decrease in repeatability. The use of 100 mm Hg is recommended in the optimized test method because the detrimental effect of a higher vacuum on repeatability is so pronounced. The use of an absolute pressure gauge or precise calibration of a relative pressure gauge with a manometer is highly recommended, due to the extreme sensitivity of the test to changes in solidification pressure.

Sample type was found to significantly affect the RPT density level. The ANOVA indicates that the use of a riser results in a higher RPT density. This confirms that providing a riser over the sample diminishes the amount of shrinkage voids in the sample. Sample type was not shown to have any effect on the S/N ratio, hydrogen prediction accuracy or porosity prediction accuracy. These results clearly demonstrate that the use of a riser does not improve the robustness of the RPT, and is therefore not necessary.

Sample size was found to have a significant effect on hydrogen prediction accuracy. The ANOVA indicates that the use of a 200-g sample yields a slightly better hydrogen accuracy. Sample size was not shown to have a significant effect on S/N ratio, porosity prediction or sample size.

At first, the observed effect of sample size in Matrices One and Two experiments may be a bit perplexing and require some elaboration. In Matrix One, sample size was found to affect repeatability, but no influence on accuracy was detected. In Matrix Two, sample size was found to affect accuracy, but no influence on repeatability was detected. Further examination reveals that the target sample size of 100 g was relatively well achieved in both Matrices One and Two. However, the 200-g samples averaged approximately 180 g in Matrix One and approximately 150 g in Matrix Two. This suggests that, when comparing 100-g samples to 180-g samples, 100-g samples are preferable; when comparing 100-g samples and 150-g samples, 150-g samples are preferable. For this reason, the suggested test method includes the use of 100–150-g samples.

Table 23.
Significance, Confidence and Percent Contribution of Matrix Two Factors Resulting from ANOVA of S/N Ratios

Factor	Description	S/N Significance and Confidence	S/N Percent Contribution
F	Vibration	90 %	2 %
G	Solidification Rate	90 %	2 %
H	Solidification Pressure	99 %	82 %
I	Sample Type	–	–
J	Sample Size	–	–
K	RPT Sample Filtering	–	–
FG	FxG Interaction	–	–
FH	FxH Interaction	–	–
FI	FxI Interaction	–	–
GH	GxH Interaction	–	–
GI	GxI Interaction	–	–
GJ	GxJ Interaction	–	–
HI	HxI Interaction	–	–
HJ	HxJ Interaction	–	–
IJ	IxJ Interaction	–	–
e	Error	–	11 %

Table 24.
Significance, Confidence and Percent Contribution of Matrix Two Factors Resulting from ANOVA of Hydrogen Prediction Accuracy

Factor	Description	H_2 R^2 Significance and Confidence	H_2 R^2 Percent Contribution
F	Vibration	–	–
G	Solidification Rate	–	–
H	Solidification Pressure	99 %	20 %
I	Sample Type	–	–
J	Sample Size	90 %	9 %
K	RPT Sample Filtering	–	–
FG	FxG Interaction	–	–
FH	FxH Interaction	–	–
FI	FxI Interaction	–	–
GH	GxH Interaction	–	–
GI	GxI Interaction	–	–
GJ	GxJ Interaction	–	–
HI	HxI Interaction	–	–
HJ	HxJ Interaction.	–	–
IJ	IxJ Interaction	–	–
e	Error	–	51 %

Table 25.
Significance, Confidence and Percent Contribution of Matrix Two Factors Resulting from ANOVA of Porosity Prediction Accuracy

Factor	Description	%P R^2 Significance and Confidence	%P R^2 Percent Contribution
F	Vibration	–	–
G	Solidification Rate	–	–
H	Solidification Pressure	90 %	9 %
I	Sample Type	–	–
J	Sample Size	–	–
K	RPT Sample Filtering	–	–
FG	FxG Interaction	90 %	9 %
FH	FxH Interaction	–	–
FI	FxI Interaction	–	–
GH	GxH Interaction	–	–
GI	GxI Interaction	–	–
GJ	GxJ Interaction	–	–
HI	HxI Interaction	90 %	8 %
HJ	HxJ Interaction	–	–
IJ	IxJ Interaction	–	–
e	Error	–	64 %

Table 26.
Significance, Confidence and Percent Contribution of Matrix Two Factors Resulting from ANOVA of RPT Density Levels

Factor	Description	S/N Significance and Confidence	S/N Percent Contribution
F	Vibration	–	–
G	Solidification Rate	99 %	4 %
H	Solidification Pressure	99 %	53 %
I	Sample Type	99 %	20 %
J	Sample Size	–	–
K	RPT Sample Filtering	99 %	4 %
FG	FxG Interaction	–	–
FH	FxH Interaction	–	–
FI	FxI Interaction	–	–
GH	GxH Interaction	99 %	2 %
GI	GxI Interaction	97.5 %	2 %
GJ	GxJ Interaction	–	–
HI	HxI Interaction	99 %	8 %
HJ	HxJ Interaction	–	–
IJ	IxJ Interaction	–	–
e	Error	–	8 %

Sample filtering was found to significantly affect the RPT density level. The ANOVA indicates that the use of a filter results in a lower RPT density. While it might be expected that a filter would decrease the number of oxides in the sample, and therefore increase the RPT density, there are some possible explanations for this unexpected result. One possibility is that the metal picks up impurities from the filter, such as particulate that has settled out of the air during storage or that is left on the filters during cutting. It may also be that the metal becomes contaminated with oxides again, as it leaves the filter in multiple streams then falls into the sampling crucible. Sample filtering was not shown to have any effect on the S/N ratio, hydrogen prediction accuracy or porosity prediction accuracy.

The interaction of vibration and solidification rate was found to have a significant effect on porosity accuracy. The ANOVA indicates that low vibration and a steel chill yield the best porosity prediction accuracy. This correlates well to the individual results found for vibration and solidification rate. However, due to the concern about Laskowski's results indicating a strong detrimental effect of a steel chill on hydrogen porosity, the suggested test method conservatively includes low vibration and a refractory disc. This interaction was not found to have a significant effect on S/N ratio, hydrogen accuracy or RPT density level.

The solidification rate/solidification pressure interaction was found to significantly affect the RPT density level. The ANOVA indicates that a refractory disc and 5 mm Hg results in the lowest RPT density, and a steel disc and 100 mm Hg results in the highest RPT density. These results indicate that a slower solidification rate combined with a strong vacuum permits hydrogen porosity to form and possibly enter the vacuum degassing stage, while a faster solidification rate combined with a relatively weak vacuum does not allow hydrogen bubbles to evolve. This fits well with the individual observations regarding solidification rate and solidification pressure. This interaction was not shown to have any effect on the S/N ratio, hydrogen prediction accuracy or porosity prediction accuracy.

The solidification rate/sample type interaction was found to significantly affect the RPT density level. The ANOVA indicates that a refractory disc and 100-g sample results in the lowest RPT density, and a steel chill and 200-g results in the highest RPT density. These results indicate that a slow solidification rate and a small sample allow hydrogen porosity to form with vacuum degassing, while a rapid solidification rate and large sample does not permit hydrogen bubbles to form. A slow solidification rate with a large sample gives an intermediate density because vacuum degassing begins to occur. These results correlate well with those seen individually for solidification rate and sample size. This interaction was not shown to have any effect on the S/N ratio, hydrogen prediction accuracy or porosity prediction accuracy.

The interaction of solidification pressure and sample type was found to have a significant effect on porosity accuracy and RPT density level. The ANOVA indicates that the use of 100 mm Hg on a constant volume sample yields a very poor correlation to casting porosity, while any other combination of solidification pressure and sample type provides much better correlation. An open top sample solidified under 5 mm Hg results in the lowest density, while a constant volume sample solidified under 100 mm Hg results in the highest density. This result is expected, since the open top sample will contain more shrink voids and the higher vacuum makes it easier for hydrogen porosity to form. This correlates well to the individual results found for solidification pressure and sample type. The solidification pressure/sample type interaction was not shown to have any significant effect on repeatability or hydrogen prediction accuracy.

The vibration/solidification pressure, vibration/sample type, solidification rate/sample size, solidification pressure/sample size and sample type/sample size interactions were not shown to have any effect on the S/N ratio, hydrogen prediction accuracy, porosity prediction accuracy or RPT density level.

Based on the analysis of the Matrix Two results, a partially optimized test method was developed and is presented in Table 27. The combination of the two partially optimized sampling procedures presented in Tables 22 and 27 with the results of Phase One then becomes the complete suggested test method for the RPT presented in the conclusions.

Phase Three

The results of the MSV study for each of the three sampling methods in Phase Three are shown in Table 28. The optimized sampling procedure derived from Matrix One and Two results, Method A, was found to be the most repeatable and reproducible sampling procedure, with a %MSV of 89. Because the %MSV is between 60 and 100, the RPT with this sampling procedure is a viable quantitative test, but any further possibilities for reducing variability should be investigated.

The variation of the optimized test method excluding the decoupling of the vacuum pump for low vibration, Method B, was found to be slightly less repeatable and reproducible than Method A, with a %MSV of 96. This sampling procedure is just within the cutoff for a viable quantitative test. This confirms that isolating of the pump is a significant improvement on the current standard RPT apparatus design. Although this modification may be performed on an RPT tester in approximately half an hour with a couple of wrenches and a few feet of flexible vacuum hose, it remains to be seen whether this practice will be adopted as an industry standard, since the test is technically in the viable range with the current apparatus design.

The worst-case test method, Method C, does exhibit the worst repeatability and reproducibility of those sampling procedures studied. This confirms the results of Phase Two, and demonstrates that the use of either Method A or B is necessary for the RPT to be a repeatable and reproducible quantitative test.

The results of the hydrogen and porosity prediction accuracy studies for each of the three sampling methods in Phase Three are shown in Table 29. There is not a significant difference between the accuracy of the three sampling methods. This is most likely due to the turbulence repeatability/accuracy tradeoff.

Methods A and B included the use of low sampling turbulence because the Phase Three experiments were designed to validate the suggested test method for a combined hydrogen/oxide test, since this is how most metalcasters intend to use the RPT. This decision was made knowing that low turbulence would greatly improve repeatability with a less substantial sacrifice to accuracy. Method C was designed to be the opposite of all the logic used to develop Methods

Table 27.
Optimization Results From Matrix Two

Factor	Description	Optimized Level
F	Vibration	Low
G	Solidification Rate	Refractory Disc
H	Solidification Pressure	100 mm Hg
I	Sample type	Open Top
J	Sample size	100 to 150 g
FG	Interaction of F and G	F1G1
HI	Interaction of H and I	H1I1

A and B, and therefore included the use of high sampling turbulence, knowing that high turbulence would be significantly detrimental to repeatability while having a slight positive impact on accuracy.

These results indicate that, for Methods A and B, the turbulence related sacrifice in accuracy is balanced by the improvements in accuracy made by optimizing all of the other sampling factors.

The Phase Three confirmation study results confirm that the suggested test method results in an improvement in repeatability and reproducibility while maintaining the same accuracy level. These results also confirm that repeatability is improved significantly by isolating the vacuum pump to reduce vibration, and it is recommended that the test be modified to produce consistent and reproducible results.

CONCLUSIONS

The knowledge gained through this comprehensive study of the factors affecting RPT results during sample collection and sample evaluation is compiled and summarized into the following optimized test method:

1. The RPT sample should be solidified in an RPT such as the Stahl GasTech II. This tester is recommended as a standard, since it is the unit most commonly used by metalcasters today, and it is not known whether the difference in pumping rates in other units will significantly affect the density level obtained in the RPT sample.
2. The base of the vacuum chamber should contain a refractory disc.
3. The vacuum pump of the tester should be removed from the main plate of the tester and reconnected with flexible vacuum hose so that the pump is a few feet away from the vacuum chamber. The pump is adequately isolated if no vibration ripples are visible on the surface of the sample during solidification. It may also be necessary to use a vibration damping pad beneath the main plate of the tester if there are other sources of vibration near the tester.

Based on this work, the following steps are recommended for the RPT operator.

Step 1—Take a thin-walled steel crucible and notch the side wall so that it will hold 100 to 150 g of aluminum. A Fischer Scientific catalog # 08-00050C 100-ml crucible, cut down 25 to 30 mm from the top, is recommended as a standard, as the effects of using different crucibles is unknown. However, as long as the cup is thin walled, changes in geometry should have a minimal effect on solidification rate.

Table 28.
Results of Phase Three
Measurement System Variance Confirmation Study

Sampling Method	Description	%EV	%AV	%PV	%MSV
A	Optimized	67	8	58	89
B	Optimized, except high vibration	72	8	63	96
C	Worst case	49	34	93	110

Table 29.
Results of Phase Three
Hydrogen and Porosity Prediction Accuracy Confirmation Studies

Sampling Method	Description	H_2 R^2	2" %P
A	Optimized	0.76	0.85
B	Optimized, except high vibration	0.75	0.83
C	Worst case	0.79	0.89

Step 2—Use dry tongs to handle this crucible. Any moisture on the tongs could influence the results of the test by contaminating the sample with extra hydrogen. Contact between damp materials and molten aluminum can also be very dangerous due, to the extremely rapid expansion of water into steam.

Step 3—Gently skim the surface of the aluminum melt with the underside or lip of the crucible.

Step 4—Gently submerge the crucible and hold it below the surface until it becomes cherry red (usually about 5 seconds).

Step 5—Gently lift the crucible out of the melt such that the crucible is filled to the notch with molten aluminum. [Take the sample gently if the test is being used as a general melt cleanliness test. If some independent method of evaluating oxide content is being used and the RPT is being used to evaluate hydrogen content alone, use a second crucible to pour the metal from about 3 to 4 inches above into the sampling crucible. This creates more oxides and increases the sensitivity of the test to hydrogen.]

Step 6—As quickly as possible, without causing danger to the operator, place the crucible of molten aluminum in the vacuum chamber of an RPT tester such as the Stahl Specialty GasTech II. The tester should be located close enough to the furnace that the time to vacuum is easily kept under 15 seconds.

Step 7—Immediately turn on the vacuum pump, then start a timer set for 5 minutes.

Step 8—Adjust the bleed valve on the tester such that the vacuum chamber will be pumped down to 100 mm Hg. The pressure in the chamber should be measured with an absolute pressure gauge or a relative pressure gauge that is frequently (at least once per shift) and precisely calibrated using a manometer.

Step 9—Do not interrupt the vacuum until the timer goes off.

Step 10—Once five minutes (or more) has passed, shut off the vacuum pump, release the pressure in the chamber and remove the sample from the crucible.

Step 11—Use a separate set of tongs to place the sample in a bucket of cold water.

Step 12—Once the sample has cooled to room temperature (usually about a minute), remove the sample from the bucket and dry it thoroughly with a rag or paper towel.

Step 13—If this is the first sample that has been taken in about half an hour, so that the surface of the vacuum chamber was cool to the touch at the beginning of the test, throw this sample away. The surface of the chamber should be fairly warm to the touch (at least 50C or 125F) at the beginning of sample solidification for a valid sample.

Step 14—Once a valid sample has been obtained, place a wire basket on the bottom hook of the weighing pan of a scale. A piece of coathanger or welding rod bent so that there is a hook at the top and branching out into two supports at the bottom has been found to make a good wire basket.

Step 15—Zero the scale.

Step 16—Take a container at least 4-in. in diameter and fill it with at least 3-in. of water. The water level should be marked so that it can be maintained at this level throughout the course of several readings.

Step 17—Raise the container of water under the scale and wire basket until the water covers an RPT sample sitting in the basket.

Step 18—Place a block under the water container so that the amount of wire under water can be kept constant through the course of several readings.

Step 19—Record the weight showing on the scale. This is the basket-compensation factor.

Step 20—Remove the support block and lower the water container.

Step 21—Remove the wire basket from the scale's bottom hook and dry it thoroughly with a rag or paper towel.

Step 22—Replace the basket on the bottom hook and rezero the scale.

Step 23—Weigh the RPT sample on the scale and record this number as the weight in air. The sample may be weighed on the top of the scale or resting in the wire basket.

Step 24—Place the RPT sample on the wire basket (if it is not already there) and raise the container of water so that the RPT sample is covered with water. Use the same block to support the water container.

Step 25—Record the weight showing on the scale. This is the weight in water.

Step 26—Record the air temperature. This is the temperature used to determine the water temperature compensation. If the operator knows of a reason that the water in the container is not at air temperature, then the actual water temperature should be recorded instead.

Step 27—Calculate the density according to:

$$d_{RPT} = m_{air}c_{WT} / (m_{air} - m_{water} - c_B) \tag{7}$$

where d_{RPT} = RPT sample density (g/cm^3)
c_B = basket-compensation factor (g)
c_{WT} = water temperature compensation factor or water density (g/cm^3) (see Table 1)
m_{AIR} = mass of sample in air (g)
m_{WATER} = mass of sample in water (g)

Step 28—Remove the RPT sample from the wire basket.

Step 29—To collect another RPT sample, repeat steps 6–16.

Step 30—To evaluate another RPT sample:

Step 31—If less than 10 RPT samples have been evaluated, no change in the wire basket configuration has occurred since the last basket-compensation measurement, and less than 8 hours have passed since the last basket-compensation measurement, repeat steps 21 through 28.

Step 32—If more than ten RPT samples have been evaluated, a change in the wire basket configuration has occurred since the last basket-compensation measurement, or more than eight hours have passed since the last basket-compensation measurement, repeat steps 14 through 28.

It is hoped that this test method will be accepted as an industry standard, giving manufacturers and researchers alike more confidence in the meaning of their test results.

Future work could include the use of this standard test method for the development RPT/hydrogen and RPT/porosity correlation curves for various alloys, with and without grain refiner and with and without modification.

REFERENCES

1. DeWeese, S.K., Atkinson, R. and Rasmussen, W., "RPT Measures Hydrogen Gas, Effects on Casting Quality," *Modern Casting*, Apr 1992, pp 29-31.
2. Gallo, R., "Measurement of Hydrogen Content in Molten Aluminum Alloys Using Crucibles and Reverberatory Furnaces for Sand and Permanent Mold Castings," *4th Inter. Conf. on Molten Alum. Proc.*, 1995, pp 209-226.
3. Gruzleski, J.E., LaOrchan, W. and Mulazimoglu, H., "New Reduced Pressure Test Quantifies Hydrogen Content," *Modern Casting*, Sep 1995, pp 47-49.
4. LaOrchan, W., Mulazimoglu, M.H., Chen, X.G. and Gruzleski, J.E., "Quantified Reduced Pressure Test," *AFS Transactions*, 1995, vol 103, pp 565-574.
5. Rasmussen, W. and Eckert, C.E., "RPT Gauges Aluminum Porosity," *Modern Casting*, Mar 1992, pp 29-31.
6. Rooy, E.L. and Fischer, E.F., "Control of Aluminum Casting Quality by VSTs," *AFS Transactions*, vol 76, 1968, pp 237-240.
7. Rooy, E.L., "Mechanisms of Porosity Formation in Aluminum," *Modern Casting*, Sep 1992, pp 34-36.
8. Sigworth, G.K. and Nilmani, M., "Control and Measurement of Hydrogen in Aluminum," *4th Inter. Conf. on Molten Alum. Proc.*, 1995, pp 227-260.
9. Major, J.F., "Porosity Control and Fatigue Behavior in A356-T61 Aluminum Alloy," *AFS Transactions*, 1997, vol 105, pp 901-906.
10. Acklin, T.E., "Effect of Sample Size on Density Testing of Aluminum Alloys," *3rd Inter. Conf. on Molten Alum. Proc.*, 1992, pp 503-517.
11. Brondyke, K.J. and Hess, P.D., "Interpretation of Vacuum Gas Test Results for Aluminum Alloys," *Trans. TMS-AIME*, 1964, vol 230, pp 1542-1546.
12. Church, J. and Herrick, K., "Qualitative Gas Testing for Production Control of Aluminum Casting Soundness," *AFS Transactions*, 1970, vol 78, pp 277-280.
13. Ohira, G. and Kondic, V., "Testing the Gas Content of Molten Metals," *Foundry Trade Journal*, 96, Mar 1954, pp 331-333.
14. Rosenthal, H. and Lipson, S., "Measurement of Gas in Molten Aluminum," *AFS Transactions*, 1955, vol 63, pp 53-55.
15. Sulinski, H. and Lipson, S., "Sample for Rapid Measurement of Gas in Aluminum," *AFS Transactions*, vol 67, 1959, pp 56-64.
16. Laskowski, J., Makhlouf, M. and Apelian, D., "Optimization of the Reduced Pressure Technique," *4th Inter. Conf. on Molten Alum. Proc.*, 1995, pp 247-260.
17. Potter, M.C. and Wiggert, D.C., *Mechanics of Fluids*, Englewood Cliffs: Prentice Hall, 1991.
18. "Gas Tech II Operating Instructions," Stahl Specialty Company, Kingsville, MO.
19. "Measurement Systems Analysis," Automotive Industry Action Group, 1995.
20. Volkmar, A.P., "Effectively Using Gage R&R and Measurement System Variability," *Modern Casting*, Nov 1993, pp 30-33.
21. Ross, P., *Taguchi Techniques for Quality Engineering*, New York: McGraw Hill, 1996.
22. Hamilton, H., "The Taguchi Method: Designing for Robust Quality Seminar," *WPI Continuing Education Seminar*, Mar 22, 1996.
23. Moore, D.S. and McCabe, G.P., *Introduction to the Practice of Statistics*, New York: W.H. Freeman, 1993.
24. Jensen, F., "PANEL - Gadgets and Gimmicks in Aluminum Foundries, Part II: A Homemade Rotary Degasser for Under $1000," Paper No. 96-229, presented at AFS 100th Casting Congress, Apr 20-23, 1996, Philadelphia, PA.

1.3 Development of an Inclusion Monitoring System

Inclusion Removal and Detection in Molten Aluminum: Mechanical, Electromagnetic and Acoustic Techniques

S. Makarov
D. Apelian
R. Ludwig
Worcester Polytechnic Institute
Worcester, Massachusetts

ABSTRACT

The role of inclusions in aluminum is of great importance, in that every aspect of quality is affected by the presence of second phases. Thus, during processing operations, attention should be paid to mitigate the formation of inclusions, and, more importantly, to remove those that are present in the melt. However, the weak link is how one quantitatively determines the level of inclusions.

In this paper, we briefly review the classification of inclusions in molten aluminum, review inclusion removal techniques, and discuss the means available to detect second-phase particles in aluminum. A novel concept for detecting inclusions is under development at the Metal Processing Institute at WPI, and is presented and discussed in this paper.

Table 1.
Classification of Inclusions Observed in Molten Aluminum[1–12]

Type	Form	Density (ρ_p g/cm^3)	Dimensions (µm)	MP (°C)
OXIDES				
$MgAl_2O_4$ (spinel)	Particles, skins, flakes	3.60	0.1–100, 10–5000	2825
Al_2O_3 (corundum)	Particles, skins	3.97	0.2–30, 10–5000	2047
MgO	Particles, skins	3.58	0.1–5, 10–5000	2115
SiO_2	Particles	2.66	0.5–30	1650
CaO	Particles	3.37	<5	2630
CARBIDES				
Al_4C_3	Particles, clusters	2.36	0.5–25	2100
SiC	Particles	3.22	0.5–5	2540
BORIDES				
TiB_2	Particles, clusters	4.5	1–30	2790
AlB_2	Particles	3.19	0.1–3	2160
NITRIDES				
AlN	Particles, skins	3.26	10–50	2227
OTHER				
Chlorides and salts ($CaCl_2$, NaCl, $MgCl_2$)	Liquid droplets	1.9–2.2	0.5–1	712–800
Fluorides (cryolite)	—	2.9–3.0	—	1000
Sludge Al(FeMnCr)Si	—	>4.0	—	—
ULTRAFINE GAS BUBBLES	—	—	10–30	—
Argon bubbles				
N_2 bubbles				
INTERMETALLICS ($TiAl_3$, TiAl, , NiAl, Ni_3Al)	Particles, clusters	—	10–100	—

INTRODUCTION

Metal quality is comprised of three interrelated components: the control of trace elements (i.e., alkali elements); reduction of dissolved gas content (i.e., hydrogen); and removal of nonmetallic inclusions. Inclusions in aluminum alloys reduce mechanical properties, are detrimental to surface finish, increase porosity, and have a tendency to increase corrosion. Nonmetallic inclusions act as stress raisers, and can cause premature failure of a component. The size, shape, type and distribution of nonmetallic inclusions in the final product are considered the performance fingerprints of the cast shop.

In this paper, we review inclusion detection and removal technologies during metal casting of aluminum. We examine the source of inclusions and removal techniques, and subsequently review the means by which one can detect inclusions. Special attention is given to electromagnetic and acoustic methods. A recent development to detect inclusions using electromagnetic *forces* is also presented.

INCLUSIONS IN ALUMINUM

The level of second-phase inclusions in aluminum alloys can be substantial. For example, if we assume that the average size of the inclusions is 40 microns, then at an inclusion concentration of 1 ppm (a minimum level), one pound of aluminum metal contains 5000 inclusion particles. In fact, in some instances, when the melt is not adequately processed, the cast product is more of a composite than an aluminum alloy.

Inclusions in molten aluminum can be classified according to their size, chemical content and phase (solid or liquid). Table 1 summarizes the experimental data for various inclusion types.[1–12]

Sources of Inclusions

Oxide films and particles are generated during melting and alloying. These Al_2O_3 films are either suspended on the melt surface and/or entrapped within it, due to turbulence. Although oxide inclusions have a greater density than molten aluminum, they float out because of density differences with respect to the melt and the high surface-to-volume ratio of the inclusions. In addition, oxide inclusions have a tendency to agglomerate because they are poorly wetted by molten aluminum.[6] Also, Al_2O_3 inclusions become buoyant as a result of absorbed gases, and rise to the melt surface.[11]

Spinel inclusions originate from melting scrap, as well as adding magnesium to the holding furnace. Since MgO has a lower free energy of formation than Al_2O_3, it tends to form preferentially, particularly in alloys containing more than 0.5% Mg by weight. The addition of magnesium to molten aluminum causes nonmetallic inclusions other than spinel to form.[13] Nitride inclusions (AlN) originate from magnesium nitride (Mg_3N_2). MgF_2 and MgS particulates have been observed to form when "dirty" magnesium is added to the melt.[13]

Silica particulates mostly originate from erosion of ceramic materials used as accessories in the melting operation. These refractory particles do agglomerate, and compounds such as $Al_2O_3 \cdot SiO_2 \cdot CaO$ are often observed.[9] Recycled aluminum melts contain a large amount of aluminum carbides due to the presence of hydrocarbons.[14]

To further complicate matters, liquid-phase inclusions form in molten aluminum as a result of fluxing and chlorine degassing, i.e., chlorides and chloride salts ($CaCl_2$, NaCl, $MgCl_2$ and KCl). These salts may also contain fine solids, such as NaF, AlF_3 and CaF_2, originating from furnace additives or potroom metal.[3] These liquid-phase inclusions do affect interfacial energies of the system; for example, borides used as grain refiners do agglomerate when coated with liquid salt phases.[8]

Size Distribution of Inclusions

A dirty aluminum melt from a melting furnace may have, on average, about 10,000 inclusions equal to or greater than 15 µm in diameter per kilogram, prior to settling in a holding furnace. Spinels can reach sizes as large as 0.5 mm in diameter,[9] and are quite deleterious to the mechanical properties of the cast product. As a result of implementing molten metal processing technologies, much of the macroscopic inclusions are removed; as a result of filtration, most of the inclusions found are less than 30 µm in size. Coulter counter-detection techniques have been used to assess the size distribution of inclusions in the melt. The number of inclusions in a kilogram of molten aluminum exceeding 15 µm is on the order of several hundreds (Liquid Metal Cleanliness Analyzer or LiMCA measurements;[12,15,16] cf. also[17]). As expected, the number of inclusions greatly increases for small particle sizes of about 1–5 µm.

Thus, it is not sufficient to have an assessment of the size of inclusions that are present; also needed is an assessment of the size distribution of inclusions required to control molten metal quality.

INCLUSION REMOVAL TECHNIQUES

In general, inclusion removal methods can be grouped into two broad categories: 1) volumetric force driven separation and 2) externally assisted methods—by an external force applied to accentuate the density difference between the inclusions and the melt and thus cause separation, or a vehicle for transport of the inclusions to the surface (gas bubbles), agglomeration of the inclusions, separation of the inclusions through filtration, applied Lorentz forces, etc. (see Table 2). Each of these methods for inclusion removal is briefly reviewed, to establish a context for the discussion on inclusion detection that subsequently follows.

Volumetric Separation

Gravity Sedimentation

Gravity sedimentation methods (see Fig. 1) are limited to inclusion sizes larger than 90 µm. The reason is due to inordinately low particle terminal velocities and high drag forces. For example, the free settling velocity, $v_s = g(\rho_p - \rho) D^2 / 18\eta$, due to Stokes' drag is about 3 mm/s for a spherical spinel particle of 100 µm in size (assuming an aluminum shear viscosity of $\eta = 0.02$ poise at 720C and a melt density ρ of 2.4 g/cm^3). The actual settling velocity, v, is smaller than v_s, because of particle-particle interactions. The relationship is approximated by $v = v_s (1 - \phi)^{4.7}$, where ϕ is the particle concentration. Stirring and moderate turbulence stimulates particle agglomeration and enhances sedimentation efficiency.[20,21] The level of turbulence necessary to optimize inclusion agglomeration and subsequent separation is currently being pursued at the Metal Processing Institute.[22,23]

Table 2.
Inclusion Removal Methods[9,10,18,19]

Method	Particle Sizes Affected, µm
Volumetric Separation	
Gravity sedimentation in holding furnaces (metal settling):	>90
Externally Assisted Methods	
Flotation in degassing units:	>1
Filtration:	>1
Electromagnetic sedimentation:	>50
Ultrasonic treatment:	>10

External Assistance

Flotation

Degassing units are used in a holding furnace to achieve a low level of inclusions and to decrease the gas content of the melt (reduce hydrogen content). During degassing, the nonmetallic solid particles are swept to the melt surface by flotation where they accumulate in the dross (Fig. 2). Flotation techniques are widely used throughout the metalcasting industry, because the treatment is effective and it does reduce both gas content and inclusion content. During the last five years, we have seen much effort go into the development of new and improved methods of degassing, such as the Revrot unit developed by Apogee Corp.[24,25] Computational modeling efforts currently underway at MPI are aimed to optimize the design of degassers to enhance melt cleanliness.[22,23]

Filtration

Filtration technologies offer an effective way of removing inclusions in the size range less than 30 µm. At present, almost all the primary aluminum cast is filtered through deep bed filters. The theoretical basis for inclusion separation during filtration, as well as experimental validation of these principles, has been developed and studied by several researchers.[26–34]

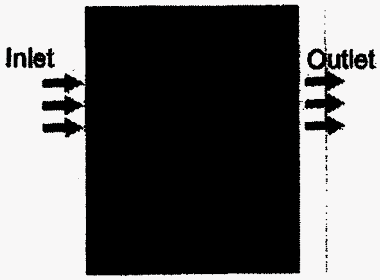

Fig. 1. Schematic representation of gravity sedimentation.

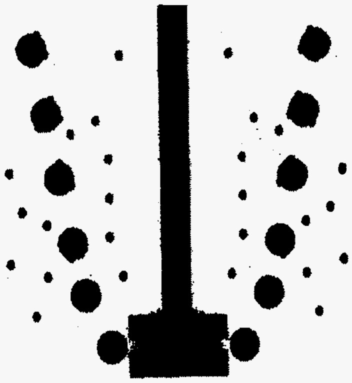

Fig. 2. Schematic representation of inclusion removal by gas bubbles.

As to the use of filters in the foundry, in the past, sieves and other strainers have been utilized; however, these are only useful for the removal of large inclusions. Ceramic foam filters, extruded monoliths or porous tubes are used in the foundry, rather than deep bed filters. These cartridge-like filters are easily installed in the gating system, and, in addition to minimizing turbulence and providing a laminar flow into the cast cavity, the filter does remove inclusions less than 30 microns. The weak link in the overall equation has been that the industry has not had a robust and an economical means of assessing the degree of inclusion removal by the filter. Recent work[16] utilizing the LiMCA has shown that filtration is most effective, and that ceramic foam filters are quality enablers in the cast shop.

Electromagnetic Sedimentation

In this technique, an externally applied electromagnetic force acts upon the melt. As a reaction to this externally applied force, the inclusions move in the opposite direction—as a result of Newton's third law—and are thus separated. As shown in Fig. 3, the current density, J, traverses left to right, as indicated by the arrows in the melt. Note that there is no current in the inclusion since the particles are nonconducting, and thus $J = 0$.

The magnetic field, B, is applied in the direction out of the plane of the schematic in Fig. 3. The resultant Lorentz force, which is the cross product of J and B, is in the south direction (Fig. 3). The inclusions present in the melt experience a force opposite to the direction of the applied Lorentz force (see the upward motion of inclusions in Fig. 3). This force, acting on the inclusions, is called the Archimedes electromagnetic force.

In laboratory-scale experiments, large force densities can be achieved. To estimate the available magnitude of the electromagnetic force, let us consider a current density of 6.4×10^5 A/m^2 (total current of 5 kA through a 10 cm wide tube). If B is about 0.5 tesla, for a spinel particle, the electromagnetic force value is nearly 30 times greater than the gravitational force. This allows sedimentation of smaller particles to take place, thus separating the inclusions from the bulk melt.

We can classify conventional electromagnetic separation techniques for molten metal into two groups and four subgroups, as Table 3 shows. This classification mainly relies upon the sources of the Lorentz force and, consequently, the Archimedes electromagnetic force. More precisely, it revolves around the manner in which the electric and magnetic fields in the melt are produced. However, the resulting physical effect always remains the same. It is the electromagnetic flotation of inclusions and their attachment to the refractory walls, the free melt surface, etc., with subsequent removal from molten metal.

It must be pointed out that large force densities in large volumes are difficult to achieve, mainly due to the complexity of producing strong, highly homogeneous magnetic fields. For this reason, separation efficiencies are quite low when the inclusion size is below 50 μm.[48] This is why electromagnetic separation has not been widely utilized.

The use of high DC magnetic fields generated by modern superconducting coils can considerably improve the separation efficiency and move the size limit toward smaller particles.[49–51] For large force densities, the main problem remains the homogeneity of the force distribution through the volume. If the force field is not uniform, very strong electromagnetically driven fluid motion and turbulence may appear, thus creating an uncontrollable situation.

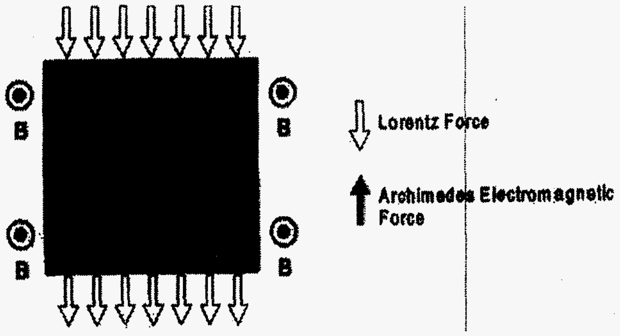

Fig. 3. Schematic diagram illustrating electromagnetic separation.

Table 3.
Electromagnetic Separation Methods for Metalcasting[35–51]

Induction Current Separation
1. Induction coil separation
   (El-Kaddah and coworkers[35–37])
2. Traveling magnetic field separation
   (Asai and coworkers[38–40])

Injection Current Separation
3. Pinch-effect separation[41,42]
4. Separation in a superimposed magnetic field[43–47]

Ultrasonic Treatment

Ultrasonic absorption in many liquid metals, including molten aluminum, is relatively small,[52] giving rise to the opportunity for ultrasonic treatment of the melt. The ultrasonic treatment includes, in particular, acoustic degassing of the aluminum melt and fine filtration of molten aluminum alloys in the cavitation field.[53] The technique remains very expensive and additional efforts are necessary to develop industrially viable techniques.

The application of ultrasound to the melt has been shown to affect the wettability of the inclusions.[54] Separation of inclusions from molten aluminum may be enhanced by the use of filters and ultrasonics. Recent work with ultrasonic treatment and filters in water has shown that particles up to two orders of magnitude and smaller than the pore size of the filter used can be separated out.[55]

INCLUSION DETECTION METHODS

It is well known that it is difficult, if not impossible, to control a process if key parameters cannot be measured. In molten metal processing, the assessment of the level of inclusions present in the melt has been, and is, the key parameter that needs to be monitored. The problem is a challenging one, in that the level of inclusions is low, their size ranges from 1 to 50 μm, and one would like to have an on-line system to be able to control the quality of the cast part, rather than after the fact, as in an off-line test. Table 4 summarizes the various methods available. Each of these tests are further discussed.

Pressure Filter Tests

In this technique, a certain volume of metal is passed through a fairly impermeable filter, thus concentrating the inclusions present in the melt as a cake on the filter. The collected inclusions are then analyzed metallographically. An advantage here is that the volume of inclusions collected per volume of metal sampled is known. The main disadvantage is that the test is tedious, labor intensive and an off-line test.

Table 4.
Inclusion Detection Methods[10,17,56–58,83–86]

DETECTION METHODS	Sample Weight, g	Particle Size Effected, µm	Operation
Pressure Filter Tests		All sizes	
PoDFA	≤2000		Off-line
LAIS	≤1000		Off-line
Prefil Footprinter			On-line
Electric Resistivity Test			
LiMCA, LiMCA II	≤100/min	>15	On-line
Acoustic Detection		>10	On-line
Signal-noise technique			
Pulse-echo technique			
Electrochemical Dissolution	≤100	All sizes	Off-line
Chemical Analysis			
Emission spectroscopy; Hot extraction; Combustion analysis; Neutron activation; Gas chromatography	0.5–30	All sizes	Off-line
Eddy Current Method	—	—	On-line
Capacitance Probe	—	—	On-line
X-Ray Detection	—	—	Off-line
Electromagnetic Detection Technique	≤200/min	>10	On-line

Alcan's PoDFA (Porous Disk Filtration Apparatus) and LAIS (Liquid Aluminum Inclusion Sampler) of Linde's Industrial Gas Division are based on this principle; Fig. 4 shows the operation of the LAIS test (Foseco Ltd. 97). Similar pressure filter samplers are also used in magnesium melts.[13,59] The LAIS and PoDFA methods allow one to measure the level of inclusions present, as well as the ability to determine the types of inclusions present. The vulnerability of these tests is that the results can be influenced by the presence of inclusion particles less than 10 µm in size. Nevertheless, these tests are quite effective and have been used successfully to assess inclusion levels in cast shops.

A derivation of the LAIS test is the Prefil Footprinter.[60] In this test, the filtration rate is recorded during a standardized pressure filtration test, and it is compared with pre-programmed information. Essentially, melts that are heavily contaminated will have a much lower flow rate through the filter, versus a clean melt that will flow through the filter with much less resistance.

Electric Resistivity Tests

LiMCA (LiMCA II) is an elegant modification of the familiar Coulter counter (Beckman Coulter, Inc.[61]), as applied to liquid metal processing.[62–68] A circular aperture of diameter D = 2R (Fig. 5) is used in the test to flow molten metal through it. The flow path from electrode 1 to electrode 2 includes the aperture and the surrounding metal volume. If a spherical particle of diameter d passes through the aperture, the increase in the total resistance, ΔR, of the current path can be obtained in the form $\Delta R = 1/(4\pi)\,\rho\, d^3/R^4$ [cf.[69]], where ρ is the resistivity of molten metal. The total voltage drop ΔV is given by $I/(4\pi)\,\rho\, d^3/R^4$, where I is the total current through the aperture. The key point of the method is that the voltage drop does not depend on other parameters (total current path, electrode location, etc.) and is directly related to the particle radius.

During the LiMCA test, the momentary voltage drops are counted and classified according to their magnitudes. Hence, both concentration and size distribution of inclusions larger than 15–20 µm are provided.[15,17,52,64] Today, LiMCA is considered to be a reliable tool for on-line detection of small particles in liquid metals. It can be used either alone or together with PoDFA or LAIS for larger inclusions.[12,58,70] The cost of the LiMCA system is quite high, and it is clear that this method will not be widely used by the foundry industry; it is widely used throughout primary producers of aluminum.

There are certain critical issues that require special attention regarding the electric resistivity test. Since the voltage drop is inversely proportional to the fourth power of the aperture radius, very narrow openings of 200–500 µm are necessary to detect small particles of 15–20 µm in diameter. This limits the sampling capacity of a particular aperture size to 10–30 g of molten metal per minute. Multiple apertures increase the capacity up to 100 g per minute. Additionally, nonconducting inclusions of the same size but of different chemical contents (silica particles and gas bubbles) cannot be distinguished by the LiMCA, which is a significant disadvantage of the technique. A more sophisticated setup[71] apparently allows to separate solid particles from liquid and/or gaseous inclusions.

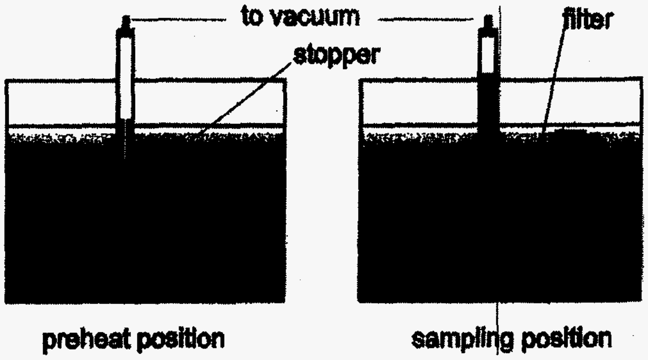

Fig. 4. LAIS sample equipment.

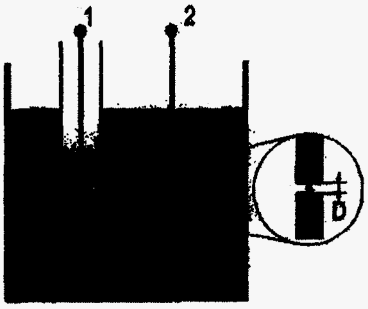

Fig. 5. Schematic representation of LiMCA

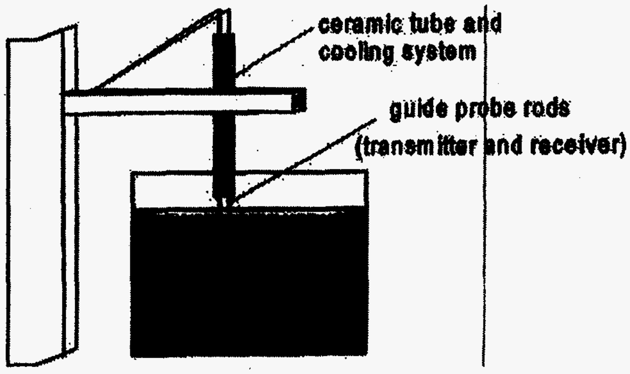

Fig. 6. Ultrasonic probe technique.

Acoustic Detection

Acoustic transducers and receivers for molten metal (sodium at 650C) applications were developed at Argonne National Laboratory during 1971–1975 (see Ref. 56, pp 513-515). The early steps concerning molten aluminum cleanliness treatment with ultrasound were undertaken in the late sixties–early seventies. In comparison with standard nondestructive evaluation (NDE) ultrasonic techniques for molten metal applications, an important issue is the proper construction of the buffer rods and waveguides to avoid the effect of high temperatures on piezoelectric transducers.[72,73]

Reynolds Metal Company developed the Mansfield Molten Metal Monitor (4M™) system[74] for inclusion detection based on the pulse-echo principle. In this technique, molten metal is forced through an aperture of 10x10 cm^2 and subjected to a low-frequency signal of 10 kHz. The wavelength of 47 cm allows for low-frequency scattering of small particulates in the insonified domain. By measuring the number of echoes and associated sound damping, the concentration of large inclusions (>60 μm) can be evaluated. The Mansfield probe is capable of analyzing 2–20 kg of molten metal/minute. Although the system can distinguish between an extremely contaminated metal and a clean melt, the sensitivity of the unit is limited. The technique does not provide any information regarding particle size distribution, and it is only effective in detecting "rocks" in the melt. The 4M is not widely used, and interest in the system has declined over the years.

Eckert[72] proposed an ultrasonic detection apparatus with the working frequency of 8–25 MHz. Particles as small as 50 μm have been detected and the probe is theoretically capable of detecting particles in the 1–10 μm diameter range.

Mountford and coworkers[57,75,76] have studied ultrasonic probing of molten aluminum and have reported results with a prototype probe. Their apparatus[57] consists of two guided rods (transmitter and receiver) immersed into liquid aluminum (Fig. 6). The pulse-echo technique is used with a carrier frequency of 1–2.25 MHz and with a pulse repetition rate of 120 times per second. Hence, only low-frequency isotropic scattering is recorded with $0 < kd < 0.1$ (where k is the wave number and d is an average particle diameter).

The reported minimum size of detected inclusions is 10–15 μm, which translates into extremely high input power requirements. The probe works quite well as a counter for the total number of particles. However, only the "effective" size of inclusions is assessed. A disadvantage of this technique is the deposition of particles on the interface of the immersed rods, which interfere with sound propagation.

Recent work at ALCOA[77] in the development of an ultrasonic probe may have promise, in that this apparatus utilizes the pulse-echo technique with the carrier frequency in the radio range, and the apparatus has two buffer rods for the transmitter and the receiver, respectively.

Electrochemical Dissolution

The principle of extracting out the nonmetallic inclusions by dissolving the aluminum matrix through electrolytic dissolution consists of:[9,78]

- Collecting aluminum samples that are cast in the form of an anode suitable for electrochemical dissolution in an aqueous electrolyte.
- Electrochemically separating the inclusions by preferentially dissolving the matrix metal.
- Collecting of inclusions by filtering the aqueous electrolyte.

Subsequently, the collected inclusions are examined and analyzed through traditional metallographic analysis. This is a time-consuming, tedious and an off-line test, which also has the disadvantage of not being able to capture the NaCl-, $CaCl_2$-containing inclusions,[7] which are water soluble and are lost out during the electrolyte treatment.

Chemical Analysis

Elemental composition is determined either via wet or spectrographic analysis in unfiltered and filtered samples. Filter performance is then assessed by an efficiency parameter, η:

$$\eta = 100\% \, (C_i - C_o) / C_i,$$

where C_i and C_o are the concentrations of the specific element, s, at inlet and outlet points of the filter, respectively. This method has been used by many researchers over the years; however, it is not accurate, in that the analyzed samples are so terribly small, with respect to the bulk melt being assessed.

Techniques based on wet chemical or instrumental analyses of inclusions have not been very successful, owing to the nonuniform distribution of the inclusions. Furthermore, measurement of the bulk concentration of elements does not indicate how the elements are distributed within the sample.

For example, it has been determined that there is no direct correlation between the oxygen concentration (determined by neutron activation analysis) and the concentration of inclusions greater than 20 μm. Neutron activation can be used to measure oxygen concentration, and gas chromatography can be used to detect the presence of carbides.

Several other techniques, including gravimetric determination and emission spectroscopy, have been used by Siemensen and coworkers[79] for laboratory-type applications. However, these techniques do not provide a practical means of assessing inclusion levels in the cast shop.

Eddy Current Method

Measurement of magnetic fields as a result of applied eddy currents in the melt makes it possible to determine the distribution of the electrical conductivity and flow velocities. Such measurements can be used for an early detection of slag in molten metal flows through insulating tubes.[80] After appropriate modifications, the method can theoretically be applied to the detection of inclusions in molten metal.[81] The critical parameter is the lower conductivity of the particle, similar to the electric resistivity test (see Ref. 82 for theoretical issues). Eddy current testing does not require intimate contact between the sensor and the melt, thus allowing for remote sensing applications.

Capacitance Probe

Electric capacitance tomography has been used with great success in chemical and biochemical applications;[83] however, in these cases, the medium is a poor conductor. Thus, it is doubtful whether this method is applicable in aluminum, though it should not be completely discounted. It is interesting to note that a capacitance probe has been applied to gas bubbles in molten aluminum[84] to detect the change in permitivity while a bubble is passing between two capacitor plates. This technique is cumbersome, and yet holds potential for on-line control of melt quality.

X-Ray Detection

In the x-ray detection technique,[85] a metal sample is levitated in an induction crucible. Due to the effect of the electromagnetic force, nonmetallic inclusions move to an outer periphery of the levitating sample. Then, the metal sample is cooled and moved to an analysis position in an x-ray fluorescence analyzer. Thus, the nonmetallic inclusions are detected.

Electromagnetic Detection

The concept to use electromagnetic forces to move inclusions to an inspection location was developed at the Metal Processing Institute (at WPI) during the last few years. A new detection technique, based on this concept,[86] potentially has a better resolution performance among other on-line methods, and is inexpensive in its construction. The first step is to bring the nonconducting inclusions by electromagnetic Archimedes force to a detection location (the free melt surface). Further, an optical image system can be applied to detect them, visually.[86]

In one embodiment, the measurement setup (Fig. 7) includes container (A); permanent magnet yoke (B); peristaltic pump (C) to enable melt flow throughout the container; and microscope (D), coupled with a digital camera.

The Lorentz force density reaches 7.2×10^5 N/m^3 in the central section of the container. This is more than 30 times the gravitation force density acting on the molten aluminum. Simultaneously, this is more than 60 times the gravitation Archimedes force on spinel inclusions (with density of 3600 kg/m^3) in molten aluminum. These simple considerations underscore the fact that the electromagnetic treatment is quite effective if the cross section of the flow is sufficiently *small*.

An instantaneous treatment volume of the sensor is typically on the order of 1–2 cm^3. To ensure good representation of the actual concentration of inclusions, we enabled the steady-state melt flow throughout the treatment volume. We continuously "clean" the free melt surface, so that new particles appear during the sensing period. If the flow velocity is reasonably small (less than or equal to 1 cm/sec), the likelihood of collecting the inclusions from the total sensing volume is very high.[86]

Fig. 7. Measurement setup: (A) container; (B) permanent magnet; (C) pump; (D) microscope and digital camera.

To validate the theoretical concept,[86] low-temperature experiments with liquid gallium (melting point is 30C) were conducted. The use of gallium is common for low-temperature modeling, since some parameters (melt conductivity, surface tension) are quite similar to molten aluminum close to its melting point.

Figure 8 shows a cluster of synthetic inclusions on the free gallium melt surface. The time duration between each frame is about 1.7 sec. Figure 9 demonstrates particle appearance on the free melt surface and the resolution of the method. The contaminated trace on the left is due to cluster disintegration. We observe partially escaped particles on the order of 10–30 μm. The concept has shown promise, in that concentrations of low-conducting particles as small as 10 μm can be detected on the free melt surface.

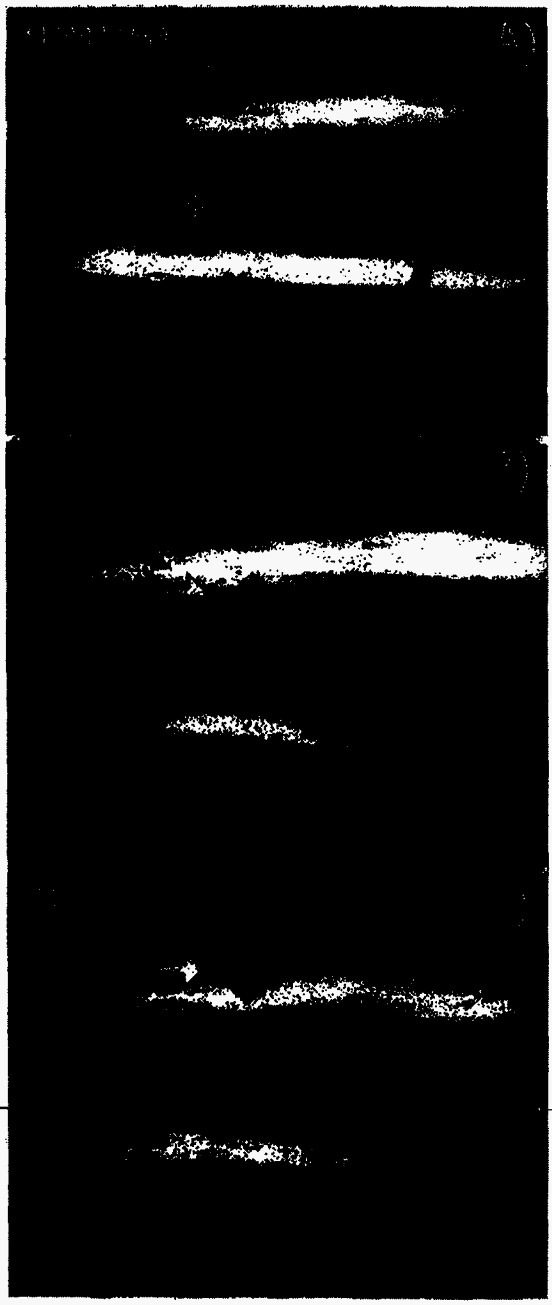

Fig. 8. Cluster appearance on free melt surface. Time duration between each frame is about 1.7 sec.

CONCLUSIONS

It is an interesting paradox that metals are strengthened through the nucleation of second phases throughout the matrix; however, inclusions that are also second-phase particulates render the metal weak and are undesirable. The difference between these two scenarios is control of the size and distribution of the second-phase particulates/ inclusions. The aluminum processing industry has been at a disadvantage by not having the ability to accurately detect inclusions in the melt, on an on-line basis.

In this paper, we have addressed two specific areas—inclusion removal and detection. The methodologies available for removal may be appropriate for detection, and vice versa. The various mechanical, electromagnetic and acoustic techniques available have been reviewed and assessed.

A novel concept of inclusion detection utilizing Lorentz forces to separate the inclusions from the melt and subsequently analyze the aggregate has been described and discussed. This concept has much merit, and experiments, to date, have validated its feasibility.

REFERENCES

1. W. P. Peterson: "The Role of Casting Technology in the Development of New and Improved Fabricated Products," *Light Metals*, 1988, pp 329-339.
2. E. Bathen and T. A. Engh: "Deposition of Inclusions Down Through a Sandwich-Type Ceramic Foam Filter Studied by Automatic Image Analysis," *Light Metals*, 1988, pp 423-430.
3. D. H. DeYoung, D. Apelian and R. Mutharasan: "Method for Separation and Removal of Suspended Liquid Particles from Molten Metal and Associated Apparatus," U.S. Patent 5,336,295 of Aug 9, 1994.
4. S. T. Johansen, S. Grådahl, Ø. Dahle, I.-R. Johansen, R. Tangen and E. Myrbostad: "Experimental Determination of Bubble Sizes in Melt Refining Reactors," *Light Metals*, 1996, pp 1027-1031.
5. D. Sampath, P. G. J. Flick, J. Pool, W. Boender and W. van Rijswijk: "Sampling of Aluminum Melts and Detection of Nonmetallic Inclusions Using LAIS," *Light Metals*, 1996, pp 817-821.
6. K. Hoshino, T. Nishizaka, K. Kakimoto and T. Yoshida: "The Filtration of Molten 1XXX Series Aluminum Alloys with Rigid Media Tube Filter," *Light Metals*, 1996, pp 833-838.
7. P. Pouly and E. Wuilloud: "On the Efficiency of In-Line Devices to Clean the Melt," *Light Metals*, 1997, pp 829-835.
8. T. Gudmundsson, G. Saevarsdottir, T. I. Sigfusson and D. G. McCartney: "Chlorination of TiB_2 Grain Refined Aluminum Melts," *Light Metals*, 1997, pp 851-855.
9. X. Wang: "Morphological Aspects of Inclusions in AA3104 D&I Can Stock Alloy," *Light Metals*, 1997, pp 963-972.
10. D. Apelian: "Advances in Metal Treatment of Aluminum and Foundry Alloys," *Proceedings of the International Symposium on Light Metals 1997 Métaux Légers*, C. M. Bickert and R. I. L. Guthrie, Eds., Canadian Institute of Mining, Metallurgy and Petroleum, Montreal, Canada, 1997, pp 117-139.
11. P. N. Crepeau: "Molten Aluminum Contamination: Gas, Inclusions and Dross," *Modern Casting*, vol 87, 1997, pp 39-41.
12. H. P. Krug and W. Schneider: "A Contribution to Inclusion Measurement After In-Line Degassers with PoDFA and LiMCA," *Light Metals*, 1998, pp 863-870.
13. P. Bakke, J. A. Laurin, A. Provost and D. O. Karlsen: "Consistency of Inclusions in Pure Magnesium," *Light Metals*, 1997, pp 1019-1026.
14. F. Frisvold, P. Bakke, E. Øvrelid, N. E. Hald and T. A. Engh: "Hydrogen and Inclusion Content in Recycled Aluminum at Holmestrand Rolling Mill," *Light Metals*, 1996, pp 1011-1016.
15. J.-P. Martin: "The Need for Fast, Dynamic Measurement Techniques in Understanding and Controlling the Casting Process," *Proceedings of The International Symposium on Quality and Process Control in the Reduction and Casting Aluminum and Other Light Metals*, D. W. MacMillan, Ed., Pergamon Press, NY, 1987, pp 123-132.
16. N. J. Keegan, W. Schneider, H.-P. Krug and V. Dopp: "Evaluation of the Efficiency of Ceramic Foam and Bonded Particle Cartridge Filtration Systems," *Light Metals*, 1997, pp 973-982.
17. C. Carozza, P. Lenard, R. Sankaranarayanan and R. I. L. Guthrie: "On the Development of a LiMCA Probe for Liquid Magnesium," *Proceedings of the International Symposium on Light Metals 1997 Métaux Légers*, C. M. Bickert and R. I. L. Guthrie, Eds., Canadian Institute of Mining, Metallurgy and Petroleum, Montreal, Canada, 1997, pp 185-196.
18. C. E. Eckert, R. E. Miller, D. Apelian and R. Mutharasan: "Molten Aluminum Filtration: Fundamentals and Model," *Light Metals*, 1984, pp 1281-1304.
19. P. Waite and R. Thiffault: "The ALCAN Compact Degasser: a Trough-Based Aluminum Treatment Process. Part I: Metallurgical Principles and Performance," *Light Metals*, 1996, pp 1001-1005.
20. S. L. Soo: *Fluid Dynamics of Multiphase Systems*, Blaisdell Publishing Co, Massachusetts, 1967.
21. S. T. Johansen and S. Taniguchi: "Prediction of Agglomeration and Break-up of Inclusions During Metal Refining," *Light Metals*, 1998, pp 855-861.
22. M. Maniruzzaman and M. Makhlouf: "Modeling of Flotation Process in Aluminum Melt Treatment," *Proceedings of the Eighth International Symposium on Modeling of Casting and Welding Processes 1998*, B. G. Thomas and C. Beckermann, Eds., TMS, 1998, pp 705-712.
23. M. Maniruzzaman and M. Makhlouf: "Computer Simulation of Flotation Treatment Methods Used in Aluminum Alloy Processing," *Light Metals*, 1998, pp 797-803.
24. C. E. Eckert: "Molten Metal Fluxing System," U.S. Patent 5,397,377 of Mar 14, 1995.
25. C. E. Eckert: "Method for Fluxing Molten Metal," U.S. Patent 5,630,863 of May 20, 1997.
26. T. A. Engh: *Principles of Metal Refining*, Oxford University Press, Oxford, 1991.
27. J. A. Clumpner, R. E. Herchey and W. L. Hoffmann: "Mint®—An In-Line Melt Purification System: Predicting Commercial Performance with Aluminum Alloys," *Light Metals*, 1986, pp 815-819.
28. D. V. Neff and E. P. Stankiewicz: "The Multicast™ Filtration System," *Light Metals*, 1986, pp 821-828.
29. P. Netter and C. Conti: "Efficiency of Industrial Filters for Molten Metal Treatment Evaluation of a Filtration Process Model," *Light Metals*, 1986, pp 847-859.
30. L. S. Aubrey, M. A. Cummings and C. L. Oliver: "The Development and Performance Evaluation of a Dual Stage Ceramic Foam Filtration System," *Light Metals*, 1996, pp 845-855.

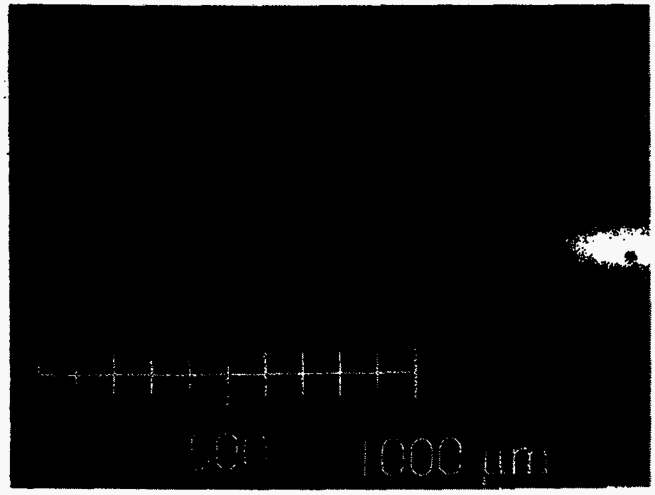

Fig. 9. Particle appearance on the free melt surface and the resolution of the method.

31. D. Barbis, D. D. Smith, L. S. Aubrey and W. C. Miller: "Performance of a Staged Filtration System Installed at Norandal Usa, Inc. to Filter Continuous Twin Roll Cast Converter Stock," *Light Metals*, 1998, pp 917-938.
32. C. Brochu, R. Dault, J. Déry and S. P. Tremblay: "Liquid Metal Filtration and Distribution Using Fiberglass Fabric," *Light Metals*, 1996, pp 839-844.
33. G. Mabry, J. Kaems, D. Granger and W.C. Setzer: "Characteristics of Particulate Captured by a Rigid Tube Filter," *Light Metals*, 1997, pp 983-989.
34. A. W. Cramb: "High Purity, Low Residual and Clean Steels," *Impurities in Engineering Materials: Impact Reliability and Control*, Marcel Dekker Inc., 1998.
35. N. El-Kaddah: "A Comprehensive Mathematical Model of Electromagnetic Separation of Inclusions in Molten Metal," *Conf. Records of IEEE on Industrial Applications*, 1988, pp 1162-1167.
36. T. Sawai and N. El-Kaddah: "Kinetics of Inclusion Removal in Electromagnetically Driven Recirculating Flows," *Proceedings of The First International Symposium on Electromagnetic Processing of Materials*, Nagoya, Japan: ISIJ, 1994, pp 260-265.
37. A. D. Patel and N. El-Kaddah: "Kinetics of Inclusion Removal from Molten Aluminum Under an Applied Alternating Magnetic Field," *Light Metals*, 1997, pp 1013-1018.
38. J. P. Park, K. Sassa and S. Asai: "Elimination of Nonmetallic Inclusions in Metals Using Electromagnetic Force," *Metallurgical Processes for the Early Twenty-First Century*, vol 1, H. Y. Sohn, Ed. Warrendale, PA: Minerals, Metals & Materials Society, 1994, pp 221-230.
39. J. P. Park, Y. Tanaka, K. Sassa and S. Asai: "Elimination of Tramp Elements in Molten Metal Using Electromagnetic Force," *Proceedings of The First International Symposium on Electromagnetic Processing of Materials*, Nagoya, Japan: ISIJ, 1994, pp 497-504.
40. S. Asai: "Recent Activities on Electromagnetic Processing of Materials," *Proceedings of The Julian Szekely Memorial Symposium on Material Processing*, H. Y. Sohn, J. W. Evans and D. Apelian, Eds. Warrendale, PA: Minerals, Metals & Materials Society, 1997, pp 301-311.
41. S. Tanigushi and J. K. Brimacombe: "Separation of Nonmetallic Inclusions from Liquid Metal by Pinch Force," *Proceedings of The First International Symposium on Electromagnetic Processing of Materials*, Nagoya, Japan: ISIJ, 1994, pp 429-434.
42. A. I. Raitchenko, V. P. Popov and A. V. Derevjanko: "Behavior of the Solid Alloy Particles Dispersed in Liquid Tin Under the Electric Current Passage," *Fluid Flow Phenomena in Metals Processing*, N El.-Kaddah, D. G. C. Robertson, S. T. Johansen and V. R. Voller, Eds. Warrendale, PA: Minerals, Metals & Materials Society, 1999, pp 603-606.
43. R. Moreau: "Metallurgical Applications of Magnetohydrodynamics," *Proceedings of the 15th Congress on Theoretical and Applied Mechanics*, Toronto: UITAM, 1980, pp 107-118.
44. P. Marty and A. Alemany: "Theoretical and Experimental Aspects of Electromagnetic Separation," Metallurgical Application of Magnetohydrodynamics, *Proceedings of The UITAM Symposium*, H. K. Moffatt and M. R. E. Proctor, Eds. London: The Metal Society, 1984, pp 245-259.
45. D. O. Hobson, I. Alexeff and V. K. Sikka: "Method and Apparatus for Removal of Gaseous, Liquid and Particulate Contaminants from Molten Metals," U.S. Patent 4,786,320 of Nov 22, 1988.
46. T. Koji, "Method for Cleaning Molten Steel:" JP Patent 1995000107999 of Oct 29, 1996.
47. S. Asai, K. Sasa, J. P. Baku: "Method for Removing Impurity Element from Molten Metal and Device Therefor," JP Patent 1994000219570 of Mar 5, 1996.
48. M. Garnier: "Actual and Future Developments of Electromagnetic Processing of Materials" *Proceedings of The Julian Szekely Memorial Symposium on Material Processing*, H. Y. Sohn, J. W. Evans and D. Apelian, Eds., Minerals, Metals &Materials Society, 1997, pp 313-322.
49. B. Pillin, P. Gillon and E. Beaugon: "Method and Device for Separating Particles from an Electrically Conductive Liquid Flow Using Electromagnetic Forces," EP Patent 879087A1 of Nov 25, 1998.
50. P. Gillon and B. Pillin: "Electromagnetic Separation of Particles from a Conducting Liquid Using a Strong DC Magnetic Field," *Proceedings of Induction Heating Seminar HIS-98*, Padua, Italy, 1998.
51. B. Pillin: "Utilisation Des Champs Magnétiques Intenses Pour la Separation d'Inclusions: Application aux Particules Solides Immergées Dans les Métaux Liquides," PhD, EPM, CNRS-Grenoble, 1997. In French.
52. G. M. B. Webber and R. W. B. Stephens: "Transmission of Sound in Molten Metals," *Physical Acoustics*, Academic Press, New York, 1968, Vol IV-B, pp 53-97.
53. G. I. Eskin: *Ultrasonic Treatment of Light Alloy Melts*, Gordon and Breach, Amsterdam, Netherlands, 1998, chapter 2, 3.
54. Y. Genma, Y. Tsunekawa, M. Okumiya and N. Mohri: "Incorporation of Alumina Particles with Different Shapes and Sizes into Molten Aluminum Alloy by Melt Stirring with Ultrasonic Vibration," *Materials Transactions*, JIM, vol 38, 1997, pp 232-239.
55. S. Gupta and D. L. Feke: "Acoustically Driven Collection of Suspended Particles Within Porous Media," *Ultrasonics*, vol 35, 1997, pp 131-139.
56. L. C. Lynnworth: *Ultrasonic Measurements for Process Control*, Academic Press, New York, 1989 (720 pp).
57. N. D. G. Mountford, I. D. Sommerville, A. Simeonescu and C. Bai: "Sound Pulses Enable the On-Line Visualization of Liquid Metal Quality," *Proceedings of the International Symposium on Light Metals 1997 Métaux Légers*, C. M. Bickert and R. I. L. Guthrie, Eds., Canadian Institute of Mining, Metallurgy and Petroleum, Montreal, Canada, 1997, pp 197-211.
58. D. D. Smith, L. S. Aubrey and W. C. Miller: "LiMCA II Evaluation of the Performance Characteristics of Single Element and Staged Ceramic Foam Filtration," *Light Metals*, 1998, pp 893-915.
59. K. A. Bowman: "Magnesium by the Magnetherm Process—Process Contamination and Fused Salt Refining" *Light Metals*, 1986, pp 1033-1038.
60. P. G. Enright and I. R. Hughes: "A Shop Floor Technique for Quantitative Measurement of Molten Metal Cleanliness of Aluminum Alloys," *Institute Annual Conference—Castcon '96*, Bolton, UK, 1996, pp 9-14.
61. R. W. Deblois and C. P. Bean: "Counting and Sizing of Submicron Particles by the Resistive Pulse Technique," *Review of Scientific Instruments*, 1970, vol 41, pp 909-916.
62. D. A. Doutre, B. Gariépy, J.-P. Martin and G. Dubé: "Aluminum Cleanliness Monitoring: Methods and Applications in Process Development and Quality Control," *Light Metals*, 1985, pp 1179-1195.
63. J. D. A. Doutre and R. I. L. Guthrie: "Method and Apparatus for the Detection and Measurement of Particulates in Molten Metal," U.S. Patent 4,555,662 of Nov 26, 1985.
64. J. D. A. Doutre and R. I. L. Guthrie: "Apparatus for the Detection and Measurement of Particulates in Molten Metal," U.S. Patent 4,600,880 of Jul 15, 1986.
65. R. Hachey: "Apparatus for the Detection and Measurement of Suspended Particulates in a Molten Metal," U.S. Patent 4,763,065 of Aug 9, 1988.
66. R. Hachey and G. Deschene: "Apparatus for Particle Determination in Liquid Metals," U.S. Patent 5,039,935 of Aug 13, 1991.
67. R. I. L. Guthrie and H. Nakajama: "Continuous-Use Molten Metal Inclusion Sensor," U.S. Patent 5,241,262 of Aug 31, 1993.
68. R. I. L. Guthrie: "Molten Metal Inclusion Sensor Probes," U.S. Patent 5,789,910 of Aug. 4, 1998.
69. J. C. Maxwell: *A Treatise on Electricity and Magnetism*, 3rd. ed., Clarendon, Oxford, 1892, vol I, Chapter 9.
70. W. Schneider, H. P. Krug, V. Dopp and N. J. Keegan: "Evaluation of a Bounded Particle Cartridge Filtration System," *Light Metals*, 1996, pp 831.
71. D. A. Doutre: "Method and Apparatus for the Detection and Measurement of Solid Particles in Molten Metal," U.S. Patent 5,834,928 of Nov 10, 1998.
72. C. E. Eckert: "Apparatus and Method for Ultrasonic Detection of Inclusions in Molten Metals," U.S. Patent 4,563,895 of Jan 14, 1986.
73. Yi. Liu, L. C. Lynnworth and M. A. Zimmerman: "Buffer Waveguides for Flow Measurement in Hot Fluids," *Ultrasonics*, 1998, vol 36, pp 305-315.
74. T. L. Mansfield: "Probe for the Ultrasonic Inspection of Molten Aluminum," U.S. Patent 4,261,197 of Apr 14, 1981.
75. N. D. G. Mountford: "Testing of Liquid Melts and Probes for Use in Such Testing," U.S. Patent 4,981,045 of Jan 1, 1991.

76. N. D. G. Mountford and A. Simeonescu: "Detection of Particles in Liquid Aluminum," Final Report AFS Research, Liquid Metal Sonic L.T.D., Aug 1996.
77. R. C. Stiffler, R. C. Wojnar, M. F. A. Warchol, L. W. Cisko and J. M. Urbanic: "Apparatus and Method for Ultrasonic Particle Detection in Molten Metal," U.S. Patent 5,708,209 of Jan 13, 1998.
78. M. Pohl, M. Merz and W. G. Burchard: *Proceedings of the Conference of Progress in Metallography*, Leoben, Austria, Oct 1982, pp 126-139.
79. C. J. Siemensen and G. Strand: *Zeitschrift. Anal. Chem.*, vol 292, 1978, pp 207-212; vol 308, 1981, pp 11-16.
80. F. R. Block and R. Dittmer: "Field Distribution in Rotationally Symmetric Moving Conductors Inside Slag Detection Systems," *International Conference on Energy Transfer in Magnetohydrodynamic Flows*, Cadarache, France, Institut de Mecanique de Grenoble, 1991, pp 213-214.
81. F. R. Block, R. Dittmer and G. Gerbeth: "Electromagnetic Detection of Nonconducting Inclusions in a Liquid Metal Flow," *Proceedings of The First International Symposium on Electromagnetic Processing of Materials*, Nagoya, Japan, ISIJ, 1994, pp 61-67.
82. G. Alessandrini and E. Rosset: "Efficient Detection of an Inclusion in a Conductor," ARGESIM report 1997; No 11, I. Troch and F. Breitenecker, Eds., ARGE Simulation News, Technical University Vienna, Wien, 1997, pp 1015-1020.
83. E. Favre, P. Voumard, U. V. Stockar and P. Peringer: "A Capacitance Probe to Characterize Gas Bubbles in Stirred Tank Reactors," *Chemical Engineering Journal and the Biochemical Engineering Journal*, vol 52, 1993, pp 1-8.
84. Q. Fu and J. W. Evans: "Measurement of Bubbles in Aluminum by Means of a Capacitance Probe and the Removal of Magnesium by Gas Fluxing," *Proceedings of The Julian Szekely Memorial Symposium on Material Processing*, H. Y. Sohn, J. W. Evans and D. Apelian, Eds., Minerals, Metals & Materials Society, 1997, p 695.
85. Y. Hideaki and U. Yoshiyuki: "Method and Apparatus for Analyzing Nonmetal Inclusion in Metal," JP Patent 1997000129870 of Dec 4. 1998.
86. S. Makarov, R. Ludwig and D. Apelian, "Electromagnetic Visualization Technique for Nonmetallic Inclusions in a Melt," *Meas. Sci. Technol.*, vol 10, 1999, to appear.

Chapter 2

MELT CONTAMINATION AVOIDANCE

The objectives of this task are to study and understand the aluminum melt contamination process during processing; and particularly to develop and prescribe methods to reduce melt oxidation and hydrogen adsorption. Expected Benefits from this study are:

- Improved understanding of metal contamination process and the requirements and functions of fluxes;
- Development of fluorine-free, environmentally friendly fluxes, which can reduce both hydrogen adsorption and melt oxidation.

The following research methodology has been employed

Survey the aluminum melt contamination process and cleanliness methods in the literature and make a critical review of aluminum melt cleanliness;

- Characterize the physical properties and effectiveness of various fluxes – commercial and experimental - and propose fluxes that are more effective and less harmful to the environment.
- Determine the effect of composition of fluxes on the interfacial tension between the aluminum melt and the flux.
- Optimize the composition of the most promising non fluoride fluxes;
- Conduct trials with prospective fluxes to investigate their effectiveness.

Aluminum alloy castings have a potentially widespread application in automobile, aerospace and defense industries due to their excellent castability, corrosion resistance, and, particularly, high strength to weight ratio. However, the use of aluminum castings in fracture-critical structures is still limited in comparison with aluminum wrought alloys, even though casting of the parts would be a more economical production method. This is because the aluminum castings always contain some casting defects such as porosity and inclusions and, as a consequence, have less strength and particularly less reliability in properties compared with their wrought counterparts.

In order to increase the application of aluminum castings, reducing and eliminating casting defects is imperative. It is generally accepted that many casting defects, for instance gas porosity, oxide and other inclusions, are strongly related to the cleanliness of the aluminum melt. This task is aimed at developing methods to avoid melt contamination.

The use of fluxes for melt contamination avoidance is common in the Aluminum foundry industry. Gaseous fluxes are used to reduce the hydrogen content of aluminum melts. Chlorine is commonly purged into the melt through a rotary impeller, and this operation is broadly termed "degassing". Another set of solid fluxes is often used as a cover to reduce the oxidation of the melt and to separate oxide skins from the surface of the melt. Commercial fluxes used for this purpose consist of an equimolar mixture of NaCl and KCl with some fluoride or chloride additives. Such fluxes are reported in the literature to be extremely effective in acting as a cover and recovering metal that is lost to the dross. However, there are consistent environmental hazards in dealing with fluoride-based fluxes in the cast shop. In view of this, it was sought to study and develop alternative fluxes that are free of fluorides to accomplish the same tasks as the commercial fluxes currently in use. To achieve this end, some experimental compositions of fluxes were tested on a standard aluminum alloy to observe the effects of various alternative additives on the performance of the fluxes. Results from these tests are reported in this section and some detailed discussion is provided as well. This work will set the stage for further investigation in this area.

The objectives of this study are two–pronged. The study aims at improving the understanding of the melt contamination process in aluminum casting alloys and the mechanisms by which solid fluxes are capable of reducing melt contamination. Also, the study aims at developing environmentally friendly fluxes to reduce melt oxidation and metallic aluminum content in the dross. Environmentally friendly fluxes refer to salts that are free of fluorine, which is a toxic and hazardous component. Use of fluorine calls for special and expensive maintenance systems that must be used in order to control its emission into the environment.

The two primary goals of solid salt fluxes that are the object of the focus of this study are:

- To cover the molten metal and prevent surface oxidation
- To separate aluminum oxide from the metal

There are many kinds of salt fluxes that have been developed and used to remove oxide films and act as a cover. A literature review by Rao and Dawson[23] presents a bewildering array of fluxes that have been proposed. Most fluxes contain an equimolar mixture of sodium and potassium chlorides (NaCl-KCl) that forms a low-melting eutectic (685°C). The study here is also based on such a mixture. The mixture also has a low viscosity and surface tension. This increases the fluidity of the salt and helps it act as a better cover against oxidation of the melt.

During melting of aluminum, a wet dross layer consisting of oxide and small, entrapped globules of molten aluminum forms on the surface of the melt of an unfluxed bath of molten aluminum. This can easily be skimmed out. However, the metallic aluminum trapped in the dross is also lost in the process. The NaCl-KCl mixture cannot promote the separation of the metal from the dross and hence cannot affect the recovery of aluminum. Studies have clearly shown that additions of small amounts of fluorides to this mixture help in separation of the metal from the dross and hence promote coalescence of the metallic globules of aluminum [1, 2]. This allows the metal to be recovered from the dross. Fluorides are known to decrease the interfacial tension between the salt flux and the metal, hence their effectiveness. In addition, a second mechanism, based on thermal effects of the flux has been utilized to enhance the removal of metallic aluminum from the wet dross. The principle of this mechanism is based on the fact that fluxes that contain exothermic compounds, release oxygen and generate heat by combusting a portion of the metallic aluminum (and alloying elements). As a result, the dross is heated to high temperatures and this facilitates the coagulation of the larger droplets of aluminum, improves wettability of the flux and may also dissolve some of the thin oxide films. Some metal is lost by this reaction, but the resulting dry, powdery dross has a low metallic content.

In this study a set of experimental flux compositions were tested for oxidation resistance and metal recovery. A commercial flux was also tested for comparison. Eight different variations of the NaCl-KCl equimolar mix were tested during the study. These chemicals were obtained in cooperation with FOSECO and were manually mixed in the laboratory in correct proportion for the various tests. The compositions of these fluxes are listed in Table1.

Table 1. Experimental flux compositions used for testing

Flux No.	NaCl %	KCl %	Na_2SO_4 %	Na_2CO_3 %	K_2SO_4 %	K_2CO_3 %	$NaNO_3$ %	KNO_3 %
1	45	55	-	-	-	-	-	-
2	45	50	5	-	-	-	-	-
3	40	50	5	5	-	-	-	-
4	35	45	20	-	-	-	-	-
5	35	45	10	-	-	-	10	-
6	45	50	-	-	5	-	-	-
7	45	35	-	-	20	-	-	-
8	40	40	5	-	5	5	-	5

In addition to the above experimental fluxes, Coveral74 (a commercial flux) was also tested. This flux contained fluoride and was prescribed as a cover flux. However the exact composition was not revealed for proprietary reasons.

The TGA allows one to heat a sample and progressively measure the change in weight of the sample. Using this apparatus, samples were prepared from the cylindrical sections of failed test bars and heated in an oxidizing environment. The alloy used for all the tests was A356.

When a metal is placed in an oxidizing environment only the surface of the metal undergoes oxidation. Therefore, the geometry of the sample is an important factor in determining the amount of surface area available for oxidation. In view of this all the samples taken were of the same geometry. The samples used for TGA tests were disks weighing 3g and having a radius of about 4mm.

Each solid flux was prepared by mixing its components in their respective proportions. The majority of the salts were hygroscopic. Therefore, the prepared flux was thoroughly dried in an oven for 3-4 hours at 200°C prior to adding to the charge. The weight of flux taken for a sample was about half the weight of the sample. The metallic disk was placed in a crucible and the powder flux was added on top of it such that the surface of each sample was totally covered. Thereafter, the crucible was placed on one of the arms of a balance attached within the TGA unit. The furnace was brought up around the "hanging" test piece such that it completely surrounded the sample. The TGA was set to the RUN mode after making the necessary settings. The entire testing duration was divided into several segments, and within each segment, the heating rate, duration of the segment, temperature and gas flows were set according to Table 2.

The test duration for all samples was about 9 hours. During the first hour, the samples were heated to 770°C, such that the metal and flux were both in molten condition. The furnace was made inert by passing Nitrogen during this stage. Helium was always circulated to promote effective flow of gases and vapors emanating from the sample. For the remainder of the duration, the furnace was held at this temperature and the furnace atmosphere was set in such a way that compressed air was circulated into it. The sample was allowed to stand in this oxidizing environment and the change in weight with respect to time was automatically recorded. At the end of the duration of the test, the furnace was cooled to room temperature. Subsequently, the sample was retrieved from the TGA apparatus. The data for the change in weight with respect to time was automatically recorded to a file that was later used for analysis. Since most fluxes contain one or more volatile components, a base run of a sample consisting of the flux alone was made in each case. This data was subtracted from the data of the combined metal and flux samples. In this way, the change in weight with time for each sample was made to represent the actual weight change for the metallic sample only, and not of the flux associated with it.

Table 2 TGA settings for furnace heating cycles and furnace atmosphere control

	Schedule					
Segments	Rate (°C/min)	Temp (°C)	Time (h:m:s)	Helium	Nitrogen	Air
1	0	25	00:01:00	On	On	Off
2	50	750	00:14:30	On	On	Off
3	0	750	00:30:00	On	On	Off
4	0	750	08:00:00	On	Off	On
5	-40	25	00:18:00	On	On	Off

Note: The flux was preheated at 200°C for 4hrs before TGA analysis.

The dross produced during melting of aluminum alloys contains a significant amount of aluminum metal trapped in it. This is lost on skimming. However salt fluxes have been known to be effective in recovering some of this metal from the dross. The aim of this set of experiments was determining the effectiveness of salt fluxes in achieving metal recovery from a standard dross. The method of experimentation has been adapted from Shell, Nilmani et. al. [3].

Homogeneous dross was prepared in the laboratory using A356 alloy. Primary ingots of the alloy were melted in a 40 lb electric resistance furnace. A rotary impeller was used to introduce oxygen at a constant flow rate and at constant speed of impeller. After exactly 10 minutes, the dross formed on the surface was skimmed from the top, taking care not to skim from too close to the surface of the melt. The dross was cooled on a steel plate and separated into small, even-sized pieces. This dross was subsequently used for the experiments assuming a constant metal content and homogeneity.

One-hundered grams of salt flux were melted in 80mm internal diameter graphite crucible (see Fig. 1). An electrical resistance furnace was used for this purpose and the furnace temperature was initially set to 900°C. Once the flux reached a molten state, the temperature of the furnace was set to 800°C. The crucible was held at this temperature for about 60 minutes to ensure that the flux was homogeneously heated. Thereafter, 50 grams of standard dross was added to the crucible containing molten flux. The crucible was then held for about 1 hour before the furnace was turned off. The crucible was allowed to slow cool to room temperature to avoid any turbulence. Subsequently, the crucible was submerged in boiling water and the frozen salt cake was dissolved. The undissolved parts were then filtered, dried in an oven, and divided into three parts:

- Metal pad collected at the bottom of the crucible
- Metal beads greater than 600 micron in size
- Fine powder (oxide + salt + metal) under 600 micron size

The effectiveness of the flux is determined by its ability to strip away the oxide film from the metal and to promote coalescence of the metal. It was thus assumed that the spherical metal pad or pads formed at the bottom of the crucible were representative of the total metal recovered from the dross. The beads and irregular shaped parts were assumed to be dross from which metal was not recovered. The fine powder fraction was discarded as it was assumed that it did not contain any metal. Hence the recovery was calculated by:

$$\%\ \text{Recovery} = \frac{Metal\ Pad}{Metalpad + Metalbeads(> 0.6mm)} \times 100\% \qquad (1)$$

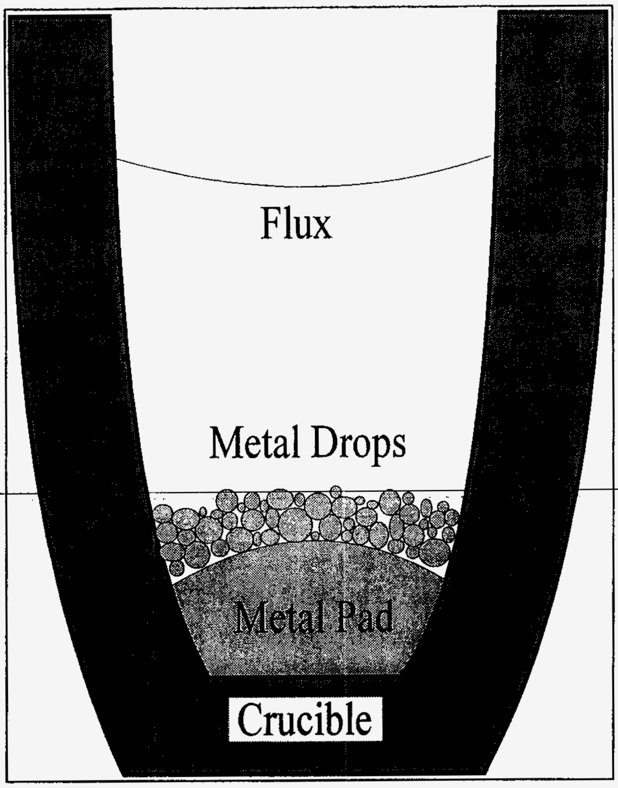

Figure 1. Recovery of metal by salt flux inside the graphite crucible

Figure 2 shows the normalized weight against time for the different flux compositions tested. The weights of different samples tested in the TGA were slightly different. To account for this difference, each weight value was normalized by representing it as a fraction of the initial weight of each sample. The curves were obtained by doing two runs for each sample to ensure repeatability of the data.

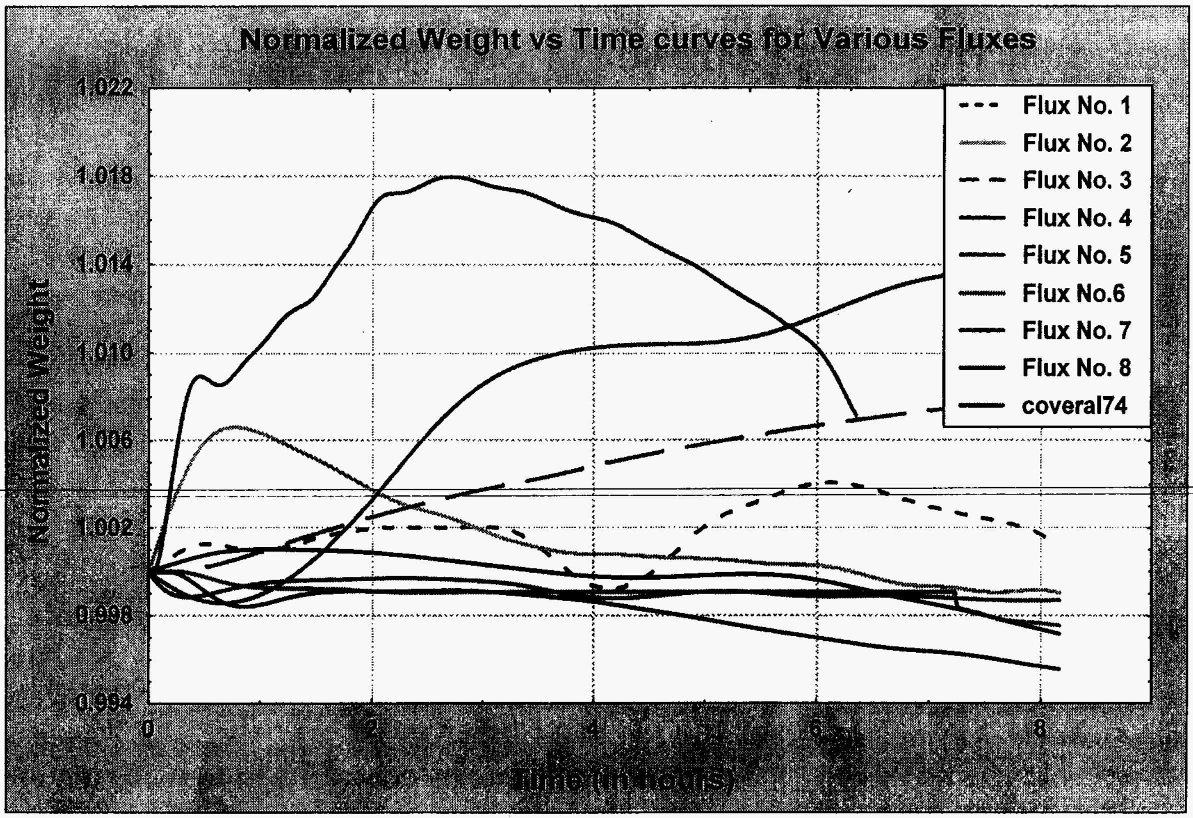

Figure.2. Normalized Weight vs Time for Various Fluxes tested in a TGA

The % metal recovery was calculated for the various fluxes as mentioned earlier. Two experiments were done for each flux and the average was taken. The results are shown in Figure 3. Figures 4-7 show the actual morphology of recovered metal using some of the fluxes during this testing.

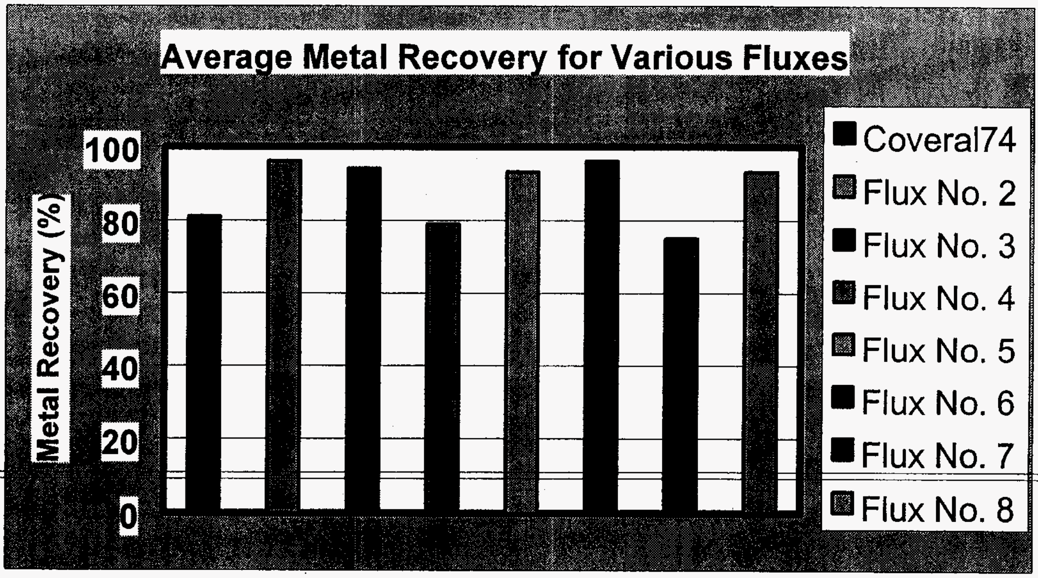

Figure 3. Average Metal Recovery for the Various Fluxes Tested

Figure 4. Morphology of Recovered Metal Using Coveral74

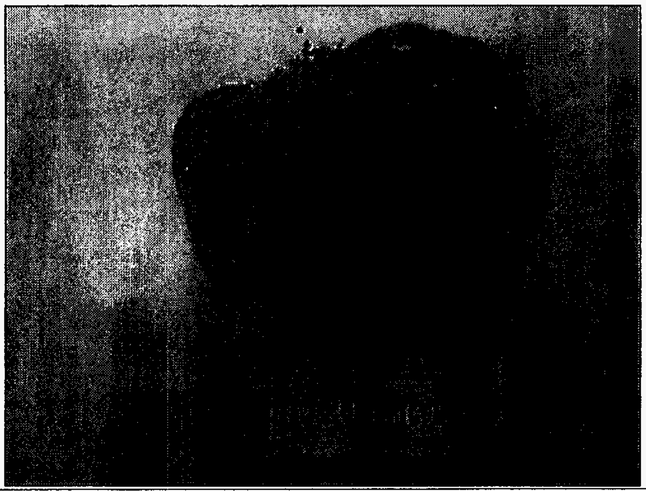

Figure 5. Morphology of recovered metal from Flux No. 2

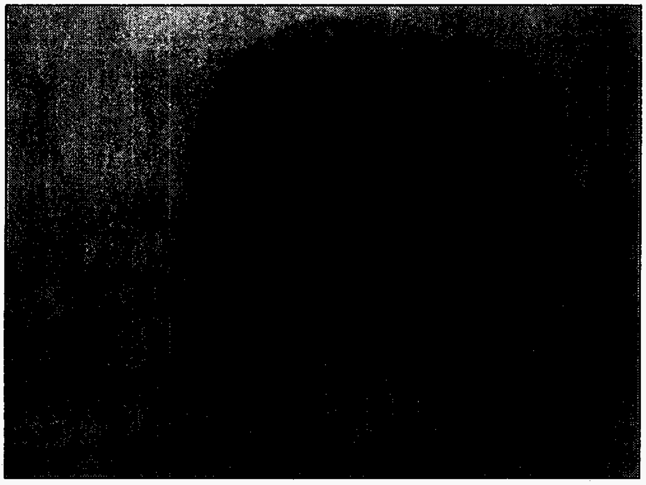

Figure 6. Morphology of Recovered Metal from Flux No.4

Figure 7. Morphology of Recovered Metal from Flux No. 6

It is evident from results shown in Figure 2, that not all the flux compositions are effective in preventing surface oxidation of the metal. In particular, Coveral74, Flux Nos. 1, 3, 5 and 7 all result in significant weight gain due to oxidation of the part. On the other hand, Flux Nos. 2, 4, 6, 7, 8 show good resistance to surface oxidation. Upon closely examining the compositions of these fluxes (See Table 1), it appears that fluxes containing Na_2SO_4 and K_2SO_4 function well as cover fluxes. Exceptions to this are Flux Nos. 3 and 5. These fluxes contain some amounts of Na_2CO_3 and $NaNO_3$ respectively. Both these compounds decompose on heating to release oxygen. This “released” oxygen may cause surface oxidation and hence conflict with the purpose of using these fluxes as a barrier for oxidation. $NaNO_3$, in particular, decomposes at about 450°C. Flux No.2 is a eutectic mixture of NaCl-KCl, with no additives. It causes a stable increase in weight before the magnitude of the increase drops progressively and the sample shows no further change in weight. Pure metals show this behavior. Flux No.8 is a mixture of Na_2SO_4 and K_2SO_4 coupled with a mixture of K_2CO_3 and KNO_3. This flux performs well in spite of the decomposition of the carbonates and the nitrates. The positive contribution by the sulfate mixture appears to offset the effect of the carbonates and the nitrates. Coveral74 is a commercial flux consisting of fluorides. It does not perform well as a cover flux as is seen from Figure 2. This may be explained by considering that the fluorides are extremely volatile. As a result, they may vaporize on heating and expose some of the metal to surface oxidation. The other components of Coveral74 are not known, as the composition is proprietary. One or more volatile components may also cause the failure of the flux to act as a protective layer.

Figure 3 shows the average metal recovery for various fluxes. Coveral74 does not perform as well as most of the other fluxes as shown by Figure

3. The other two flux compositions that do not show a very high recovery (>90%) are Flux No.4 and Flux No.7. Both these compositions consist of a high percentage of sulfates (20%). However, the fluxes containing lower amounts of sulfate work well. This is testified by the high recovery obtained using Flux Nos. 2,3,5,6 and 8. Flux No. 1 was not tested for metal recovery as it is reported in the literature [4]that a pure equimolar mixture of NaCl and KCl does not help in metal recovery from the dross.

The criteria for a flux to achieve good "drossing", depends on the ease with which molten metal can separate from the dross or oxide layer. Wang and Brochu [5] proposed the initial stage for oxide film removal. When the metal inside the oxide layer melts, it tends to assume a spherical shape by which it becomes most thermodynamically stable. However, the solid oxide layer restricts this. The underlying metal expands more than the oxide layer and thus small cracks are created that weaken this layer. This does not remove the droplet from the oxide layer, but it becomes partially detached. The salt comes into contact with the metal/oxide interface through the cracks. At this stage there are three phases co-existing and three tensile forces act at a common point (See Figure 8).

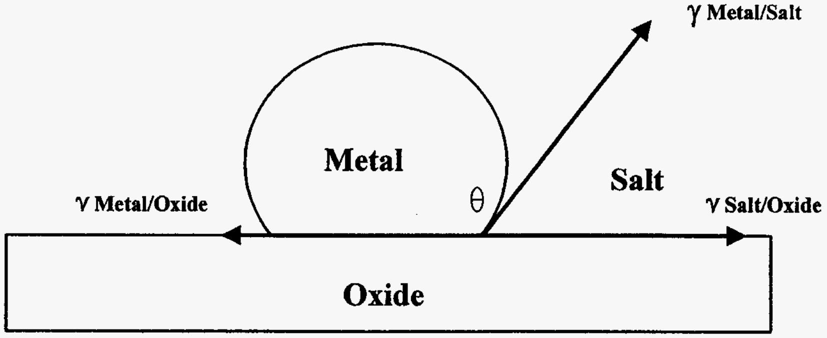

Figure 8. Energetics of a Metal Drop on Oxide Film

By conserving forces about the common contact point, we get:

$$\gamma_{Metal/Oxide} = \gamma_{Salt/Oxide} - \gamma_{Metal/Salt} * \cos\theta \qquad (2)$$

where γ represents the interfacial energy between two phases.
In order for the droplet to form and detach, the contact area of the droplet must ideally decrease to a point contact. This is possible if $\gamma_{Metal/Oxide}$ is of a high value. This force will try to push the point of contact towards the center and strip the metal drop from the oxide layer. The value of $\gamma_{Metal/Oxide}$ will be high if $\gamma_{Salt/Oxide}$ has a high value and/or $\gamma_{Metal/Salt}$ has a low value. It has been reported by Roy ^{27} that the

interfacial tension between the Aluminum metal and salt decreases significantly when the salt contains fluoride additives (NaF, KF, Na_3AlF_6). This behavior was explained in terms of the activity of Na or K in the system. Dewing and Desclaux [6] stated that Na and K act as surface active metals and may get adsorbed to the surface of the metal, thus causing the interfacial tension between the metal and salt ($\gamma_{Metal/Salt}$) to decrease.

Fluorides will cause an increase in the activity of sodium in the molten flux by so-called "Exchange Reactions" [7] . For the case of pure Al in equilibrium with equimolar NaCl-KCl (without additives), the activity of Na will be controlled by the following exchange reaction:

$$3NaCl + Al \rightarrow AlCl_3 + 3Na \qquad (3)$$

K_{eq} at 740°C = $8.34 * 10^{-24}$, a_{Na} is directly proportional to $K_{eq}^{1/3}$
For a similar exchange reaction [7] with KCl, $K_{eq} = 3.28 * 10^{-27}$
In the presence of fluorides [7], the following exchange reaction may occur.

$$3NaF + Al \rightarrow AlF_3 + 3Na \qquad (4)$$

$$K_{eq} = 3.9 * 10^{-9}\ ,\ a_{Na} \propto K_{eq}^{1/3}$$

It is observed that this value of K_{eq} is much greater than the value obtained in the absence of fluorides (See Eq. 2). This causes the activity of Na to be controlled by the reaction shown by Eq. 3 rather than that shown by Eq. 2, in the presence of fluorides. This would lead to an increase in Na activity in the metal and hence decrease the value of $\gamma_{Metal/Salt}$. A lower value of $\gamma_{Metal/Salt}$, as previously described, favors stripping of the metal drop from the oxide.

In the current study, fluoride-free compositions were investigated. In particular, it was seen that Na_2SO_4 and K_2SO_4 appear to work well in small amounts with or without nitrates or carbonates. An exchange reaction for Na_2SO_4 and K_2SO_4, and a calculation of the value of K_{eq} is shown here;

$$\frac{3}{2}Na_2SO_4 + Al \rightarrow \frac{1}{2}Al_2(SO_4)_3 + 3Na \qquad (5)$$

At 740°C (1013 K):
$\Delta G^f (Na_2SO_4) = -940.701$ kJ/mol.[30]
$\Delta G^f (Al_2(SO_4)_3) = -2264.351$ kJ/mol.

$\Delta G^f(Al) = \Delta G^f(Na)$
$\Delta G^{rxn} = \Delta G_{products} - \Delta G_{reactants}$
$\Delta G^{rxn} = 1/2 * \Delta G^f (Al_2(SO_4)_3) - 3/2 * \Delta G^f (Na_2SO_4)$
Thus, $\Delta G^{rxn} = 345.9355$ kJ/mol.
$\Delta G^{rxn} = -RT\ln K_{eq}$
$\ln K_{eq} = -\Delta G^{rxn} / RT = -(345.9355 * 1000) / (8.314*1013)$
$K_{eq} = 4.11 * 10^{-15}$

The similar exchange reaction for K_2SO_4 is:

$$\frac{3}{2} K_2SO_4 + Al \rightarrow \frac{1}{2} Al_2(SO_4)_3 + 3K \qquad (6)$$

At 740°C:
$\Delta G^f (K_2SO_4) = -1024.650$ kJ/mol [30]
Upon similar calculation we get:
$K_{eq} = 1.31 * 10^{-21}$

These values, especially the K_{eq} of Na_2SO_4, although lower than the K_{eq} in the presence of fluorides, is still significantly higher than the value of K_{eq} for a pure, equimolar mixture of NaCl-KCl. Hence, one can state that sulfate additions ease the exchange reactions and increase the activity of Na in the metal. This causes a decrease in the interfacial tension between metal and salt and hence explains the positive performance of sulfate additives in the salt flux. Nitrates and carbonates decompose on heating releasing a lot of heat. This heat improves wettability of the flux and may also dissolve some thin oxide films thus enhancing metal recovery. However, too much combustion of such compounds will result in burning metal to form Al_2O_3, thus promoting loss of metal. This explains the good performance of Flux No.8 (contains small amounts of nitrates and carbonates) in metal recovery.

The mechanism of “cover fluxes” is not well reported in the literature. Intuitively, it is tacit that “cover fluxes” should act as a physical barrier to surface oxidation. The overall density of the flux is much lower than that of the metal, so that it floats on top of the metallic surface. The oxygen from the air has to diffuse into the metal through the molten salt flux cover, in order that oxidation of the metal may take place. Alternately, direct contact of the oxygen with the metal is possible at points where the metal is not effectively covered with flux. Diffusivities of all liquids are of the same order; hence a more significant criterion is the efficacy with which a molten salt flux covers a molten metal surface. The physical situation is depicted in Figure 9, where there are three phases (Salt flux, Metal and Air) in contact at one point.

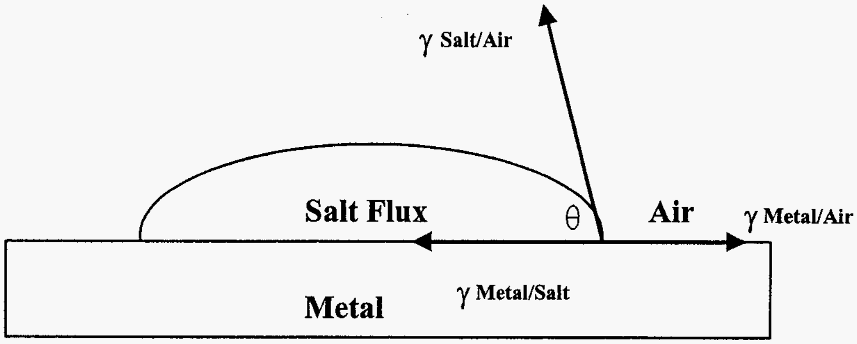

Figure 9. Energetics of a Cover Flux over Metal

Unlike the condition for extraction of metal drops from the oxide layer, in this case it would be necessary for the molten flux to spread uniformly over the metal such that the contact area between the metal and salt is as large as possible. Again, conserving the three interfacial energies at a point we have:

$$\gamma_{\mathrm{Metal/Salt}} = \gamma_{\mathrm{Air/Metal}} - \gamma_{\mathrm{Air/Salt}} * \cos\theta \qquad (7)$$

For the salt to spread the value of $\gamma_{\mathrm{Metal/Salt}}$ should be low, such that the contact area of the flux and metal increases. Hence we observe that this condition is the same as that for metal recovery. It has been shown earlier that sulfates reduce $\gamma_{\mathrm{Metal/Salt}}$. This explains the good performance of fluxes containing sulfate additives in preventing surface oxidation. Needless to say that this is not the sole criterion for effective fluxing but it is one that is controlled easily by altering the chemistry of the salt flux.

It can be concluded from this study that Sodium Sulfate and Potassium Sulfate are prospective cover as well as drossing fluxes. Additives of Nitrates and Carbonates abet the performance of drossing fluxes and may work well in conjunction with the sulfate additives for recovering metal from dross. However, they do not perform well as cover fluxes to prevent surface oxidation.

References

1. Friesen, K.J., Utigard, T.A., Dupuis, C., and Martin, J.P., "Coalescence Behaviour of Aluminum Droplets under a Molten Salt Flux Cover", *Light Metals*, 1997, Pp. 857-864.
2. Peterson, R., "Effect of Salt Flux Additives on Aluminum Droplet Coalescence", *2nd International Symposium on Recycling of Metals and Engineering Materials*, The Minerals, Metals and Materials Society, 1990, Pp. 69-83.

3. Shell, D.J., Nilmani, M., Fox, M.H., and Rankin, W.J., "Aluminum Dross Treatment Using Salt Fluxes", 4th Australasian Asian Pacific Conference on Aluminum Cast House Technology, 3-6 July 1995, edited by Madhu Nilmani, Pp.133-146.
4. Utigard, T.A., Friesen, K., Roy, R.R., Lim., J., Silny, A., and Dupuis, C., "The Properties and Uses in Molten Aluminum Processing", *JOM,* November 1998, Pp. 38-42.
5. Wang, Z., and Brochu, L., "Aluminum Melt Loss Fundamentals", *(Report Alcan International Limited),* 1993.
6. Dewing, E., and Desclaux, P., " Interfacial Tension Between Aluminum and Cryolite Melts Saturated with Alumina", *Met. Trans. B.*, v 8B, 1977, Pp. 555-561.
7. Roy,R., Sahai,Y., "Interfacial Tension in Molten Aluminum Alloys and Salt Systems", *Light Metals,* 1993, Pp. 1067-1072.

Chapter 3

PHASE SEPARATION TECHNOLOGY

1. INTRODUCTION

The objective of this task is to expand the existing knowledge about phase separation technology used in clean metal processing of aluminum alloys. Specifically, the research focuses on sedimentation, flotation, filtration and electromagnetic separation.

To design and implement an efficient melt treatment process, it is important to develop a clear understanding of the physics of the basic mechanisms involved in phase separation. In this task, the treatment process is investigated both numerically and empirically. The goal is to develop comprehensive, reliable models of the processes. These models may be used in

- the optimization of the operating parameters of treatment furnace and rotary degasser for the removal of solid inclusions,
- the development of ceramic filters with enhanced sintering capture mechanisms, and
- the investigation of the effectiveness and the ideal method of deploying electromagnetic separation in aluminum melt treatment.

The strategies of investigation used in this study are as follows:

- Augment existing knowledge base of phase separation technology as it applies to clean metal processing of aluminum alloys by conducting an extensive literature search, identifying various technologies used in melt treatment, and producing a critical literature review.
- Develop a mathematical/computational model to simulate the flotation treatment process and optimize the process parameters.
- Develop a mathematical/computational model to simulate the sedimentation treatment process and optimize the process parameters.

A mathematical model has been developed for flotation/fluxing treatment process. This model considers the removal of solid inclusions from the aluminum melt using rotary degasser. The model has two main modules: CFD module, collision module and bubble attachment module. The Taguchi method for design of experiments has been employed to optimize the flotation process parameters

2. LITERATURE REVIEW

2.1 Introduction

The role of molten metal treatment has become increasingly important in the overall scheme of the foundry operation. By treating molten metal, one is able to add value to the end product, improve productivity, and increase quality. The quality of molten metal can be improved by proper control of two interrelated parameters: chemical composition and unwanted phases. In particular, control of unwanted phases in the molten metal is a critical element in the melting/casting sequence. The term "unwanted phases" refers to exogenous solid particles (inclusions), liquid phases that are present above the liquidus temperature of the alloy, and gaseous phases (such as dissolved hydrogen in the melt).

Several general classes of inclusions exist in aluminum foundry products. These are:

- Oxides, which originate from direct oxidation in the melt or which are introduced by furnace charges. For example, alumina (Al_2O_3) inclusions are found in magnesium-free alloys while magnesia (MgO) inclusions (resulting from oxidation of localized concentrations of magnesium) are found in magnesium alloys. Magnesium aluminate spinel ($MgAl_2O_4$) is another oxide formed by melt oxidation.

- Salts, which can form when argon/nitrogen chlorine mixtures are used to remove hydrogen from melts (e.g., $MgCl_2$ in Mg-alloys).

- Carbides (e.g., Al_4C_3), which may form during the aluminum melting process or when certain solid degassing tablets (e.g., C_2C_{16}-hexachloroethane) are used. Their size ranges from 1 to 50 microns.

- Intermetallic compounds such as titanium aluminide ($TiAl_3$) particles that originate from the use of poor quality grain refining materials. They are generally under 5 microns.

- Exogenous refractory inclusions arising from spalling of high silica refractories into the melt.

Though there are several aspects to molten metal quality, the focus of this review is the removal of impurities from aluminum alloys rather than chemical composition control. Most of the inclusions presents in aluminum alloys exhibit a complex structure and are hard and brittle. The critical size of inclusions that may be tolerated in a casting depends on the end application. In most cast components, inclusions with sizes greater than 10 to 20 μm may have a drastic effect on the quality of the part. The presence of inclusions or impurities in a casting may cause undesirable problems or deficiencies in the final fabricated aluminum alloy product. These include the reduction of mechanical properties, excessive tool wear during machining, increased porosity, poor surface finish and lack of pressure tightness.

The common methods of inclusion removal from molten metal are flotation and/or fluxing of inclusion particles using small gas bubbles, sedimentation during holding and filtration through cake filters or porous, rigid media filters. Another promising technique is electromagnetic separation. This review provides a description of the basic mechanisms underlying the flotation process, along with the various systems that are currently available on the market. In addition, the review provides a description of the various mathematical models developed to simulate particle flotation in molten metals.

2.2 Flotation and Fluxing

In a typical flotation and fluxing treatment process, a reactive or inert gas, or a combination of both gases, is purged into the liquid metal. Chlorine and fluorine are the most commonly used reactive gases, and argon and nitrogen are the most commonly used inert gases. As the gas bubbles rise to the surface, they come in contact with the inclusions and dissolved hydrogen and carry them to the top slag. The inclusions removal efficiency depends largely on the contact time between the bubbles and the metal. It also depends on the ratio of interfacial gas : metal surface, and the gas volume that is injected into the melt.

2.2.1 Physical Mechanisms in Flotation and Fluxing

Following are the models/mechanisms operating to remove impurities from the melt when using fluxing and flotation:

- Hydrogen gas that is dissolved in the melt diffuses to the fluxing gas, which has a low hydrogen partial pressure and therefore can absorb hydrogen. The hydrogen removal rate is limited by diffusion kinetics.

- Sodium and other alkaline earth metals that are dissolved in the melt diffuse fairly quickly in the melt (sodium is the fastest), but the equilibrium pressure of these elements in an inert fluxing gas is low and, therefore, only small amounts can be absorbed. To speed up the absorption, an active gas (such as chlorine) is sometimes used. With this gas-mixture, the removal of alkaline metals is also limited by diffusion kinetics.

- Non-metallic particles are removed by flotation to the melt surface. The size and number of gas bubbles limit the removal of particulates.

The removal efficiency also depends on the agglomeration of particles caused by turbulence in the melt.

It is believed that the addition of chlorine or other halogens to the purging gas affects the surface tension of the bubbles and makes the oxides and inclusions stick more quickly to the surface of the bubbles. Reactive gases decrease the hydrogen partial pressure in the bubbles and may enhance hydrogen removal. Chemical reactions may take place that produce salts from the dissolved alkaline metals; the salts are then removed from the melt.

Depending on the hydrodynamics in the molten metal, the rate-determining step for impurity removal may depend on mass transfer or on chemical reactions at the bubble surface. The impurities must be transported from the bulk metal to the surface of the bubble through a diffusion boundary layer. At this boundary, either a chemical reaction may occur or the impurity species may simply cross into the bubble. The impurity removal kinetics will be decided by the rate-determining step, which must be determined experimentally for given flux conditions. The transport of the impurities to the bubble surface and the flotation of the bubble largely depend on the velocity and turbulence fields due to the flow of melt and gas bubbles in the treatment reactor.

2.2.2 Governing Equations for Flotation and Fluxing

Impurity Removal (Depletion) Kinetics

The depletion kinetics for impurities can be expressed as follows:

$$-r_i = \frac{\partial C_i}{\partial t} \tag{1}$$

where, r_i = reaction rate of component *i*
C_i = concentration of component *i*
t = time

Hence, the reaction rate, which in the case of fluxing is equivalent to the depletion rate, is dependent on the change in concentration of the particular species. However, the removal reaction for each impurity may occur at a different kinetic order.

To evaluate the kinetic order of the depletion rate, an integral method of data analysis was used by first expressing the rate equation as:

$$\frac{\partial C_i}{\partial t} = k\, f(C) \tag{2}$$

where, k = the rate constant
$f(C)$ = concentration function

By rearranging and gathering the concentration terms on one side of the equation and integrating, a concentration function is produced that is proportional to time.

$$-\int_{C_{AO}}^{C_A} \frac{\partial C_A}{f(C_A)} = kt \tag{3}$$

where, C_A = concentration of component A at time t
C_{AO} = starting concentration of component A

A plot of this concentration function with time will produce a straight line with a slope of k.

The concentration function will vary for different depletion mechanisms. The two most common depletion mechanisms are either first order or zero order. The rate of a first-order reaction is dependent on the concentration of the reactants as described by the following equation:

$$-\ln \frac{C_A}{C_{AO}} = kt \tag{4}$$

On the other hand, zero-order reaction kinetics imply that the rate of impurity removal is independent of the species concentration:

$$C_A = kt \tag{5}$$

In most cases, these two mechanisms are able to adequately describe the reactions occurring during fluxing operations.

Flotation Theory

A theoretical analysis of flotation of inclusions in aluminum melts was first presented by A.G. Szekely [1]. Szekely showed that successful flotation of inclusions required the generation of a large surface area for collecting the inclusions in the form of small gas bubbles, and vigorous stirring of the molten metal. He also showed that large inclusions (greater than 80 µm) are collected from molten aluminum by inertial impact on the gas bubbles that range in size from 1 to 10 mm; smaller particles are captured by peripheral interception, as shown in Figure 1; and very small particles (less than 1µm) are agglomerated by Brownian coagulation or turbulent coagulation and then floated out by the gas bubbles. The analysis made by Szekely was later extended by Simensen [2] to include both in-line fluxing units and furnaces. Simensen found that heavier particles with spherical diameters above 110 µm are removed mainly by impact collision (*Inertial Impact Theory),* while smaller particles are removed by peripheral interception with the bubbles (*Peripheral Interception Theory).* Both theories are described in the following paragraphs.

Inertial Impact Theory - For a given bubble and particle size, the number of particles collected by the first, second, third, etc. bubbles rising in a column in succession is proportional to the particle collection efficiency, E, and to the instantaneous concentration of the particles present in the column [1].

The concentration of particles left in the column after collecting by N_x bubbles is:

$$C = C_0(1-E)^{N_x} \tag{6}$$

where C_o is the original concentration of particles.

The number of bubbles encountered by the inclusions in a column of diameter d_B during a time period t is [2]:

$$N_x = \frac{3Gt}{2Ad_B} \tag{7}$$

where G is the total amount of gas purged into the melt per unit time and A is the surface area of the melt.

In the case of gas fluxing in a holding furnace, Equations (5), (6) and (10) give the concentration of inclusions after a treatment time, t. In the case of in-line gas fluxing, if the melt is kept for time t in the unit, the amount of gas purged:

$$G = \dot{W}m \tag{8}$$

and the number of bubbles used in the removal of inclusions is:

$$N_x = \frac{3\dot{W}mt}{2Ad_B} \tag{9}$$

where, $\dot{W}$ is the amount of melt moving through the in-line fluxing unit per unit time and m is the amount of gas purged for each kilogram of molten metal.

The collection efficiency, E, has been derived based on the assumption that large inclusion particles may collide with the bubbles by establishing their own path due to inertia, as shown in Figure 1a. On the other hand, small particles will follow the streamline and will not collide with the rising bubbles. Based on Langmuir and Blodgett's analysis—cited by Szekely [1]—the collection efficiency for inertial impact is:

$$E = \frac{S^2}{(S+0.06)^2} \qquad for \quad S \geq 0.08 \tag{10}$$

where the Stoke's number, S is equal to :

$$S = \frac{2 \mathrm{Re} \rho_f a_i^2}{9 \rho_i d_B^2} \tag{11}$$

and where, a_i is the particle diameter, ρ_i is the particle density, ρ_f is the melt density and *Re* is the Reynold's number. For bubbles about 5 mm in diameter, the impact theory is valid for particles larger than 100μm in diameter.

Peripheral Interception Theory - According to Szekely [1], smaller particles, which are completely entrained by the streamline, have only a small chance of being captured by the rising bubbles. Only those particles which can come within touching distance of a bubble around its equator, may have a chance to be captured, as shown in Figure 1b. Szekely defined the efficiency of such peripheral interception as:

$$E = \left(1 + \frac{2a_i}{d_B}\right)^2 - 1 \cong \frac{4a_i}{d_B} \tag{12}$$

by neglecting the second power of a_i/d_B and assuming a particle size less than 0.1 mm and a bubble size on the order of 1 to 10 mm.

According to Simensen (1989), the collection efficiency is approximated as:

$$E = 3a \frac{f}{d_B} \tag{13}$$

The above expression is based on Ranz and Wong's work [Simensen(1989)], where f is a probability parameter that is determined by the particle's wettability by the melt and the gas bubbles. f is close to 1 when the surface energy is high toward the melt and low toward the gas bubbles. It is much less than 1 when the particles are well wetted by the melt. The concentration of the particles after peripheral interception can be derived using Equations (6) and either (12) or (13).

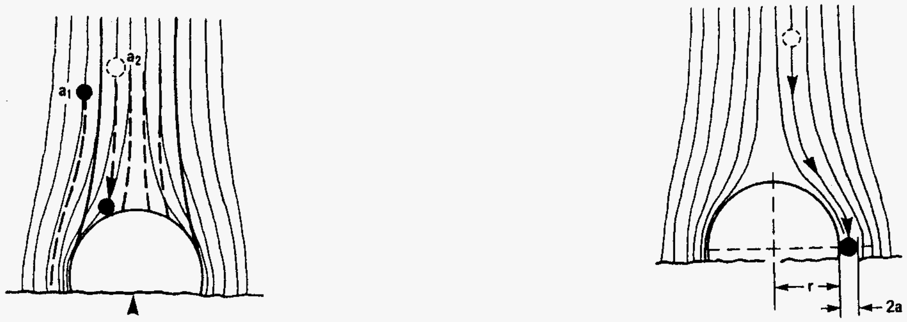

a) Inertial impact

b) Peripheral interception

Figure 1. Inertial impact and peripheral interception of particles by gas bubbles [1]

2.3 Commercial Flotation and Fluxing Systems

A number of commercial gas-purging systems are available. Depending on the method of gas purging into the melt, they can be grouped in the following categories:

- Porous lances
- Porous floor plugs
- Flux injection units
- Rotary gas purging units

Each of these categories of systems is discussed in some detail in the following paragraphs.

2.3.1 The Porous Lance

Porous lances are available in configurations ranging from straight lances to T and L shapes in order to fit each furnace application. Many foundries still use the old straight graphite lance with a small hole at the bottom. These lances may have been effective with chlorine, but they are slow and inefficient when used with inert gasses or gas mixtures. Figure 2 shows an L-shaped lance used in British Aluminum Co.'s FILD (Fumeless In-line Degasser) unit [3]. In this unit, metal is treated with nitrogen under a salt flux cover, followed by passage through a bed of flux-coated ("sticky") alumina balls. Nitrogen is introduced into the melt through the L-shaped lance at such a rate as to produce vigorous turbulence whereby most of the oxide in the molten aluminum is wetted and absorbed by the salt flux.

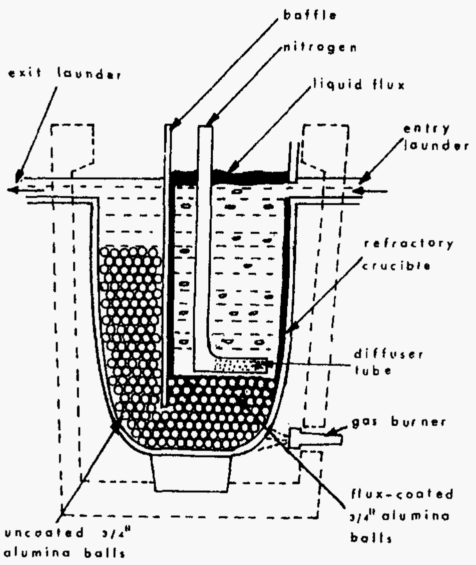

Figure 2. **L-shaped lance in FILD in-line melt treatment process [3]**

2.3.2 Porous Floor Plugs

The use of refractory porous plugs imbedded in the refractory floors of furnaces has proved to be quite effective. The plugs must be carefully installed in proper patterns to create a wide dispersion of bubbles and they should not be turned off during operation. Figure 3 shows a typical porous plug. These plugs are normally used in high-production degassing boxes or on the floor of large holders. They are not normally used in smaller foundries due to their high cost and difficulty in replacement.

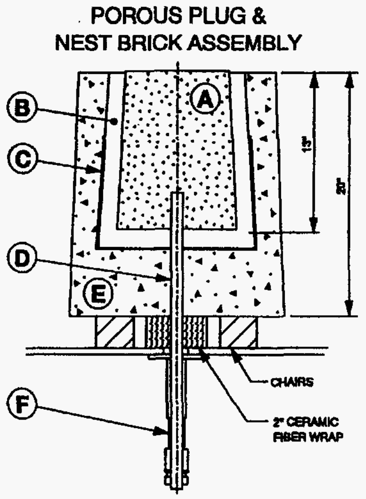

A → round reverse tapered porous refractory core

B → non-porous refractory lining
C → inconel can
D → inconel flux gas supply pipe
E → refractory nest block
F → external packing gland

Figure 3. **Schematic of a porous plug [4]**

Metal quality can be greatly improved by using porous plugs [4]. Tests have indicated that hydrogen levels in the bath immediately following fluxing are reduced by up to 50% compared to levels achieved with a standard fluxing lance. Particulate counts also appear to improve despite significant reductions in settling times. Using the porous plug instead of the hand-held fluxing lance significantly reduces fluxing time and the chlorine content of the flux gas. Another significant benefit of the porous plug is its ability to eliminate temperature stratification in the holding furnace.

2.3.3 Flux Injection

Flux injectors introduce flux and gas through a lance submerged in the furnace. The flux reaction removes gas and inclusions from the aluminum melt in a relatively short period of time. These systems are used primarily in batch type applications, such as crucible furnaces and holders.

The flux injection method addresses the major drawback of conventional practices–limited contact of melt surfaces with the unwanted impurities in the melt. Flux injection overcomes this limitation by delivering predetermined amounts of powdered flux beneath the melt surface. Upon leaving the lance, the flux melts into small droplets that expose a large specific surface to the melt as they float to the surface, which accelerates flux-induced metal cleaning. Degassing occurs when injected fluxes release halide gases that sparge hydrogen.

Typical flux injection equipment includes a dry-powder feeder that mixes powdered flux into an inert gas stream, carrying it through a lance immersed in the melt. Further developments include hybrid equipment that combines the best traits of flux injection and spinning nozzle degassing.

The MINT System, developed by Consolidated Aluminum, is an in-line treatment process in which fluxing gas is injected into the melt by high-pressure nozzles [5]. Figure 4 shows a schematic of a typical MINT system. Metal from a furnace enters through the tangential port near the top of a "swirling tank" reactor. The metal flows downward in a helical fashion and leaves the bottom of the reactor. Small bubbles of fluxing gas are injected into the melt by high-pressure nozzles located in the conical section at the reactor bottom. These gas bubbles rise counter-current to the flowing metal. The rotating motion of the metal causes an even distribution of the rising bubbles and reduces the tendency of the gas to channel through the liquid metal.

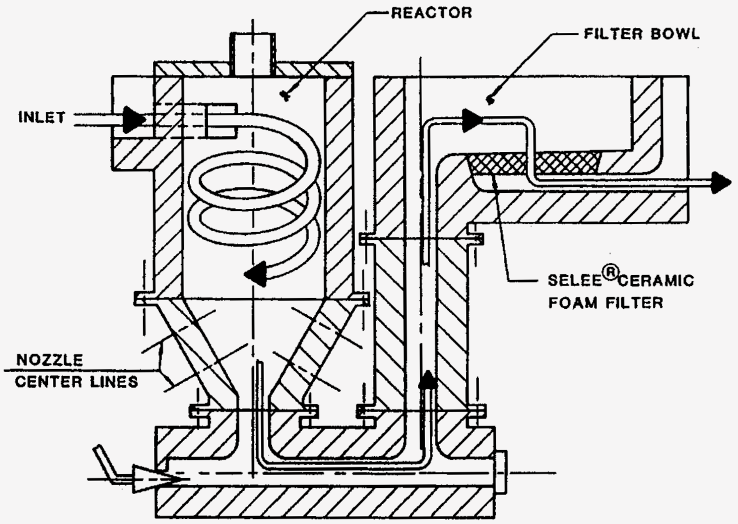

Figure 4. Schematic of MINT system [5]

Counter-current flow between the molten metal and the treatment gas is a major advantage of the MINT system. Higher concentrations of the dissolved hydrogen are removed at the top of the reactor where there is contact with the less pure treatment gas, while the fresh treatment gas reduces hydrogen levels in the melt near the bottom of the reactor. Note that the dispersion of treatment gas bubbles is achieved without any moving parts in contact with the molten metal.

Metal cleansed of soluble impurities leaves the reactor through a bottom port, flows through a horizontal crossover section, and moves vertically up a riser pipe to the filter bowl. Nonmetallic inclusions are removed by a disposable ceramic foam filter, which is placed in the filter bowl. Fully treated metal then flows into an adjacent casting machine.

The unique features of the MINT System have provided hydrogen removal efficiencies up to 75% and sodium and lithium removal efficiencies up to 64% and 78%, respectively. Inclusion removal has exceeded 90% with the use of SELEE filters.

The cast house trough reactor, as shown in Figure 5 [6], is based on a new design concept that involves increasing the degassing bubble population density in the molten aluminum by a factor of ten (in comparison to the spinning nozzle reactor) and creating extreme turbulence. These have been achieved by using closely spaced high-velocity submerged jets to introduce argon into the melt in the form of very small bubbles. The time required for a hydrogen molecule to get to a bubble surface has thus been substantially reduced and the relative velocity between the argon bubble and the molten metal has been greatly increased. Because of the reduction in the required bubble residence time and the extreme turbulence, the reactor can be small and therefore sturdy in construction. The single-stage cast house trough reactor occupies little more space than a four-foot section of a transfer trough. Heating is not required and cleaning can be accomplished in a matter of minutes. There are no moving parts, and with the exception of the argon flowmeter and valves, there are no controls or instrumentation that require special maintenance.

A typical hydrogen removal performance of the cast house trough reactor is 60%, while particulate removal varies from 34% to 100%, depending on the type of particulate present in the melt.

Figure 5. Cast house trough reactor [6]

2.3.4 The Rotary Gas Purging Unit

The use of a rotary gas purging unit is a highly effective method of removing inclusions from molten aluminum. An electric or air motor rotates a graphite rotor with a specially shaped impeller at 350 to 900 rpm, thus creating a mass dispersion of small bubbles. The rotary unit is highly effective in all types of foundry applications, from small batch crucible furnaces to large continuous casting systems. One, two or more rotors may be mounted on the same rotor shaft. The rotary unit has been used for many years, but only within the last 10 years has the system cost been affordable for the smaller foundries. A number of manufacturers offer these systems and their efficiency is high compared with other methods. They include:

- R.D.U., FOSECO Intl.
- SNIF, Union Carbide
- Alpur Refining System, Aluminum Pechiney

- ÅSV inline system, Årdal og Sundal Ver a.s. and SINTEF
- ALCOA 622, Alcoa
- Hycast Metal Refining System, Hydro Aluminum
- GBF System
- REVROT, Apogee Technology

These rotor gas-purging units can be used in different configurations, such as

- In-line units for melt treatment during casting operations.
- Batch units for treatment of melts in furnaces or transportable crucibles.
- Units for pretreatment of pot room metal and removal of sodium and lithium.

Each of these units is described in detail in the following paragraphs.

The RDU - Figure 6 shows a schematic diagram of an RDU. This system is developed by FOSECO International [7]. The gas stream is ejected horizontally from the orifice of the rotor. The rotor of the RDU unit provides intimate mixing of gas and molten metal at the point of gas introduction. The system can use either pure argon or argon/chlorine as the purging gas.

When using an argon/chlorine mixture of gases, typical hydrogen reductions are from 0.30 ml/100 gm down to 0.05ml/100gm for 2000, 3000, 5000 and 7000 series aluminum alloys [7]. These reductions are possible with a single rotor and 2.5 to 4 minutes contact time.

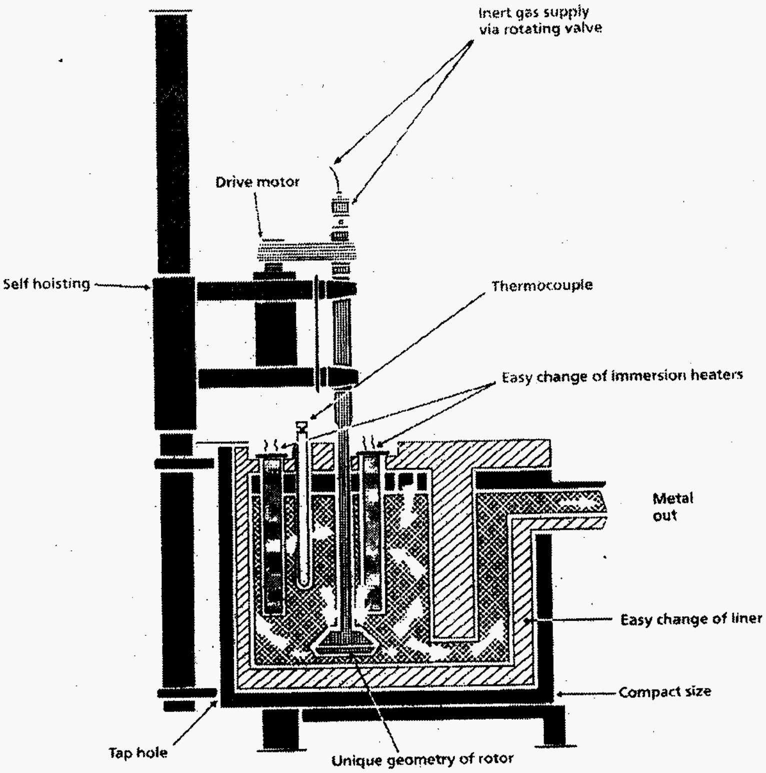

Figure 6. A Typical RDU [7]

The Spinning Nozzle Inert Flotation (SNIF) Unit - The spinning nozzle inert flotation (SNIF) is a highly efficient way of dispersing gas bubbles throughout the aluminum melt, thereby removing dissolved hydrogen, solid inclusion materials and alkali metals. SNIF equipment was first introduced by Union Carbide in 1974. Figure 7 [8] shows a typical SNIF nozzle and chamber. The system injects a process gas, typically argon, through three-piece spinning graphite nozzles (i.e., stator, shaft and rotor). The stator permits high-speed rotation without creating a vortex and without excessive wear from surface dross. The stator also allows for the use of a stationary seal at the cover, which, combined with entrance and exit seals, ensures a controlled, oxygen-free, atmosphere above the liquid aluminum.

Since 1985, the standard SNIF "R" (refractory) system has consisted of a refractory-lined steel shell. Three chamber walls are constructed of an inner layer of poured-in-place cast refractory and multiple layers of insulating boards. The fourth wall contains a graphite heater block with removable electric heater elements to keep the metal at casting temperature. Multistage SNIF systems contain ceramic baffles that divide the system into separate stages and direct the metal flow for optimum refining efficiency. Standard SNIF systems are available with one, two, three or four chambers. Each chamber includes one spinning nozzle.

The SNIF SHEER system (patent owned by Foseco International Ltd.) is an improved version of the standard SNIF in-line refining system. Figure 8 is a cross-sectional view of a SNIF SHEER refining system. A rib has been added to the bottom of each stage, and the spinning nozzle has been redesigned. The bottom rib evenly splits the metal and gas flow as it exists the rotor, creating a symmetric flow pattern. It also prevents metal from crossing underneath the rotor, which can lead to vortexing. The overall result is a flatter bath surface with little or no turbulence and better bubble distribution.

Tests done at National Luxembourg Aluminum Co. showed significant improvement in molten metal quality when porous plugs are replaced with SNIF units [9]. After passing through SNIF, the average hydrogen content in the molten aluminum was reduced from 0.25 ml/100 g (std. dev.: 0.09) to 0.065 ml/100g (std. dev.: 0.015). The decrease in particulate count was estimated to be 90%.

The performance of a standard (non-SHEER) SNIF R-140 system was compared to a SNIF SHEER R-140 system in the refining of AA6061 aluminum alloy [10]. The SNIF SHEER R-140 removed 20% more hydrogen using 22% less argon gas, compared to the standard R-140. Inclusion removals for both the SNIF and SNIF SHEER R-140 systems ranged from 70 to 90 percent, based on standard metallographic analyses.

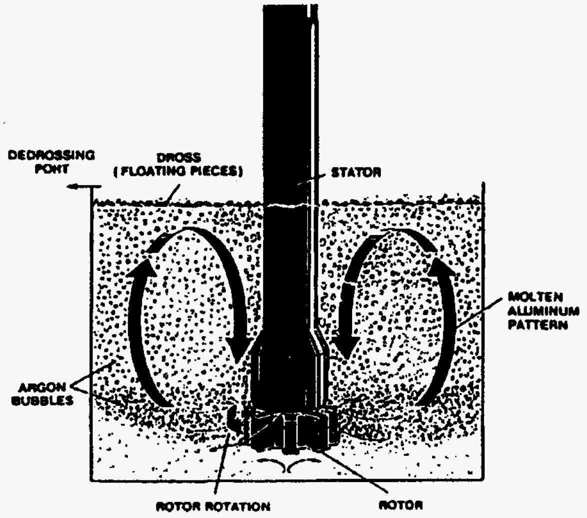

Figure 7. SNIF principles [8]

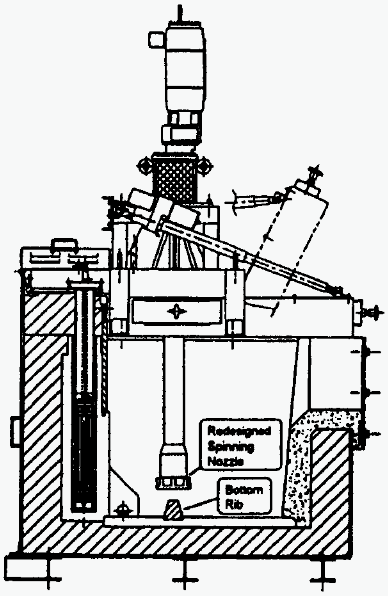

Figure 8. SNIF SHEER R-180U system [8]

The ALPUR **-** Aluminum Pechiney Research Center developed the ALPUR rotary mixer, shown in figure 9 [11]. The dispersion of bubbles is obtained by connecting two different networks of pipes, a set of several small diameter (1~3 mm) pipes placed radially and another set of larger diameter pipes (8~15 mm) placed in a cone-shaped distribution. These two networks of pipes converge on the outer cylindrical surface of the rotor. Small pipes, which act as nozzles, distribute the gas flowing from the hollow shaft of the rotor. For normal gaseous flow in the rotor (3 to 10 Nm^3/h) the gas speed at the injection point is high (>50 m/s). In the second network of pipes, liquid metal flows in the same way as in a centrifugal pump.

At the concurrent point of these networks, there is a junction of the metal flow and the gas flow. The result is a fine dispersion of the two phases and close contact between the gas and the metal along the lateral surface of the rotor. This biphasic mixture is immediately distributed through into the entire volume of the melt. The physiochemical transfer continues until the bubbles reach the surface, where they burst.

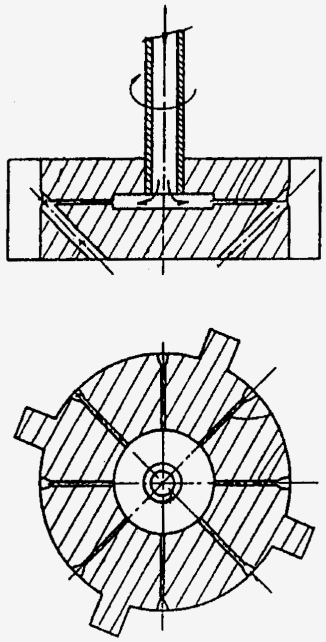

Figure 9 – Alpur rotary mixer [11]

Typical results for an ALPUR D 5000 system [12] are: reduction in hydrogen content by 70% from 0.35-0.45 ccH/100g to 0.10-0.12 ccH/100g, sodium content by 75% from 4-13 ppm to <2ppm, calcium content by 25-30% and inclusion content by 86-93% from 15 ppm to 1ppm.

The Årdal og Sundal Verk (ÅSV) System - Årdal og Sundal Verk, in cooperation with SINTEF, developed the ÅSV system for purifying liquid metals, both as an inline system and as a batch system [13]. The rotor gives a good gas distribution and a calm surface, and has a favorable construction with respect to erosion. The rotor, shown in figure 10, is cylindrical and has one hole in the bottom and two or more holes in the sidewall. Melt is sucked into the rotor through the bottom hole, and a paraboloid melt meniscus is formed within the rotor. The shape of the paraboloid depends on the rotation speed and the gas flow rate. Both melt and gas are ejected through the side holes, resulting in good mixing and efficient small bubble generation. It should be mentioned that there are no blades in the rotor, which reduces rotor erosion. More of the energy input is used to create small bubbles, and less to create uncontrolled mixing, which often leads to vortex formation. However, controlled mixing, which is quite important, is taken care of by the pumping effect of the rotor. By using the proper operating conditions, a calm metal surface may be obtained.

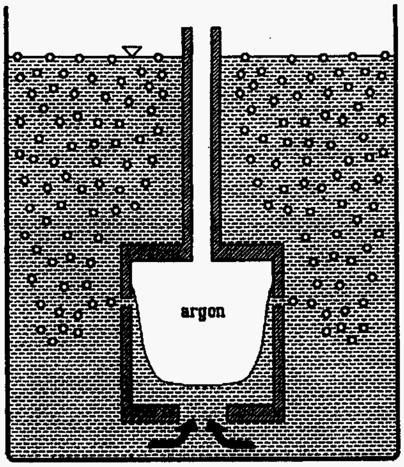

Fig 10. The ÅSV rotor [13]

Using an ASV inline system, average hydrogen content in Al-11%Si and Al-5%Mg-1%Si alloys [13] was reduced from 0.21 ppm (std. dev. 0.13) to 0.07 ppm (std. dev. 0.01). The decrease in sodium was from 4.2 ppm (std. dev. 1.7) to 1.7 ppm (std. dev. 0.4). The decrease in oxide films was estimated to be 60-70% and oxide lumps to be 40-90%.

The ALCOA 622 process - Figure 11 [14] shows a single-stage ALCOA 622 process. A silicon carbide baffle divides the refractory-lined reaction vessel into inlet and outlet compartments. Metal temperature is maintained with immersion heaters. A chlorine and argon gas mixture is introduced through the disperser shaft. The gas mixture exits the underside of the disperser and is broken into fine, discrete bubbles as it passes up between the rotating vanes.

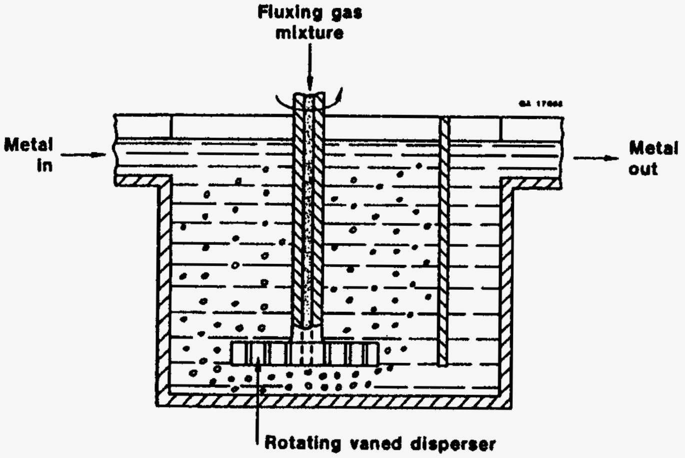

Figure 11. One stage ALCOA 622 unit [14]

In a typical single rotor Alcoa 622 system, the reduction of Ca from the Al alloy 5454 melt is 77% with 0.0048 scf/lb gas flow rate. The reduction of Ca with a triple-rotor (High efficiency and high speed) system is 85% with 0.0071 scf/lb gas flow rate [15].

The HYCAST Melt Refining System - In the Hycast melt refining system [16], the rotor that distributes fluxing gas, is cylindrical and has no fins. The metal is sucked through a hole at the bottom. Together with gas injected through a hollow shaft in the rotor, the melt then ejected through peripheral holes arranged in a circle in the rotor wall, as shown in figure 12.

The cylindrical rotor can be run at high speeds. A rotor with a diameter of 200 mm driven at 500 to 900 rpm attains a peripheral speed of 315-565 m/min, pumping about 40 tons of melt per hour [16]. The resulting high shear forces create very small gas bubbles, with the size of the bubble being determined by the shear force and not by the size of the holes. This means that the size of the bubbles remains the same at a constant rotor speed, giving constant and efficient melt cleaning through the entire lifetime of the rotor.

The cylindrical shape of the rotor gives little stirring and turbulence in the melt close to the surface, but highly efficient mixing in the lower part of the reactor. Slight friction between the melt and the rotor may cause the melt to begin rotating, but a stream breaker strategically placed in the treatment chamber prevents this.

The gas flow produces a vertical melt flow in the upper part of the reactor, thus floating particles to the surface. The low turbulence in the treatment chamber insures that the particles that float remain in the surface slag and do not return to the melt bulk. The cylindrical shape results in little wear and tear to the rotor, thus insuring a long operating life.

The efficiency of a typical two-rotor HYCAST system (HI422) in treating an Al-(1-3%)Mg alloy is shown in Table I [16].

Table I The efficiency of a typical two-rotor HYCAST system (HI422) in treating an Al-(1-3%)Mg alloy

Impurity	After	% Removal
Hydrogen	0.09 ppm	61
Sodium	2 ppm	71
Oxides	0.805 ppm	70
Oxides	0.025 mm^2/kg	71
Particle, Total	0.068 mm^2/kg	67

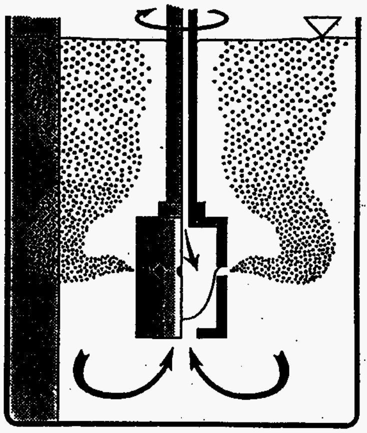

Figure 12. Principle of the HA rotor [16]

The GBF System - Figure 13 shows a schematic diagram of a typical GBF system. The system uses a disc-shaped rotor to purge gas into the melt in order to ensure a uniform distribution of fine bubbles throughout the reactor. Studies have shown that when purging gas from the bottom of a rotary cylinder in a water bath, the rising gas bubbles spin around the cylinder and become attracted to its middle part. The fine bubbles then diffuse in a centrifugal pattern. Bubbles are sheared into tiny bubbles and disperse in a centrifugal pattern at the middle level of the spinning cylinder, where the collision of flow from the top and bottom directions causes strong turbulence. If the height of the cylinder is reduced to a disc shape and rotated near the bottom of the bath, the flow pattern remains unchanged, but one can observe a uniform distribution of fine bubbles from the bottom throughout the entire bath. This observation has been used in the design of the rotor in the GBF system.

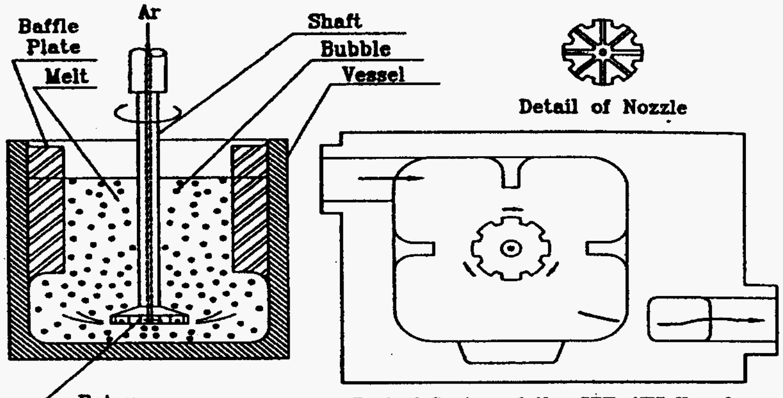

Typical Design of the GBF-1WS Vessel

Figure 13. Schematic diagram and typical detail of the GBF [17]

Figure 14 shows the design of a super rotor for the GBF system [17]. This design enables the process gas to diffuse at a higher flow rate without appreciable growth in bubble size. The rotor is most efficient when its operation speed is between 600 rpm and 950 rpm, depending on the vessel design, metal volume and rotor diameter. Also, two to three baffle plates are configured within the vessel lining to promote the agitation effect in the molten metal and to prevent turbulence or vortex formation at the metal surface.

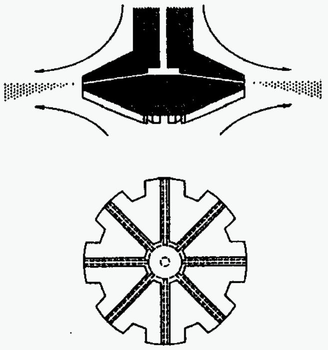

Figure 14. Design of the super rotor [17]

Typically, GBF treatment achieves final hydrogen levels of 0.05-0.12 cc/100g corresponding to 60-83% reduction from the original hydrogen content [17]. It also has excellent efficiency in inclusion removal.

The REVROT - In the REVROT, developed by Apogee Technologies, Inc., the fluxing gas is purged into the molten aluminum through an impeller, as shown in Figure 15 [18]. The primary difference between this technology and the conventional impeller-purging unit is the periodic reversal of the direction of rotation of the impeller. Reversing the rotation direction reduces the formation of vortices in the melt, thus reducing the reentrance of inclusions from the top slag. Figure 16 shows the various configurations of the impeller that can be used in the REVROT system.

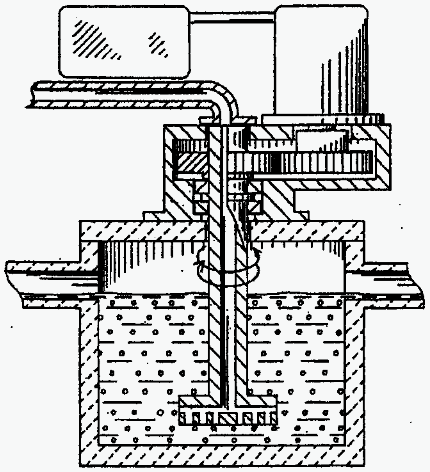

Figure 15. Schematic diagram of a REVROT unit [18]

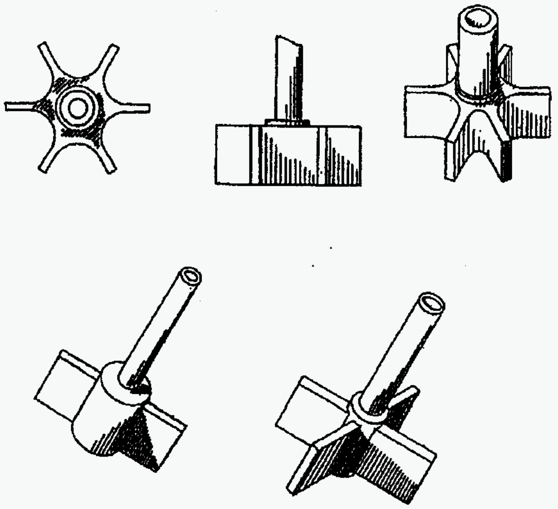

Figure 16. Various configurations of impellers used in the REVROT unit [18]

To determine the effectiveness of this technology, an 8 mm diameter REVROT impeller was immersed in molten aluminum to a depth of 25 inches. The treatment chamber had a circular cross-section. The impeller was rotated at a speed of 425 rpm and the direction of rotation was reversed every 24 seconds. Molten aluminum passed through the chamber at a rate of 61,000 lbs/hr and the metal residence time in the chamber was 97 seconds. For purposes of hydrogen removal, argon gas was introduced through the impeller at the rate of 150 SCF/hr. Aluminum alloys AA6111 and AA3004 were treated according to this procedure and the reduction in hydrogen concentration was 61~79%. For alkali removal from AA5052 alloy, a combination of argon and chlorine gases was used; argon gas was passed through the melt at the rate of 150 SCF/hr and chlorine flowed at the rate of 7.5 SCF/hr. The other conditions were as noted previously. The overall percent stoichiometric reduction of sodium, calcium and lithium was 97%.

2.4 Mathematical Models of Flotation and Fluxing

Historically, the optimization of melt treatment processes relied largely on operator experience. However, better understanding of the processes are now achieved through computer modeling, and the simulations are used not only to optimize existing processes, but also to design new processes, and to determine causes and/or corrective actions for specific problems. Computational Fluid Dynamics (CFD) simulations can provide an overall picture of flows and temperatures inside the melt treatment reactor. CFD is a numerical solution of the basic equations that describe the conservation of mass, heat and momentum of fluids. The removal of inclusions from a liquid melt is a process that involves a large number of complex flow phenomena, including turbulence. The use of CFD to model turbulence is becoming well established due to the recent improvements in software capabilities, the development of faster hardware and the increased validated experience with this technology. The available CFD models can be grouped into two categories: (i) analytical models based on certain simplifying, but rather restrictive assumptions, and (ii) numerical models based on the Navier-Stokes equations with appropriate turbulence models. The analytical models tend to oversimplify the flow situation, mainly due to potential flow assumptions, and are therefore not often used to simulate complex problems.

Previous studies using CFD simulation of the flotation melt treatment process focused mainly on the flow field induced by the injected gas bubbles [19, 20]. Dong et al [21] and Ilegbusy and Szekely [22] investigated the flow field induced by a flat-pedal impeller in a cylindrical melt reactor. The main objective of their work, however, was to investigate the effectiveness of the agitation provided by the impeller in mixing the melt, and not the flotation of inclusions. Johansen et al [23] and Hop et al [24], in the simulation of a Hydro gas-purging unit, considered the effect of the impeller, as well as the injected gas, on the induced flow field. These authors [23, 24] estimated the flow-field induced by the impeller, rotating in one direction, using single-phase transport equations. The purged gas, in the form of bubbles, was introduced into the computational domain as a dispersed phase; the bubbles' trajectories were tracked using a Lagrangian approach. The inclusion removal efficiency was computed based on the bubble trajectories along with the theory of particle deposition onto bubbles [23, 24]. However, the authors did not model the free surface and its effect on the flow field. Maniruzzaman and Makhlouf [25] modeled the rotary degasser using an Eulerian multiphase approach. In their model, they included the effect of the free surface on the flow field and investigated the effect of periodically reversing the rotation direction of the rotor on the efficiency of the degasser.

References

1. Szekely, A.G., *The Removal of Solid Particles from Molten Aluminum in the Spinning Nozzle Inert Flotation Process.* Metallurgical Transactions B, 1975. **7B**(June): p. 259-270.

2. Simensen, C.J. *Inclusion Removal by Flotation.* in *Aluminum Melt Refining and Alloying - Theory and Practice, Short Course and Workshop.* 1989. Melbourne.

3. Emley, E.F. and V. Subramanian. *In-Line Treatment of Liquid Aluminum by the F.I.L.D. and Other Processes.* in *Light Metals.* 1974: The Minerals, Metals & Materials Society.

4. Guttery, J.R. *A Two-Year User's Experience with Porous Plug Fluxing in a Modern Casting Facility.* in *Light Metals.* 1993: The Minerals, Metals & Materials Society.

5. Clumpner, J.A., R.E. Hershey, and W.L. Hoffmann. *MINT - An In-Line Melt Purification System: Predicting Commercial Performance with Aluminum Alloys.* in *Light Metals.* 1986: The Minerals, Metals & Materials Society.

6. Spotlight, N.P., in *Light Metal Age.* 1998. p. 138.

7. Snow, G., D. Pattle, and G. Walker. *R.D.U. - An Efficient Degassing System for the Aluminium Cast House.* in *Light Metals.* 1987: The Minerals, Metals & Materials Society.

8. Simmons, S. and R. Frank. *SNIF Aluminum In-Line Refining.* in *Third Australian Asian Pacific Course and Conference on Aluminium Cast House Technology, Theory and Practice.* 1993. Melbourne, Australia.

9. Davis, R. and R.N. Dokken. *Product Quality Improvements Through In-Line Refining with SNIF.* in *Light Metals.* 1987: The Minerals, Metals & Materials Society.

10. Buehler, J.E. and R.A. Frank. *Start Up and Evaluation of the SNIF SHEER System at kaiser Aluminum, Trenwood Works.* in *122nd TMS Annual Meeting.* 1993. Denver, Colorado: The Minerals, Metals & Materials Society.

11. Hicter, J.H. *ALPUR refining Process.* in *Light Metals.* 1983: The Minerals, Metals & Materials Society.

12. Bibby, P.G. and J.L. Bildstein. *Comalco Rolled Products Experience with an ALPUR D 5000 Degassing Unit.* in *Light Metals.* 1988: The Minerals, Metals & Materials Society.

13. Myrobstad, E., *et al. The ASV Inline System for Refining of Aluminum.* in *Light Metals.* 1986: The Minerals, Metals & Materials Society.

14. Stevens, J.G. and H. Yu. *Mechanisms of Sodium, Calcium and Hydrogen Removal From An Aluminum Melt in a Stirred tank Reactor - The ALOCOA 622 Process.* in *Light Metals.* 1988: The Minerals, Metals & Materials Society.

15. Chesonis, D.C. and H. Yu. *In-Line Fluxing with High Speed Multiple Rotoe Dispersers.* in *Light Metals.* 1997: The Minerals, Metals & Materials Society.

16. Aarflot, A. *New Melt Cleaning Technology.* in *Light Metals.* 1991: The Mineral, Metals & Materials Society.

17. Ohno, Y., D. Hampton, T., and A.W. Moores. *The GBF Rotary System for Total Aluminum Refining.* in *Light Metals.* 1993: The Minerals, Metals & Materials Society.

18. Eckert, C.E. (1997), US Patent no 5616167, April 1997.

19. Johansen, S.T. and F. Boysan, *Fluid Dynamics in Bubble Stirred Ladles: Part II. Mathematical Modeling.* Metallurgical Transactions B, 1986.

20. Ilegbusy, O.J. and J. Szekely. *The Role of Gas Plumes in Agitation and Mass Transfer in Metallurgical Systems.* in *International Symposium on Injection in Process Metallurgy.* 1991: The Minerals, Metals & Materials Society.

21. Dong, L., S.T. Johansen, and T.A. Engh, *Flow Induced by an Impeller in an Unbaffled Tank - I. Experimental.* Chemical Engineering Science, 1994. **49**(4): p. 549-560.

22. Ilegbusi, O.J. and J. Szekely, *The Modeling of Gas-bubble Driven Circulation Systems.* ISIJ International, 1990. **30**(9): p. 731-739.

23. Johansen, S.T., A. Fredriksen, and B. Rasch. *Particle Flotation to Bubbles in Rotor-Stirred reactors for Melt Treatment.* in *Light Metals.* 1995: The Minerals, Metals & Materials Society.

24. Hop, B.I., S.T. Johansen, and B. Rasch. *A 3D Numerical Model for Removal of Inclusion to Gas Bubbles.* in *EPD Congress.* 1996: The Minerals, Metals & Materials Society.

25. Maniruzzaman, M. and M. Makhlouf. *Computer Simulation of Flotation Treatment Methods used in Aluminum Alloy Processing.* in *Light Metals.* 1998: The Minerals, Metals & Materials Society.

3. MATHEMATICAL MODELING AND COMPUTER SIMULATION OF THE ROTATING IMPELLER PARTICLE FLOTATION PROCESS

3.1 FLUID FLOW

3.1.1 Introduction

The quality of cast products largely depends on effective treatment of the molten metal prior to casting in order to remove unwanted second phases. These "*unwanted phases*" include all exogenous solid particles and liquid phases that may be present above the liquidus temperature of the alloy, as well as all gaseous phases dissolved in the melt. When present in a cast product, second phases can cause a variety of property changes including increase in the modulus of elasticity [1, 2], reduction in the fatigue strength [1, 3-5] and ductility, increase in corrosion rate [1], and reduction in electrical and thermal conductivity [1, 6]. Solid inclusions that exist in aluminum foundry products can be classified into several general categories. These include oxides, carbides, intermetallic compounds, and many other exogenous refractory particles. In general, most of these solid inclusions exhibit a complex structures and are very hard and brittle. The critical size of solid inclusions that may be tolerated in a casting depends on the end application. In most applications, inclusions with particle sizes greater than 10 to 20 μm have a drastic effect on the quality of the part. Flotation of these particles to the surface of the melt in a rotary degasser is an effective method of removing them from molten alloys. In this process, a reactive or inert gas, or a combination of both types of gases is purged through a rotating impeller into the liquid metal. Figure 1 shows a typical rotating impeller flotation treatment process. While the gas, in the form of discrete bubbles, rises to the surface, it encounters the inclusions and carries them to the top slag. The efficiency of inclusion removal in a rotary degasser depends on the interaction between the bubbles and the metal. This interaction largely depends on the flow field inside the melt created by the flow of the bubble as well as by the impeller rotation. Inclusion removal also depends on the agglomeration of the particles caused by turbulence in the flow field. The velocity and turbulence fields, largely, govern the transport of inclusions to the bubble surface.

Historically, the optimization of melt treatment processes relied largely on operator experience, but better understanding of the process may be achieved through mathematical modeling and computer simulations. In addition, simulations may be used to optimize existing processes, design new processes, and determine causes and/or corrective actions for specific problems. However, the rotating impeller flotation treatment process is quite difficult to model since it encompasses a flow system that consists of multiple, separate yet interacting, phases including a liquid phase (the molten alloy), a gaseous phase (the purged gas) and one or more solid phases (the inclusion particles). The difficulty of modeling such a system stems from the inability of current hardware to handle models that provide a detailed description of the flow field inside the reactor including the turbulence created by the impeller rotation and gas flow, the interaction between the liquid and gas phases, and the dynamics of the colliding particles. In order to simplify the analysis and make it amenable to solution, previous simulations of the process focused on the flow field induced by the injected gas bubbles [7-9]. For example, Johansen et al [10] and Hop et al [11], in the simulation of a Hydro gas-purging unit, modeled the flow-field induced by the impeller by using single-phase transport equations. They assumed the purged gas, in the form of bubbles, was introduced into the computational domain as a dispersed phase and its trajectory was then tracked using a Lagrangian approach. The inclusion removal efficiency was computed based on the bubble trajectories along with the theory of particle deposition onto bubbles [10, 11]. To further simplify the model, Johansen et al [10] and Hop et al [11] did not model the reactor's free surface and consequently excluded its effect on the flow field from the analysis.

We propose a different approach to modeling and simulating the rotary degasser. The complex flow system that consists of multiple interacting phases is modeled as two separate but interdependent subsystems. The first subsystem, which is the subject of this paper, is the turbulent flow field arising from the impeller rotation and bubble flow. Standard fluid flow and turbulence equations are used in modeling this subsystem, and a special CFD routine that uses an Eulerian multiphase approach and tracks the interface between the gas phase and the liquid phase is employed in the computer simulation. The second subsystem deals with particle collisions and particle to bubble attachment. A model of this subsystem, which is presented elsewhere [12], accepts input from the flow field simulation in the form of turbulence dissipation energy and bubble distribution and uses a special particle population balance to track the change in particle population with duration of the treatment process. By modeling the two subsystems separately, it is possible to include more complexity into the models without prohibitively taxing computer time. For example, unlike previous models, the current fluid flow model allows possible movement of the melt's free surface and thus can reflect any possible "*vortexing*" at the melt's surface.
In this paper, we present the fluid flow model and use it to simulate the performance of a batch process rotary degasser.

3.1.2 The Mathematical Model

The Euler-Euler method [13, 14] is used to formulate the mathematical model, and the Volume Of Fluid (VOF) technique [15] is used to solve the model equations. In the Euler-Euler method, the different phases are treated mathematically as interpenetrating continua where volume fractions of all phases are assumed continuous in space and time and their sum is equal to one. By using the VOF technique, only one set of transport equations is needed, and the interface between the phases is defined by transport equations in which diffusion across the interfaces is not allowed. The use of the VOF technique allows modeling the free boundaries between phases. Free boundaries are considered to be free surfaces of the molten metal or interfaces between two fluids such as the molten metal and the purging gas in the case of the flotation treatment process. The reason for the "*free*" designation arises from the large difference in the densities of the gas and liquid. In order to represent a free surface or an interface in a two-phase fluid, a function f is defined. The value of f is unity at any point occupied by one particular phase, say the primary phase, and zero otherwise. The average value of f in a cell would then represent the volume fraction of the cell that is occupied by the primary phase. Thus the volume of fluid (VOF) method provides the coarse interface information and requires only one storage word for each computational cell, which is consistent with the storage requirements for all other dependent variables.

In the VOF method, the volume fraction of each of the fluids is tracked throughout the domain. The tracking of the interface between the melt and the gas phase is accomplished by the solution of a continuity equation for the volume fraction, f, of each phase. For the k_{th} phase, the continuity equation has the form

$$\frac{\partial f_k}{\partial t} + u_j \frac{\partial f_k}{\partial x_i} = 0 \tag{1}$$

where, k is either molten metal or purging gas.

A single momentum equation is solved throughout the domain, and the resulting velocity field is shared among the phases. The momentum equation, Eq (2), is dependent on the volume fraction through the phases' volume-fraction-averaged density and viscosity, ρ and μ, respectively.

$$\frac{\partial}{\partial t}\rho u_j + \frac{\partial}{\partial x_i}\rho u_i u_j = -\frac{\partial p}{\partial x_j} + \frac{\partial}{\partial x_i}\mu\left(\frac{\partial u_i}{\partial x_j} + \frac{\partial u_j}{\partial x_i}\right) + \rho g_j \tag{2}$$

where

$$\rho = f_1\rho_1 + f_2\rho_2 \tag{3}$$

and,

$$\mu = f_1\mu_1 + f_2\mu_2 \tag{4}$$

In Eqs. (3 and 4), the subscripts 1 and 2 represent the primary and secondary phases.

Since turbulence plays a major role in the flotation treatment process, the momentum equations, Eq. (2), is modified to describe the effects of turbulent fluctuations of velocity and scalar quantities using Reynolds' time averaging procedure supplemented by the standard *k*-ε turbulence model [16]. In the Reynolds averaging of the momentum equations, the velocity at a point is taken as a sum of the mean (i.e., time-averaged) and fluctuating components. Substituting this into Eq. (2) yields the ensemble-averaged momentum equation for predicting turbulent flows,

$$\frac{\partial}{\partial t}\rho u_i + \frac{\partial}{\partial x_i}\rho u_i u_j = -\frac{\partial p}{\partial x_j} + \rho g_j + \frac{\partial}{\partial x_j}\left(\mu_{eff}\left[\frac{\partial u_i}{\partial x_j} + \frac{\partial u_j}{\partial x_i}\right] - \left(\frac{2}{3}\mu_{eff}\frac{\partial u_l}{\partial x_l}\right)\right) + \frac{\partial}{\partial x_j}\left(-\rho\,\overline{u_i' u_j'}\right) \tag{5}$$

In Eq. (5), μ_{eff} is the effective viscosity which is the sum of the molecular viscosity, μ and the turbulent viscosity, μ_t where $\mu_t = \rho C_\mu \frac{\kappa}{\varepsilon}$. u_i, u_j or u_l are time-averaged velocity components, u_i' is the fluctuating velocity component, $C_\mu = 0.09$ is an empirical constant, and $\rho\overline{u_i' u_j'}$ are Reynolds stresses through which the effect of turbulence is incorporated into the momentum equation.

Modeling turbulent flows requires appropriate modeling procedures to describe the effects of turbulent fluctuations of velocity and scalar quantities on the basic conservation equations. Many models with varying complexity have been proposed ranging from the simple mixing length model [17] to the more sophisticated large eddy simulations [17]. The widely used *k*-ε model [16] provides a compromise between the two extremes. The *k*-ε turbulence model is an eddy viscosity model in which the Reynolds stresses are assumed proportional to the mean velocity gradients, with the constant of proportionality being the turbulent viscosity, μ_t. This assumption provides the following expressions for the Reynolds stresses.

$$\rho\overline{u_i' u_j'} = \rho\frac{2}{3}k\delta_{ij} - \mu_t\left(\frac{\partial u_i}{\partial x_j} + \frac{\partial u_j}{\partial x_i}\right) + \frac{2}{3}\mu_t\frac{\partial u_i}{\partial x_i}\delta_{ij} \tag{6}$$

In Eq. (6), the turbulent energy, k, is given by

$$k = \frac{1}{2}\sum_i \overline{u_i'^2} \tag{7}$$

The values of k and ε are obtained by solving the conservation equations

$$\frac{\partial}{\partial t}(\rho k)+\frac{\partial}{\partial x_i}(\rho u_i k)=\frac{\partial}{\partial x_i}\left(\frac{\mu_t}{\sigma_k}\frac{\partial k}{\partial x_i}\right)+G_k-\rho\varepsilon \tag{8}$$

$$\frac{\partial}{\partial t}(\rho \varepsilon)+\frac{\partial}{\partial x_i}(\rho u_i \varepsilon)=\frac{\partial}{\partial x_i}\left(\frac{\mu_t}{\sigma_\varepsilon}\frac{\partial \varepsilon}{\partial x_i}\right)+C_{1\varepsilon}G_k\frac{\varepsilon}{k}-C_{2\varepsilon}\rho\frac{\varepsilon^2}{k} \tag{9}$$

where the empirical constants $C_{1\varepsilon}=1.44$, $C_{2\varepsilon}=1.92$, and the effective Prandtl numbers, $\sigma_k=1.0$ and $\sigma_\varepsilon=1.3$. G_k is the rate of production of turbulent kinetic energy given by Eq. (10)

$$G_k=\mu_t\left(\frac{\partial u_j}{\partial x_i}+\frac{\partial u_i}{\partial x_j}\right)\frac{\partial u_j}{\partial x_i} \tag{10}$$

3.1.3 Solution Procedure and Boundary Conditions

The fluid flow pattern, the gas bubble distribution, and the turbulence dissipation rate in a melt treatment reactor are determined using the model presented in Eqs. (5) to (10). The Volume Of Fluid (VOF) free surface model in a commercial fluid-dynamics code[1] is employed in the simulation. A non-uniform grid is used throughout the domain; however, the grid node density is made higher close to the free surface and around the gas inlet region. Equation (1) requires that *f* moves with the fluid, and in an Eulerian mesh, the flux of *f* moving with the fluid through a cell must be computed. However, standard finite-difference approximations would lead to smearing of the *f* function and interfaces would lose their definition. Fortunately, *f* being a step function with values of zero or one permits the use of a flux approximation that preserves its discontinuous nature. This approximation is known as a donor-acceptor approximation [15].

The semi-empirical "wall-function" is used to approximate the shear stress due to the "no-slip" condition at all solid surfaces and the values of k and ε at the walls are taken as those derived from the assumption of an equilibrium boundary layer. At the gas inlet into the melt, the radial and tangential components of velocity are assumed uniform. At the gas exit from the reactor's top, diffusion fluxes of all flow variables in the direction normal to the exit plane are assumed zero. The impeller is simulated by a wall that rotates with a velocity that is defined by specifying the velocity component in the circumferential direction. Whenever symmetry exists, symmetry boundary conditions may be used,

---

[1] FLUENT V4.4 marketed by Fluent Inc., Lebanon, New Hampshire.

i.e., assuming zero flux for all variables across the symmetry boundary. Figure 2 shows a block diagram of the solution procedure.

3.1.4 Application of the Mathematical Model

The process parameters that most significantly affect the efficiency of a rotary degasser are the purging gas flow rate, the rotation speed of the impeller, the duration of gas purging, and reversing the direction of impeller rotation. A statistically robust computer experiment that includes these process parameters as variables was designed and used to optimize a batch rotary degassing process. The molten metal was an aluminum alloy held at 750°C in an electric furnace and the purging gas was high purity argon. In order to extract the maximum amount of unbiased information from as few simulations as possible, the Taguchi method for design of experiments was used [18, 19]. The experiment matrix was based on an L_8 orthogonal array with two levels at each factor as shown in Table I. Table II shows the Taguchi L_8 layout along with the calculated mean turbulence dissipation rate. The mean values of the turbulence dissipation rate are computed as a volume-weighted average of the turbulence dissipation rate. The volume-weighted average considers the cell size differences and thus yields an average value that accounts for the spatial distribution of the variable.

Table I Design of the experiment.

Factor	**Level 1**	**Level 2**
Rotation speed, *rpm*	675	350
Gas flow rate, *l/min*	36	15
Cycle (Rotation direction), *sec.*	0	25
Purge duration, *min*	5	10

Table II Taguchi L_8 Layout and simulation results.

Factor	**rpm A**	**Flow Rate l/min B**	**A × B**	**Cycle sec C**	**A × C**	**B × C**	**D**	**Mean dissipation rate, m^2/s^3**
Trial/Column	*1*	*2*	*3*	*4*	*5*	*6*	*7*	*(y)*
1	675	36	1	0	1	1	1	23.09
2	675	36	1	25	2	2	2	31.51
3	675	15	2	0	1	2	2	7.67
4	675	15	2	25	2	1	1	26.43
5	350	36	2	0	2	1	2	0.1542
6	350	36	2	25	1	2	1	0.1729
7	350	15	1	0	2	2	1	0.1448
8	350	15	1	25	1	1	2	0.1644

Figure 3 shows the calculated velocity vectors for the reactor with the impeller rotating at 675 rpm and a gas flow rate of 36 l/min at two different purging times. These plots show the characteristic circulation patterns that are expected in mechanically stirred melt treatment systems. The velocity vectors near the rotor shaft are the highest in magnitude because of the upward motion of the gas bubbles. Near the free surface, the radial component of the velocity becomes significant at the lower purge time. However, at the higher purge time, a re-circulation zone forms just below the free surface.

Figure 4 shows the argon gas distribution in the melt treatment furnace at two different gas purge times. The average volume fraction of argon gas in the reactor is calculated to be 0.0431.

Velocity vectors and gas distributions for a reverse rotation flotation reactor are shown in Figures 5 and 6 respectively. In the reverse rotation flotation reactor, the velocity vector near the free surface is more or less radial. In addition, the circulation zone inside the furnace is more prominent thereby ensuring good mixing of the melt, and enhancing the probability of interaction between inclusions and gas bubbles. The average volume fraction of argon gas in this reactor is 0.046.

Figures 7 and 8 show the computed turbulence dissipation rate for the conventional and the reverse rotation flotation reactors respectively. These plots show that the turbulence dissipation rate is non-uniform in both flotation reactors, being highest near the impeller and its shaft. However, in the reverse rotation reactor, the higher dissipation rates are more spread and cover a larger volume of the furnace than in the traditional reactor. It should be noted that, the absolute values of the dissipation rate in the rotary degasser are in the range of 0.01 to 2×10^4 m^2/s^3. These values are quite high in comparison to those obtained using only a gas bubble stirring system, e.g., a porous plug or a stationary lance [20]. The mean values of turbulence dissipation rates are 23.09 m^2/s^3 in the conventional flotation reactor and 31.51 m^2/s^3 in the reverse rotation reactor operating at the conditions given in Table II.

Analysis of Variance (ANOVA) was performed on the data in order to identify the effect of each process parameter and each interaction on the variance in the mean turbulence energy dissipation rate. The procedure for performing ANOVA is detailed elsewhere [18, 19]. Results of the pooled analysis of variance are shown in Table III. The percent contribution is an indication of the relative influence of a particular parameter or an interaction to affect variation in the mean turbulence energy dissipation rate. Table III shows that, for the system modeled, at the levels studied, the process parameter that affects variation in the mean turbulence energy dissipation rate most significantly is the rotation speed. Its relative contribution to the variation is about 74%. Periodic reversal of the rotation direction also has an effect on the mean turbulence energy dissipation rate contributing over 6% to the variance. Higher rotation speeds and periodic reversal of the rotation direction increase the mean turbulence energy dissipation rate. All other process parameters seem to have comparatively insignificant effects on the mean turbulence energy dissipation rate. The percent contribution due to the error term provides an estimate of the adequacy of the experiment [18, 19]. If the error term is low, i.e., 15% or less, it is assumed that no important factors were omitted from the design of the experiment and computational errors were insignificant. On the other hand, if the percent contribution due to the error term is high, then some important factors were omitted, or computational errors were excessive. The percent contribution due to the error term in this analysis is about 7%, which is acceptable.

Table III Pooled ANOVA table for turbulence dissipation rate.

Factor	**Sum of Squares**	**Variance**	**Percent Contribution**
Rotation speed	969.587	969.586	74.37
Gas flow rate	52.580	52.579	3.05
Speed × gas flow rate	52.397	52.396	3.04
Rotation direction	92.547	92.547	6.16
Speed × rotation direction	92.027	92.026	6.12
Gas flow rate × rotation direction	(13.345)	Pooled	
Duration	(13.340)	Pooled	
Error	26.685	13.342	7.26
Total	**1285.823**		**100.00**

3.1.5 Summary

A mathematical model for simulating the multiphase flow-field inside a rotating impeller flotation unit for removal of solid inclusion from molten metal has been developed. The model estimates the turbulence energy dissipation rate and the purge gas volume fraction in the treatment furnace.

In addition to providing insight into the physical mechanisms underlying the rotating impeller flotation process, the mathematical model was used to simulate a batch type rotary degasser. Since a high mean turbulence energy dissipation rate implies more inter-particle collisions and a higher probability of particle attachment to gas bubbles, and consequently more efficient performance of the rotary degasser [12], the simulations were used to determine the optimum parameters for operating a small batch type rotary degasser. The simulation results indicate that the impeller's rotating speed has the most significant effect on the turbulence energy dissipation rate; consequently, it is the most important process parameter. The simulations also indicate that periodic reversal of the impeller's rotation direction has a positive effect on the process efficiency.

References

1. T. A. Engh: Principles of Metal Refining, Oxford University Press, New York, 1992, pp. 1-35.
2. G. Sachs, A. W. Dana, and L. J. Ebert: AFS Transactions, 1947, vol. 55, pp. 102.
3. Q. G. Wang, D. Apelian, and J. R. Griffiths: 1st International Aluminum Symposium, 1998.
4. G. R. Wakefield and R. M. Sharp: Mater. Sci. and Technol., 1996, vol. 12, pp. 518-522.
5. C. Nyahumwa, N. R. Green, and J. Campbell: AFS Casting Congress, 1998.
6. R. Cook, M. A. Kearns, and P. S. Cooper: Light Met., 1997, pp. 809-814.
7. S. T. Johansen and F. Boysan: Metall. Trans. B, 1986, vol. 19B, pp. 755-764.
8. O. J. Ilegbusi and J. Szekely: ISIJ Int., 1990, vol. 30, pp. 731-739.
9. O. J. Ilegbusy and J. Szekely: International Symposium on Injection in Process Metallurgy, 1991, pp. 1-34.
10. S. T. Johansen, A. Fredriksen, and B. Rasch: Light Met., 1995, pp. 1203-1206.
11. B. I. Hop, S. T. Johansen, and B. Rasch: EPD Congress, 1996, pp. 647-656.
12. M. Maniruzzaman and M. Makhlouf: Worcester Polytechnic Institute, Worcester, USA, unpublished research, 2000.
13. C. Crowe, M. Sommerfeld, and Y. Tsuji: Multiphase Flows with Droplets and Particles, CRC Press, Boca Raton, 1997.
14. FLUENT: FLUENT User's Guide , FLUENT Inc., Lebanon, New Hampshire, 1996, vol. 2 & 4.
15. C. W. Hirt and B. D. Nichols: J. Comput. Phys., 1981, vol. 39, pp. 201-225.
16. B. E. Launder and D. B. Spalding: Lectures in Mathematical Models of Turbulence, Academic Press, London, 1972.
17. O. J. Ilegbusi, M. Iguchi, and W. Wahnsiedler: Mathematical and Physical Modeling of Materials Processing Operations, Chapman & Hall/CRC, Boca Raton, 1999.

18. P. J. Ross: Taguchi Techniques for Quality Engineering, McGraw-Hill Book Company, New York, 1988.
19. R. K. Roy: A Primer on the Taguchi Method, Society of Manufacturing Engineers, Dearborn, Michigan, 1990.
20. O. J. Ilegbusi and J. Szekely: Metall. Trans. B, 1988, vol. 21B, pp. 183-190.

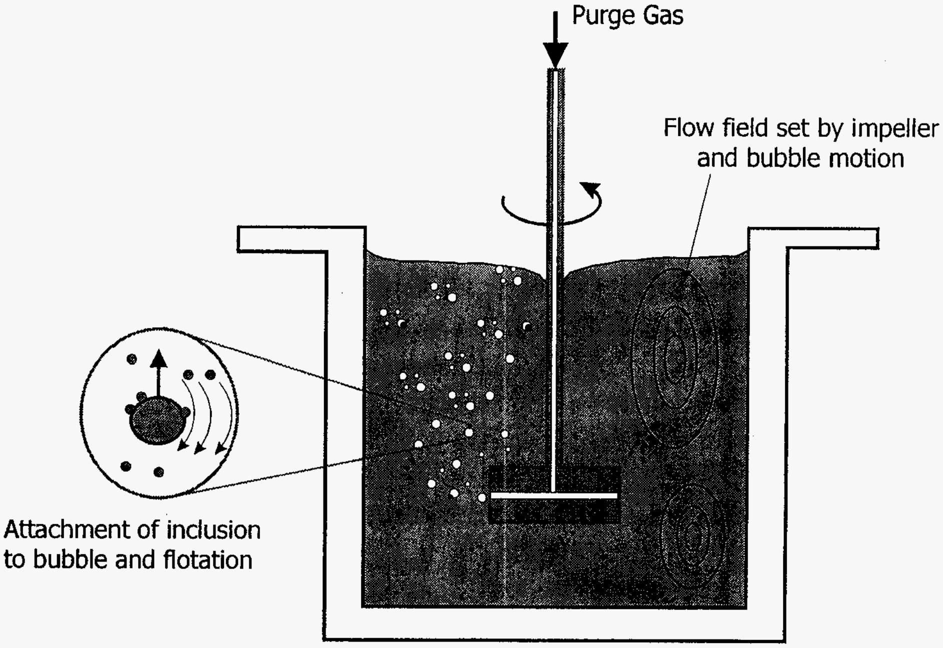

Figure 1 Schematic diagram describing the flotation treatment process.

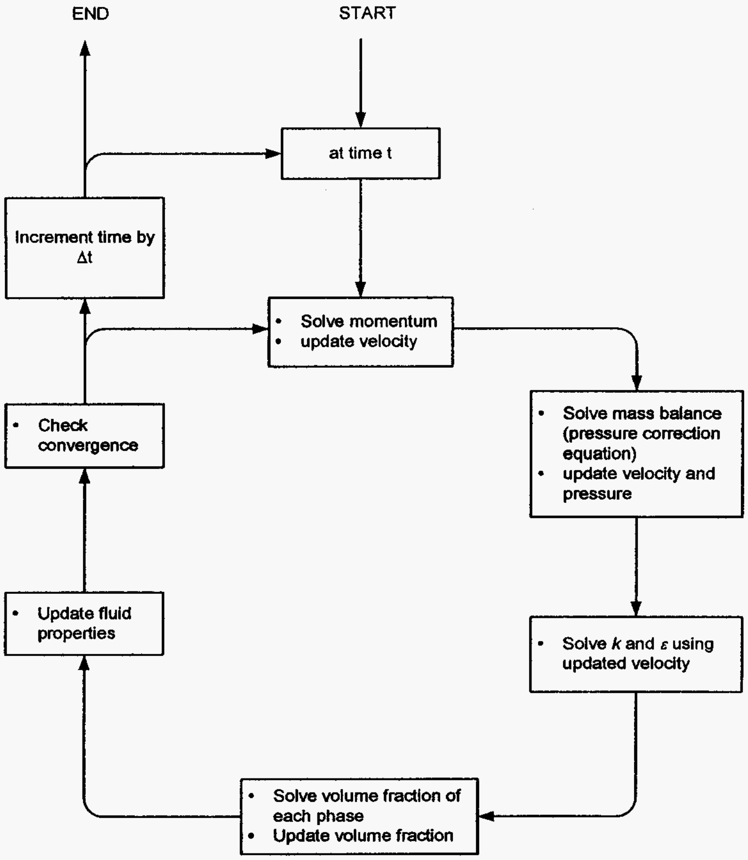

Figure 2 Overview of the solution procedure.

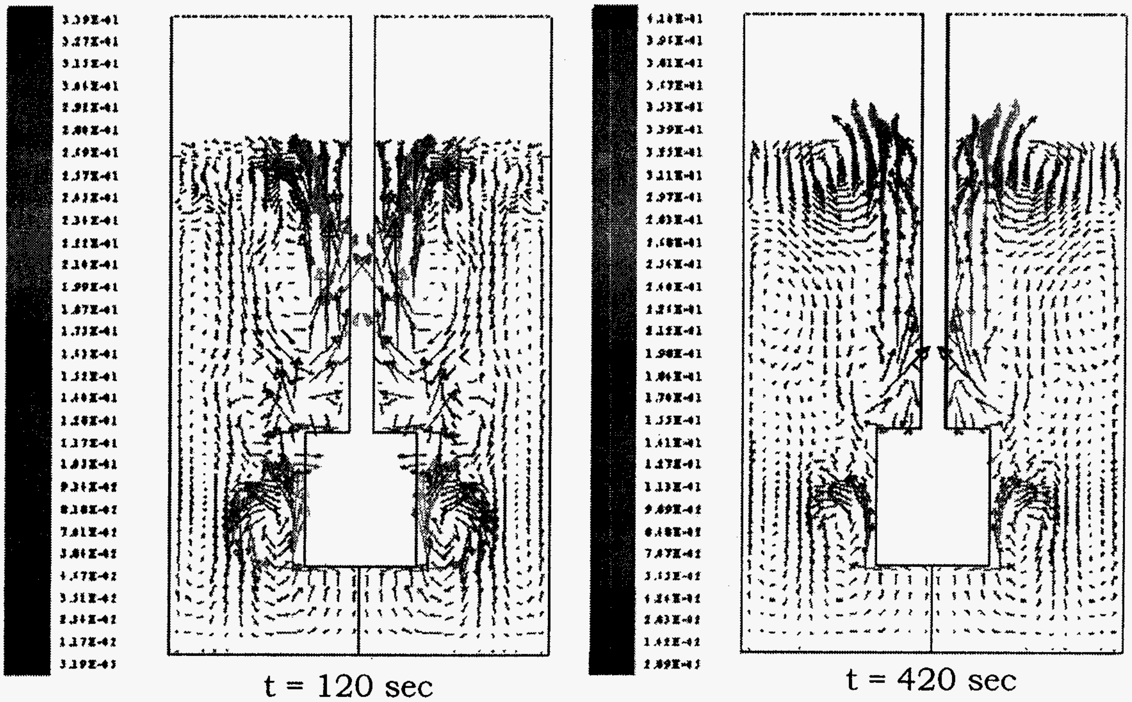

t = 120 sec

t = 420 sec

Figure 3 **Aluminum flow field in a conventional flotation reactor with impeller rotating at 675 rpm and gas flow rate of 36 l/min.**

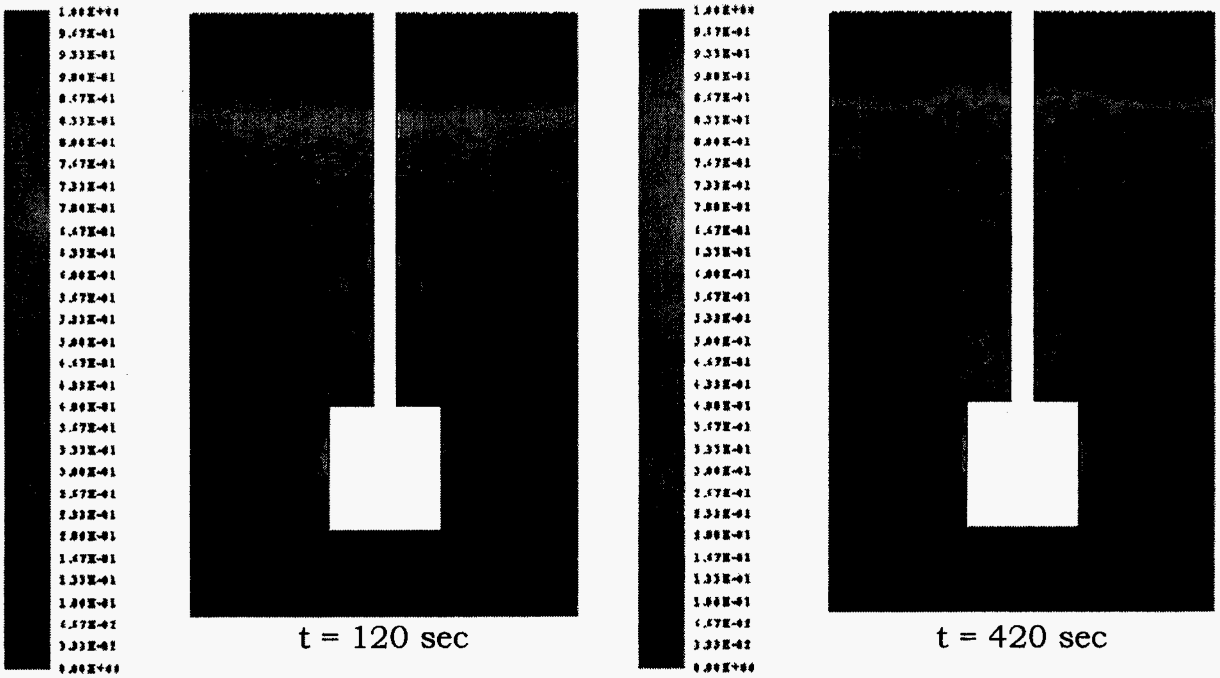

t = 120 sec

t = 420 sec

Figure 4 **Argon gas distribution in the melt treatment furnace in a conventional degasser rotating at 675 rpm.**

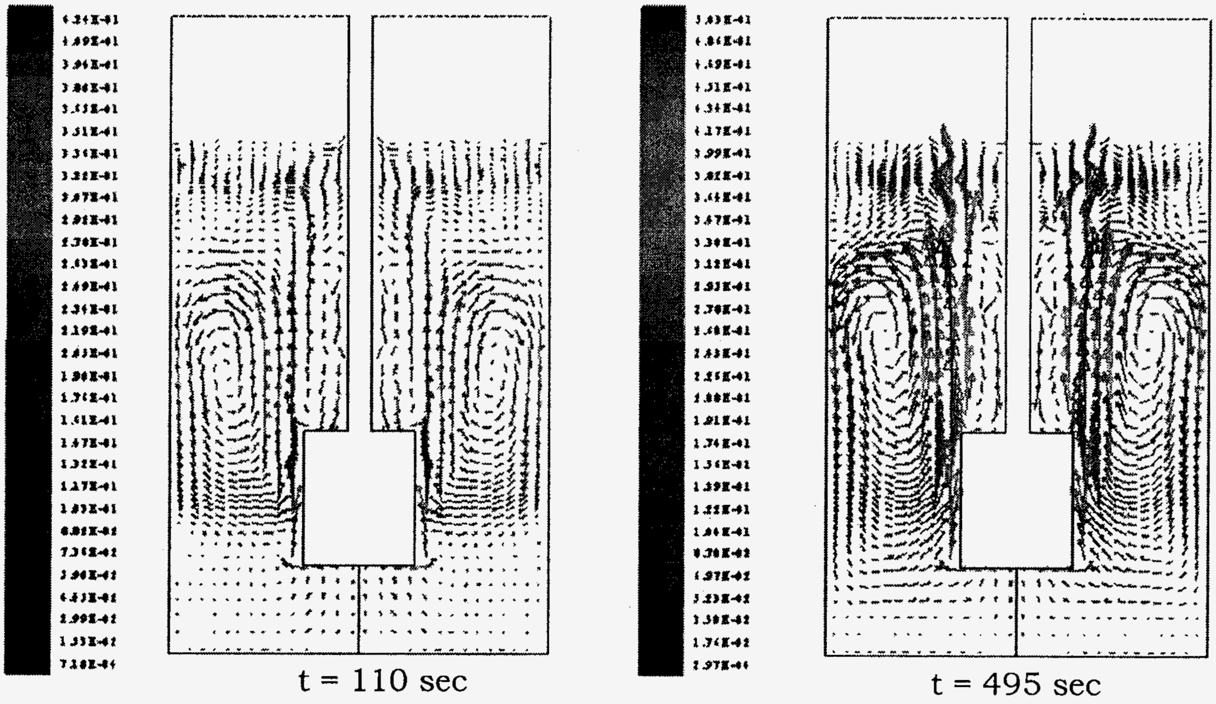

t = 110 sec

t = 495 sec

Figure 5 **Aluminum melt flow field in a reverse rotation flotation reactor with impeller rotating at 675 rpm (cycles every 25 sec) and gas flow rate of 36 l/min.**

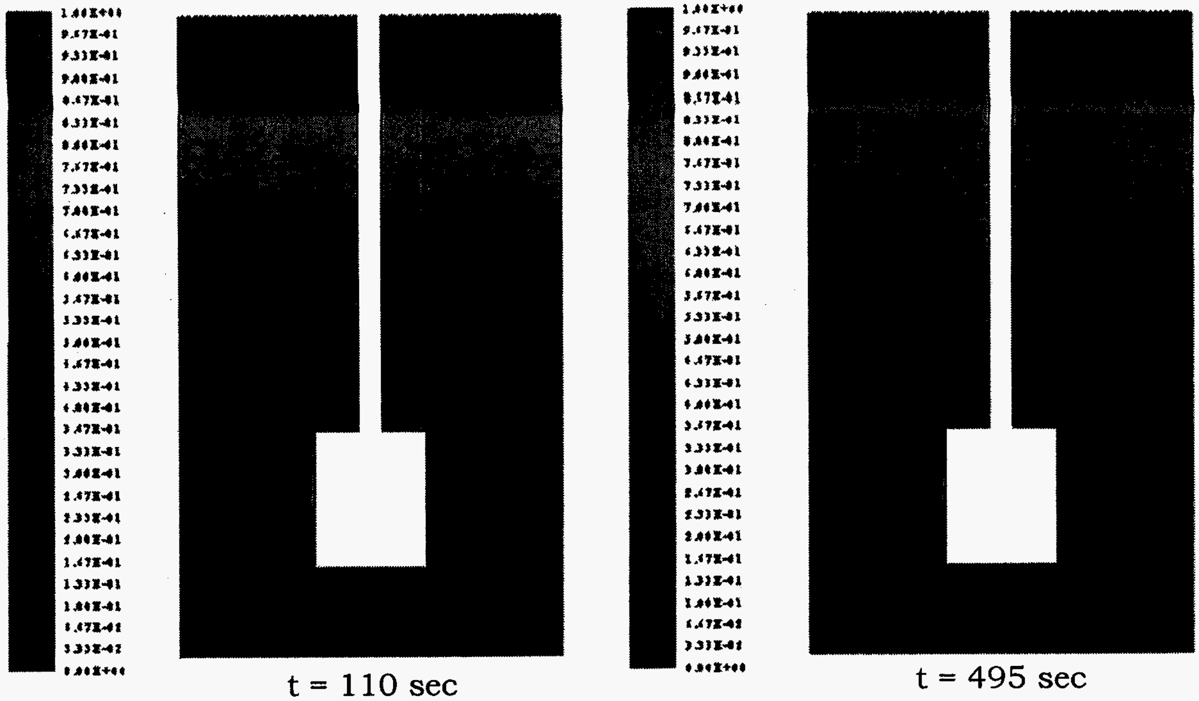

t = 110 sec

t = 495 sec

Figure 6 Argon gas distribution in the melt treatment furnace in a reverse rotation flotation reactor with impeller rotating at 675 rpm (cycles every 25 sec) and gas flow rate of 36 l/min.

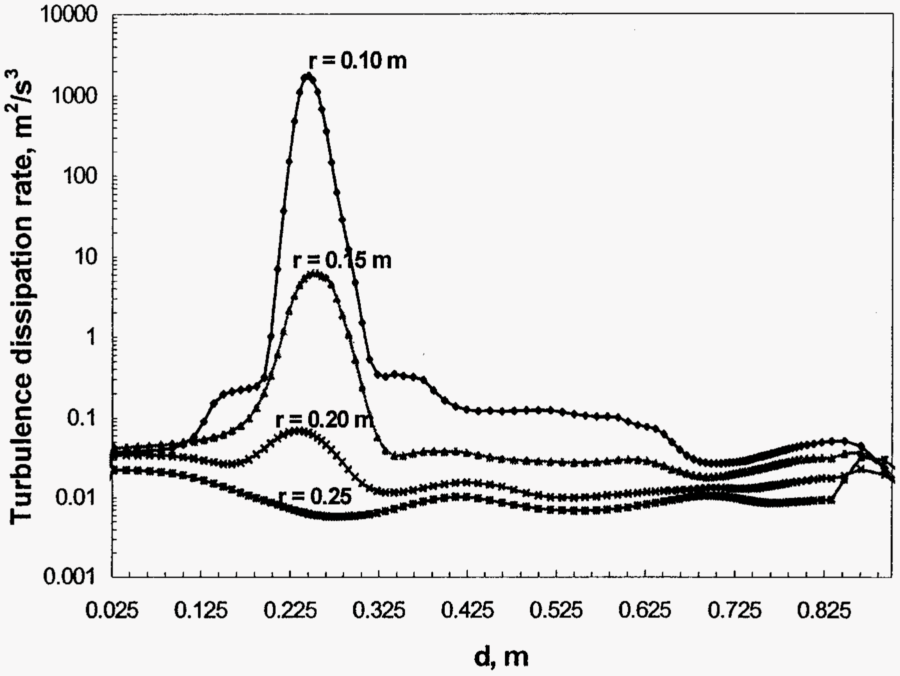

Figure 7 Turbulence dissipation rate as a function of the distance from the furnace bottom (d) and radial distance from the center of the furnace (r) for a conventional flotation reactor at t = 420 sec, 675 rpm of rotation speed and 36 l/min of gas flow rate.

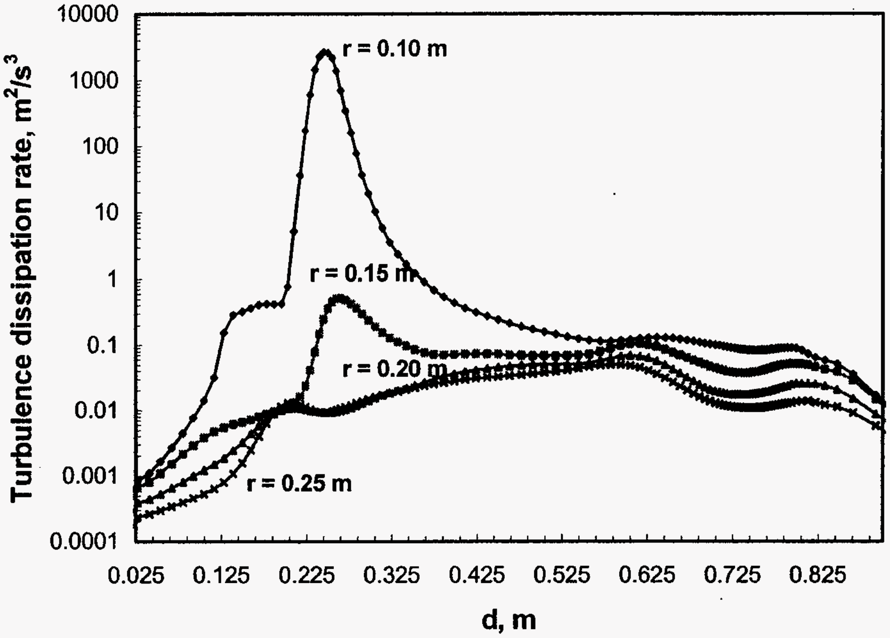

Figure 8 Turbulence dissipation rate as a function of the distance from the furnace bottom (d) and radial distance from the center of the furnace (r) of a reverse rotation flotation reactor at t = 420 sec, rotating at 675 rpm and gas flow rate of 36 l/min.

3.2 PARTICLE AGGLOMERATION AND FLOTATION

3.2.1 Introduction

The quality of molten metal can be improved by proper control of unwanted phases and impurities. In this context, the term "unwanted phases" refers to exogenous solid particles and/or liquid phases present above the liquidus temperature of the alloy as well as any gaseous phases dissolved in the melt. Among the various unwanted phases, solid particles and films have the most detrimental effect on a metal's properties. Consequently, various melt treatment techniques have been developed and are employed to remove solid particles and films from molten alloys [1]. Particle flotation using a rotary degasser, also known as fluxing, is one of the most widely used techniques for removing unwanted phases from molten alloys. In this process, a reactive or inert gas, or a combination of both types of gases is purged through a rotating impeller into the liquid metal. The most commonly used reactive gases are chlorine and fluorine, and the most commonly used inert gases are argon and nitrogen. While the gas, in the form of bubbles, rises to the surface, it encounters the particles and carries them to the top slag [2]. The efficiency of particle removal depends on the interaction between the bubbles and the particles. This interaction largely depends on the flow field inside the melt created by the flow of the bubbles as well as the impeller rotation, and the size and number of bubbles. Particle removal also depends on the agglomeration of the particles caused by turbulence in the flow field [3-5]. The velocity and turbulence fields govern the transport of particles to the bubbles' surfaces. The addition of chlorine or other halogens affects the surface tension of the bubbles in such a way as to make the particles stick to the bubbles' surfaces more efficiently [6-9]. Figure 1 shows a schematic diagram of a rotary degasser.

A useful way of mathematically describing the dynamics of particle agglomeration in a rotary degasser is by means of a particle population balance. Although the mathematical formulation of the population balance is rather simple, it cannot be solved analytically to yield the particle size distribution. Moreover, a straightforward numerical approach to the problem puts practically prohibitive demands on computer time and memory. In this study, a mathematical model is presented to describe the agglomeration and removal of solid particles of varying sizes from an alloy melt during rotary degassing. A particle population balance is used to describe the system mathematically, and a special discretization scheme is employed to reduce the computational complexity and computer time required for solving the population balance equation. The model is used to investigate the effect of the rotary degasser's operational parameters on particle agglomeration and removal from a molten metal bath. This model is useful in the design of efficient rotary degassers and in selecting the operation parameters for optimum degasser performance.

3.2.2 Theoretical Background

The state of a suspension of particles in a fluid may be conveniently described by a particle size distribution density function, $n_v(v,t)$, where $n_v(v,t)dv$ is the number of particles with volumes in the range v to $(v+dv)$ per unit volume of fluid. The dynamics of such a system in which individual particles may grow in size by accretion of mass from the fluid phase or shrink by loss of mass, and in which particles may collide and coagulate, is described by the general population balance equation [see [10]]

$$\begin{aligned}\frac{\partial n_v(v,t)}{\partial t} = -\frac{\partial}{\partial v}\left[I_v(v,t)n_v(v,t)\right] + \int_0^{v/2} W_v(v-\tilde{v},\tilde{v})n_v(v-\tilde{v},t)n_v(\tilde{v},t)d\tilde{v} \\ - n_v(v,t)\int_0^{\infty} W_v(v,\tilde{v})n_v(\tilde{v},t)d\tilde{v} + S_v\left[n_v(v,t),v,t\right]\end{aligned} \tag{1}$$

where, $I_v(v,t) = dv/dt$, the rate of change of the volume of a particle of volume v by transfer of material between the particle and the fluid phase, $W_v(v,\tilde{v})$ is the rate of collision between particles of volumes v and $\tilde{v}$, and S_v is the net rate of addition of new particles into the system. The first term on the right hand side of equation (1) represents the rate of growth of particles by transfer of material to individual particles. The second term represents the rate of accumulation of particles in the size range $(v, v+dv)$ by collision of two particles of volume $(v-\tilde{v})$ and $\tilde{v}$ to form a particle of volume v (assuming conservation of volume during coagulation). The third term represents the rate of loss of particles in the size range $(v, v+dv)$ by collision with all other particles. The last term represents all possible particle sources and sinks.

A number of approximation techniques for solving the population balance equation exist [11-13]. These include (a) defining the particle size distribution with a continuous function, (b) approximating the particle size distribution with a parameterized lognormal function, (c) describing the particle size distribution function by using moments of the particle size distribution function, and (d) discretizing the population balance equation. Method (a) was shown to be very accurate but requires a large amount of computer time [12]. Method (b) was demonstrated to be extremely fast but is limited in accuracy [12]. Method (c) is also limited in accuracy because it yields only the average properties of the particle size distribution. However, the loss of accuracy and resolution due to averaging is compensated for by an increase in computational speed and a reduction in computer memory requirements [11]. Method (d), in which the continuous particle size distribution is approximated by a finite number of sections with the properties within each section averaged, usually requires a large number of sections in order to achieve satisfactory accuracy, and therefore is computer intensive [11, 12].

The solution of Eq. (1), by use of a conventional finite difference technique is also very difficult because of the complex integral terms involved. To overcome this difficulty, the continuous population balance equation is replaced by a set of discretized equations [4, 14]. For spherical particles, where the particle's volume is a function of the third power of the particle's radius, the discretized equations can be expressed in terms of the particle radius. Accordingly, the discretized equations for the rate of change in concentration of particles with average radius, r_k, in the k-th size range (n_k) is given by:

$$\frac{dn_k}{dt} = \frac{1}{2}\sum_{\substack{i=1\\ i+j=k}}^{i=k-1} n_i n_j W(r_i, r_j) - \sum_{i=1}^{\infty} n_i n_k W(r_i, r_k) - S_k(n_k) \qquad (k = 1, 2, \cdots, \infty) \tag{2}$$

In Eq. (2), $W(r_i, r_j)$ is the rate of collision between particles of radii r_i and r_j where the condition $r_i^3 + r_j^3 = r_k^3$ must always be satisfied. The first term on the right hand side of equation (2) represents mass generation through collision and coagulation between the i-th and j-th particles and the second term represents mass destruction through collisions of the k-th particle with other particles. The last term, S_k is the sink term that describes the rate of removal of particles by flotation. This flotation can be due to the density difference between the particles and the melt, as well as due to particle adhesion to the rising gas bubbles.

In order to solve equation (2), the size domain is divided into intervals of equal size ranges. This method gives greater numerical stability, but usually requires a very large number of intervals. For example, to remove particles of the size range 1 μm to 40 μm with constant volume intervals assuming that the first interval spans the particle size range from 1 μm^3 to 2^3 μm^3, a total of $\frac{40^3 - 1^3}{2^3 - 1^3} = 9143$ particle size intervals are required. If a smaller, more manageable number of size intervals is maintained in the discretization scheme, virtually no information will be conveyed about the smaller size particles.

3.2.3 The Mathematical Model

The number of particle size intervals in a relatively wide size range can be reduced considerably without sacrificing information about the smaller size particles by employing a geometric series instead of a constant size interval. Indeed, if the series is geometric in length, it is also geometric in volume. Hunslow's method [15], which is based on binary interaction mechanisms, is employed. In this method, the wide particle size domain over which particle agglomeration occurs is divided into intervals. Within each of these intervals, equations describing the change in particle concentration are used. Each interval is represented by a characteristic volume V_k that is the average volume of the particle sizes in the interval

$$V_k = \frac{b_{k-1} + b_k}{2} \tag{3}$$

where b_k is the upper boundary volume of interval *k*. V_k is related to the previous interval V_{k-1} by a geometric series relationship such that, $V_k / V_{k-1} = 2$. In terms of length-domain discretization, $r_k / r_{k-1} = \sqrt[3]{2}$. This discretization scheme allows covering a great range of particle sizes in a manageable manner.

Four binary interaction mechanisms are necessary to fully describe particle agglomeration in a flow field. These are listed in Table I.

Table I. Binary interaction mechanisms that are necessary to fully describe particle agglomeration in a flow field.

Mechanism #	Birth or Death in interval i	Collision between Particles in Intervals	
①	Birth	i-1	1 → i-2
②	Birth	i-1	i-1
③	Death	i	i → i-1
④	Death	i	i → ∞

The particle size distribution is discretized in such a way that any interval of volume v_i, is twice the width of the previous interval, v_{i-1}, and the density function in the interval *i* is given by $n' = N_i / v_i$. N_i is the total number of particles in the interval *i*. It is convenient to assign the lower bound on interval *i*, a size (i.e. volume) 2^i and the upper bound a size 2^{i+1}. The density function in this interval is therefore $n = N_i / 2^i$.

<u>Mechanism ①</u> Birth in the i^{th} interval can occur only when a particle in the $i\text{-}1^{th}$ interval agglomerates with a particle in the 1^{st} to $i\text{-}1^{th}$ intervals. Consider the agglomeration of a particle of size *a* in the j^{th} interval, where $j < i - 1$. In order to form a particle in the i^{th} interval it must collide with particles in the size range $2^i - a \leq v < 2^i$, all of which are in the $i\text{-}1^{th}$ interval. The number of particles available for collision is thus $aN_{i-1} / 2^{i-1}$.

The differential rate of agglomeration by the first mechnism, $dR^{[1]}$, for particles in the size range $a < v < a + da$ (of which there are dN), resulting in particles in the *i*th interval is given by

$$\begin{aligned} dR^{[1]}_{i,j} &= W\frac{aN_{i-1}}{2^{i-1}}dN \\ &= W\frac{aN_{i-1}}{2^{i-1}}n(a)da \\ &= W\frac{aN_{i-1}}{2^{i-1}}\frac{N_j}{2^i}da \end{aligned}$$

Thus, allowing that $W=W_{i-1,j}$ for particles in the *i-1*th and *j*th intervals,

$$\begin{aligned} R^{[1]}_{i,j} &= W_{i-1,j}\int_{2^j}^{2^{j+1}} a2^{1-i-j}N_{i-1}N_j da \\ &= 3\cdot 2^{j-i}W_{i-1,j}N_{i-1}N_j \end{aligned}$$

$R^{[1]}$ is the rate of birth in the *i*th interval resulting from agglomeration between particles in the *j*th interval by the first mechanism. If this rate is summed over all possible values of *j*, the total rate of birth in the *i*th interval by the first mechanism may be determined from

$$R^{[1]}_{i,j} = \sum_{j=1}^{i-2} 3\cdot 2^{j-i}W_{i-1.j}N_{i-1}N_j \tag{4}$$

<u>Mechanism ②</u> A similar process may be used to describe agglomerates formed in the *i*th interval by collision between particles both in the *i-1*th interval. Any agglomerate formed by collision between a particle in the *i-1*th interval and another particle in the same interval will result in the formation of a particle in the *i*th interval, consequently the number of particles available is N_{i-1}, and the differential rate of birth is

$$dR^{[2]}_i = \frac{1}{2}W_{i-1,i-1}N_{i-1}\frac{N_{i-1}}{2^{i-1}}da$$

The leading factor of ½ is included to avoid counting collisions twice.

$$\begin{aligned} R^{[2]}_i &= W_{i-1,i-1}\int_{2^{i-1}}^{2^i}\frac{N_{i-1}^2}{2^i}da \\ &= \frac{1}{2}W_{i-1,i-1}N_{i-1}^2 \end{aligned} \tag{5}$$

<u>Mechanism ③</u> Death by agglomeration will occur to a particle in the *i*th interval should it collide and adhere to a particle of sufficient size for the

resultant agglomerate to be larger than the upper size limit of the *i*th interval.

First, consider collisions with particles from smaller size ranges. Death in the *i*th interval will occur when a particle of size *a*, in the *j*th interval, agglomerates with a particle ranging in size from $2^{i+1}-a$ to 2^{i+1}. The number of particles in this latter range is $aN_i/2^i$.
The rates may be calculated as before

$$R_{i,j}^{[3]} = 3 \cdot 2^{j-i-1} W_{i,j} N_i N_j$$

By summing this last equation over all possible values of *j*, death by the third mechanism may be represented by

$$R_i^{[3]} = N_i \sum_{j=1}^{i-1} 3 \cdot W_{i,j} 2^{j-i-1} N_j \tag{6}$$

<u>Mechanism ④</u> If a particle in the *i*th interval agglomerates with a particle from that or higher interval, a death occurs in the *i*th interval. This final mechanism may be given by

$$R_i^{[4]} = N_i \sum_{j=i}^{\infty} W_{i,j} N_j \tag{7}$$

The overall rate of change of number of particles $\left({dN_i}/{dt} \right)$ may be computed by combining eqs. (4) to (7), i.e.,

$$\frac{dN_i}{dt} = CR_i^{[1]} + R_i^{[2]} - CR_i^{[3]} - R_i^{[4]} \tag{8}$$

C in equation (8) is a volume correction factor. It is shown [15] that in order to conserve particle volume, the value of *C* should be *2/3*. Equation (9) is the expanded form of Eq. (8).

$$\frac{dN_i}{dt} = N_{i-1} \sum_{j=1}^{i-1} 2^{j-i+1} W_{i-1,j} N_j + \frac{1}{2} W_{i-1,i-1} N_{i-1}^2 - N_i \sum_{j=1}^{i-1} 2^{j-i} W_{i,j} N_j - N_i \sum_{j=i}^{\infty} W_{i,j} N_j \tag{9}$$

Finally, a "sink" term (S_k) is introduced into Eq. (9) to account for particle removal from the system.

$$\begin{aligned} \frac{dN_k}{dt} = {} & \sum_{i=1}^{i=k-2} 2^{i-k+1} N_{k-1} N_i W(r_{k-1}, r_i) + \frac{1}{2} N_{k-1}^2 W(r_{k-1}, r_{k-1}) \\ & - \sum_{i=1}^{k-1} 2^{i-k} N_i N_k W(r_i, r_k) - \sum_{i=k}^{\infty} N_i N_k W(r_i, r_k) - S_k N_k \end{aligned} \tag{10}$$

Determination of the particle agglomeration rate, $W(r_i, r_j)$

Particle agglomeration in a flotation melt treatment process is the consequence of collision between particles. The collision mechanism largely depends on the type of flow; i.e., on the hydrodynamics of the melt and the size of the particles. Several agglomeration mechanisms are possible. These include Brownian agglomeration, which is more active in sub-micron size particles, gravitational agglomeration, which is typical of very large particles, and turbulent agglomeration, which is typical of intermediate size particles. In typical rotary degassers, the melt hydrodynamics is such that only turbulent agglomeration is relevant. Consequently, Brownian and gravitational agglomeration mechanisms are excluded from the model. During rotary degassing of molten metals, mechanical energy is supplied to the melt by the rotation of the degasser's impeller and by the flow of the purged gas. This energy creates turbulence within the melt. The turbulence creates eddies, which in turn help dissipate the energy. The energy is transferred from the largest eddies to the smallest eddies in which it is dissipated through viscous interactions. The size of these smallest eddies is the Kolmogorov microscale, η, which is expressed as a function of the kinematic viscosity ν and the energy dissipation rate ε

$$\eta = \left(\frac{\nu^3}{\varepsilon} \right)^{1/4} \tag{11}$$

The rate of particle agglomeration, $W(r_i, r_j)$, consists of two components [14],

$$W(r_i, r_j) = W_t + W_s \tag{12}$$

where, W_t is the collision rate of particles caused by turbulence eddies and W_s is the rate of collisions caused by the difference in flotation velocity between large and small particles, known as Stokes collisions.

In the turbulent flow field, agglomeration can occur by either of two mechanisms. The first mechanism, which will be referred to as the *viscous sub-range mechanism,* is active when the particles are smaller than the Kolmogorov microscale, η. In this case, agglomeration is assumed to take place under local shear flow conditions [4, 5, 16]. The second mechanism, which will be referred to as the *inertial sub-range mechanism,* is active when the particles are larger than the Kolmogorov microscale, η. In this case, the colliding particles assume independent velocities. The model presented here incorporates both turbulent flow mechanisms – the *viscous sub-range mechanism* and the *inertial sub-range mechanism* - since in a rotary degasser the turbulence intensity is quite high and the particle size distribution is such that it may satisfy the requirements of both mechanisms. A parameter, β_1, is used to determine which agglomeration mechanism is dominant in a given turbulent flow field. The parameter β_1 is defined as the ratio of the particle size to the Kolmogorov microscale, η. When $\beta_1 < 1$, the viscous sub-range mechanism is dominant; on the other hand, when $\beta_1 > 1$, the inertial sub-range mechanism is dominant.

For $\beta_1 < 1$, the approach velocity of the colliding particles is determined by their motion within the eddy. Therefore, particle collisions are influenced by the local shear within the eddy. Based on work by Saffman and Turner [17], the rate of collision between two particles of size ranges r_i and r_j in the viscous sub-range region can be described by equation (13)

$$W_t(r_i, r_j) = 1.30\, \alpha_T (r_i + r_j)^3 \left(\frac{\varepsilon}{\upsilon}\right)^{0.5} \Delta \tag{13}$$

In Eq. (13), ε is the turbulence dissipation rate and ν is the kinematic viscosity of the melt. Δ is a correction coefficient which is introduced to account for any turbulence heterogeneity that may be present in the treatment reactor[2]. The empirical capture efficiency coefficient of collision, α_T describes the hydrodynamic and attractive interactions between agglomerating particles. Higashitani et al [4] suggested the following relationship for evaluating α_T.

$$\alpha_T = 0.732\left(\frac{5}{N_T}\right)^{0.242} \quad ; \quad N_T \geq 5 \tag{14}$$

where N_T is the ratio between the viscous force and the Van der Waals force,

$$N_T = \frac{6\pi\mu (r_i + r_j)^3 \dot{\gamma}}{A} \tag{15}$$

In Eq. (15), A is the Hamaker constant, and $\dot{\gamma}$ is the fluid deformation rate,

$$\dot{\gamma} = \left(\frac{4\varepsilon}{15\pi\upsilon}\right)^{0.5}$$

On the other hand, for $\beta_1 > 1$, the particles are larger than the smallest eddy; consequently, they are dragged by velocity fluctuations in the flow field and collide with one another. In this case, the rate of collision is expressed using Abrahamson's model [18]. Abrahamson assumed 100 percent collision efficiency. In the model presented here, Abrahamson's equation is modified by a capture efficiency coefficient, α_T, which accounts for attractive and hydrodynamic interactions between particles

---

[2] For example, heterogeneity may be introduced when a non-cylindrical impeller is used.

$$W_t(r_i, r_j) = 5\alpha_T (r_i + r_j)^2 \sqrt{\left(\overline{U}_i^{\,2} + \overline{U}_j^{\,2}\right)} \tag{16}$$

where $\overline{U}_i^2$ is the mean squared velocity for particle i. When the flow is highly turbulent and the particles are relatively large in comparison to the smallest eddy, which is the case in typical rotary degassing of molten metals, the particles acquire momentum from the eddies and are projected into neighboring eddies without necessarily following the fluid fluctuations. In this case, the mean squared velocity is calculated using equation (17) [18].

$$\overline{U}_i^{\,2} = \frac{\overline{U}^2}{1 + 1.5\tau_p \varepsilon / \overline{U}^2} \tag{17}$$

where, $\overline{U}^2$ is the mean squared velocity deviation of the fluid and τ_p is the relaxation time of a particle of radius r_p $\left(\tau_p = 2\rho_p r_p / 18\mu\right)$. Equation (17) is applicable only when one of the colliding particles has a radius

$$r = \sqrt{\left(15\mu\overline{U}^2\right) / \left(4\rho_{particle}\varepsilon\right)} \tag{18}$$

When the particles are smaller than the limiting size given by Eq. (18), they are not completely influenced by the eddies, and equation (19) instead of equation (17) is used to calculate the mean squared particle velocity, $\overline{U}^2$ [19],

$$\overline{U}_i^2 = \frac{4a^2}{(2a+3)^2} (\varepsilon\nu)^{1/2} \frac{3}{\delta(\delta+1)} \tag{19}$$

where, $a = \left(\rho_{particle} - \rho_{melt}\right) / \rho_{melt}$ and $\delta = \left(9\rho_{melt} / 2\rho_{particle} + \rho_{melt}\right)(\eta / r_i)^2$

The Stokes collision rate, W_S, is calculated from equation (20) [20]:

$$W_s = \frac{2\pi\Delta\rho g}{9\mu} (r_i + r_j)^3 \left| r_i - r_j \right| \tag{20}$$

where $\Delta\rho$ is the difference in density between the particles and the melt.

Figure 2 shows the particle agglomeration rate as a function of β_1 after 10 minutes of degassing in a rotary degasser that is operating at 675 rpm with a flow rate of 36 liters of nitrogen gas per minute. These operation parameters result in a turbulence dissipation rate $\varepsilon = 23.09$ m^2/s^3 [18]. The turbulent collision rate, W_t is calculated from equations (13) and (16) and the Stokes collision rate, W_S is calculated from equation (20). Figure 2 shows that for a particular size class, r_k, both W_t and W_S increase as the radii of the colliding particles increase, but as the radius of one of the colliding particles approaches that of the other, W_s begins to decrease and approaches zero as the particle radii become equal. Due to the combined effect of W_t and W_s, W within a particular particle size interval initially increases and then rapidly decreases.

Determination of the particle flotation rate, S_k

Removal of particles from the melt by flotation, represented by S_k in equation (10), is due to Stokes flotation and settling of relatively large particles, S_s, and attachment of particles to the rising gas bubbles, S_b.

$$S_k = S_s + S_b \tag{21}$$

Assuming Stokes terminal velocity and a homogeneous distribution of particles in the melt, the Stokes flotation rate for particles of size class k is calculated using equation (22) [14]

$$S_s = \frac{2g}{9\mu L}\Delta\rho r_k^2 \tag{22}$$

In equation (22), L is the depth of molten metal in the reactor, g is gravitational acceleration, μ is viscosity of the molten metal , and $\Delta\rho$ is the difference in density between the solid particles and the melt. Fig. 3 shows a typical Stokes' flotation curve. The larger the particle size, the higher is the flotation rate.

The rate of attachment of particles to the gas bubbles, S_b, is calculated assuming the particles' centerlines flow along streamlines and that attachment to the bubbles occurs whenever the streamline carrying the particle comes within a distance that is smaller in magnitude than the particle's radius [14]. Assuming that the particles are distributed homogeneously within the melt, the entrapment rate of particles of size class k on gas bubbles is given by Eq. (23) [14, 21]:

$$S_b = \frac{N_b v_b b_k^2 \pi}{V} \tag{23}$$

In equation (23), N_b is the number of bubbles, v_b is the velocity difference between the bubbles and the melt, V is the volume of the melt, and b_k is the critical entrapment distance between bubbles and particles of size class k. Equation (23) assumes that when the particles are within a volume $v_b b_k^2 \pi$, they instantaneously attach to the bubble. However, particle attachment to bubbles requires time, hence S_b is modified by an entrapment efficiency, E, where $E = 4r_k/r_b$ and r_b is the average stable bubble radius [2, 22],

$$S_b = \frac{N_b v_b b_k^2 \pi}{V} E \tag{24}$$

The terminal velocities of gas bubbles in molten metals are difficult to measure accurately. However, Szekely [2] proposed equation (25) based on measurements of the terminal velocity of gas bubbles in water.

$$v_b = \sqrt{\sigma We \big/ 2\rho r_b} \tag{25}$$

In equation (25), ρ is the density of the melt, σ is the surface tension of the melt and We is Weber's number. The number of bubbles in the reactor (N_b) is calculated from the volume fraction of the purged gas and the average stable bubble radius, r_b. The volume fraction of purged gas is estimated from numerical simulations of the flow field within the reactor [23], and the average stable bubble radius in a turbulent flow field is estimated using Hinze's formula [24] with a modification applicable to a rotary degasser suggested by Johansen et al [25, 26],

$$r_b = \frac{1}{2} D \left(\frac{Q_g}{Q_{go}}\right)^m \left(\frac{We_c \sigma}{\rho}\right)^{0.6} \frac{1}{\varepsilon^{0.4}} \tag{26}$$

In equation (26), $Q_{go} = 25$ *l/min*, $D = 0.878$, $m = 0.28$ (assuming a cylindrical impeller), and Q_g is the gas flow rate in *l/min*. A critical Webber number, $We_c \approx 4$, is necessary for the bubble to be stable [21].

The streamlines around a gas bubble of radius r_b, shown in Figure 4, is calculated using equation (27) which assumes potential flow around the bubble [27]

$$\psi = \frac{1}{2} u_b r_b{}^2 \sin^2\theta \left(\frac{R^2}{r_b{}^2} - \frac{r_b}{R}\right) \tag{27}$$

In equation (27), ψ is the stream function and u_b is the bulk velocity. Equation (27) is used to back calculate the critical entrapment distance, b_k as follows. First, Equation (27) is rewritten in the form

$$\psi = u_b r_b^2 \sin^2\theta \left[\frac{1}{2} x^2 - \frac{1}{2x}\right] \tag{28}$$

where $x = R/r_b$. When $\theta = 90^\circ, R = r_p + r_b$, and therefore $x = x_E = 1 + r_p/r_b$. Recognizing that at a distance far removed from the bubble $\sin\theta = \frac{b_k}{R}$, and substituting into Eq. (28), b_k is expressed in terms of ψ and u_b,

$$b_k^2 = \frac{2\psi}{u_b} \tag{29}$$

Figure 5 shows the critical entrapment distance for particles of radius varying between 5μm and 100μm by 6mm diameter nitrogen gas bubbles.

Figure 6 shows the variation in flotation rate due to particle attachment to bubbles, S_b with particle radius. S_b is calculated using equation (24) and Figure 6 shows that S_b increases linearly with particle size. Figure 7 shows the variation of the product of flotation rate, S_k, and the number of particles in the size class k, N_k, with particle radius.

3.2.4 Verification of the Model Predictions

In order to verify the model predictions, aluminum oxide particles were introduced into commercially pure molten aluminum that was held at 750°C in an electrical furnace. The furnace was 0.224 m in diameter and 0.45 m high, and the initial melt depth was 0.3 m. A laboratory size rotary degasser was used to purge high purity argon gas into the melt. The diameter of the degasser's rotor shaft was 24 mm and the diameter of the cylindrical impeller was 80 mm. The gas was purged at a rate of 2 l/min through 12, eight mm diameter side holes that were equally spaced around the circumference of the impeller. The impeller was placed so that its bottom was 5 cm above the bottom of the furnace and was operated at 560 rpm. Maniruzzaman and Makhlouf [23, 28] used computational fluid dynamics to simulate a similar reactor and obtained a mean turbulence energy dissipation rate of 0.333 m^2/s^3 and an argon gas volume fraction of 0.0725.

Melt samples were taken from the holding furnace before purging with argon and after purging for 20 minutes. The solidified samples were sectioned, mounted in epoxy, and polished using standard metallographic procedures. The aluminum oxide particle size distribution in each sample was determined using image analysis[3]. A minimum of fifty fields from each sample was examined at 350X magnification, and the particle count per unit area was converted to particle count per unit volume using standard stereological estimation techniques [29]. Figure 8 shows the measured initial particle concentration vs. particle radius

---

[3] AnalySIS 2.11 software manufactured and marketed by Soft Imaging System GmbH, Hammer Str. 89, D-48153 Münster, Germany.

curve, as well as the measured particle concentration vs. particle radius curve after 20 minutes of purging with argon. Also shown in Fig. 8 is the computer predicted particle concentration vs. particle radius curve after 20 minutes of purging. Fig. 8 shows good agreement between the model predicted and the measured particle concentration profiles.

3.2.5 Simulation Results and Discussion

The model was used to evaluate the change in aluminum oxide particle size distribution during treatment of molten aluminum in a rotary degasser. The evolution of the particle size distribution is simulated by solving the discretized population balance, equation (10). The initial particle radius domain, which spans the range 0.05 μm to 120 μm, is discretized into 35 sections each representing a particle radius range. The discretized ordinary differential equations system is solved using the explicit Euler method.

Two inputs are necessary for calculating the particle collision rate. These are the mean turbulence dissipation rate and the volume of purged gas. Mairuzzaman and Makhlouf [23] used computational fluid dynamics and calculated these parameters for a rotary degasser operating with the parameters shown in Table II.

Table II. Rotary degasser operation parameters used in the simulations and their corresponding mean turbulence dissipation rate (ε) and volume fraction of bubbles (V_f) [18].

Case #	Impeller speed (*rpm*)	Rotation direction	Gas flow rate (*l/min*)	ε (m^2/s^3)	V_f
1	675	Unidirection	36	23.09	4.31
2	675	Reverse rotation	36	31.51	4.60
3	350	Reverse rotation	36	0.17	4.70
4	675	Reverse rotation	15	26.43	3.97

Other physical data necessary for calculating the particle collision rate are shown in Table III.

Table III. Physical properties and data used in the simulations.

Molten aluminum at 973K	
Density	2300 kg/m^3
Viscosity	2900 Pa.s
Surface tension	0.9 N/m
Kinematic viscosity	1.3×10^{-6} m^2/s
Aluminum oxide particles at 973K	
Density	3500 kg/m^3
Hamaker constant	0.45×10^{-20} J [14].

Figure 9 shows the particle size distribution in a rotary degasser operating under the conditions of case 3 in Table II. Figure 9 shows that, under these conditions, the number of particles with radii smaller than 20 □m initially decreases rapidly. This rapid decrease in the number of small sized particles is due to their rapid rate of agglomeration into larger particles. Because the rate of agglomeration of particles with radii less than 20 □m into particles with radii larger than 20 □m exceeds the rate of removal of the large particles by flotation, there is an initial net increase in the number of particles with radii larger than 20 □m. Only after degassing for more than 20 minutes does the rate of particle removal catch up with the rate of particle agglomeration and an overall reduction in the number of particles occurs[4].

Figure 10 shows the effect of reversing the direction of rotation in a rotary degasser on particle removal when the degasser is operating at a relatively high rotation speed and relatively high gas flow rate. Figs. 10(a) and 10(b) show the variation in particle size distribution with time for cases 1 and 2 of Table II, respectively. In both cases, particles smaller than 25 µm agglomerate rapidly due to turbulent collisions. Removal of the large particles depends mainly on a combination of turbulent agglomeration, which leads to formation of even larger particles, and flotation by attachment to bubbles and Stokes' flotation. Although there is an accumulation of larger particles during the early stages of degassing, with time, the larger particles are removed. Figure 10(c) compares the particle removal efficiency of two similar degassers one operating under the conditions depicted in case 1 of Table II, the other under conditions depicted by case 2. The particle removal efficiency is calculated in terms of the fraction of particles removed from each particle size range normalized to the initial number of particles in the size range. The negative particle removal efficiency values indicate

---

[4] It should be noted that the critical particle radius for transition between the viscous sub-range model and the transition sub-range model is about 30 µm, and between the transition sub-range model and the inertial sub-range model is about 815 µm.

an increase in the number of particles of the given size. Fig. 10(c) shows that the efficiency of the degasser operating under the conditions depicted in case 2 of Table II is higher than that of the degasser operating under the conditions depicted in case 1 of Table II.

The particle removal efficiency vs. particle size curve shown in Fig. 10(c) can be divided into three distinct regions. In region I, which includes particle sizes up to 15 μm, the dominant mechanism responsible for particle removal is turbulent agglomeration. The initial number of particles in this size range is very high; consequently, despite the high particle removal rate in this size range, many particles remain in the melt. In region II, which includes particles between 15 and 40 μm, the rate at which particles grow by turbulent agglomeration is not balanced by the rate of particle removal by flotation; consequently, particles in this size range are difficult to remove. In region III, which includes all particles larger than 40 μm, although there is continued formation of particles in this range by turbulent agglomeration of smaller particles, given time, this supply of particles is more than balanced by the high removal rate.

Figure 11 shows the effect of rotation speed on degasser performance. Figs. 11(a) and 11(b) show the particle concentration profiles for cases 2 and 3 of Table II, respectively. Figs. 11(a) and (b) show that the rate of particle removal is slow when the impeller rotation speed is low. Figure 11(c) compares the particle removal efficiency of two degassers one operating under the conditions depicted in case 2 of Table II, the other under the conditions depicted in case 3. Figure 11(c) shows that increasing the rotation speed greatly enhances particle removal. At the high rpm, particles with radii ranging between 25 and 40 μm are the most difficult to remove, while at the low rpm, the difficult to remove particle size range includes all particles larger than 10 μm. Figure 9 shows that degassing for a relatively long time (more than 20 minutes) at the low rpm is necessary to remove these particles.

Figure 12 shows the effect of the purge gas flow rate on degasser performance. Figs. 12(a) and 12(b) show the particle concentration profiles for cases 2 and 4 of Table II, respectively. The rate of particle removal is similar for both cases indicating that at high impeller rotation speeds, the gas flow rate does not have a very pronounced effect on the degasser's performance. Figure 12(c) compares the particle removal efficiency of two degassers one operating under the conditions depicted in case 2 of Table II, the other under the conditions depicted in case 4. Figure 12(c) shows that increasing the purge gas flow rate enhances particle removal but only slightly.

3.2.6. Conclusion

A model that describes particle collision and removal by flotation during rotary degassing of molten metals is developed. The model is based on the classical theory of turbulent agglomeration and is unique in that it accounts for both high and low intensity turbulent flow conditions. A particle population balance is used to describe the system mathematically, and a special discretization scheme is employed to reduce the computational complexity and the computer time required for solving the population balance equation. The model is used to investigate the effect of the rotary degasser's operational parameters on the agglomeration of aluminum oxide particles and their removal from molten aluminum. The model explains the interrelationships between the various mechanisms responsible for particle removal and is useful in the design and efficient operation of industrial rotary degassers.

References

1. M. Maniruzzaman and M. M. Makhlouf: Phase Separation Technology in Aluminum Melt Treatment, American Foundrymen's Society, Des Plains, IL, 2000.
2. A. G. Szekely: Metall. Trans. B, 1975, vol. 7B, pp. 259-270.
3. R. Gammelsæter, K. Bech, and S. T. Johansen: Light Met., 1997, pp. 1007-1011.
4. K. Higashitani, K. Yamauchi, Y. Matsuno, and G. Hosokawa: J. of Chem. Eng. Japan, 1983, vol. 16, pp. 299-304.
5. K. Nakanishi and J. Szekely: Trans. Iron Steel Inst. Jpn, 1975, vol. 15, pp. 522-530.
6. O. Hjelle, T. A. Engh, and B. Rasch: Int. Semin. Refin. Alloying Liq. Alum. Ferro-Alloys, 1985, pp. 345-360.
7. B. Kulunk and R. Guthrie: Light Met., 1992, pp. 963-975.
8. G. Sigworth: Light Met., 2000, pp. 773-778.
9. E. M. Williams, R. W. McCarthy, S. A. Levy, and G. Sigworth, K.: Light Met., 2000, pp. 785-793.
10. F. Gelbard and J. H. Seinfeld: J. Comput. Phys., 1978, vol. 28, pp. 357-375.
11. J. D. Landgrebe and S. E. Pratsinis: J. Colloid Interface Sci., 1990, vol. 139, pp. 63-86.
12. M. Frenklach and S. J. Harris: J. Colloid Interface Sci., 1987, vol. 118, pp. 252-261.
13. J. J. Wu and R. C. Flagan: J. Colloid Interface Sci., 1988, vol. 123, pp. 339-352.
14. Y. Miki, Y. Shimada, B. G. Thomas, and A. Denissov: I&SM, 1997, pp. 31-38.
15. M. J. Hounslow, R. L. Ryall, and V. R. Marshall: AIChE J., 1988, vol. 34, pp. 1821-1838.

16. H. Saint-Raymond, F. Gruy, and M. Cournil: J. Colloid Interface Sci., 1998, vol. 202, pp. 238-250.
17. P. G. Saffman and J. S. Turner: J. Fluid Mech., 1956, vol. 1, pp. 16-30.
18. J. Abrahamson: Chem. Eng. Sci., 1975, vol. 30, pp. 1371-1379.
19. S. Panchev: Random Functions and Turbulence, ed. 1st, Pergamon Press, Oxford, 1971.
20. U. Lindborg and K. Torssell: Trans. Metall. Soc. AIME, 1968, vol. 242, pp. 94-102.
21. T. A. Engh: Principles of Metal Refining, Oxford University Press, New York, 1992, pp. 1-35.
22. A. N. Van and S. Kmet: Int. J. of Miner. Process., 1992, vol. 35, pp. 205-223.
23. M. Maniruzzaman and M. Makhlouf: Worcester Polytechnic Institute, Worcester, USA, unpublished research, 2000.
24. J. O. Hinze: AIChE J., 1955, vol. 1, pp. 289-295.
25. S. T. Johansen, S. Gradahl, P. Tetlie, B. Rasch, and E. Myrobstad: Light Met., 1998, pp. 805-810.
26. S. T. Johansen, R. Anvar, and B. Rasch: Light Met., 1999.
27. F. M. White: Fluid Mechanics, ed. 3rd, McGraw-Hill, Inc., New York, 1994, pp. 487-488.
28. M. Maniruzzaman and M. Makhlouf: Light Met., 1998, pp. 797-803.
29. E. E. Underwood: Quantitative Stereology, Addison-Wesley Publishing Company, Reading, Massachusetts, 1970.

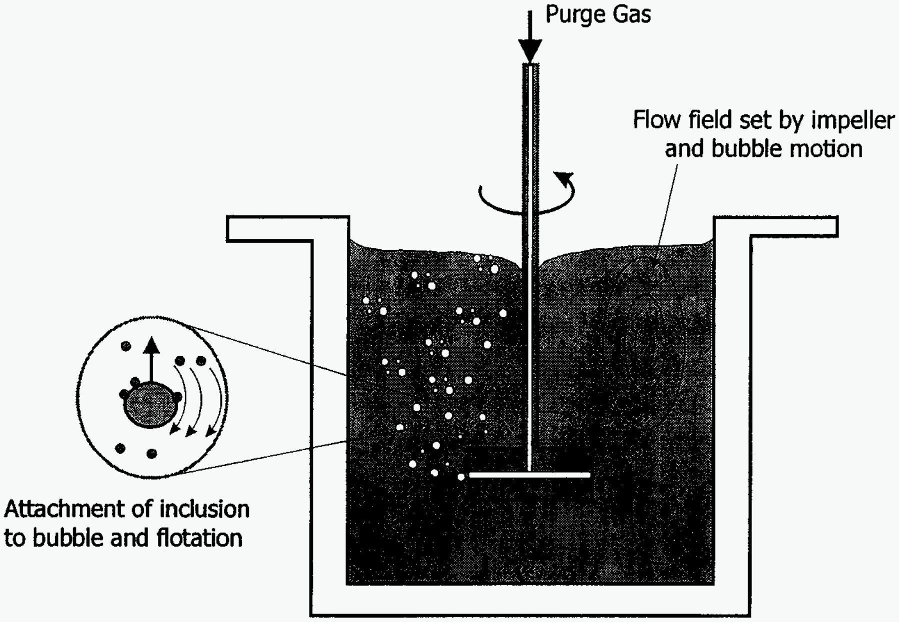

Figure 1: Flotation treatment process using a rotary degasser

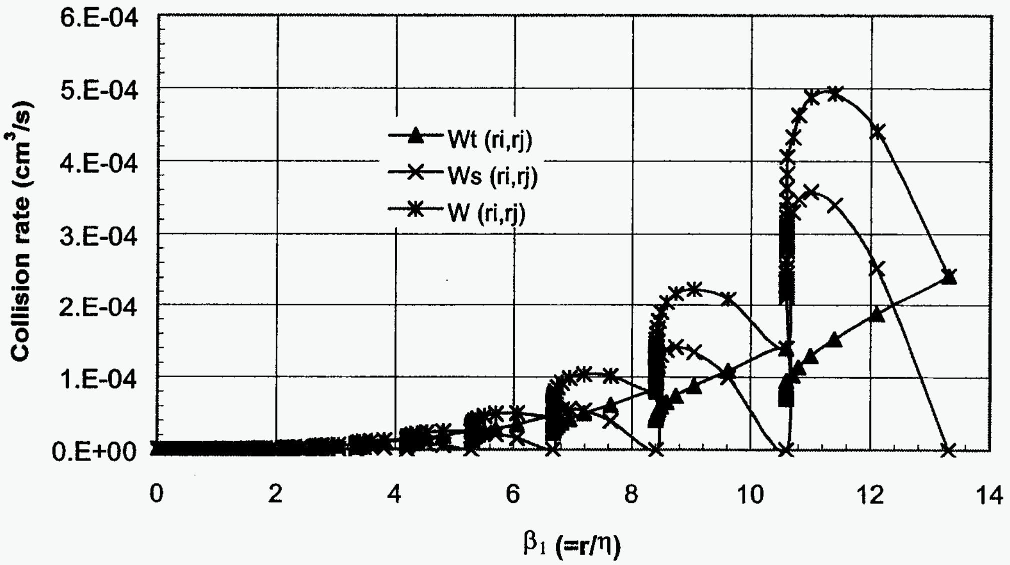

Figure 2: Variation of particle collision rate with particle size in a rotary degasser operating at 675 rpm with a gas flow rate of 36 liters of argon per minute.

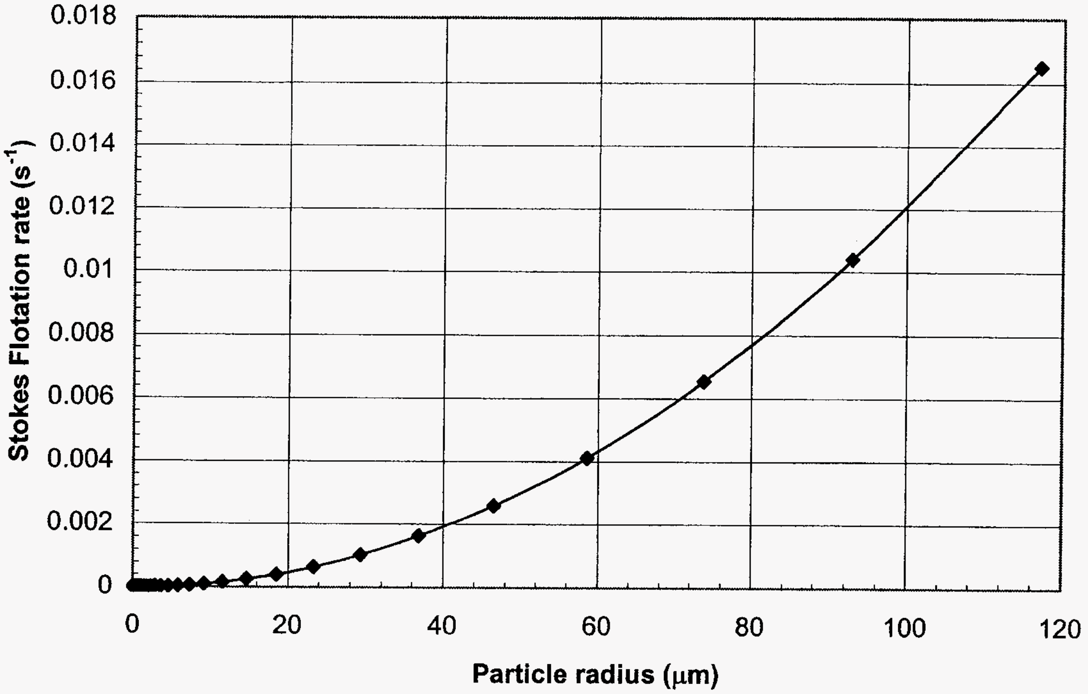

Figure 3: Variation of Stokes flotation rate with particle size in a typical rotary degasser.

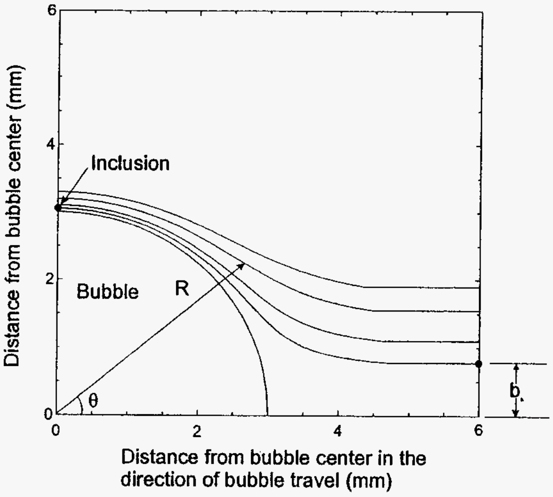

Figure 4: Streamlines around a 6 mm diameter argon gas bubble based on the assumption of potential flow.

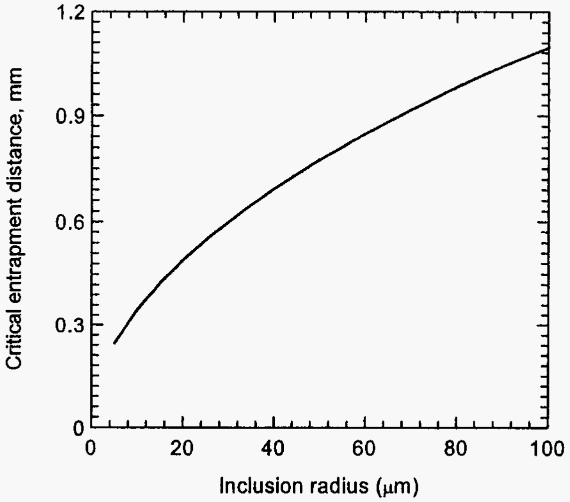

Figure 5: Critical entrapment distance as a function of particle radius.

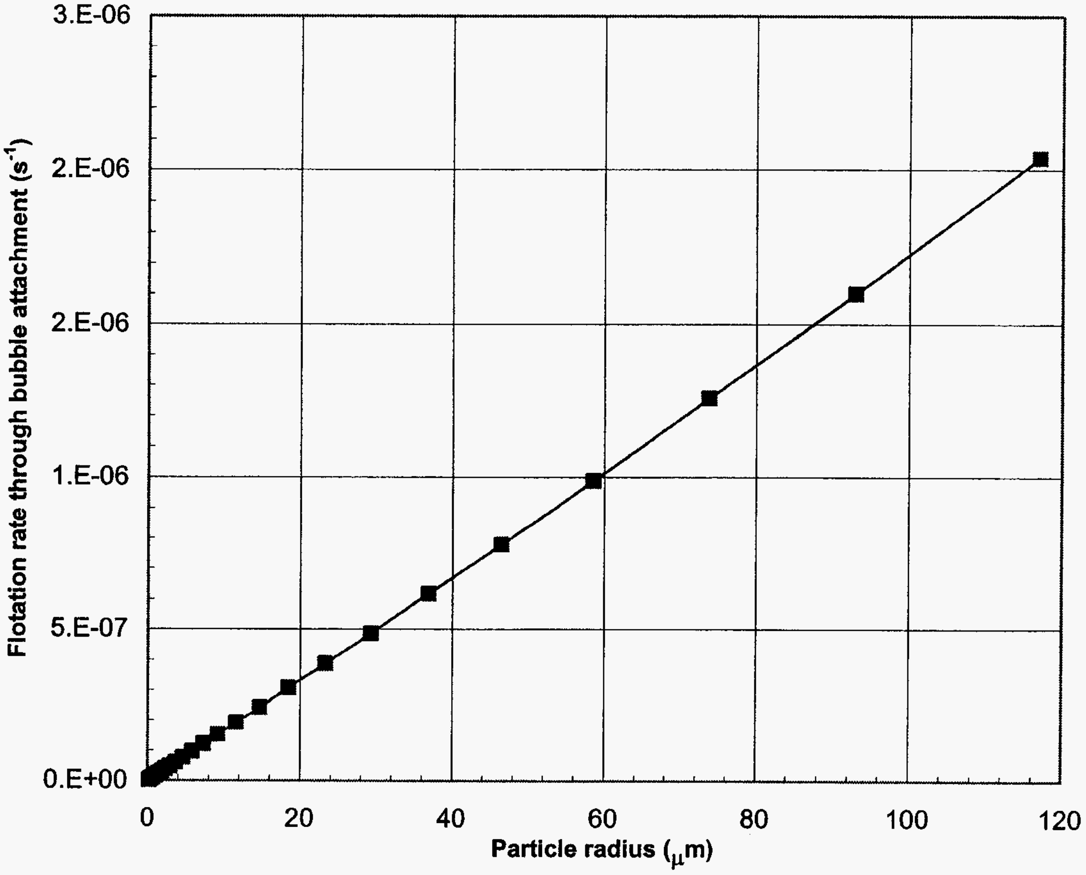

Figure 6: Variation of the flotation rate due to bubble attachment with particle size.

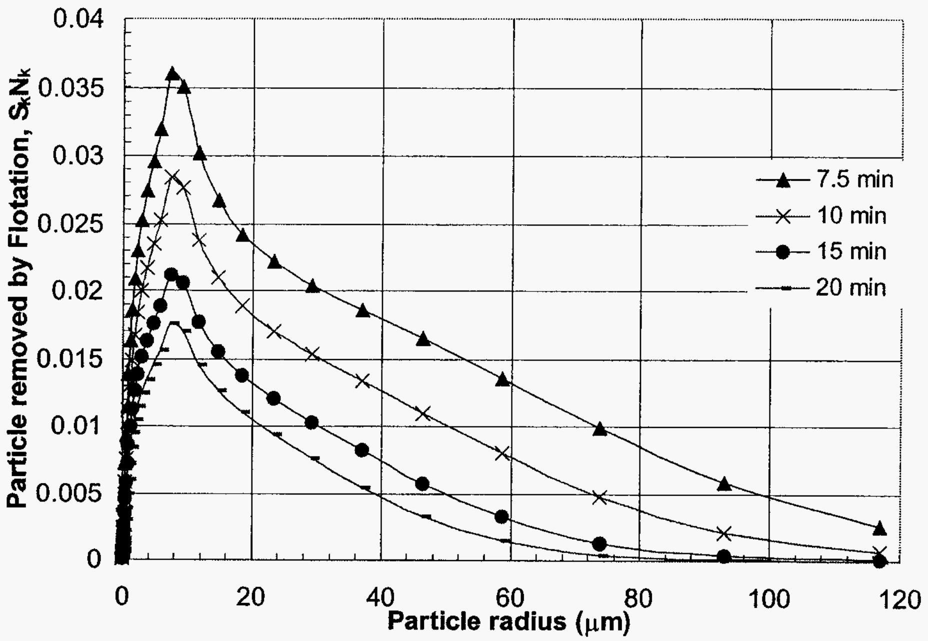

Figure 7: Variation of S_kN_k, with particle size.

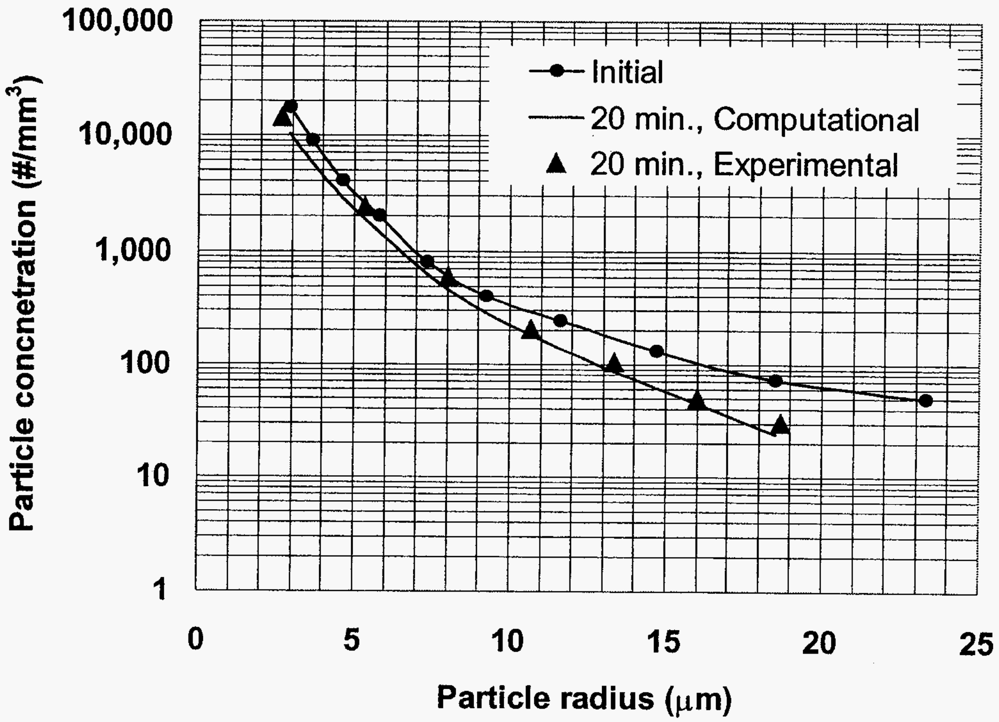

Figure 8: Comparison between measured and model predicted particle concentration vs. particle radius curves.

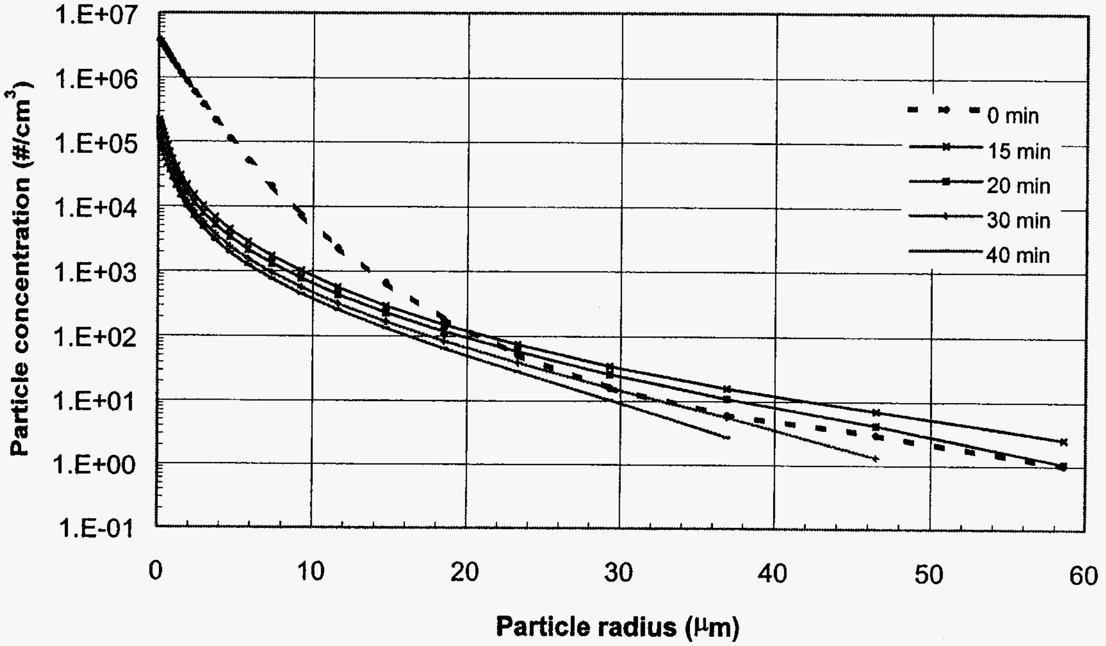

Figure 9: **Particle size distribution in a rotary degasser operating at 350 rpm, 36 l/min gas flow rate and periodic reversal of rotation direction.**

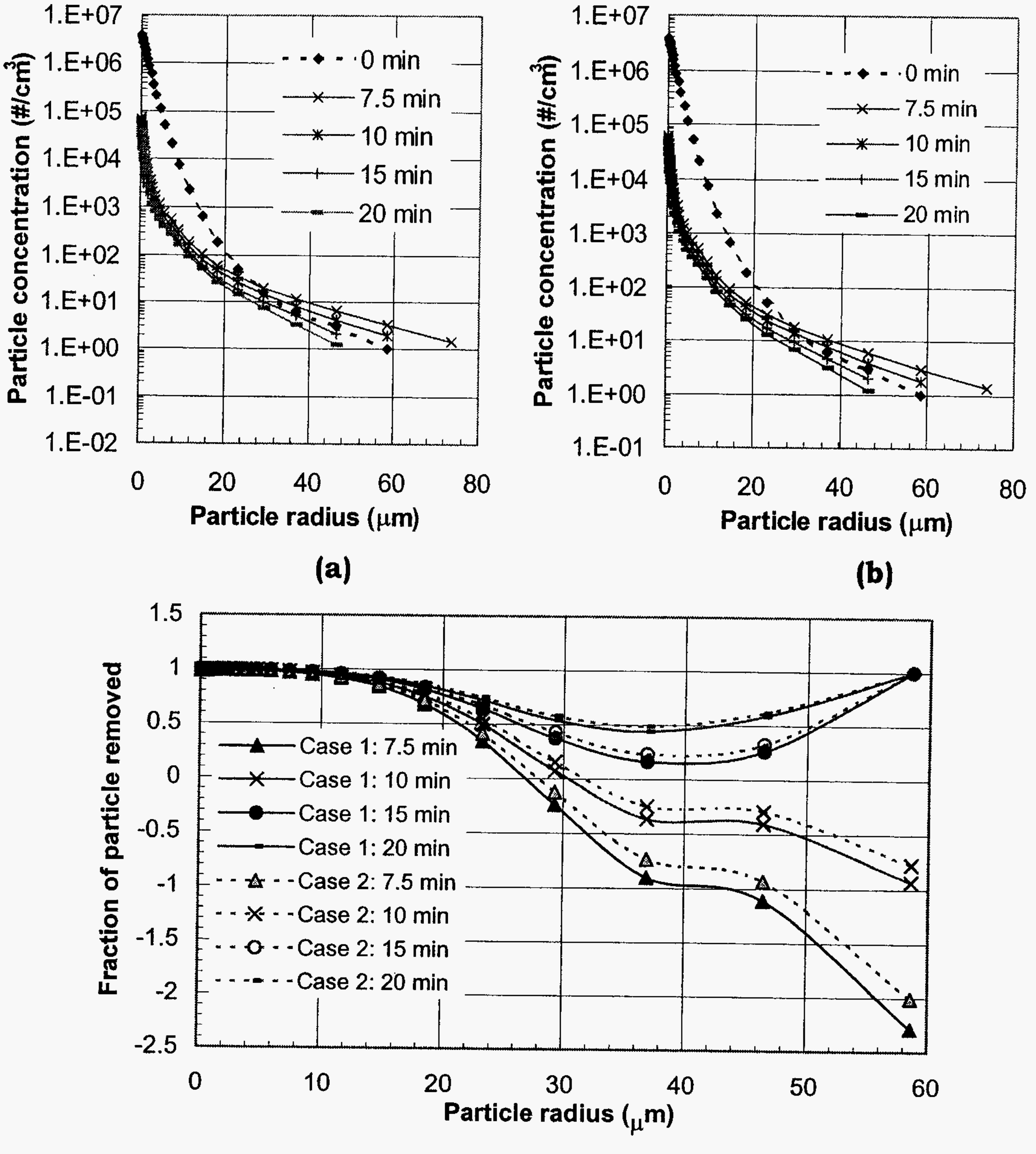

(a)

(b)

(c)

Figure 10: **Effect of rotation direction on particle size distribution in a rotary degasser. (a) Particle concentration profile for case 1, (b) Particle concentration profile for case 2, and (c) Particle removal efficiency.**

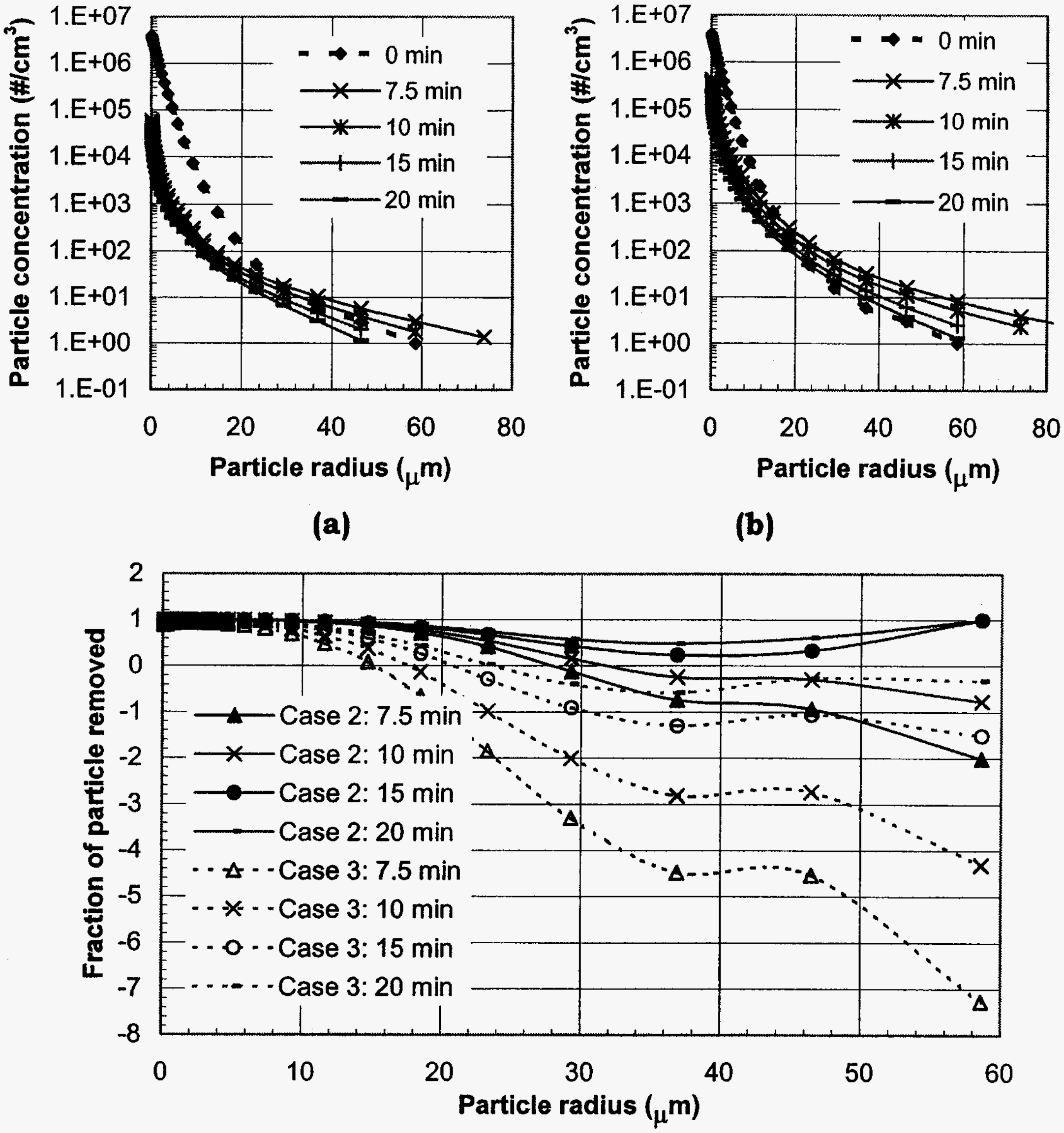

(a) (b)

(c)

Figure 11: Effect of rotation speed on particle size distribution in a rotary degasser. (a) Particle concentration profile for case 2, (b) Particle profile for case 3, and (c) Particle removal efficiency.

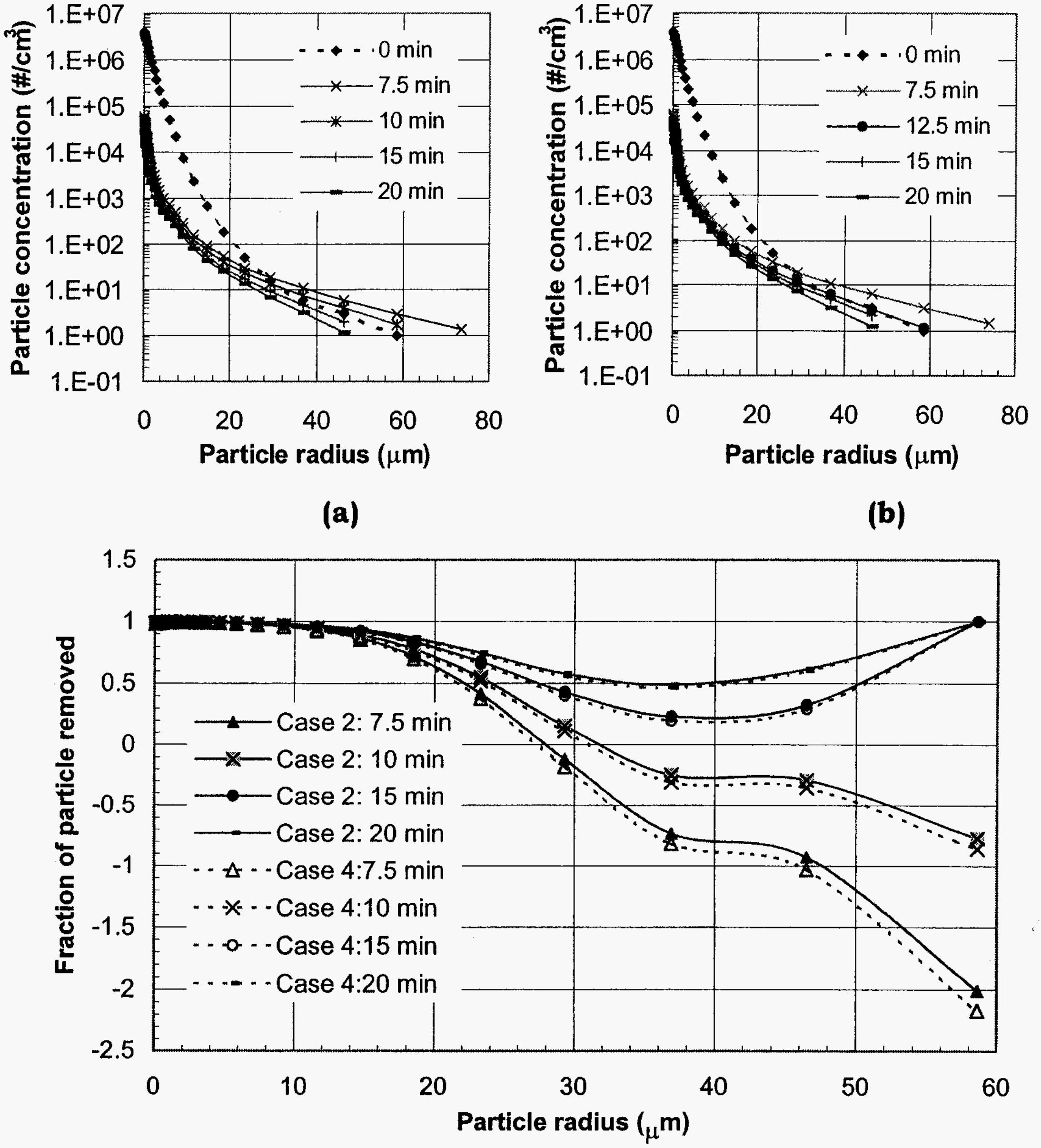

(a) (b)

(c)

Figure 12: **Effects of gas flow rate on particle size distribution in a rotary degasser. (a) Particle concentration profile for Case 2, (b) Profile for Case 4, (c) Particle removal efficiency.**

Chapter 4

CORRELATING LEVEL OF MELT CLEANLINESS WITH MECHANICAL PROPERTIES

4.1 INTRODUCTION

A variety of melt refining techniques has been proposed for the casting of Aluminum alloys over the years. These include several methods of degassing and filtration of the melt before it is cast. However, the casting processes inherently introduce some gas and other particles, which render the metal unclean. In such an eventuality, it is possible that the cast parts will not reflect the amelioration in properties rendered to them by the melt refining treatments. Such treatments are costly and hence become a liability if they are rendered null and void by the casting process itself.

In view of the above, the primary goal is to investigate the interaction of the cleanliness level, casting process and product performance. As part of this study, four beta sites were visited. These included three different casting technologies; sand casting, permanent mold casting and die casting. At each site, several different melt cleanliness levels were obtained using degassing and filtration techniques. Each level was quantitatively characterized. In addition, at each level test bars were poured to represent the product performance as a function of the melt cleanliness level. These test bars were subsequently subjected to room temperature tensile testing to obtain tensile properties associated with each level of cleanliness and for each casting process. Finally, all the data thus obtained, was synthesized to provide some insight into the interaction of cleanliness, casting process and performance.

To date, results have been obtained for all sites barring one. These results have been published in the proceedings of the fifth molten aluminum processing conference organized by AFS in Orlando in November, 1998 under the title " Interaction of Initial Melt Cleanliness, Casting Process and Product Quality: Cleanliness Requirements Fit for a Specific Use". The one site that remains to be investigated is representative of the die casting process. Data for this site is being obtained presently and will be analyzed in the next month. The upshot of this final task will enable us to correlate the clea~~nlin~~ess data across three casting technologies: Sand, Permanent Mold and Die Casting.

4.2 CORRELATION OF RPT DENSITY MEASUREMENTS WITH ALSCAN HYDROGEN MEASUREMENTS

Much has been written in the literature [1, 2, 3, 4, 5, 6] about the need for tools and enabling technologies to assess the level of cleanliness in the cast shop. Many of the tests which exist at present are either (i) very specific to measuring either hydrogen or a specific size range of inclusions; are (ii) not proven technologies; or are (iii) quite expensive instruments such as the LIMCA (based on the coulter counter principle). Thus some of these methods are limited in the information they provide, or are prohibitively expensive to utilize. The RPT test which has been around for over 30 years and was shown to be an indirect measure of both hydrogen content as well as inclusions by

Brondyke and Hess [7] has been used by foundries to obtain an indication of the melt cleanliness. The disadvantages of the RPT test have been discussed in some detail by Parmenter and Apelian [8] elsewhere. Moreover, the procedure followed from one cast shop to the other to obtain RPT densities varies widely. It is for this reason that a correlation between hydrogen content and RPT values has not been widely utilized on the production floor. However, during the last year, it has been shown by Parmenter and Apelian [8] that utilizing a specific optimized procedure, one can obtain RPT values with a high confidence level.

The purpose of this task is to address the question of how one can obtain usable operational information from the RPT, specific to hydrogen content of the melt. Because there are many test parameters that dramatically affect the results of the RPT, the accuracy of the RPT depends highly on the consistent and accurate adherence to a test protocol [9]. Although the RPT has been widely used throughout the aluminum casting industry for approximately fifty years, there has never been a standardization of the test protocol. As a result, each foundry has established their own test procedure and a related cutoff point for acceptable metal. To date, it has been highly unreliable to compare RPT results obtained from different facilities. Although correlation curves between RPT results and Telegas measurements have been developed, these curves are based on a specific test protocol, which has only been partially optimized and may be incomplete [2, 3, 4]. The R^2 correlation coefficients of these curves are typically between 0.5 and 0.6, which is not reliable. If metalcasters are to use correlation curves to have an indication of hydrogen levels from RPT results, it is first necessary to optimize the variables in the RPT procedure and develop correlation curves based on the resulting standard test method.

Earlier studies have revealed a very large scatter in the values of RPT densities for a given hydrogen value as shown in Figure 1. At any given hydrogen value there is a large variation span in the RPT densities and one cannot accurately pinpoint as to what density corresponds with what value of hydrogen. A motivation for this study has been to reduce the scatter in the data by optimizing the RPT test method and arriving at a correlation curve by employing the optimized test method. A curve resembling Figure 2 was sought in this study thus reducing the variability in the densities for a given hydrogen content and increasing the confidence of the test.

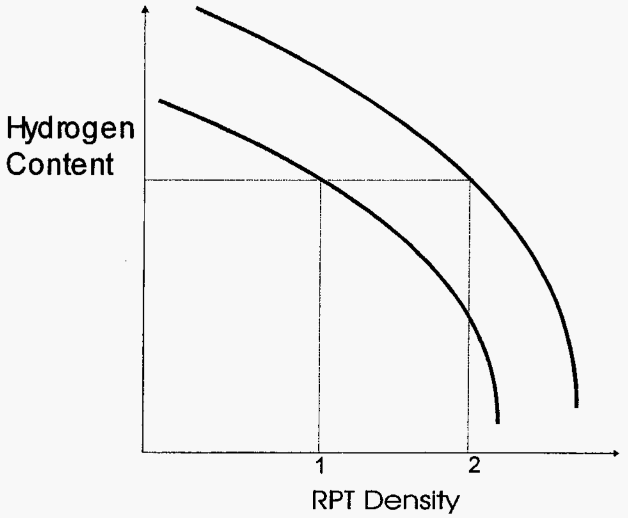

Figure 1: Typical Hydrogen vs. RPT density curve not following a“standard” procedure

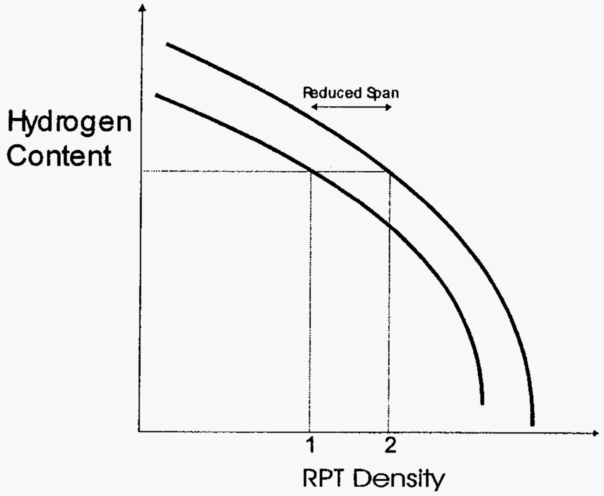

Figure 2: Targeted Hydrogen vs RPT density curve using the optimized RPT measurement procedure

Alloy 356 in the unmodified and non-grain refined condition was used to establish correlation curves; between ALSCAN hydrogen values and the RPT test. The procedure developed by the ACRL and Palmer Foundry has previously been presented [10]. A bona-fide correlation curve would have to be at a constant level of oxides. Not only is this difficult to maintain experimentally, but also it is unrealistic with respect to actual foundry conditions where oxide contents vary across different heats. In this regard, the curve sought was at varying oxide levels and at different melt temperatures. As a result, the curve obtained would certainly be weaker with respect to statistical correlation; however it would be more robust and useful to the foundryman.

For this experimental program 25 heats were prepared. The first 12 of these heats were prepared at Palmer Foundry. The remaining 13 heats were prepared at the Advanced Casting Research Center (ACRC).

The metal at Palmer Foundry was held in a 75-ton electric holding furnace. The first set of readings for hydrogen and RPT density was taken for the melt without any degassing. An RPT sample was pulled and solidified using the Stahl Gastech II tester as per the optimized test method. Following this, the Alscan probe was immersed in the melt and three concordant readings were taken to assess the level of hydrogen. Thereafter, rotary impeller degassing was carried out on the melt for 5, 8, 12 and 15 minutes respectively and at the end of each degassing operation, an RPT sample was pulled and an Alscan hydrogen value for the melt was obtained. A first estimate of the degassing times was determined by assuming an exponential decay rate of the degassing efficiency. Thereafter specific times were determined by trial and error to get four relatively evenly spaced hydrogen values. The four RPT samples from the heat were measured for density using the method previously described. The gas used for degassing was a mixture of nitrogen and chlorine in a ratio of 3:1 by volume. At each reading, the melt temperature, atmospheric pressure and relative humidity was noted. The identical procedure was followed for all the other heats. The melt temperature at heat was maintained within a specific range (1300°F-1400°F).

The experiments at ACRL were performed in 40 pound crucibles held in an electric furnace. A small-scale degasser designed at Palmer foundry was used in these tests. However, the purge gas used was Nitrogen. The degassing times were slightly altered, again by trial and error, to get four evenly spaced hydrogen readings. A similar testing procedure, as outlined above, was followed on the 13 heats carried out at ACRL.

To establish a correlation curve between RPT and Alscan, 100 data points of Alscan readings and RPT density measurements from 25 different heats were obtained for establishing the correlation curve. Figures 3 - 6 show some salient features of the testing.

Figure 3: Standardised RPT tester with "decoupled" vacuum pump

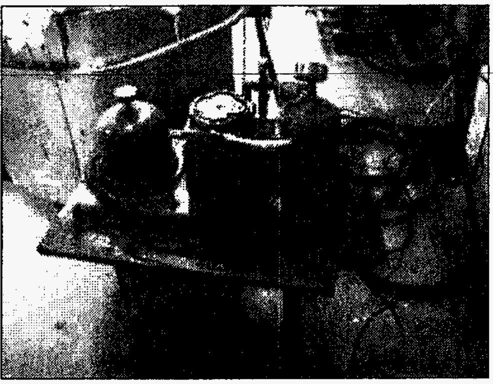

Figure 4: Usual RPT tester with pump and chamber in the same unit

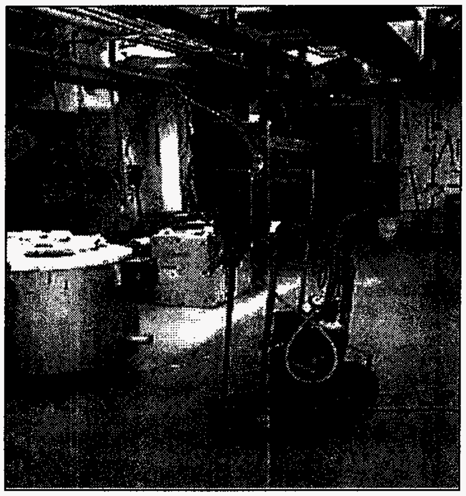

Figure 5: Alscan Unit

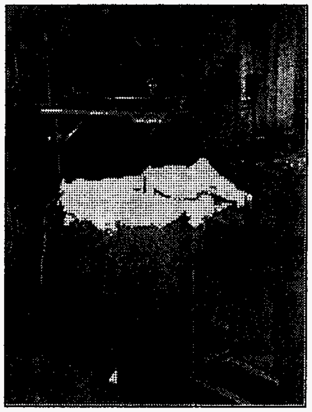

Figure 6: Holding furnace with rotary impeller degasser

Tables 1- 6 are spreadsheets of the experimental data with environmental conditions. Figure.7 is the master curve correlating RPT density to Alscan hydrogen contents in 356 alloy that has not been modified or grain refined. Table 7 shows detailed statistics of all the data points obtained in the several heats in combination.

Table1: Spreadsheet of Correlation Data

Heats 1-4

Heat	Hydrogen (ml/100g)	RPT Density (g/cc)	R Square for each heat	Relative Humidity
H1	0.238	2.557	0.627	78
	0.216	2.627		78
	0.143	2.643		78
	0.13	2.636		78
H2	0.196	2.615	0.649	78
	0.152	2.623		78
	0.152	2.623		78
	0.132	2.651		78
H3	0.239	2.611	0.990	68
	0.155	2.64		68
	0.128	2.645		68
	0.129	2.645		68
H4	0.178	2.632	0.082	68
	0.177	2.6		68
	0.152	2.643		68
	0.16	2.597		68

Table 2: Spreadsheet of Correlation Data

Heats 5-8

Heat	Hydrogen (ml/100g)	RPT Density (g/cc)	R Square For each heat	Relative Humidity
H5	0.195	2.575	0.690	35
	0.147	2.64		35
	0.098	2.634		35
	0.072	2.644		35
H6	0.169	2.639	0.714	35
	0.098	2.646		35
	0.072	2.644		35
H7	0.225	2.551	0.896	50
	0.187	2.614		50
	0.205	2.598		50
	0.199	2.625		50
H8	0.239	2.53	0.995	80
	0.216	2.567		80
	0.183	2.603		80
	0.155	2.636		80

Table 3: Spreadsheet of Correlation Data
Heats 9-12

Heat	Hydrogen (ml/100g)	RPT Density (g/cc)	R Square For each heat	Relative Humidity
H9	0.251	2.536	0.955	72
	0.224	2.545		72
	0.183	2.597		72
	0.142	2.636		72
H10	0.196	2.593	0.719	64
	0.179	2.614		64
	0.161	2.622		64
	0.157	2.594		64
H11	0.223	2.545	0.755	60
	0.202	2.545		60
	0.188	2.641		60
	0.17	2.653		60
H12	0.202	2.555	0.776	64
	0.159	2.626		64
	0.144	2.642		64
	0.185	2.604		64

Table 4: Spreadsheet of Correlation Data
Heats 13-16

Heat	Hydrogen (ml/100g)	RPT Density (g/cc)	R Square For each heat	Relative Humidity
H13	0.203	2.612	0.907	57
	0.180	2.612		57
	0.177	2.620		57
	0.145	2.643		57
H14	0.231	2.554	0.970	62
	0.201	2.602		62
	0.194	2.599		62
	0.177	2.626		62
H15	0.189	2.619	0.831	70
	0.188	2.622		70
	0.165	2.642		70
	0.122	2.646		70
H16	0.212	2.603	0.476	82
	0.208	2.576		82
	0.183	2.619		82
	0.178	2.61		82

Table 5: Spreadsheet of Correlation Data
Heats 17-20

Heat	Hydrogen (ml/100 g)	RPT density (g/cc)	R Square For each heat	Relative Humidity
H17	0.225	2.576	0.792	72
	0.204	2.612		72
	0.178	2.636		72
	0.135	2.646		72
H18	0.241	2.548	0.873	20
	0.225	2.596		20
	0.178	2.621		20
	0.101	2.676		20
H19	0.236	2.555	0.976	35
	0.196	2.592		35
	0.144	2.636		35
	0.082	2.665		35
H20	0.232	2.588	0.921	65
	0.185	2.602		65
	0.163	2.616		65
	0.170	2.617		65

Table 6: Spreadsheet of Correlation Data
Heats 21-25

Heat	Hydrogen (ml/100g)	RPT density (g/cc)	R Square For each heat	Relative Humidity
H21	0.229	2.586	0.995	65
	0.212	2.599		65
	0.155	2.623		65
	0.137	2.636		65
H22	0.125	2.64	0.961	25
	0.112	2.646		25
	0.092	2.645		25
	0.084	2.644		25
H23	0.177	2.636	0.806	40
	0.167	2.624		40
	0.118	2.639		40
	0.084	2.648		40
H24	0.184	2.598	0.880	67
	0.129	2.631		67
	0.119	2.64		67
	0.108	2.646		67
H25	0.211	2.602	0.991	69
	0.17	2.618		69
	0.135	2.637		69

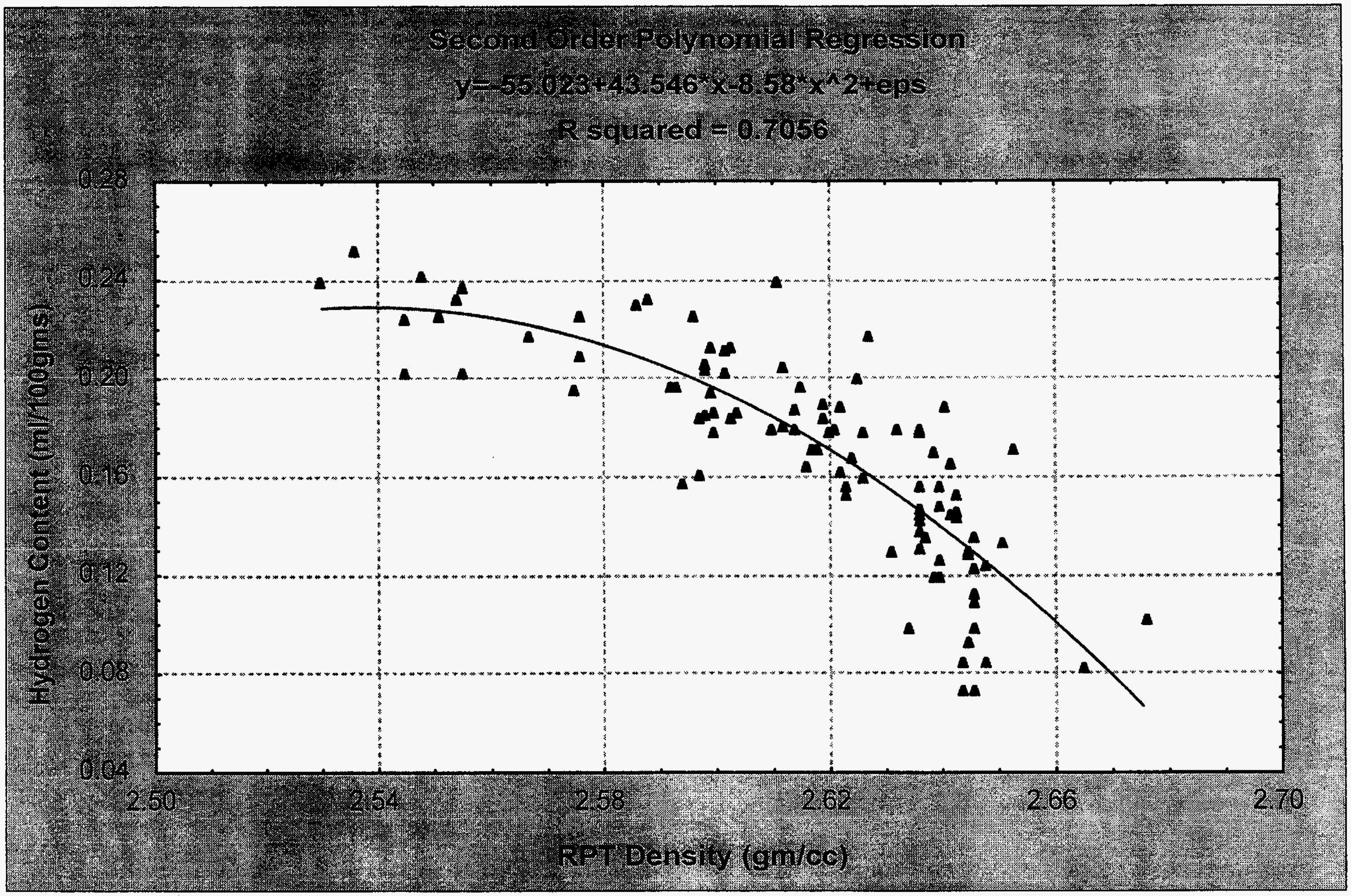

Figure 7: Correlation curve relating RPT densities to Hydrogen content in 356 unmodified and non grain refined melts

Table 7: Detailed Statistics of accumulated data of RPT density and Alscan Hydrogen contents

Variables	Mean	Standard Deviation	R	R^2	P	N
RPT density(g/cc)	2.615	0.031	-0.844	0.71	0.00000	100
Hydrogen Content (ml/100g)	0.1696	0.043				

The results are shown in Figure 7 relating RPT densities to hydrogen content in 356 melt. The correlation curve corroborates earlier studies that showed that the RPT density is inversely proportional to the hydrogen content of the melt. It can be seen that there is some degree of scatter in these data points. The 100 data points were fitted using non-linear regression (STATISTICA software), and as can be seen in Figure 7, the correlation is quite reasonable though there is some scatter of the data points. A second-degree polynomial function was fitted to the data and is shown on the graph (See Figure 7).

To analyze the confidence level of the correlation, the Pearson coefficient or Pearson Product Moment (R) was calculated. The value of R indicates the presence of correlation. An R-value of –1 indicates perfect negative correlation while an R-value of 1 indicates perfect positive correlation. The value of R^2 indicates the strength of the correlation. For example, any R^2 value above 0.5 shows correlation, and a value of 0.7 indicates fair correlation. The reliability of the data is given by a factor P that is the Probability of Error of the data. For most scientific purposes a P value of 0.05 implies borderline reliability. The lower the value of P, the more reliable the data.

The R^2 value of the consolidated data from this investigation is 0.71 while the P value is negligible (See Table 7). This implies that the number of samples for this analysis is large enough and the data is extremely reliable. However there is not a perfect correlation (R^2=1), which is reasonable due to the extraneous factors causing scatter. This is understandable when one considers the variation of oxide inclusions in the 25 melts. Another cause of the scatter is due to melt temperature variations. Temperature is directly proportional to the solubility of hydrogen in the melt but the difference is small. In certain heats the gas content could not be varied significantly by degassing. This could be attributed to the high ambient humidity on those occasions that may have caused a brisk rate of regassing of the melt (See Heats 8 and 16 in Tables 2 and 4 respectively).

From Figure 7, it appears that the strength of the correlation decreases at the high end of RPT density. In particular, a wide degree of scatter is observed when the hydrogen content is at the lower end of the spectrum. This appears to suggest that the RPT test is more sensitive to changes in oxide contents than hydrogen content when the hydrogen content is relatively high. It is also evident from the curve that the RPT densities increase broadly from 2.55 g/cc to 2.65 as we go from hydrogen content of 0.24 ml/100g to 0.08 ml/100g. The curve tapers downward at the lower end of hydrogen, the RPT density approaching the theoretical value of about 2.7 g/cc at zero hydrogen content.

In heats where four evenly spaced hydrogen values were obtained, the R^2 value of the individual heats was significantly higher (See Tables 4.2-4.6), sometimes reaching as high as 0.97. This means that within one heat, when oxide contents are more or less constant, the correlation between RPT density and Hydrogen content is very strong. But one cannot establish a standard curve on the basis of one heat as the values would be a local one to the heat and would not really represent a generic correlation curve for a particular alloy, in this case 356 Al alloy.

It can be concluded from this study that there is a correlation of RPT densities with Alscan hydrogen values for a given particular alloy. However, this correlation has an acceptable confidence level only when the ACRC optimized RPT density measurement procedure is followed. The above correlation curve can be useful for the foundryman in that one can estimate hydrogen content in the melt from the density of an RPT sample . The hydrogen content is narrowed down from the estimate normally obtained using visual examination of the RPT sample. Once the hydrogen content in the melt is estimated from the correlation curve it can be monitored as per requirement.

4.3 CORRELATION OF MELT CLEANLINESS WITH AS-CAST MECHANICAL PROPERTIES

Over the years, there have been several molten metal cleaning methods that have been proposed and utilized in aluminum processing. These include various different methods of degassing and filtration of the melt. To date, a major weakness has been the absence of a direct quantitative measurement of the cleanliness level of the melt. Because of this, control of the molten metal processing methodologies has not been adequately carried out. In the recent past, several indirect assessment techniques as well as some direct quantitative measurement techniques have become available enabling one to monitor and assess performance. An important issue is the effect of the subsequent steps in the overall manufacturing cycle on cast part properties and performance. Specifically, the melt may be adequately processed; however will the casting process introduce gases and other non-desirable second phase particles? Are there systemic issues that need to be addressed? Is it possible that the cast part may not reflect the expected amelioration in part performance due to the melt refining treatments utilized because these effects have been nullified by subsequent steps in the casting process? Thus our motivation for this study was to investigate the interaction of initial melt cleanliness, casting process and product quality.

Initial melt cleanliness in aluminum alloys is determined by the amount of impurities present in the melt before it is cast. Impurities in aluminum alloy melts can be classified into four main groups. These include volatile elements, non-reactive elements, reactive elements and inclusions. Volatile elements are elements such as hydrogen and sodium with a high vapor pressure. Reactive elements are those that can be removed easily by adding salts and other chemicals. These include calcium, lithium and titanium. A non-reactive element is one that cannot be removed by ordinary processes. An example of this is iron. Inclusions are hard extraneous particles brought in the melt either through chemical reaction within the melt or via external sources. Among the most serious quality detractors are dissolved hydrogen and inclusions [11-14].

In this study, melt cleanliness has been varied by having various different levels of hydrogen content and oxide content. Hydrogen content in the melt manifests itself as porosity in the casting and this is detrimental to tensile properties, pressure tightness of the casting and fatigue strength [12]. Similarly, inclusions can act as potential failure sites and are also detrimental to the fluidity of the melt and machinability of the casting [18]. The oxides have been found to be the largest in size among all inclusions and hence have been used as an index for cleanliness. Mechanical properties ultimately reflect the effect of processing conditions on the resultant cast product.

Two specific different casting processes were selected: a sand casting shop and a permanent mold shop; each site having different melting and molten metal processing conditions. Metal cleanliness levels were measured and subsequently tensile properties evaluated. Based on our observations of the interaction between initial melt cleanliness and casting process, we present some insight pertaining to the level of melt cleanliness required fit for a specific process / or use.

The primary purpose of this study is to investigate the interaction of initial melt cleanliness and final product properties, taking into consideration two different casting processes: sand and permanent mold.

During the course of this study, an opportunity was also presented to study the efficacy of various melt cleaning treatments and also the different measuring equipment used to characterize the various melt cleanliness levels.

An analysis of typical oxide size distributions encountered in this study is also presented.

Experiments were performed at three different sites. Two of these sites were sand casting shops and the other was a permanent mold cast shop. For obvious reasons, the identities of these sites are not revealed and are designated in this thesis as sites #1, #2 and #3. To have some uniformity across all three sites, the basic plan given below was followed:

- For each cast shop, a specific alloy was chosen to be cast. Its chemical composition was analyzed and recorded.

- The melts were categorized based on their levels of cleanliness. Cleanliness of the melt was characterized by a combination of the amount of hydrogen gas and inclusions. Specifically, this translated into having melts of varying degrees of degassing and with or without filtration. The melt treatments carried out at each site dictated the categorization of the melt into different levels of cleanliness. For each site, a minimum of three different melt levels was attempted.

- The melts were tested for gas and inclusions using the Alscan, Qualiflash and LAIS assessment techniques during the period the melt was held before casting. (Details for each technique are given under sampling procedures).

- The melts were cast into standard test bars at each different site – sand and permanent mold. The test bars were mechanically tested for tensile properties.

Site # 1

In this site, Alloy 356 was used for this study. The metal consisted mostly of primary ingot purchased from Alcoa . Three different conditions of the melt were simulated.

For the first melt condition, the alloy was simply melted in a breakdown melter, treated to achieve the required chemistry and subsequently transferred to a 75-ton electric holder. No grain refiners or modifiers were added. The testing on this melt included LAIS sampling, Qualiflash rating, Alscan readings and RPT sampling. All the tests were done in tandem. In between tests, test bars were poured. This testing procedure was carried out for the two other melt conditions.

For the second melt condition, the melt was filtered. The filter was of a ceramic foam type and was made of alumina. The pore size of the filter was 30 ppi. The melt was again transferred to the same holder as before, the metal was sampled and analyzed.

For the third melt condition, the melt was filtered and transferred into the holder as before, but in this case lance degassing was carried out for a period of 20 minutes. The degassing mixture consisted of argon and chlorine in the ratio of 9:1.

Site # 2

At this site, the alloy used was A356. The melt on an average consisted of 33% primary ingot and the remaining being remelted stock. All the testing was done in an electric pot melter (100 lbs.). Three different melt conditions were achieved at site #2 on the basis of degree of degassing treatment alone, as filters were not utilized at the site. The first melt was tested without any melt treatment whatsoever. The cleanliness analysis was based on Alscan readings for Hydrogen content, LAIS sampling for oxides, and Qualiflash ratings. At the end of the sampling tests for a given melt condition, a set of test bars was poured.

For the second melt condition, the melt was subjected to a degassing treatment that entailed purging argon through a rotary impeller for 30 minutes. Tests identical to the first condition were conducted.

For the third melt condition, the molten metal was purged with a mixture of argon and chlorine (9:1) for 40 minutes. Sampling tests similar to the other two conditions were then carried out.

Site # 3
At this site, the alloy used for the tests was 319.1. Secondary metal obtained from the open market was used. Pre-alloyed ingots were purchased with residual Ti . Grain refiner (TiBor) and Strontium as modifier were added to the melt. Strontium levels were targeted at about 0.025. Mg was added to monitor Ti levels. Also some Sr and Mg burnt out during melting hence had to be added in subsequently in small amounts. The process was a continuous one and a 6000 lb. reverberatory furnace was used. This furnace consisted of a melting holding area and a dip out area. The metal was automatically poured from the dip out area to the casting mold.

A fluoride-based flux was used on the walls of the reverberatory furnace. The dip out area had a bottomless crucible in the center. The melt used for casting was normally taken from inside this crucible, as it was understood to be cleaner than the melt outside the crucible.

Four different melt conditions were achieved and used for this study. The first melt investigated was inside the crucible in the dip out area. However the bottom of the crucible was fitted with an alumina filter having a pore size of 30 ppi. The melt was degassed using continuous Nitrogen lancing in the dip out area. This was the cleanest metal condition obtained. Alscan, Qualiflash and LAIS testing were done on this melt. RPT samples were also taken.

For the second melt condition, degassing was identical but the filter box had been removed from the crucible. The same testing methodology as before was carried out. The crucible was removed for the third condition and the testing was done in the pot. Degassing was carried out but there was no filtration. An identical testing methodology as before was followed.

For the fourth condition, the degassing was turned off and the melt was allowed to re-gas for about 10 hours. The tests were repeated in the pot. This constituted the 'dirtiest' metal.

For each melt condition, several test bars were poured into permanent mold test bars hence the test bar was a correct representation of the casting technology used at the beta site. The test bars were poured after all the tests on a given melt were completed.

Three different types of sampling were carried out namely Alscan, Qualiflash, and LAIS. RPT testing was also done at some sites but has not been reported. Details pertaining to this test are available extensively in a previous work done by L. Parmenter, D. Apelian and F.Jensen [33]. In most cases the three tests were performed in tandem for most effective utilization of time. Each sampling procedure is discussed in some detail in this section.

Alscan

The Alscan is an instrument designed to perform in-line measurement of hydrogen in molten aluminum. This unit consists of a ceramic probe that is immersed in the melt to be analyzed. A purge gas is continuously recycled into the instrument and out through the melt through the probe. Hydrogen in the melt is picked up by this purge gas and results in a drop in thermal conductivity of the gas and this is used to represent a particular hydrogen concentration in the melt. The unit has a built in microprocessor that processes data and controls its operation. Below is a summarized discussion of the procedure of operation of the instrument.

Before taking a reading, a few of the parameters on the ALSCAN unit are adjusted. The number of readings is set at 1, the time for each reading is set at 3 minutes and the alloy factor is adjusted to the required value. These settings are adjusted on the display panel of the unit. The alloy factor is a multipicative factor used to normalize the effect of the solubility of hydrogen on the chemical composition of the alloy. Hence it varies according to the type of alloy used and its chemistry.

Once the heat to be sampled is ready, the unit is brought in the vicinity of the melt and the unit is turned on. The pressure valve is previously turned on, and the outlet pressure is set at about 350-700 mbars.

Within 30 seconds of switching on the unit, the probe and the thermocouple are immersed in the melt up to 5 to 10 cm. The probe starts stirring and the first reading is read off the paper at the end of 3 minutes. This reading is discarded, as it is generally a little lower than the actual value of hydrogen present. Thereafter, the stirring was stopped, the probe was removed and the settings were changed to obtain the final set of measurements. The number of readings is set at 5 and the time for one reading is set at 10 minutes. Usually, this is sufficient time for attaining equilibrium between hydrogen entering the probe and hydrogen leaving the probe [15]. However, if the readings progressively increase significantly with time, it is an indication that the time for one reading should be higher. In this case it would be set to 15 minutes.

The system is then turned on and the probe is re-immersed in the melt. The readings are read off after 5 readings, each reading being of duration of 10 minutes. At the end of one reading, the unit automatically adjusts itself to take the next one. At the end of the last reading, the probe is removed and the unit is switched off and set aside.

This general procedure is followed when sampling any heat. Depending on the sampling area, the unit could be raised or lowered such that the probe is immersed in the melt.

Qualiflash

This unit has a crucible into which the melt to be analyzed is poured. A filter is fit at the bottom of the crucible, through which the metal passes and flows into a special mold that has steps of different depths. The level up to which the metal fills this step mold indicates qualitatively the cleanliness of the melt.

The unit is brought near the sampling area. Before using it, the filtering section has to be attached at the bottom of the funnel. There are two sizes of the filtering section and a choice is made depending on the alloy to be sampled. The extruded ceramic filter is placed at the bottom of the funnel above the filtering section. The funnel is preheated to about 450 degrees Celsius with the insulation cover on top of it. Subsequently the pouring spoon is preheated by holding it over the melt. It is then immersed in the melt and filled to the brim. The pouring spoon is then briskly brought near the unit and shoved in the space that holds the thermocouple. An instantaneous temperature of the melt in the spoon is obtained and noted. Thereafter the spoon is emptied of its contents into the funnel (the cover is removed prior to this) and the cover is replaced. The metal flows for about 15 to 20 seconds through the filter and into the step mold underneath. The number of steps filled is noted and used later on to obtain a Qualiflash cleanliness rating.

After a measurement has been made, the unit is allowed to cool for a few minutes and then the step mold is emptied of the solidified metal; so also is the funnel that has the remnant metal in solid form in it. The filter is a consumable one and it is removed and discarded. A new filter is fitted in its place for the next measurement. However, before the next measurement, the funnel temperature has to cool to the vicinity of 450 degrees Celsius. This takes about 10 minutes.

After the above steps have been followed, the unit is ready for the next measurement. Five measurements on the average were taken from a single melt.

LAIS

This technique involves pre-concentration of the inclusions present in the melt using a stringent filter. The sample that is to be analyzed is melted and made to pass through a filter. The residue on the filter is then analyzed metallographically to provide quantitative information about the inclusions in the melt.

This technique requires sampling cylinders into which the metal is pulled through a filter. Once the cylinders are prepared, the vacuum assembly is taken near the sampling area. A cylinder is fitted to a crossover, which has another cavity where the sampling cup is placed. The upper end of the cylinder is connected to the vacuum pump having an appropriate vacuum gauge. The vacuum is turned off and the cylinder and sample assembly are immersed into the melt for preheating. The assembly is held using appropriate fixtures. After about 10 minutes of preheating, the vacuum is turned on and the melt begins to get sucked into the cylinder and the sampling cup through the crossover. The end point of the test is when the metal completely fills up the cylinder. This is indicated by the emission of fumes on the top of the cylinder. At this point, the vacuum is turned off and the cylinder assembly is placed on a graphite chill block for unidirectional cooling. Thereafter, the cylinder is disassembled and the sample is removed and placed in an envelope for subsequent metallographic analysis.

The next cylinder is then preheated and the process is repeated. About 7 to 10 samples were pulled for a single melt condition.

A sample obtained from the LAIS is typically a cylinder with the dimensions of 1.7 inches by 0.7 inches. The sample is a graphite cup, which has a frit running along its cross section about an inch from one end. The metal pulled resides in the hollow of the cylinder and the oxides collect at the frit. Hence the frit has to be exposed and metallographically prepared.

The first step was to cut the samples about 0.4 inches from either end along the cross-section. The ends were discarded and the sample was sliced in half along the diameter of the cylinder. As a result, the frit and the metal were exposed. Both halves were metallographically prepared and analyzed for greater sampling area. The samples were mounted and polished using diamond paste.

Subsequent to the polishing, the samples were analyzed using a Nikon Epiphot optical microscope. At a magnification of 100X, the sample position was adjusted such that about half of the frit and half the metal were visible through the eyepiece. Gradually the specimen was moved from one end to the other so that the entire length of the frit was analyzed for oxides. Once an area was in focus, the image was acquired on a computer. MIRAGE image analysis software was used to count the oxide area.

First, the software was calibrated such that the magnification was the same as the microscope. The image was sharpened using some available filters in the MIRAGE system. Next, a grid was generated on the image in which each square was a 100 microns in length and width. The oxides, which appeared as dark phases in and above the frit, were scanned with the eye. The approximate percentage area covered by the oxides in each square on the grid was noted. The sample was then shifted to the adjacent new area under the microscope and the entire process was repeated.
When the entire cross section of the frit had been analyzed, the oxide count of the sample was calculated using the following formula:

$$\frac{\textit{Total Frames of Inclusion Material} \times \textit{Frame area}\ (mm^2)}{\textit{Sample Weight}\ (kg) \times \dfrac{\textit{Chord Width}\ (mm)}{10.4\ (mm)}} = \textit{Oxide Count}\left(\frac{mm^2}{kg}\right)$$

The area of each frame = 0.01 mm$^{2.}$
The sample wt. of a fully filled cylinder = 550 gm.
The chord width is the length of the frit analyzed. This is about 1 cm at a magnification of 100X.

The LAIS samples obtained from earlier experiments were used to calculate the LAIS oxide count of the various melts. This gave an average picture of the oxide contents of the melt but did not delineate the size distribution of various oxide particles. It is common knowledge that if the oxide particles are relatively small and evenly distributed, they do not hamper the performance of the cast parts. Hence, it was decided to use the concentrated oxide particles on the frit of the LAIS samples to represent the distribution of the oxides. It must be noted, however, that the pressure with which these particles are pulled through the frit and the random occurrence of coalescence between two or more particles may lead to distributions slightly off the actual distribution one would expect in a melt.

The digital images for the LAIS samples were revived using the MIRAGE image analysis software. Appropriate "gray-scale" settings were used such that contrast was suitable for analysis of the oxide particles and their size. It must be noted that three typical samples of untreated melts were used in the analysis. The image analysis provided a list of particle sizes that were detected by the analyzer. Each particle was manually chosen from the digital micrographs to avoid detection of darker particles that were not actually oxides, but parts of the graphite frit. The particle data from each sample was taken and all the data was appended into a master "oxide particles" file.

This file was then imported into STATISTICA, a powerful statistical software package, whereby the data was grouped into several size bins each of which had a frequency that amounted to the actual number of particles that fell within each size bin. The distribution thus obtained was representative of oxides found in each of three samples pertaining to three casting processes and hence it was generic in nature.

The data from the image analysis consisted of equivalent circle diameter (ECD) values of the detected particles, the area of the particles and the shape factor. The ECD is a parameter that describes the size in terms of the diameter of a circle whose area is equal to that of the particle.

The shape factor is a value varying between 0 and 1. The closer the value is to one, the more equiaxed the particle is. A histogram was plotted for ECDs of the various particles to represent a typical size distribution of the oxide particles. Also, the shape factors were also plotted according to their frequency of occurrence in a histogram. This was done in the same fashion as the ECDs. The distribution reveals the predominant shapes of the oxides in 2D.

At each cleanliness level, test bars were cast and evaluated in the as-cast condition. This was done intentionally because it was believed that ageing of these alloys would lower the ductility. This would imply that the sensitivity of the ductility to cleanliness conditions of the initial melt would plummet making the study of the variation in the properties with cleanliness indices that much more difficult. Also, we wanted to alleviate the variability of heat-treatment cycles performed on different bars at different cast shops.

The specimens that were tested were round in cross-section (See Figure 1). The specimens were all of 0.5-inch gauge diameter and 2 inches gauge length.

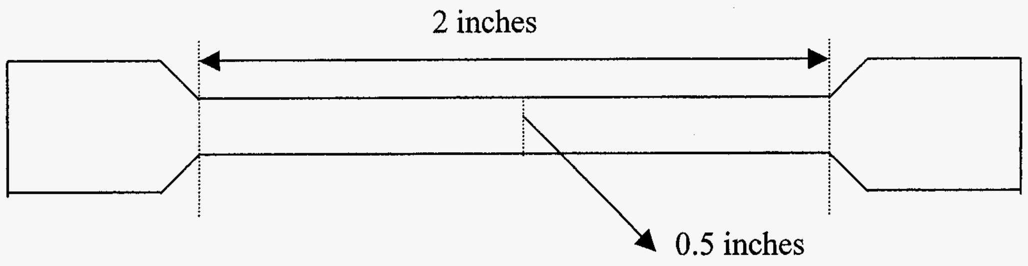

Figure 5.1 (Not to scale): Representative tensile sample

Room-temperature tensile tests were carried out on the INSTRON 5500R. A 20,000-lb load cell was used for loading the specimens. The machine was operated at a ramp-rate of 1.5 mm/min.

The strain was measured using an MTS extensometer of gauge length 2 inches. The data was collected using the Merlin Instron software system. The raw data was processed using STATISTICA to obtain percent elongation. This parameter was averaged out for about 30 testbars for a single melt condition to obtain a statistically significant figure. For each metal condition in each site, the % elongation values were averaged and an average % elongation was used as a property parameter. The standard deviations were also recorded. Being cognizant that the DAS of the test bar castings will strongly affect the tensile properties and may have a propensity to offset the effect of metal cleanliness, measures were taken to ensure that the DAS was about constant for each of the test bars within a given melt condition. The UTS was also recorded, as was the chemistry of the pertinent alloy.

Subsequent to the tensile testing of the various test bars, it was sought to examine the surface of these broken test bars. The study was aimed at studying specific causes of fracture owing to melt cleanliness levels. Certain characteristic test bars were cut into flat disc-like samples and were used to perform stereomicroscopy and SEM. SEM was performed on an AMR 6400 Scanning Electron Microscope. It was seen that on the surfaces very large oxides and occasionally discernible pores were visible. These were established as the causes of the failure of the test-bars and a detailed fractographic evaluation is presented herewith.

Figure 2 shows the distribution of the Equivalent Circle Diameter (ECD) of oxide particles. The plot shows the number of occurrences of a particular size-range of oxide particles in a typical sample. Figure 3 shows the distribution of shape factors of oxide particles. The plot, similarly, shows the number of occurrences of a particular shape factor (as a percent value).

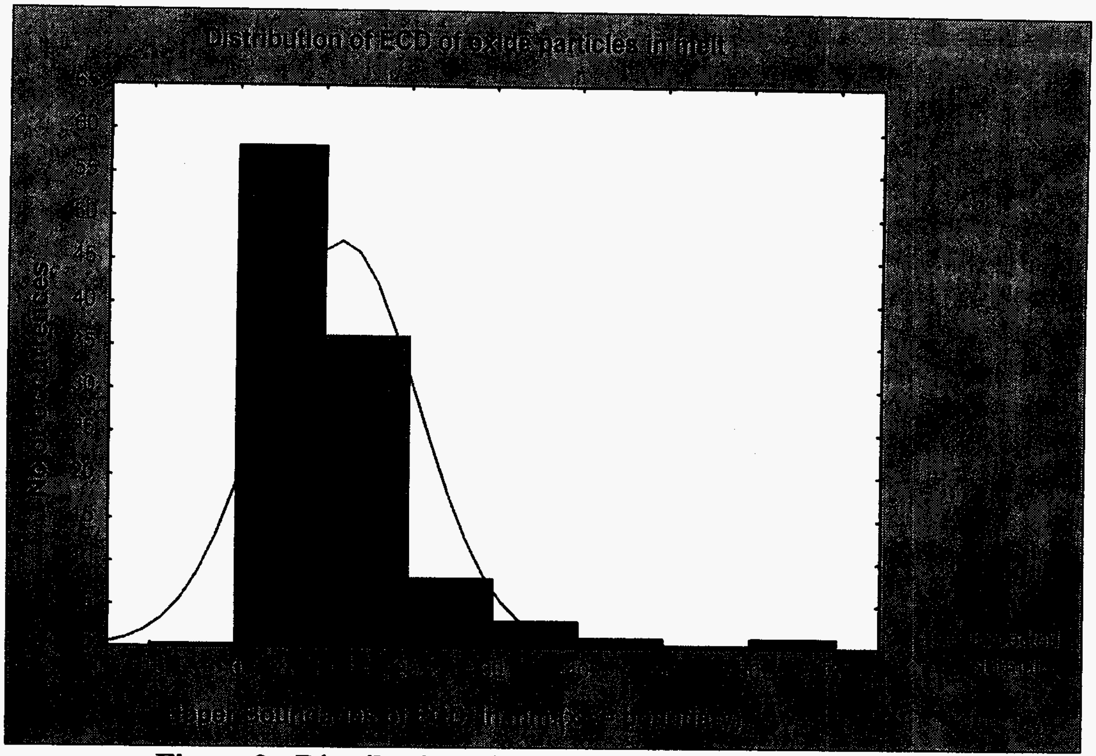

Figure 2 : Distribution of ECD of Oxide Particles in Melt

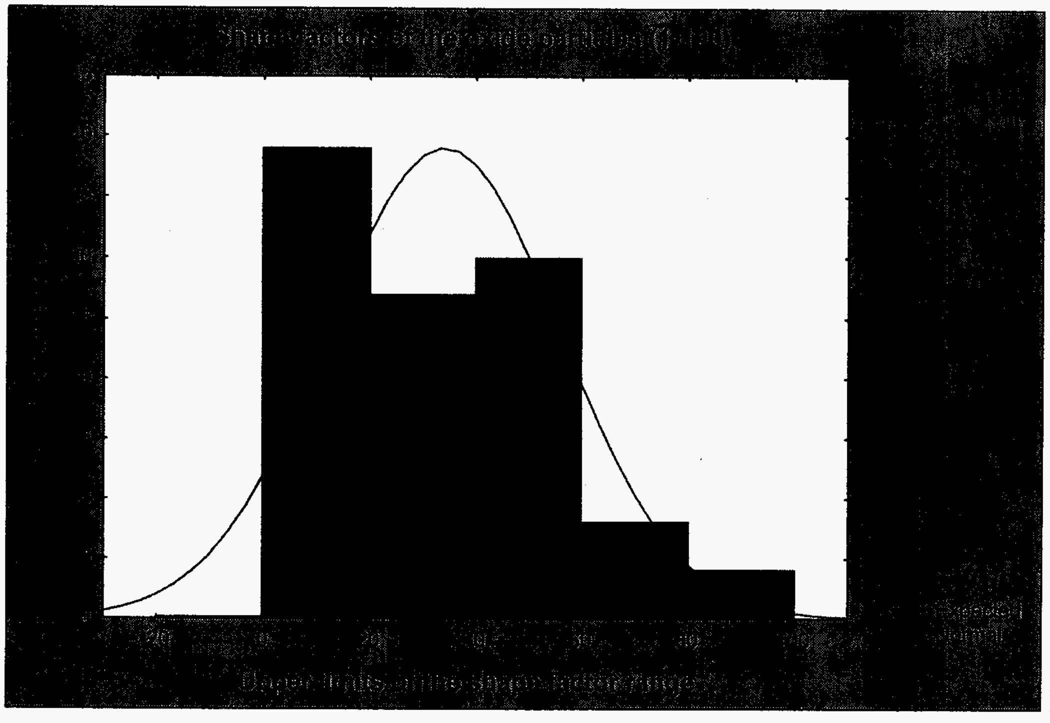

Figure

Figure 3: Shape Factors of the Oxide Particles (1-100)

Table 1 shows the specific chemical compositions of the alloys used at sites #1, #2, and #3 for the testing.

Table 1: Alloy Chemistries

Alloy	Si	Fe	Cu	Mn	Mg	Cr	Ni	Zn	Ti
356 (site #1)	6.8 %	0.6%	0.25%	0.35%	0.2%	-	-	0.35%	0.1%
A356 (site #2)	7%	0.2%	0.2%	0.10%	0.46%	-	-	0.1%	0.28%
319.1 (site #3)	6%	0.5%	3%	0.5%	0.1%	-	0.35%	1%	0.24%

After all the readings of all the tests had been obtained, their values were averaged assuming a normal distribution, as the standard deviation obtained appeared permissible. Also, the number of samples was not sufficient to establish a statistical distribution function.

The steps obtained in the Qualiflash experiments were translated to ratings using appropriate conversion charts [17]. A sample spreadsheet used for the calculations is shown in Table 2 to portray the variation in the readings obtained. In Table 2, we see the five consecutive measurements made using the Alscan- noted as A.1 through A.5. Similarly, measurements for the Qualiflash and the LAIS are given as Q.1 through Q.6 and L.1 though L.10, respectively. It is clear that scatter exists in the measurements. In this vein, the mean and the standard deviation for each measurement technique is given below in Table 3.

Table 2. Sample spreadsheet for cleanliness data obtained for a single melt condition

ALSCAN			QUALIFLASH					LAIS	
Run no.	ml/100g H_2	Temperature (°C)	Run no.	Temp. funnel (°C)	Temp. melt (°C)	Steps	Rating	Run no.	Oxide count (sq. mm/kg)
A.1	0.209	732	Q.1	435	700	4	6	L.1	0.84
A.2	0.204	732	Q.2	450	698	3.5	8	L.2	0.74
A.3	0.2	732	Q.3	452	720	3	11	L.3	0.85
A.4	0.199	732	Q.4	455	721	4	9	L.4	0.91
A.5	0.199	733	Q.5	451	721	4	9	L.5	0.93
			Q.6	448	715	3	12	L.6	0.75
								L.7	1.24
								L.8	0.93
								L.9	1.32
								L.10	1.21

Table 3. Average Values and Standard Deviations for Cleanliness Indices

	ALSCAN(ml/100g H_2)	**QUALIFLASH RATING**	**LAIS OXIDE COUNT(sq. mm/kg)**
Mean	0.2022	9.16	0.975
Standard deviation	0.0034	1.56	0.157

Site # 1

Results from the analysis at site #1 are given in Table 4. The effects of the cleaning treatments at this site are also graphically represented in Figures 4 - 6. As can be seen, for three different melt conditions, M1 (dirtiest), M2, and M3 (cleanest) results from Alscan, LAIS and Qualiflash as well as tensile properties are given. Figure 7 shows LAIS oxide count as a function of measured percent elongation. As expected, the highest elongation was observed at the lowest oxide count. Figure 8 shows Qualiflash ratings as a function of measured percent elongation with a similar trend as before. Figures 9 and 10 relate the LAIS oxide count and Qualiflash ratings with measured UTS values, respectively.

Table 4: Melt cleanliness results (Site #1)

Melt Condition	Alscan (ml/100g)	LAIS (sq. mm/kg)	Qualiflash (1-20)	UTS (MPa)	%Elongation (2" extensometer)
M1 No filter, No degass	**0.2022**	**0.975**	**9.16**	**183.05**	**5.63**
M2 30 ppi CFF, No degass	**0.22**	**0.572**	**3.83**	**198.12**	**7.54**
M3 30 ppi CFF, 20 min. degass ($Ar:Cl_2=1:9$)	**0.1646**	**0.605**	**5.88**	**195.65**	**7.72**

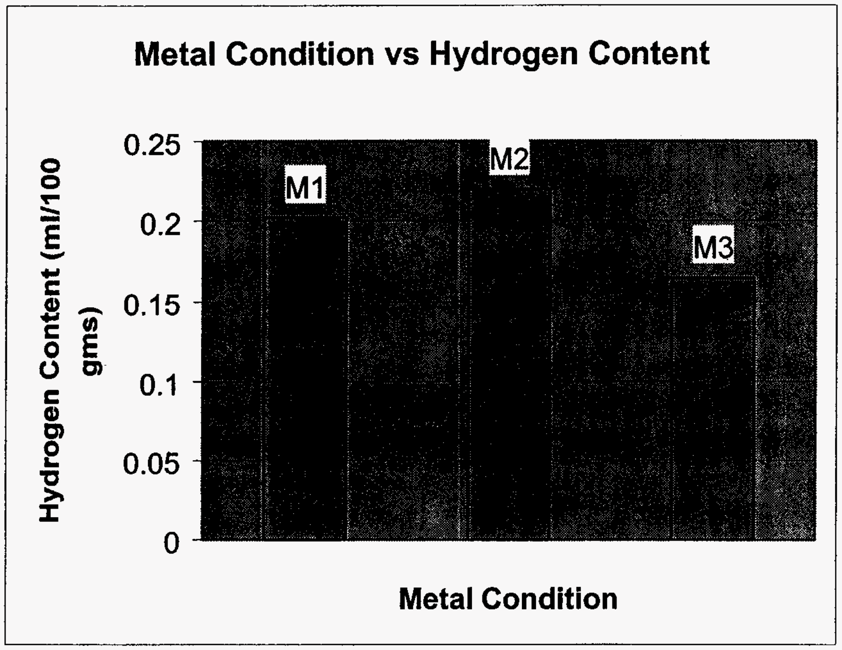

Figure 4. Metal Condition vs Hydrogen Content (Site #1)

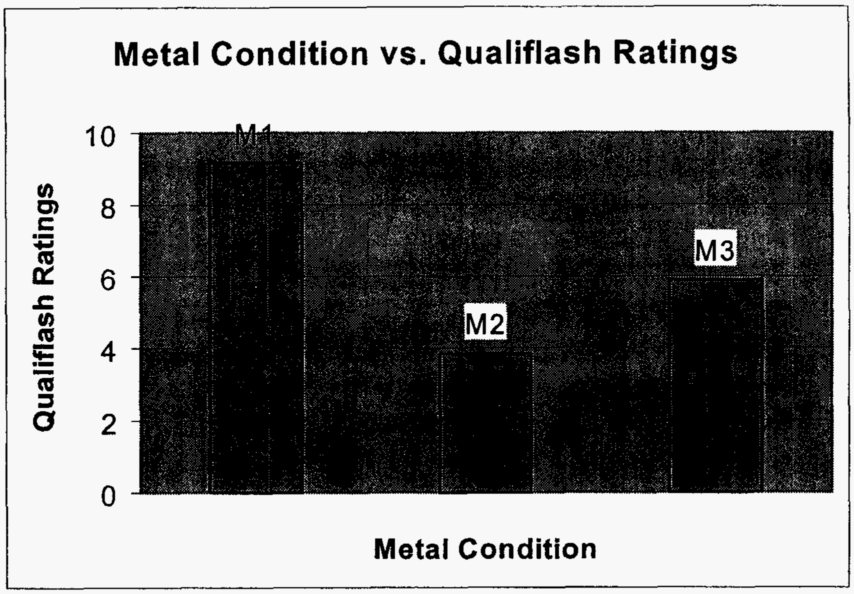

Figure 5. Metal condition vs Qualiflash ratings (Site #1)

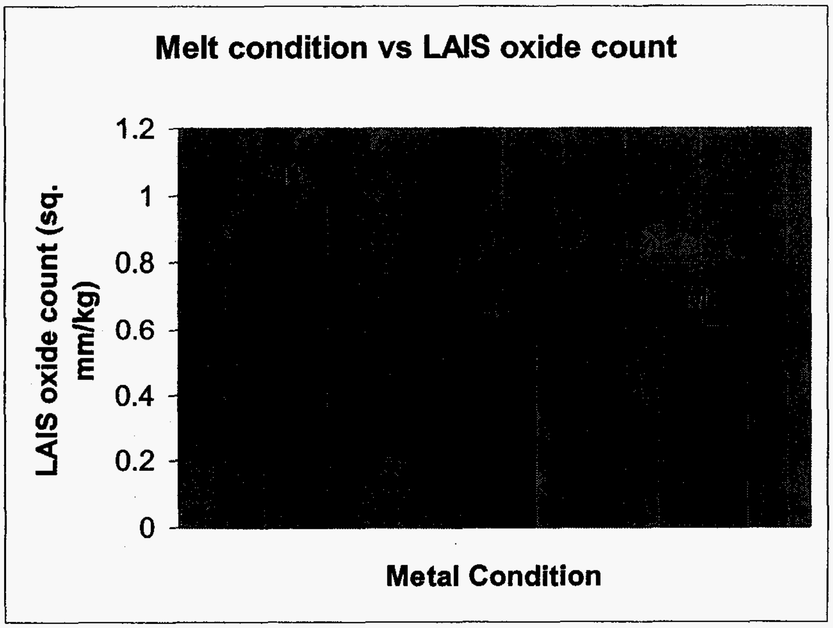

Figure 6. Metal Condition vs LAIS oxide count (Site #1)

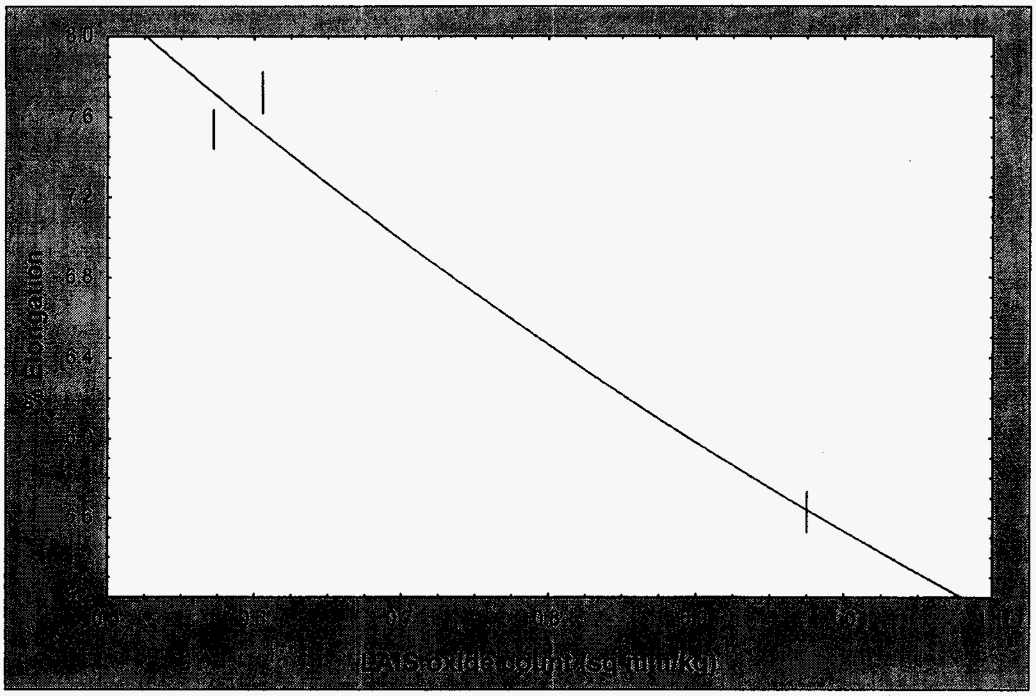

Figure 7. % Elongation vs LAIS oxide count (Site #1)
(Each data point is an average of several values)

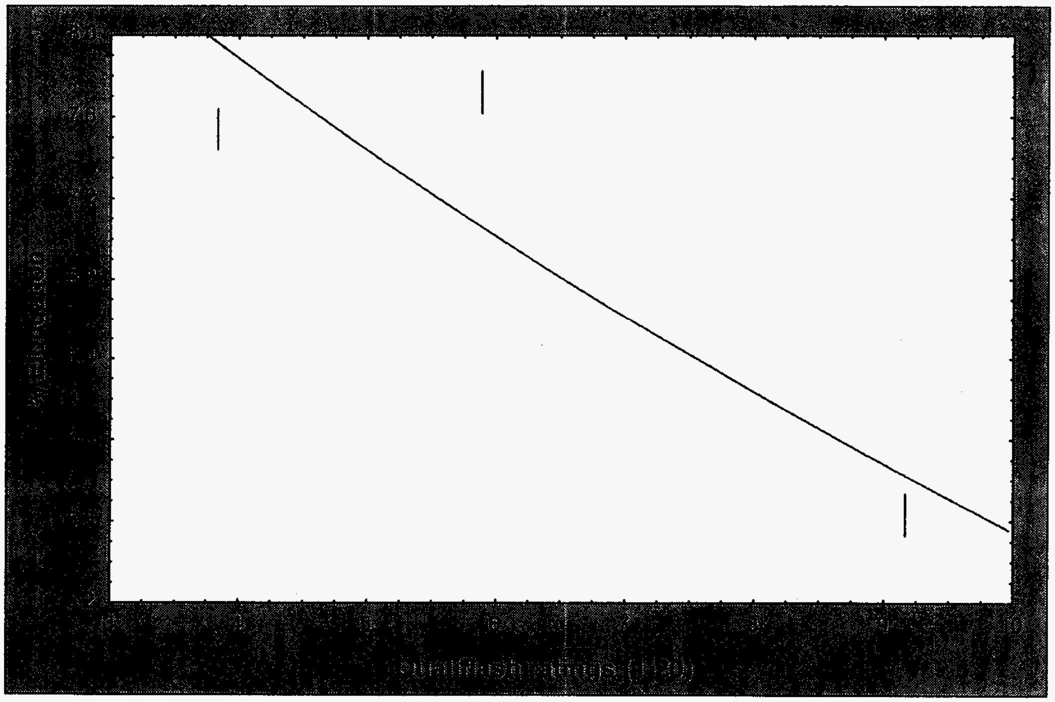

Figure 8. % Elongation vs Qualiflash Ratings (Site #1)
(Each data point is an average of several values)

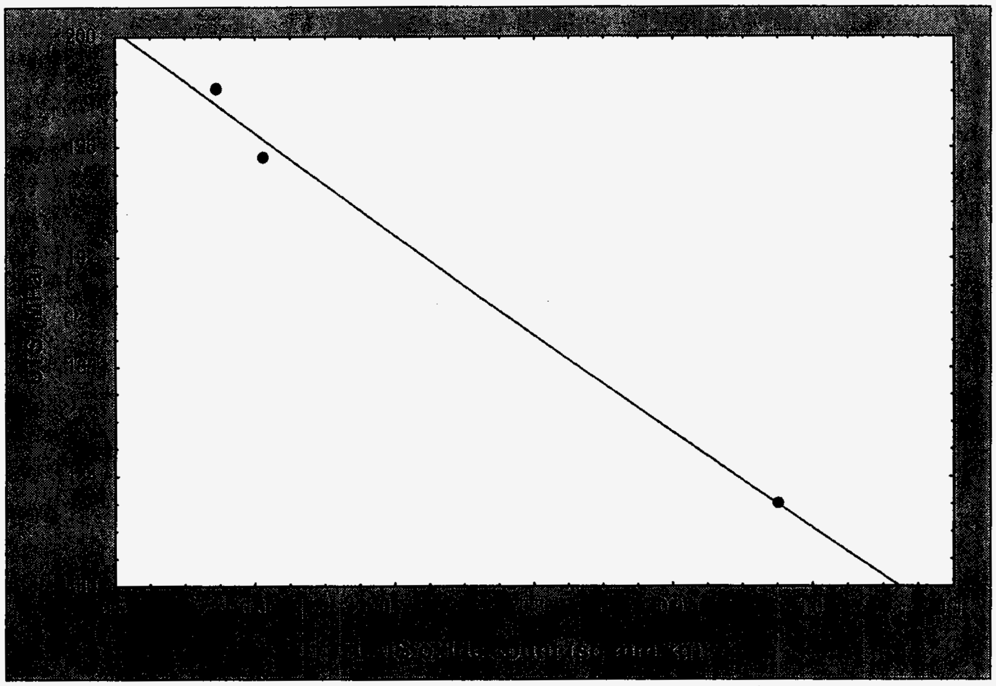

Figure 9. UTS vs LAIS oxide count (Site #1)
(Each data point is an average of several values)

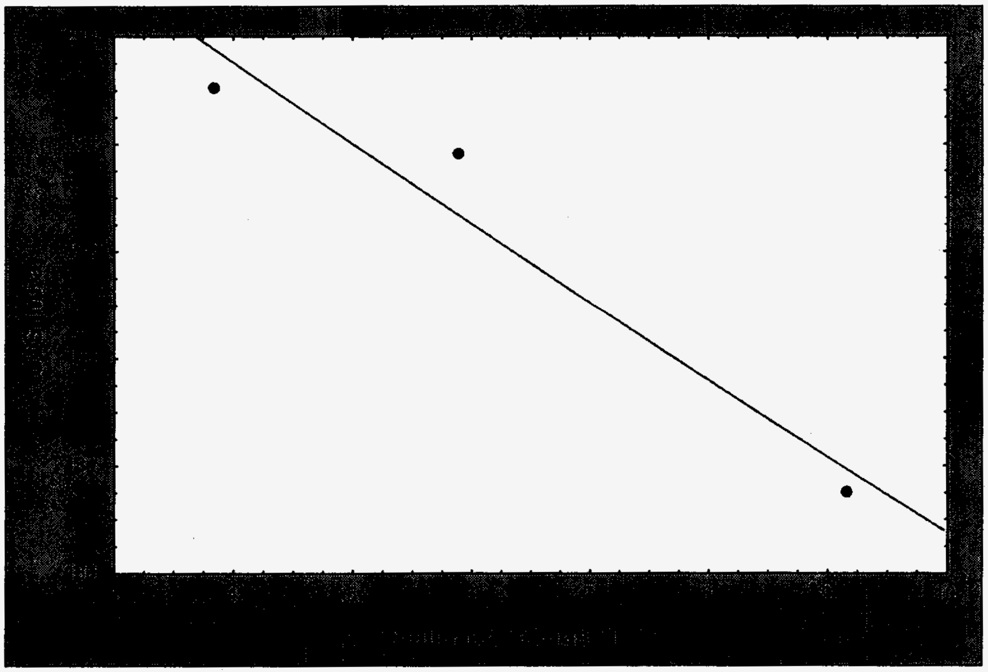

Figure 10. UTS vs Qualiflash Ratings (Site #1)
(Each data point is an average of several values)

Site #2

The results from the analysis at site #2 are given in Table 5. The effects of the cleaning treatments at this site are also graphically represented in Figures 11-13. Similar to site #1, three different melt conditions were evaluated: M1, M2 and M3. Results from Alscan, LAIS and Qualiflash, as well as tensile properties are shown and relevant plots are depicted in Figures 14 and 15.

Table 5: Melt cleanliness results (Site #2)

Metal Condition	Alscan (ml/100g)	LAIS (sq mm/kg)	Qualiflash (1-20)	UTS (MPa)	%Elongation (2" extensometer)
M1 No degass	0.179	1.16	8	176.46	3.587
M2 30min. degass (Ar) Using rotary impeller	0.14	0.779	8	176.72	3.701
M3 40 min. degass ($Ar:Cl_2=1:9$)	0.126	0.7824	8	178.53	4.168

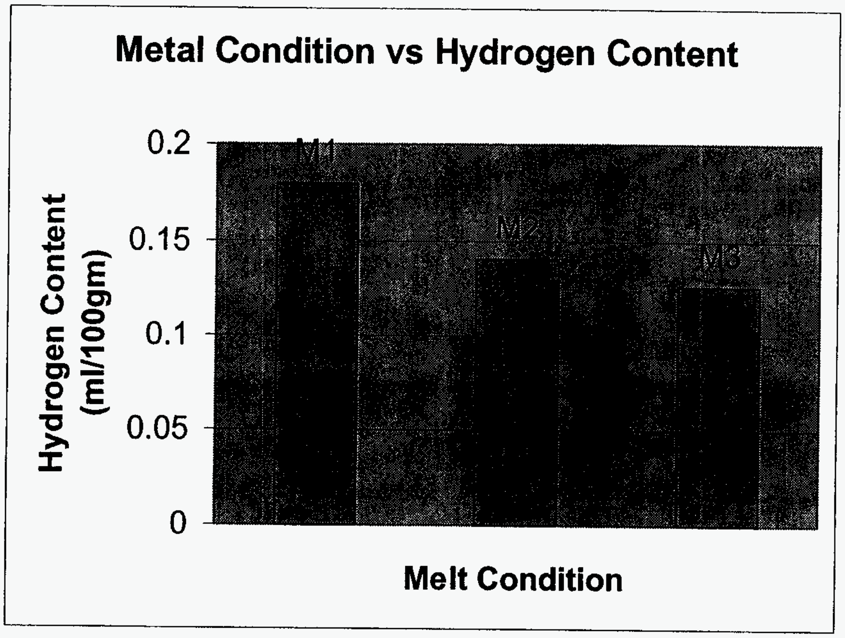

Figure 11. Metal Condition vs Hydrogen Content (Site #2)

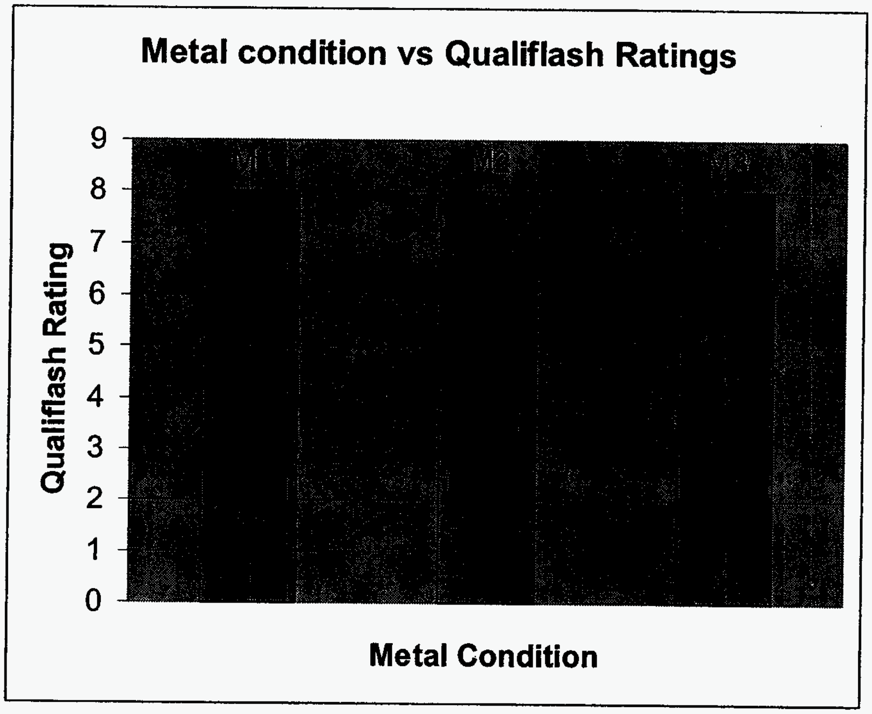

Figure 12. Metal Condition vs Qualiflash Ratings (Site #2)

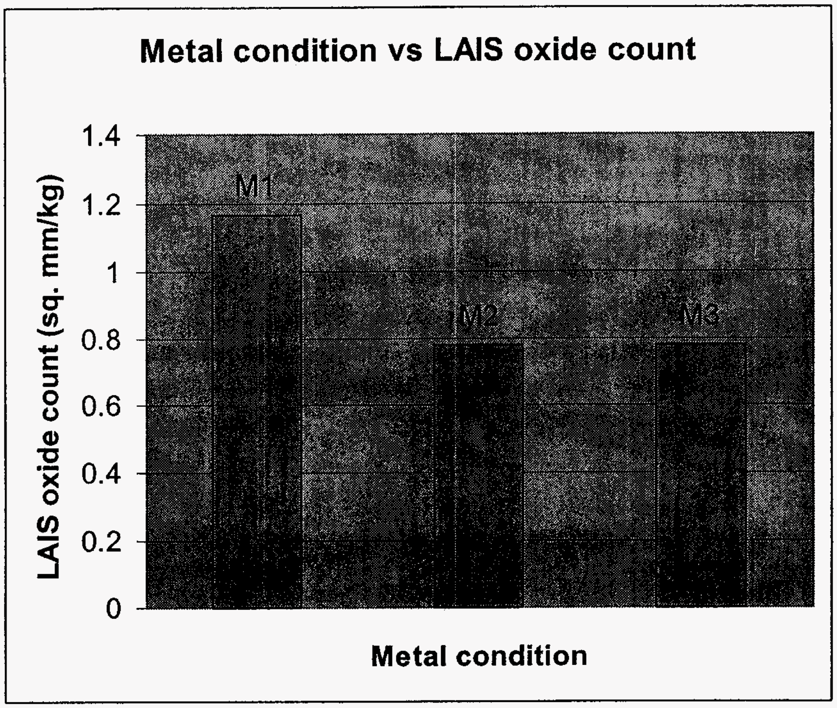

Figure 13. Metal Condition vs Qualiflash Ratings (Site #2)

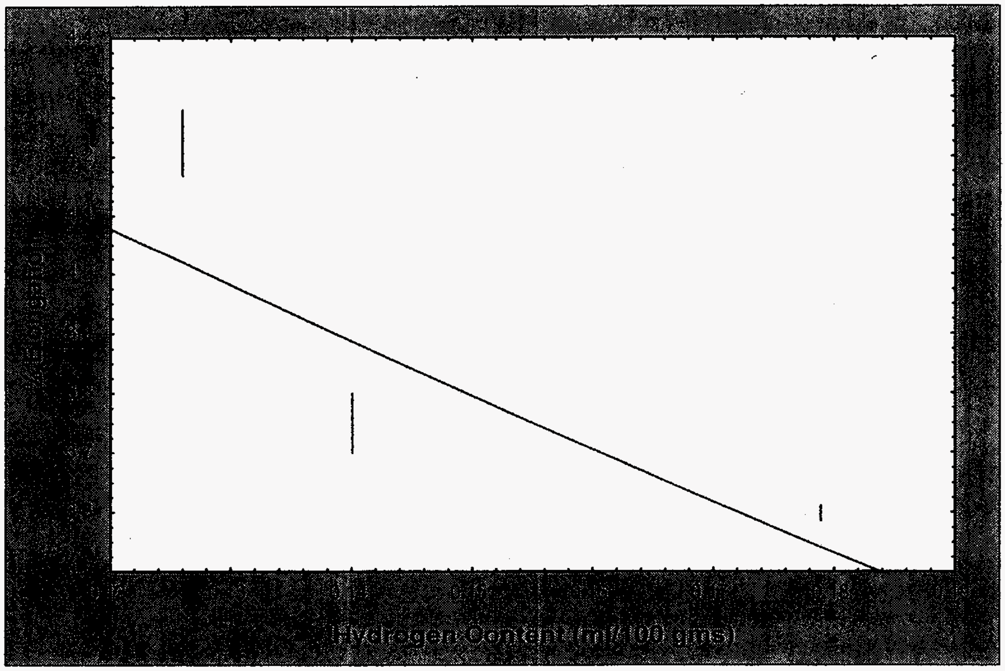

Figure 14. % Elongation vs Hydrogen Content (Site #2)
(Each data point is an average of several values)

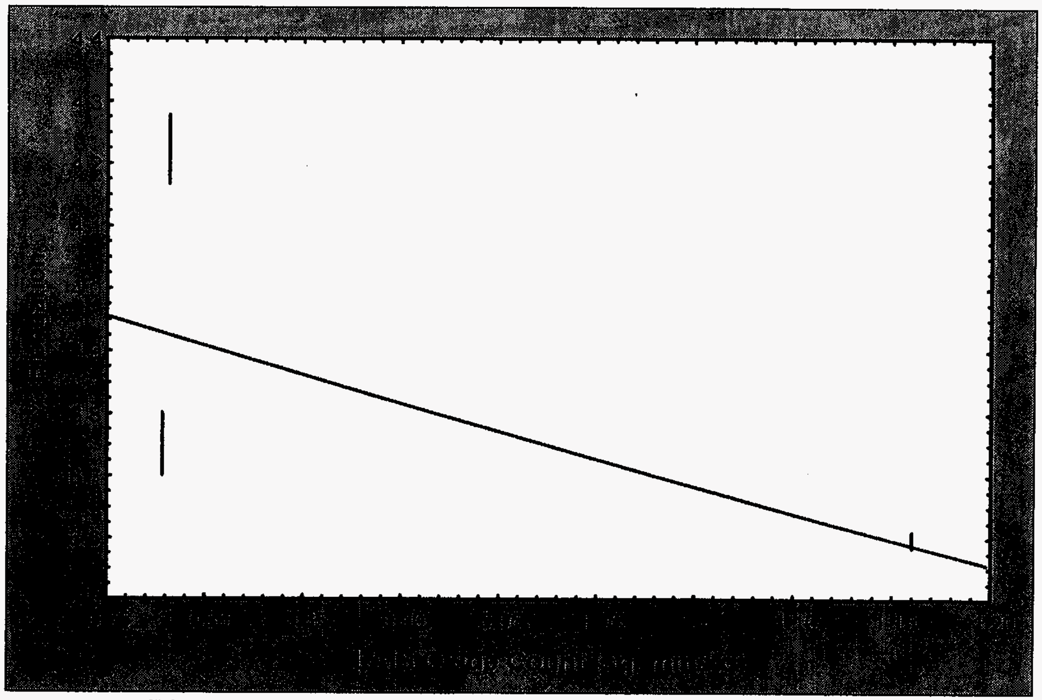

Figure 15. % Elongation vs LAIS oxide count (Site #2)
(Each data point is an average of several values)

Site #3

Results from the analysis on site #3 are presented in Table 6. The effects of the cleaning treatments at this site are also graphically represented in Figures 16-18 as before. The four different melt conditions have been designated by M1 (dirtiest), M2, M3 and M4 (cleanest). Alscan, LAIS and Qualiflash values have been represented as a function of percent elongation in Figures 19-21.

Table 6: Melt cleanliness results (Site #3)

Metal Condition	Alscan (ml/100g)	LAIS (sq mm/kg)	Qualiflash (1-20)	UTS (MPa)	%Elongation (2" extensometer)
M1 Regassed for 10 hrs, No filter	**0.287**	**1.32**	**17.5**	**222.81**	**1.202**
M2 lance degass (N_2),outside the crucible	**0.23**	**0.92**	**16**	**199.86**	**0.980**
M3 lance degass (N_2),inside the crucible	**0.22**	**0.86**	**16**	**236.50**	**1.708**
M4 Lance degass (N_2)+30ppi alumina filter	**0.181**	**0.5236**	**13**	**243.90**	**2.304**

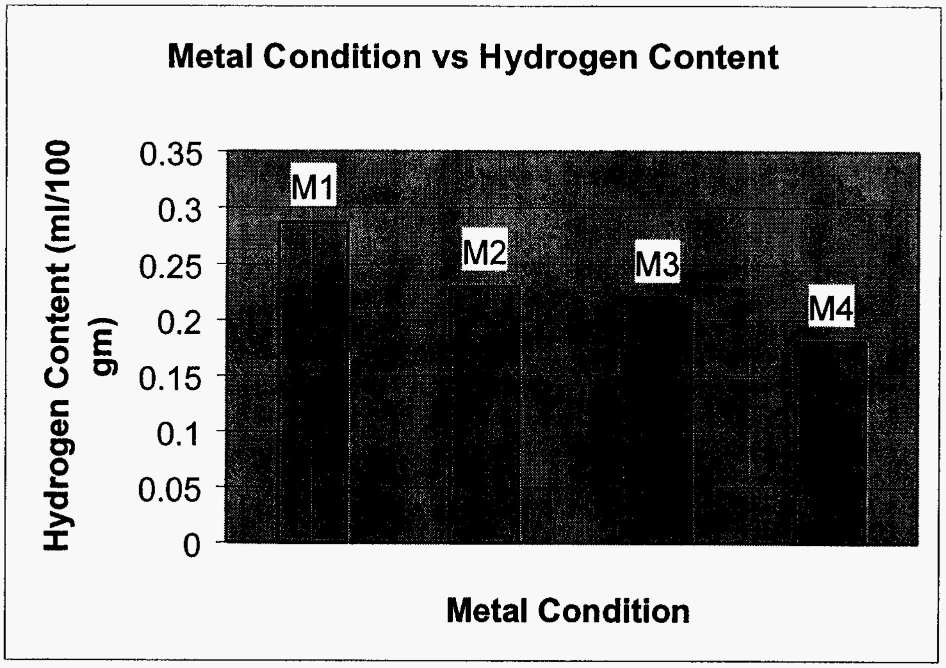

Figure 16: Metal Condition vs Hydrogen Content (Site #3)

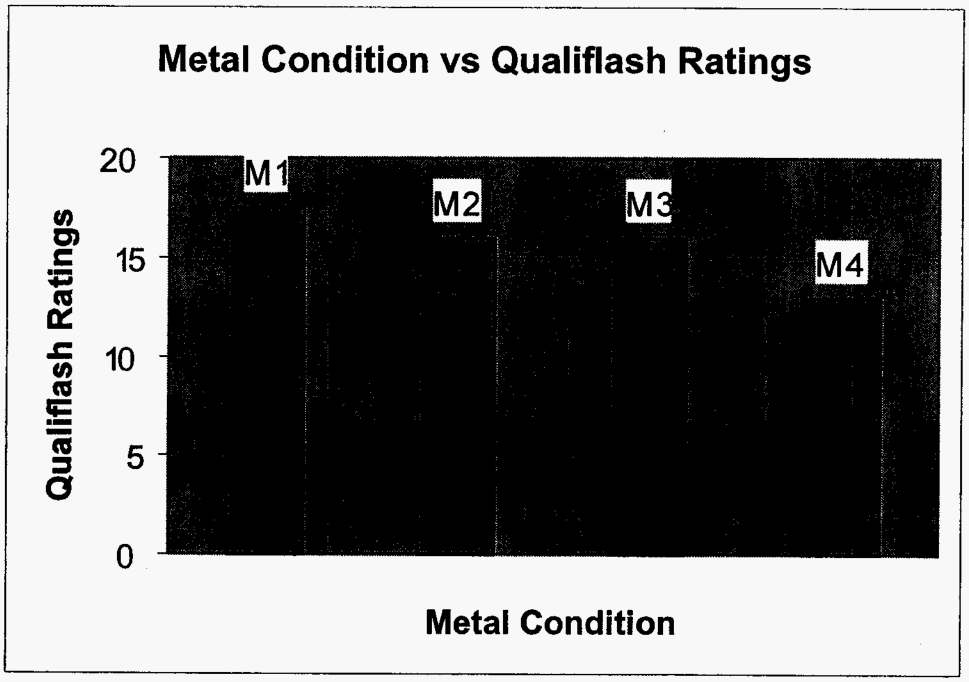

Figure 17. Metal Condition vs Qualiflash Ratings (Site#3)

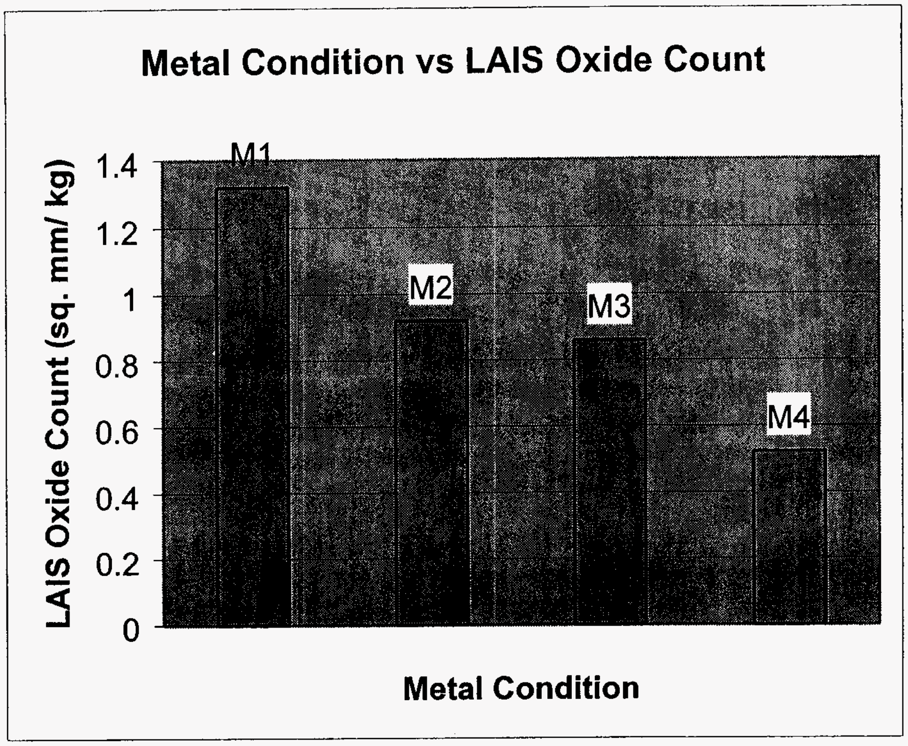

Figure 18. Metal Condition vs LAIS oxide count (Site #3)

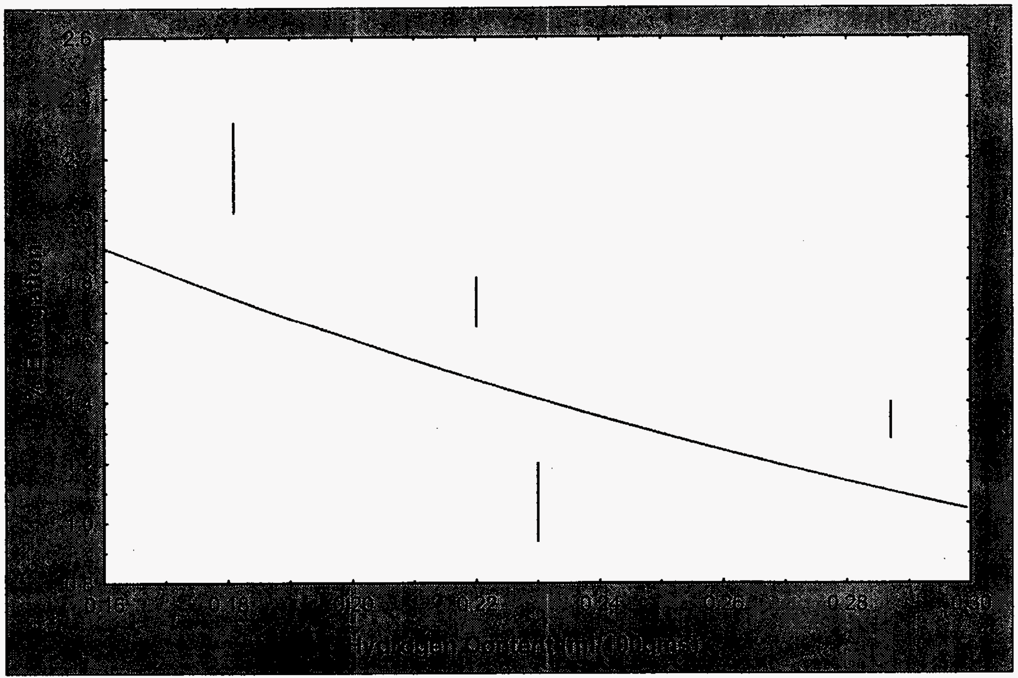

Figure 19. % Elongation vs Hydrogen content (Site #3)
(Each data point is an average of several values)

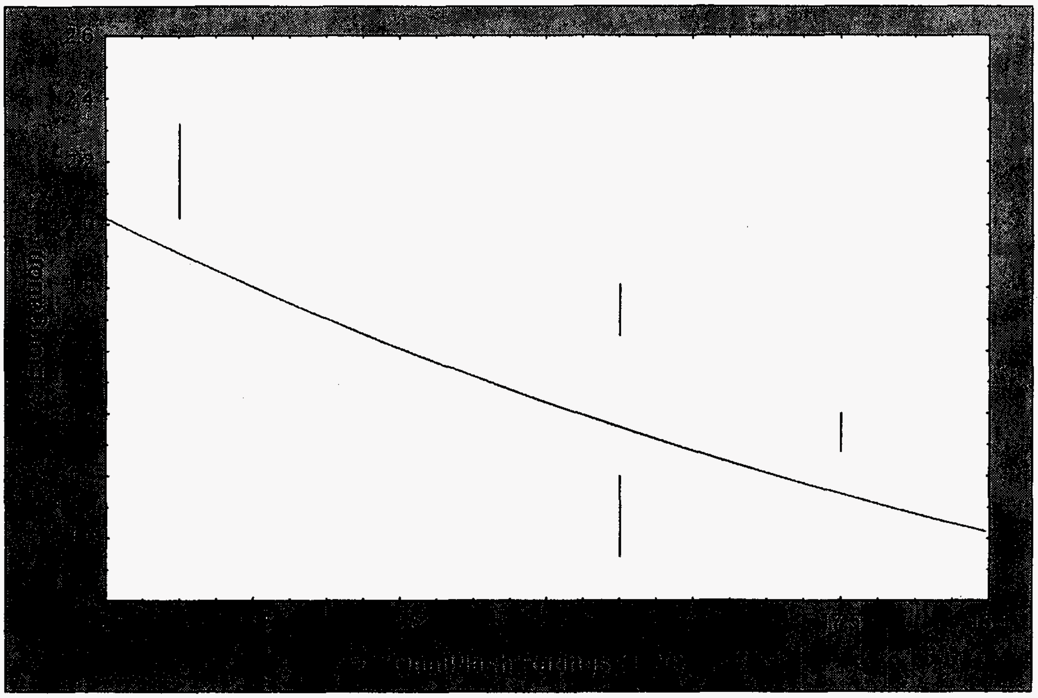

Figure 20. % Elongation vs Qualiflash Ratings (Site #3)
(Each data point is an average of several values)

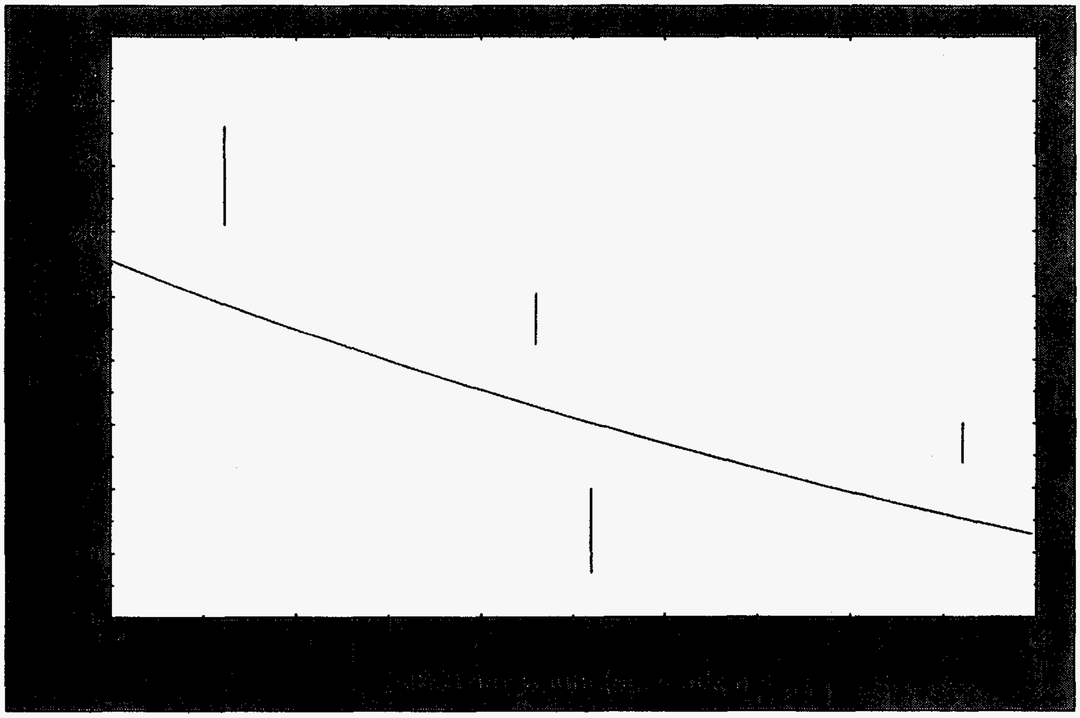

Figure 21. % Elongation vs LAIS oxide content (Site #3)
(Each data point is an average of several values)

Figures 22 through 25 show some typical LAIS microstructures that have been obtained through digital image analysis. Figure 22 shows a large oxide skin present in the alloy matrix. Figures 23 through 25 show the presence of varying amounts of oxide particles very close to the frit.

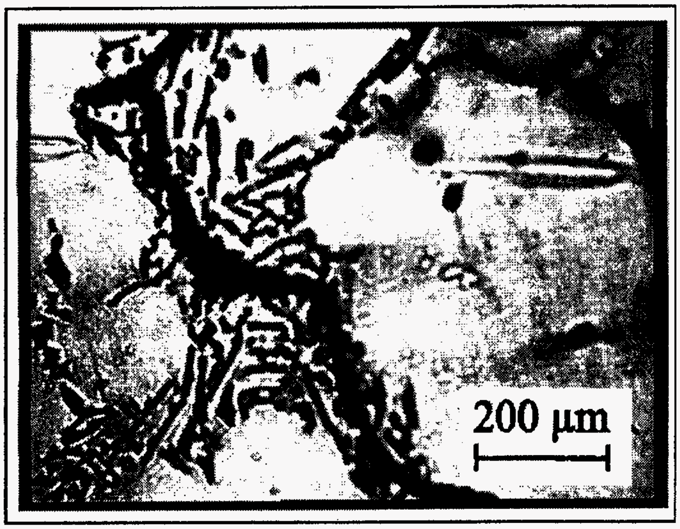

Figure 22. LAIS thermal showing oxide large oxide skin

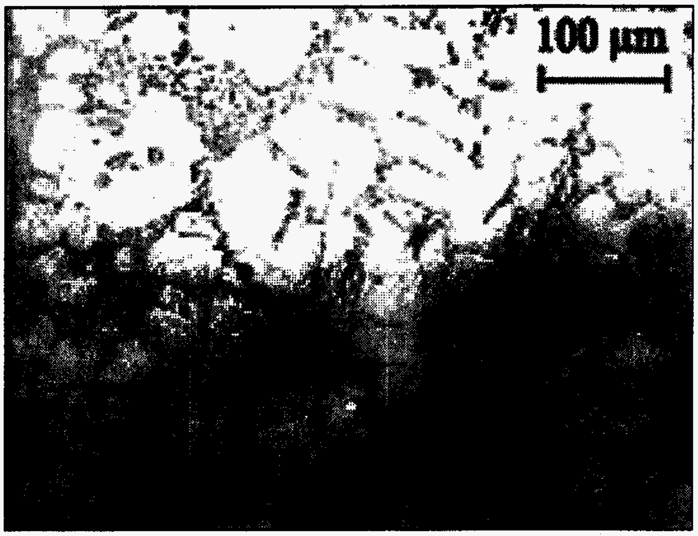

Figure 23. Relative absence of oxides near the frit

Figure 24. Dark oxide phases interspersed within the frit

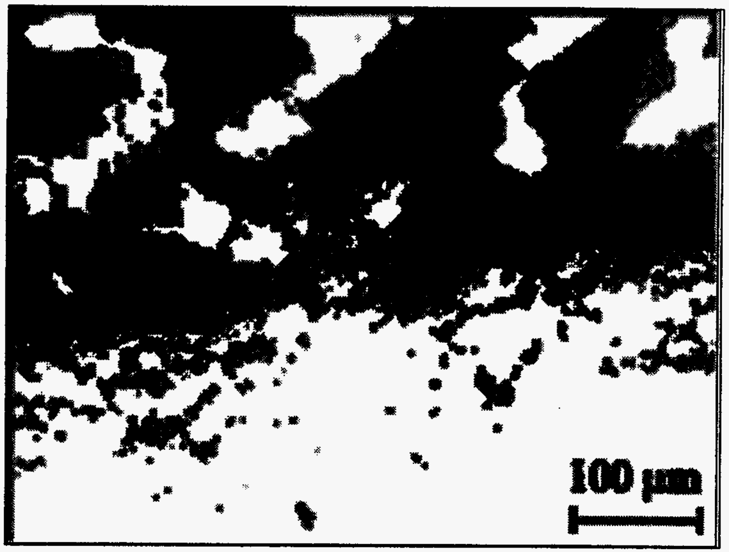

Figure 25. Digitally enhanced image showing dark oxide skin along the frit

Figures 26 and 27 are stereo pictures of 319 alloy that has failed under tensile loading. They show the topography of the fracture surface and the origin of the failure. Figures 28 and 29 are similar pictures for the 356 alloy. Figures 30 - 34 are fractographs of 319 alloy to show foreign phases and cavities as possible sites for failure initiation.

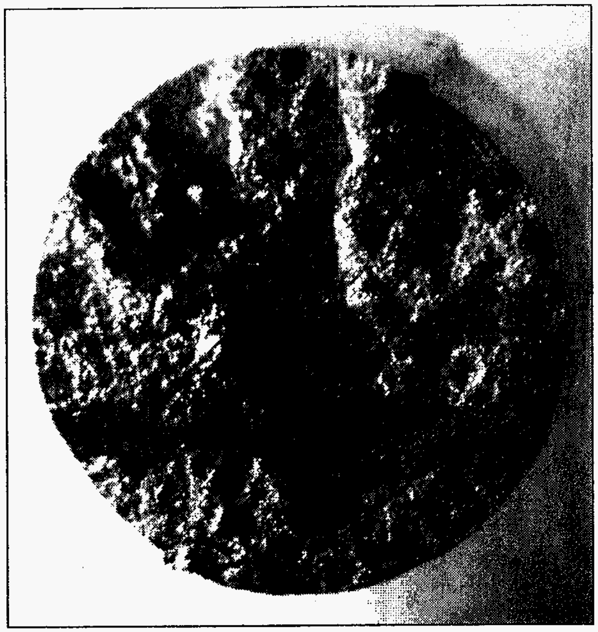

Figure 26. Stereo Picture of Fracture Surface after Uniaxial Tensile Testing of Aluminum 319 Alloy

Figure 27. Macro View of Oxide Particles on the Surface of Aluminum 319Alloy Testbar, broken under Uniaxial Tensile Loading

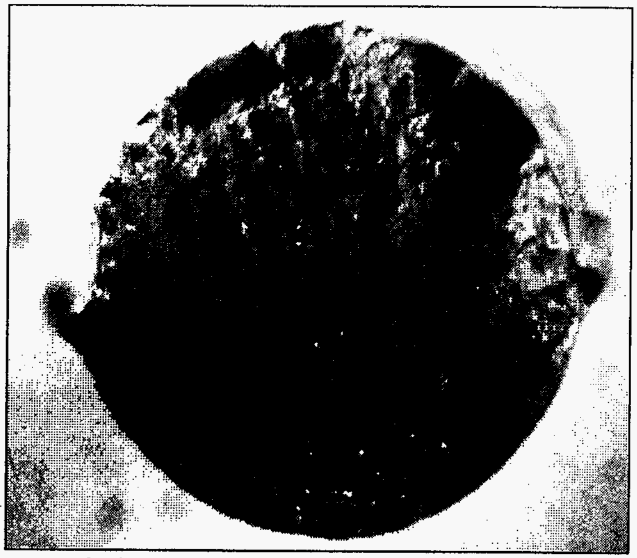

Figure 28. Characteristic Fracture Surface of Aluminum 356 Under Uniaxial Tensile Loading.

Figure 29. Fracture Surface after Uniaxial Tensile Testing of Aluminum 356 Alloy, Showing Pores

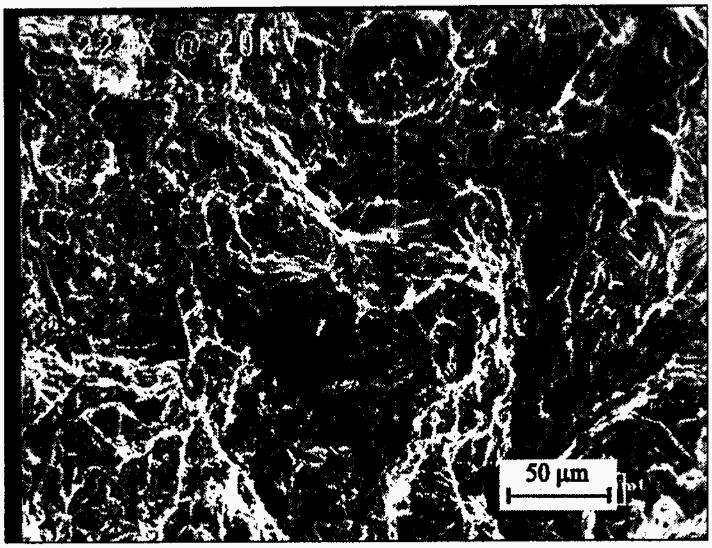

Figure 30. SEM Fracture Surface of Aluminum 319 Alloy Under Uniaxial Tensile Loading, Showing the Intermetallic Phase and the Ligaments of Aluminum Matrix at 280X @ 20 KV

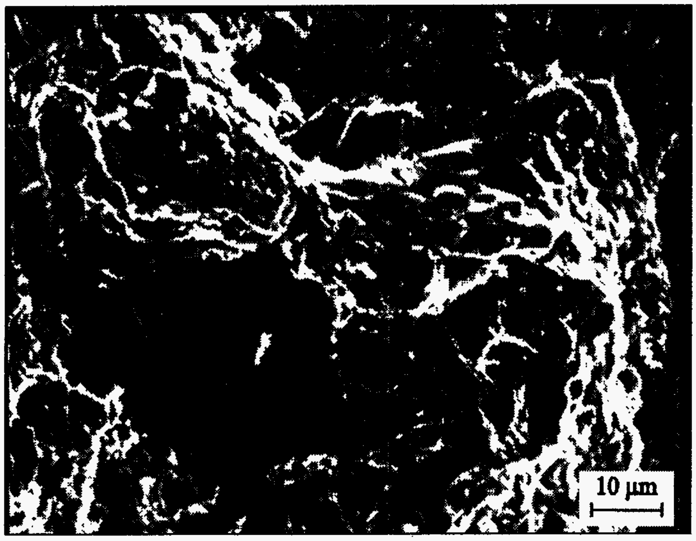

Figure 31. SEM Fracture Surface of Aluminum 319 Alloy Under Uniaxial Tensile Loading, Showing the Intermetallic Phase and the Ligaments of Aluminum Matrix at 1000X @ 20 KV

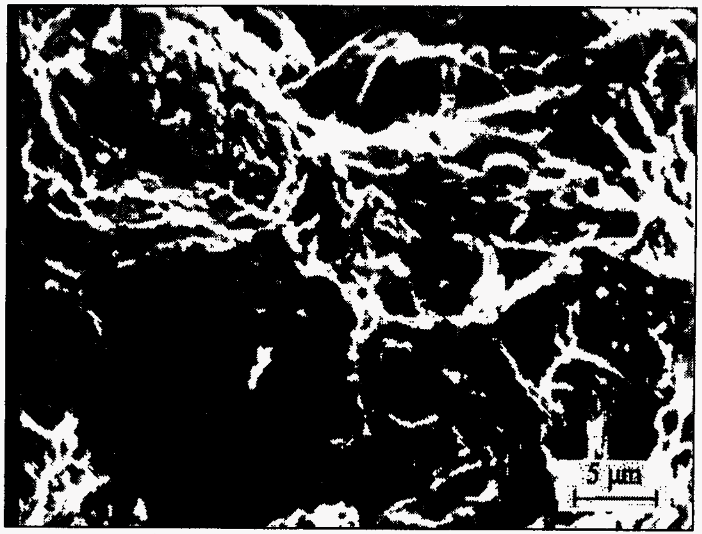

Figure 32. SEM Fracture Surface of Aluminum 319 Alloy under Uniaxial Tensile Loading, Showing the Intermetallic Phase and the Ligaments of Aluminum Matrix at 2000X @ 20 KV

Figure 33. SEM Fracture Surface of Aluminum 319 Alloy under Uniaxial Tensile Loading, showing One Prominent Oxide Particle (Inverse Imaging) at 25X @ 20 KV

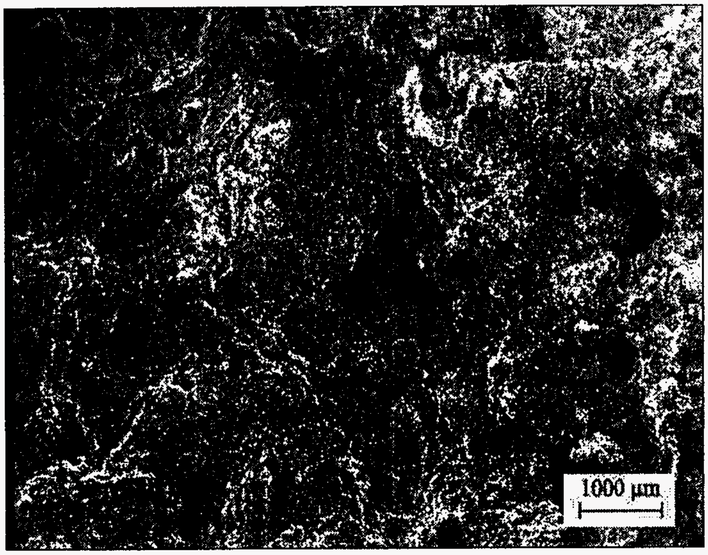

Figure 34. SEM Fracture Surface of Aluminum 319 Alloy under Uniaxial Tensile Loading, showing Shrinkage Cavity due to Excessive Oxide Distribution at10X @ 20 KV

The results of Figure 2 delineate the size distribution of the larger particles. It is clearly evident that most of the oxide particles are in the 0-10 micron size range. The distribution is skewed towards the lower size range of the oxide particles. Plotting a normal distribution we observe a peak at about 11 microns, which can be said to be the average size of the oxide particles. Particles below 2 micron were not included in the analysis. It is also to be noted that these analyses were done on untreated melts hence the oxide size range observed is obviously at the higher end of the spectrum.

Figure 3 shows the distribution of the shape factors multiplied by a factor of 100. There is skewness in the distribution towards the lower end but only very slightly. Hence it could be inferred that most of the oxides have shape factors varying from 0.2 to 0.6, hence the particles are not very equiaxed. This would imply that the oxides could act as stress concentrators and because of their shape; they could give rise to directional misfit thus facilitating failure of the part.

The results show the variation of three cleanliness indices with respect to Hydrogen and oxide content of the molten metal. The variation in each cleanliness index is subject to the local conditions of the cast shop. Many external factors are bound to affect the inherent gas and oxide contents of the melt. However, some general observations can be made and these are discussed below.

The Alscan measurements had the least degree of scatter among the three indices. There is a general decrease in hydrogen content with degassing, which is as expected. Tables 4, 5, and 6 and Figures 4, 11 and 16 show the hydrogen content at each melt condition for sites #1, #2 and #3 respectively. However, it was generally observed that the concentration of hydrogen varied with metal treatments in a relatively small range. In site #2 the metal condition was altered by degassing alone. However, the gas varied from a low value of 0.126 (maximum degas) to a high value of 0.179 (no degas) - See Table 5 and Figure 11.

There was a similar trend in all the other sites. This shows that the shop floor environment, in general, is not very conducive to removal of hydrogen. A possible explanation could be the ambient humidity of the plants. The experiments were conducted at a time when the average humidity ranged between 70%-80%. This may have caused hydrogen pickup after degassing relatively fast. Thus regassing kinetics is an issue that needs further attention and is not an insignificant factor.

There was no appreciable difference between filtered and unfiltered metal in terms of gas content. (See Tables 4 and 6 and Figures 4 and 16). Site #3 did show lower hydrogen content for the filtered metal than the unfiltered metal, but this was probably due to the fact that the degassing lance was running for more time in the filtered metal than the unfiltered metal.

It was also observed that melts made from primary metal indicated lower gas levels in the untreated state than those melts made from remelted or secondary metal.

The Qualiflash ratings were also obtained for each metal condition at each site. At site #1 (See Table 4, Figures 4-6), ratings revealed that both degassed and filtered metal were significantly cleaner than the untreated metal. However, the ratings were identical irrespective of gas content at site #2. The nature of the test suggests that the gas content should not result in a 'dirtier' count. Excessive gas in metal can increase its flowability in which case the metal albeit "dirty" can still flow thru the filter quite easily and give a dirtier Qualiflash rating. This may explain the discrepancy obtained in the Qualiflash readings at this site.

Filtered metal showed lower ratings (cleaner) than unfiltered ones at sites #1 and #3 as shown in Tables 4 and 6. This was as expected. On an absolute scale, ratings varied from about 4 (cleanest) to 17 (dirtiest melt) as seen from Tables 5.4-5.6 and Figures 5, 12 and 17. Again, it was observed that primary metal had cleaner ratings than secondary metal.

The oxide content in terms of the LAIS values show clearly that filtered metal is a lot shorter on oxides than unfiltered metal. The values in sq. mm/kg vary from a low of about 0.215 to a high of 1.32. The oxide content seems to be lower for degassed metal than undegassed metal. (See Tables 4-6 and Figures 6, 13, 18). This suggests that formation of oxides is related directly to the hydrogen content in the melt. The LAIS correlates to an extent with the Qualiflash but it is more sensitive to hydrogen content than the latter.

The LAIS microstructures reveal a variety of different oxides ranging from 10 to 60 microns in size. These stay clogged near the frit. The most commonly observed oxides are films, which appear as a black line just above and touching the top of the frit. Particulate oxides were rare. A lot of spinels (magnesium aluminum oxides) were observed at site #2. These were probably caused by magnesium burning out because of the high temperature of the melt (about 780 Celsius) [18]. A fairly large spinel can be seen in Figure 22. The frit is seen as dark grey in the micrographs. Figure 23 shows a relatively clean melt, as there are hardly any particulate or skin type of oxides between the white matrix and the dark filter. Figure 24 shows a good contrast between the dark oxide phase and the gray filter phase. It also shows oxide phases interspersed between the graphite particles of the frit. In Figure 25, which has been enhanced digitally, a layer of dark oxide film on top of the frit is quite discernable.

Inclusions other than oxides were also present, mostly as grain refiners. However they were always less than 2 microns and so were not considered critical for calculating LAIS oxide count.

The plots were made with data points obtained at each metal condition (See Figures 7-10, 14-15, 19-21). The points obtained in all the curves have been fitted to an exponential function using STATISTICA. It should be noted that this has been done merely to illustrate and suggest a generic trend. These curves should not be considered as "Correlation curves" because they could be misleading in that respect. The scope of the testing allowed for the establishment of 3 or 4 data points which is far cry from being sufficient for establishing correlation curves.

The effect of oxides and Qualiflash ratings on the percent elongation at site #1 appears to be significant (see Figures 7 and 8). There is an increase in the percent elongation as we go from the dirtiest melt (M1) to the cleanest melt (M3). The graph shows a good correlation with LAIS oxide counts. The higher the oxide count, the lower is the percent elongation. This is justified because oxides, especially of the larger size range, can act as stress concentrators and owing to their inherent brittle nature, can induce brittleness and loss of ductility in the cast parts. At this site, the increase in elongation owing to the melt treatments carried out is almost 40%, which is significant. It would seem that for sand casting, melt cleanliness is an issue and needs to be addressed for improving the performance of the cast product. There was no real trend observed between the percent elongation and hydrogen content. This is in accordance with a previous study by M.J. Young where the effects of porosity on tensile properties were found to be insignificant for the levels of hydrogen obtained [19]. The hydrogen values obtained here were not vastly different from each other owing to the prevalence of high ambient humidity during the testing. In spite of this, the highest hydrogen value did correspond to the lowest percent elongation. High hydrogen values could facilitate pore formation in the cast part. Pores provide a triaxial state of stress and have been known to be common crack initiators. Hence they are instrumental in reducing the percent elongation of the cast parts.

The percent elongation also correlates with Qualiflash ratings at this site, suggesting that the technique is capable of being used to characterize melt conditions.

At site #2, the differences in melt conditions were obtained by degassing alone and as such, not very wide differences in melt conditions were obtained. However the Qualiflash showed the same reading for all three conditions and hence was not of aid in melt characterization for this site. A possible reason for this could be that the metal used here was held at about 140° superheat. At this high temperature, the high fluidity of the melt could offset the ability of the test to discern differences in melt cleanliness. There were essentially only 2 different oxide levels and there was some degree of correlation of the percent elongation for both oxides and hydrogen. The effect of percent elongation was minimal (see Figures 14 and 15), however, and in going from the dirtiest melt to the cleanest melt, an improvement of less than 10% was observed. This was within the range of error existing during the calculation of the percent elongation during tensile testing. The oxide values obtained here were at the higher end of the spectrum since there was no filtration performed on the melt. This may have caused a lack of sensitivity to the percent elongation measured in the test bars.

The tensile properties at site #3 were extremely sensitive to the cleaning treatments. The percent elongation of the 319 (the alloy used here) is inherently low (reported as circa 1.5% for as-cast alloy in the "Standards For Aluminum Sand and Permanent Mold Castings " as was observed during the testing. However from proceeding from the dirtiest to the cleanest melt, an improvement in percent elongation of almost 80% was observed (see Figures 19-21). The scatter obtained in the percent elongation data was less than 10% hence leaving little doubt as to the amelioration in properties with treatment.

In all the sites, the UTS was similarly affected as the % elongation but the effect was sometimes minimal or within the error margins. Hence the behavior of the UTS with melt cleanliness is inconclusive. The exception to this was the 356 alloy used at site #1 (see Figures 9 and 10), which also, incidentally, had the highest % elongation among all the three alloys.

Hence it would appear that cleanliness treatments are effective in both sand and permanent mold casting technologies. The effect is tremendous in permanent mold castings that imply that the sand casting process is not as clean as the permanent mold process, and it introduces some dirt in the metal while it is being cast. Thus the sand casting process reduces the sensitivity of the metal to prior cleanliness treatments.

In summing up, it can be concluded that by and large the tensile properties are sensitive to the melt treatments before the casting process and the current melt refining techniques do result in enhancing the performance of the cast parts. The effect, as discussed before, is more prominent in permanent mold casting than sand casting. Depending on the application of a part, melt treatment can decisively be used to monitor the properties of the cast part. Oxides and hydrogen are both critical, oxides probably being the more critical of the two. Several of the fracture surfaces of bars revealed the presence of easily discernible oxides that were the cause of failure. Some surfaces also showed discernible porosity but they were relatively few. Thus filtration and degassing used in tandem appear to increase the overall cleanliness of the melt and also its properties.

References

1. Gallo, R., "Measurement of Hydrogen Content in Molten Aluminum Alloys using Crucibles and reverbeatory Furnaces for Sand and Permanent Mold Castings", *4th Inter. Conf. On Molten Alum. Proc.*, 1995, Pp. 209-226.
2. Gruzleski, J.E., La Orchan, W., and Mulazimoglu, H., "New Reduced Pressure Test Quantifies Hydrogen Content", *Modern Casting*, September 1995, Pp 47-49.
3. DeWeese, S.K., Atkinson, R., and Rasmussen, W., "RPT Measures Hydrogen Gas, Effects on Casting Quality", *Modern Casting*, April 1992, Pp 29-31.
4. LaOrchan, W., Mulazimoglu, M.H., Chen , X.G., and Gruzleski, J.E., "Quantified Reduced Pressure Test", *AFS Trans.*, 1995, Pp. 565-574.
5. Apelian,D., "How Clean is the Metal You Cast? The issue of Assessment: A Status report", *Light Metals*, 1995, TMS, Pp. 1-15.
6. Abreu, I.A., "Products Used in Treating Aluminum Baths", *AFS International Cast Metals Journal*, Pp. 57-71.
7. Brondyke, K.J. and Hess, P.D., "Interpretation of Vacuum Gas Test Results for Aluminum Alloys", *Trans. TMS-AIME*, 1964, v 230, Pp. 1542-1546.
8. Parmenter, L., Apelian, D., and Jensen, F., "Development of a Statistically Optimized Test Method for the Reduced Pressure Test", *presented at 101st Casting Congress*, 1998, #98-018.
9. Rasmussen, W. and Eckert, C.E., "RPT Gauges Aluminum Porosity", *Modern Casting*, March 1992, Pp. 29-31.
10. Acklin, T.E., "Effect of Sample Size on Density Testing of Aluminum Alloys", *3rd Inter. Conf. on Molten Alum. Proc.*, 1992, Pp. 503-517.
11. Abel Engh, T., Principles of Metal Refining, Oxford University Press, 1992, Pp 1-35.
12. Wang, L., Makhlouf, M., and Apelian,D., "Hydrogen in Aluminum Alloys, Its Measurement and Removal – A Review", a monograph published by AFS, Des Plains, IL, 1998.
13. Lessiter, M.J., "Understanding Inclusions in Aluminum Castings", *Modern Casting*, January 1993, v53, Pp. 29-31.
14. Chen, X., and Gruzleski, J.E., " Influence of Melt Cleanliness on Pore formation in Aluminum-Silicon Alloys", *International Cast Metals Research,* 1966, v 9, Pp. 17-25.
15. Alscan F User's Manual , Bomem Inc., Version 1.2, December 1994.
16. QUALIFLASH User's Manual, Bomem Inc., Revision 1.1, May 1997.
17. Selee Metallurgical Report No. 97-034.
18. Young, M.J., " Correlation of tensile Properties to the Amounts of Gas Porosity in Permanent Mold Test Bars", *AFS Transactions*, 1982, v89, Pp. 465-468.